INDIAN INSTITUTE OF TECHNOLOGY GUWAHATI

Radiative Analysis of Lepton-Proton Scattering via Low-Energy Effective Field Theory

by

Pulak Talukdar

A thesis submitted in partial fulfillment for the degree of Doctor of Philosophy

under the supervison of

Dr. Udit Raha

Department of Physics

November 2020

Department of Physics

Indian Institute of Technology Guwahati

Guwahati - 781039, India, Assam

Declaration

I, Pulak Talukdar, declare that this thesis titled, "**Radiative Analysis of Lepton-Proton Scattering via Low-Energy Effective Field Theory**" and the work presented in it are my own. I confirm that:

- This work was done wholly or mainly while in candidature for a research degree carried out at the Department of Physics, Indian Institute of Technology Guwahati, India under the supervision of Dr. Udit Raha.
- The material of this thesis has not been submitted elsewhere for any other degree.
- Wherever I have consulted the published works of others, there has been a clear attribution.
- I have acknowledged all main sources of help.

Signed: _____

Date: _____

Department of Physics

Indian Institute of Technology Guwahati

Guwahati - 781039, India, Assam

Disclaimer

The bibliography included in this thesis is, by no means complete but contains the ones which were consulted thoroughly by me in preparation for this thesis. I apologize for inadvertently missing out some of the research papers, review articles and other scientific documents pertaining to the focus of this thesis which should also have been cited. For illustration purpose some of the figures in this thesis were taken from other sources which were properly cited.

Department of Physics

Indian Institute of Technology Guwahati

Guwahati - 781039, India, Assam

Certificate

It is certified that the work contained in the thesis entitled "**Radiative Analysis of Lepton-Proton Scattering via Low-Energy Effective Field Theory**" by Mr. Pulak Talukdar (Roll no.-136121008), a Ph.D. student of the Department of Physics, Indian Institute of Technology Guwahati is carried out under my supervision and has not been submitted elsewhere for the award of any other degree. He has fulfilled all the requirements according to the rules of the institute for submission of thesis.

Supervisor Date:

(Dr. Udit Raha)

Asst. Professor (Physics)

Dedicated
to
My Late Father...

"It's not that I am smarter, its just that I stay with the problem longer"

-Albert Einstein

Acknowledgements

It is the almighty who bestowed on me power, courage, and the will to meet the ups and downs of life. I courteously bow before him. First and foremost, I would like to thank my living ideal, my GOD, Sri Sri Thakur Anukul Chanda, for giving me the strength, knowledge, ability and opportunity to undertake this research study and ultimately the perseverance to complete it satisfactorily. This journey of knowledge and accomplishment would not have been possible without His blessings and invisible guidance.

Undertaking this Ph.D. has been truly a life-changing experience for me, and it would not have been possible without the support and guidance that I received from numerous people. Throughout this long and arduous journey, I have gained a lot by learning to persevere despite numerous hurdles and hardships. I thereby would like to thank all those people who made this journey considerably pleasant and reassuring, who always stood by my side during this tenure.

First and foremost, from the core of my heart, I would like to thank my esteemed supervisor, Dr. Udit Raha, Department of Physics, IIT Guwahati, for not only giving me the opportunity to achieve my dream but also showing me what a researcher should strive to be viz., patient, thorough, passionate and personable. I thank him for his constructive criticisms and constant encouragement that carried me on through difficult times, and also for his useful insights and helpful suggestions that played a crucial role in shaping my research work, bringing it to its present form as presented in this dissertation.

Many sincere thanks go to my research collaborator, Prof. Fred Myhrer, Department of Physics and Astronomy, University of South Carolina (USC), USA, for his continuous guidance, critical comments, and invaluable assistance in improving the quality of my research works. I am immensely grateful and truly indebted to him for inviting me to USC for about a month and giving me the opportunity to work with him. In that context I would also like to thank the Department of Physics and Astronomy and Dr. Arjun Trivedi for their kind hospitality during my stay in USA. Furthermore, I wish to express my sincere gratitude to Prof. Daniel Phillips, Institute Nuclear and Particle Physics, Ohio University, USA, for inviting me to present one of my works in his department and also for his very useful comments and suggestions. Words can not express my whole hearted appreciation for all the support and encouragement of my collaborator, Dr. Vanamali Shastry through all his numerous discussions and help.

Next, I would like to thank my doctoral committee, Prof. Poulose Poulose, Prof. Bipul Bhuyan and Dr. Soumitra Nondi, for their valuable suggestions and constructive ideas given during the annual progress seminar. I express my humble and sincere gratitude to all the HODs namely, Prof. Saurabh Basu, Prof. Poulose Poulose and Prof. Subhradip Ghosh, for their various academic help during my Ph.D. tenure. I wish to thank all the technical assistants, academic and non-academic staff of the Physics department who helped me in numerous ways during my research period. My sincere thanks especially go to all the Deans of Academic Affairs, Student Affair and Research and Development section, IIT Guwahati for extending their necessary help during all my applications for financial assistance for attending various conferences and academic visits. In this context, it would be unfair if I fail to express my sincere gratitude towards Gaurish Da, who made all my formalities related to the academic section very easy.

I seize the opportunity to acknowledge the help and co-operation extended to me by my groupmate, Mr. Ghanshyam Meher as well as many other research scholars here at the Department of Physics. They have provided me with an excellent environment for research and helped me through their gentle guidance and suggestions during my Ph.D. tenure. I especially owe a deep sense of gratitude to my dear friends Deepanjali, Pankaj, Srikrishna, Deep, Arun, Pratap, Ranjan, Noor, Prahlad, Ram and Sanjib. I thank you guys for all the enjoyment, moral support, and your delightful company. Thanks are also due to my department seniors, namely, Kallol Da, Sourav Da, Abhijit Da, Debashis Da and the juniors, Indu, Joy, Payel, Budha, Govinda, Nawaz, Jagan, Santanu, Karuna, Nagendra and others for being so caring, cooperative and helpful. Special thanks go to my "Satsangee" group, viz., Sahoo sir, Subrata Da, Srijiv, Sumit and Bhargabi for making this journey enjoyable. I have some very special people from outside my Institute whose contribution I want to acknowledge viz., Gayatree, Acharjya, Sagard Da, Kalyan Da, Kshyama, Neelakshi, Ricky, Kanishka and Himangshu Da, without whom this journey would not have been possible. Thanks for being such an inspiration.

Family forms an important part of this long and enduring journey, and without their constant support and encouragement, the completion of this thesis would have remained an unaccomplished dream. I must thank my two adorable sisters Simi and Rose and my borther Tuin for all their support and encouragement. My vocabulary fails to convey the depth of my feelings for my siblings. I am also very thankful to my sister in law, brother in law, and nephews, who always encourage me to do better and help me in many ways. I have to also thank my other two cute sisters Matu and Dhunu for always being at my

side. You and your family were always there whenever I needed any help. My sincere gratitude also goes to Neelkashi aunty, Mamu and Babla for all the love and care.

Last but not the least, words that I know are rather insufficient to convey my sincerest gratitude to my parents whose moral encouragements, countless blessings, and untiring struggle lies behind all my achievements till date. Most importantly, I feel an immense admiration and humble obligation for my dear mother, who has been my constant source of happiness. My late father deserves a big salute for showing faith in me, who from my childhood days had always encouraged me to dream big and gave me full liberty to choose what I desired. Papa, I hope you are happy and proud and showering blessings on me from wherever you are. I thank you both for teaching me what books could not, and bestowing me the wisdom, courage and the presence of mind to encounter life's greatest of problems smilingly all by myself.

June, 2020 *Pulak Talukdar*

Department of Physics
Indian Institute of Technology Guwahati
Guwahati - 781039, India, Assam

Synopsis

Radiative correction to elastic lepton-proton scattering is time honored topic that had its beginning around the middle of the last century. But over the past two decades with the advent of modern sophisticated experimental facilities in different parts of the world opened up the possibility to access the very low-energy or momentum transfer domain, which were technically unfeasible in the last century with majority of such experiments restricted only to the high-energy domain. Accordingly, issues such as high-precision radiative correction analysis of *raw* experimental data have been demanding the development of special theoretical techniques to meet the systematics associated with the extraction of various physical observables. One such observable which has recently been a matter of great controversy is in regard to serious discrepancies associated with the measured values of the proton's charge radius, contrary to expectations based on current theoretical knowledge. This is the famous *Proton Radius Puzzle*. Meanwhile with the ongoing progress at PSI, the MUSE Experimental Project at PSI seeks to find a resolution to the radius discrepancy through a simultaneous study of very low-energy electron-proton ($e^{\pm}$p) and muon-proton ($\mu^{\pm}$p) scatterings with precedented accuracies. The theoretical analysis presented in the thesis is primarily concern with the systematic inclusion of model-independent hadronic effects in radiative corrections, which hitherto were predominantly *ad hoc* without much control on systematic uncertainties.

In this thesis, we have employed the technique of low-energy Effective Field Theory (EFT) to describe the radiative and proton recoil corrections to the elastic as well as inelastic processes, such as the *elastic radiative tail*, including a model-independent assessment of the controversial two-photon exchange (TPE) process in regard to the proposed MUSE

kinematic domain. Notably, the methodology used in this thesis is the so-called Heavy Baryon Chiral Perturbation Theory (HBχPT), the non-relativistic analog of Baryon Chiral Perturbation Theory (BχPT), which is tailor-made to ideally describe the dynamics of nucleon at low-energies. The work in the thesis encompasses three vital aspects associated with the systematic analysis of radiative corrections to the lepton-proton scattering process: 1) accounting for the inelastic radiative tail effects constituting the dominant background for the basic elastic process, 2) systematics associated with hadronic effects in the TPE contributions to the elastic cross section, and 3) accurate estimate of the infrared divergence free radiative contributions incorporating dominant hadronic recoil effects.

The first work of this thesis is a systematic calculation of the cross-section for the lepton-proton bremsstrahlung process ($\ell + p \to \ell + p + \gamma^*$) in HB$\chi$PT at next-to-leading order (NLO). This process corresponds to an undetected background signal for the proposed MUSE experiment. We show that the commonly used peaking approximation, which is used to evaluate the radiative tail for the elastic cross-section, is not applicable for muon-proton scattering at the low-energy MUSE kinematics.

In the second work, we evaluate the two-photon exchange (TPE) corrections to the low-energy elastic lepton-proton scattering at NLO accuracy, including a non-zero lepton mass. We consider the elastic proton intermediate state in the two-photon exchange invoking soft photon approximation. The infrared singular contributions are projected out using dimensional regularization. The resulting infrared singularity-free two-photon exchange contribution is in good numerical agreement with existing predictions based on standard diagrammatic soft photon approximation evaluations.

In the final work, the full radiative correction to the elastic lepton proton scattering, including all the virtual and corresponding soft photon emission diagrams up to NLO in HBχPT, is taken into account. We demonstrate the systematic cancellation of the infrared singularities amongst the various diagrams contributing to the elastic cross-section. In particular, we also include the magnetic form factor of the lepton, whose contribution was mostly neglected in previous works based on the analysis of high-energy processes. In our case, such a contribution constituting a part of the LO radiative corrections turn out to be significant for muon scattering. As expected, our numerical results indicate no more than 2 % radiative correction for the muon scattering process, compared to much larger corrections, nearly 25 %, for electron scattering in regards to the low-energy MUSE kinematic domain. Furthermore, we find that in the former process due to the largeness of the muon mass, the NLO corrections are kinematically enhanced, numerically becoming

as large as the LO correction. We thereby conclude that an NNLO calculation may be necessary for a more definitive analysis of future muon scattering data from MUSE.

List of Publications

Journal Publications

- **Pulak Talukdar**, Fred Myhrer, Ghanashyam Meher and Udit Raha, "Low-Energy Lepton-Proton Bremsstrahlung via Efectve Field Theory", *Eur. Phys. J.A* **A54**(11):195 (2018).
- **Pulak Talukdar**, Vanamali C Shastry, Udit Raha, and Fred Myhrer, "Lepton-proton two-photon exchange in chiral perturbation theory", *Phys. Rev. D* **101**(1):013008 (2020).
- Fred Myhrer, **Pulak Talukdar**, Vanamali C Shastry, Udit Raha, "Bremsstrahlung at Low Energies", *Few Body Syst.* **59**(4):62 (2018)

Pre-Publications

- **Pulak Talukdar**, Vanamali C Shastry, Udit Raha, and Fred Myhrer, "Radiative Correction to Elastic Lepton- Proton Scattering in Low-energy Effective Theory", *arXiv:2010.09380* (2020).

Conference Publications

- **Pulak Talukdar**, Fred Myhrer and Udit Raha, "Lepton-Proton Bremsstrahlung Distribution Function in Low-Energy Effective Field Theory", *Proceedings of the DAE Symp on Nucl. Phys.* **D15** (62) (2017).

Contents

List of Figures

List of Tables

Abbreviations

BSM	Beyond Standard Model.
BχPT	Baryon Chiral Perturbation Theory.
CODATA	Committee on Data for Science and Technology.
CREMA	Charge Radius Experiment with Muonic Atom.
DR	Dimensional Regularization.
EFT	Effective Field theory.
HBχPT	Heavy Baryon Chiral Perturbation Theory.
HQET	Heavy Quark Effective Theory.
IR	Infra Red.
ISR	Initial State Radiation.
LEC	Low Energy Constant.
LO	Leading Order.
LT	Longitudinal Transverse.
MAMI	Mainz Microtron.
MUSE	Muon Scattering Experiment.
NDA	Naive Dimensional Analysis.
NG	Nambu Goldstone.
NLO	Next to Leading Order.
NNLO	Next to Next to Leading Order.
OPE	One Photon Exchange.
PCAC	Partially Conserved Axial Current.
PRad Experiment	Proton Radius Experiment.
PRP	Proton Radius Puzzle.
PSI	Paul Sherrer Institute.

PT	Polarization Transfer .
QCD	Quantum Chromodynamics .
QED	Quantum Electrodynamics .
QFT	Quantum Field Theory .
SLAC	Stanford Linear Accelerator Center .
SPA	Soft Photon Approximation .
TOF	Time Of Flight .
TPE	Two Photon Exchange .
UV	Ultra Violet .
χ**PT**	Chiral Perturbation Theory .

Notations and Conventions

All calculations in this thesis are presented in natural units, $\hbar = c = 1$. Following are some of the important kinematical notations used in our evaluations. We will stick to these notations throughout the thesis, if not mentioned otherwise:

$p(E, \vec{p})$	four-momentum of the incoming lepton ,
$p'(E', \vec{p}')$	four-momentum of the outgoing lepton ,
$P(E_p, \vec{P})$	four-momentum of the incoming proton ,
$p_p\,(p'_p)$	residual four-momentum of the incoming (outgoing) proton ,
$P'(E'_p, \vec{P}')$	four-momentum of the incoming lepton ,
$k(E_\gamma, \vec{k})$	four-momentum of the photon ,
$Q = (p - p')$	four-momentum transfer in elastic scattering ,
$q = (p - p' - k)$	four-momentum transfer in bremsstrahlung process ,
$\beta(\beta')$	velocity of the incoming (outgoing) lepton,
$m_l(m_e/m_\mu)$	mass of the lepton (electron/muon) ,
$\mathcal{M}_q$	quark mass matrix ,
m_π	mass of the pion ,
M_0	mass of nucleon in the chiral limit ,
$M(M_N)$	mass of the proton (nucleon) ,
θ	scattering angle ,
Δ^*_γ	detector acceptance ,
Λ_χ	chiral symmetry breaking scale ,
f_π	pion decay constant ,
g_A	axial vector coupling constant ,
α	fine structure constant ,
D	chiral dimension ,
d	space-time dimension .

The Minkowski metric used in these calculations is

$$g^{\mu\nu} = \begin{pmatrix} 1 & 0 & 0 & 0 \\ 0 & -1 & 0 & 0 \\ 0 & 0 & -1 & 0 \\ 0 & 0 & 0 & -1 \end{pmatrix}$$

to define the four vector scalar product as,

$$A \cdot B = g^{\mu\nu} A_\mu B_\nu = A^\nu B_\nu = A_0 B_0 - \vec{A} \cdot \vec{B} \,.$$

Pauli matrices used are

$$\tau^1 = \begin{pmatrix} 0 & 1 \\ 1 & 0 \end{pmatrix} \,, \quad \tau^2 = \begin{pmatrix} 0 & -i \\ i & 0 \end{pmatrix} \,, \quad \tau^3 = \begin{pmatrix} 1 & 0 \\ 0 & -1 \end{pmatrix} \,.$$

Below we specify the values of the physical constants we used in our calculations.

Mass of proton	M	=	938.272 MeV .
Mass of electron	m_e	=	0.511 MeV .
Mass of muon	m_μ	=	105.658 MeV .
Mass of muon	$m_{\pi^\pm}$	=	139.570 MeV .
Fine structure constant	α	=	$\frac{1}{137.035}$.

Chapter 1

Introduction

All of the visible matters are made up of atoms, and the proton is its identity in the sense that it is the number of the protons (atomic number Z) present in an atom that decides to which element in the periodic table does it belong to. For example, an atom of Hydrogen (H) has a single proton, and if we add another one, it becomes an atom of Helium (He), adding one more yields Lithium (Li), and so on. Since its discovery by Ernest Rutherford around 1920 [1], protons have been extensively studied primarily using the principal tool/mode of investigation, viz., the electron-proton scattering. The specialty of such electron scattering experiments is that they can be employed as a high-resolution microscopes for probing the hadronic structure, allowing the measurements of the distribution of charge for nucleons and nuclear structure. It was through the scattering of high energy electrons in deep-inelastic experiments conducted in the past at the Stanford Linear Accelerator Center (SLAC) and Fermi-Lab [2–6] that has enabled us in obtaining a great deal of understanding regarding the structure of nucleons and other baryons, viz., they are not elementary objects and instead have a composite as well as extended structure being made up of the elementary subatomic fractional charge-carrying particles, namely, the quarks.

To scan an object by scattering light particles on it is a time-honored technique in physics; in elastic electron scattering of the proton, where they interact via the exchange of virtual photons, has been used for decades to un-reveal the static properties of proton, e.g.,

charge, mass, spin, form factors (yielding its electric and magnetic radii), parton distributions and polarizabilities [7–9]. The small size of the electron and as well as the high degree of accuracy of the present-day understanding of the underlying theory of *Quantum Electrodynamics* (QED) describing its interactions with the proton (mediated via photons, the U(1) gauge bosons) makes the electron an ideal candidate for studying the proton. During its interaction with the proton, the electron copiously produce virtual as well as real photons, the effect of which must be taken into account in the data analysis process in a systematic way which is known as the radiative corrections procedure [10–12]. Since Julian Schwinger used this method for the first time [13], the radiative correction treatments have evolved steadily along with the advancement in technology in the design and construction of new experimental facilities and the development of precision measurement techniques. Just when the plethora of information based on extensive studies on the proton conducted in the past seemed to convince us that much is already known regarding its nature and properties, there came two very unexpected revelations within the last two decades that shook the very foundation on which the present-day knowledge of the proton is based on:

- first, the proton's electric (G_E^p) to magnetic (G_M^p) form factor [14, 15] ratio measured using the novel high-precision recoil *Polarization Transfer* (PT) technique [16–18] seems not to follow the expected $\mathcal{Q}^2$ (mode of the square of the four-momentum transferred) scaling behavior which was found earlier using the traditional *Rosenbluth* or the *Longitudinal-Transverse Separation* (LT) method [14, 15, 18–20], and
- second, the charge radius of the proton which was otherwise understood to be precisely known, when extracted using high-precision spectroscopic muonic hydrogen Lamb-shift measurements conducted in 2010 [21], yielded a value which was significantly smaller ($\approx 4\%$) than the previously accepted results either obtained from electron scattering experiments off light nuclei or atomic hydrogen spectroscopic measurements.

It has been observed that most of the former problem could be solved by incorporating the often neglected *Two-Photon Exchange* (TPE) [22] process, where the electron and proton interact via the exchange of two virtual photons (cf. diagram (b) in Figure.[1.1]),

accurately in the elastic electron-proton scattering radiative correction. Note that the dominant contribution to electron-proton scattering comes from one-photon exchange diagram or the Born contribution (cf. diagram (a) in Fig.[1.1]). Meanwhile the latter

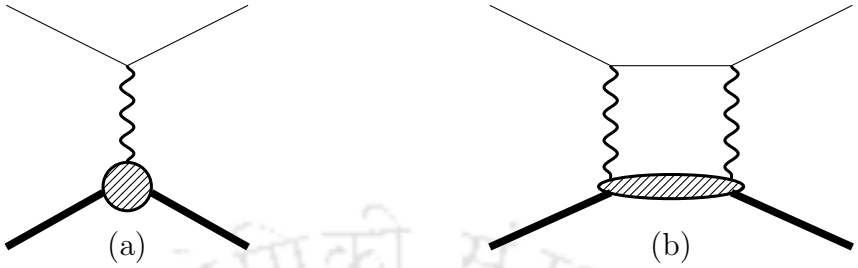

FIGURE 1.1: (a) The one-photon exchange diagram or Born contribution, where the spherical blob indicates the extended/composite nature of proton. (b) the two-photon exchange diagram, where the elliptical blob represent the intermediate elastic proton and as well as all possible inelastic excited states and resonance contributions.

problem, which has been famously termed as the *proton radius puzzle* [23–26], still continues to be an intriguing matter which demands an unequivocal explanation as to the cause of the discrepancy. Many theoretical explanations were put forward aiming at resolving the puzzle, even going beyond the Standard Model (SM) of particle physics and questioning fundamental tenets like the lepton universality [27–30]. Only very recently, two new experimental findings published results that seemed to indeed settle on a smaller value of the proton's radius based on consistent results upon redoing the atomic hydrogen spectroscopy [31] and the electron-proton scattering experiments (PRad Collaboration) [32], albeit with much higher precision at much lower energy/momentum transfers.

In high-energy scattering experiment, the virtual photons transfer very high energy/momentum to the proton, thereby unraveling its constituent fundamental structures. On the other hand, to measure the proton's charge radius or the spatial extent of its charge distribution, the virtual photon should transfer near-zero momentum/energy $t = Q^2 \to 0$ to the proton. In practical experiments, it is a matter of technical challenge to take precise scattering data close to extreme forward (scattering angle $\theta \approx 0$) kinematic configurations due to the presence of the unphysical singularity of the differential cross section due to Coulomb scattering. Hence, the goal is to push Q^2 to as low as possible and then extrapolate to zero. In light of the radius puzzle issue scattering experiments were designed to collect data at much lower energies and with higher precision levels. Two

such electron scattering experiments were commissioned soon after the confirmation of the radius puzzle, one by the A1 Collaboration at MAMI in Mainz [33] using the novel technique called the Initial State Radiation (ISR), and the other by the PRad Collaboration [34] at JLab, with momentum transfers in the range, $|Q^2| = 0.001 - 0.017$ (GeV/c)^2 and $|Q^2| = 0.00021 - 0.06$ (GeV/c)^2, respectively. Notably, the previously achieved lowest momentum transfer was $|Q^2| = 0.004 - 0.06$ (GeV/c)^2 [35–37] producing a result which was 4% larger than the muonic hydrogen measurement. The A1 collaboration published their first result in 2017 [38] which they improved in their later communication in 2019 [39]. Although they reported a smaller value of the proton's radius, due to large systematic uncertainty could not unambiguously address the radius puzzle (cf. Table 1.1). However, the recently published results from the PRad Collaboration [32], ostensibly corroborated the smaller value of the radius found from the recent atomic hydrogen spectroscopic measurements [31], as well as the muonic hydrogen experiment in 2010 [21]. Nevertheless, the puzzle is far from being over as we are yet to understand why the latest results were so different from the previously obtained results [40].

One can also measure the proton's radius from muon scattering of the proton, which is a less explored avenue due to systematic difficulties associated with performing such experiments. For example, unlike the electron beam, the muon beam are secondary ones which are produced from the decays of pions, which in turn, are produced from primary proton beams. Consequently, muon beams are less intense with large *emittance* (average spread of particle coordinates in position-momentum space) compared to electron beams, and also get contaminated with electrons and pions [23]. However, keeping in mind possible new insights into the radius discrepancy from muon scattering data, a Muon Scattering Experiment (MUSE) has been proposed [41, 42] for the πM1 beam-line at Paul Scherrer Institute (PSI) facility at Villigen, Switzerland, where the radius of the proton will be measured by scattering electrons and muons off proton at $|Q^2| = 0.0016 - 0.08$ (GeV/c)^2. The objective of the experiment is to make precision tests of any possible observed difference between ep and μp scattering scenarios, and thereby isolate possible Beyond Standard Model (BSM) signature responsible for the radius discrepancy. Note that much earlier conducted experiments testing, lepton universality [43–46] all yielded

negative results from comparisons between ep and μp scattering data at large Q^2 value and within 5-10% uncertainties, insufficient to illuminate the radius puzzle.

Radiative corrections constitute an integral part of the analysis of ep or μp scattering data. These corrections have two origins: first, due to higher-order virtual photon re-scattering or loop contributions, and second, due to *bremsstrahlung* or real photon emissions. A detailed discussion on incorporating these corrections are discussed in the next chapter. The topic of radiative analysis already has a long history and has been studied in numerous publications in the literature (see e.g., Refs. [10, 13, 47–50]) for various experimental conditions, though most of these analyses predominantly dealt with conditions suitable for high-energy scattering experiments. However, keeping in mind the low-energy kinematic domain of applicability of the newly proposed experiments, attempts are currently being made to reconsider these calculations incorporating low-energy hadron dynamics, a topic which is the primary concern of the work in this thesis.

This thesis primarily deals with the theoretical evaluations of the kind of radiative corrections necessary for the future analysis of low-energy lepton-proton scattering data expected from the MUSE. As described in details in the subsequent chapters that in contrast to traditional hadronic model-dependent approaches, we have used a systematic model-independent bottom-up approach in the context of a low-energy *Effective Field Theoretical* (EFT) framework in our quantitative estimation of various observables with particular attention to the kinematic domain relevant to the MUSE experiment. In the remaining part of this chapter, we elaborate on the two aforementioned "twists" that considerably altered our conventional wisdom we garnered in the past on the nature of the proton prior to these unexpected discoveries. This chapter is structured as follows. In the first section, we elucidate the issue on the proton form factor discrepancy and its resolution. The second section deals with the details of the radius puzzle and a brief synopsis of the various ongoing attempts, both theoretically as well as on the experimental side, to seek a resolution on this perplexing incongruity. The third section presents a brief discussion on some of the experimental details of the ongoing MUSE Program and its objectives. The final section enumerates the various aspects of the work undertaken in the subsequent chapters of this thesis.

1.1 Form Factor Discrepancy

Electromagnetic form factors of the proton are one of the most fundamental quantities characterizing its deviation from being an ideal "point-like" Dirac particle, thereby showing that it has an internal structure [20, 51]. The electric and magnetic spatial charge distributions of the proton are encrypted within the electric (G_E^p) and magnetic (G_M^p) Sachs form factors [14, 15]. Traditionally, these form factors have been calculated using the LT separation method [14, 15, 19, 20]. This technique exploits the essential fact that the one-photon exchange contribution to the un-polarized ep elastic cross section can be written as a linear function of the longitudinal photon polarization ε at fixed Q^2, namely,

$$\left[\frac{\mathrm{d}\sigma_{el}(Q^2)}{\mathrm{d}\Omega_l'}\right]_\gamma = \left[\frac{\mathrm{d}\sigma_{el}}{\mathrm{d}\Omega_l'}\right]_{\mathrm{Mott}} \frac{1}{\varepsilon(1+\tau)}\left[\varepsilon G_E^{p\,2}(Q^2) + \tau G_M^{p\,2}(Q^2)\right] \; ; \; \tau = -\frac{Q^2}{4M^2}\,, \tag{1.1}$$

where $\varepsilon = [1 + 2(1+\tau)\tan^2(\theta/2)]^{-1}$, M is the proton's mass and

$$\left[\frac{\mathrm{d}\sigma_{el}}{\mathrm{d}\Omega_l'}\right]_{\mathrm{Mott}} = \frac{\alpha^2\cos^2(\theta/2)}{4p^2\sin^4(\theta/2)}\left[1 + 2\tau\tan^2\frac{\theta}{2}\right]\,, \tag{1.2}$$

being the celebrated Mott's differential cross section formula from a point-like Dirac proton. Analyzing this linear dependence of ε at fixed Q^2 one can extract $(G_E^p)^2$ from the slope and $(G_M^p)^2$ from the ε-intercept after standard radiative corrections have been taken into account. For this extraction, at least two measurements of the cross-section at different combinations of the scattering angle θ and incoming electron momentum p for the same Q^2 are needed. The resulting proton form factor ratio extracted from this method generally agrees with expected Q^2 scaling behavior, namely,

$$\mu_p \frac{G_E^p(Q^2)}{G_M^p(Q^2)} \approx 1\,; \quad \mu_p = 1 + \kappa_p\,, \tag{1.3}$$

with μ_p being the magnetic moment of the proton [52–57].

There exists a parallel and more modern method of determining the form factor ratio, namely, the recoil Polarization Transfer (PT) method [16, 17], where it is possible to extract the ratio $\mu_p G_E^p/G_M^p$ directly by scattering longitudinally polarized electrons from un-polarized proton targets and then detecting the polarization of the recoiling proton

which in the Born approximation can either be longitudinally or transversely polarized. These longitudinal P_l and transverse P_t polarization components, written in terms of incoming E and outgoing E' electron energies, are given as [17, 58]

$$\begin{aligned} P_l &= \frac{(E+E')(G_M^p)^2}{M\left[(G_E^p)^2+\frac{\tau}{\varepsilon}(G_M^p)^2\right]}\sqrt{\tau(1+\tau)}\tan^2\frac{\theta}{2}\,, \\ P_t &= -\frac{2G_E^p\,G_M^p}{\left[(G_E^p)^2+\frac{\tau}{\varepsilon}(G_M^p)^2\right]}\sqrt{\tau(1+\tau)}\tan\frac{\theta}{2}\,. \end{aligned} \tag{1.4}$$

Subsequently, the ratio of the electric to magnetic form factors of proton can be found just by taking the ratio of the two polarization components

$$\frac{\mu_p G_E^p}{G_M^p} = -\mu_p\left(\frac{P_t}{P_l}\right)\frac{E+E'}{2M}\tan\frac{\theta}{2}\,. \tag{1.5}$$

The advantage of this method is that only a single measurement is enough to determine the form factor ratio at given Q^2, thereby considerably reducing systematic uncertainties in the extraction procedure resulting from changing the beam energies and scattering angles.

Initial measurements using the PT technique at MIT-Bates [59, 60] at low-Q^2 values were in good agreement with the finding of the LT method. But more recently experiments performed at Jefferson lab [18, 61–65]) extending these measurement up to about $|Q^2| = 6$ (GeV/c)^2, found that the ratio $\mu_p G_E^p/G_M^p$ approximately falls linearly with Q^2 beyond $Q^2 \gtrsim 1$ (GeV/c)^2, which is in stark disagreement with expected Q^2 scaling behavior. Fig.[1.2] elucidates this discrepancy which we have adopted from Ref. [66].

Resolution: Since experimental extractions primarily relied on the one-photon exchange or the Born approximation in their analyses, naturally the attention went to the next level of approximation based on including the TPE diagrams for a possible solution of this discrepancy. Keeping in mind that TPE diagrams (cf. diagram (b) in Fig.[1.1]) can get contributions from all possible energy scales, starting from a simple elastic intermediate proton state contribution at very low-energies to inelastic "soft" contributions from excited states, like the $\Delta(1232)$, Δ^*, N^*, and various possible resonance exchanges at moderate range of energies, up to the "hard" intermediate partonic contributions from the deep-inelastic scattering regime. TPE studies have revealed that the hard part of

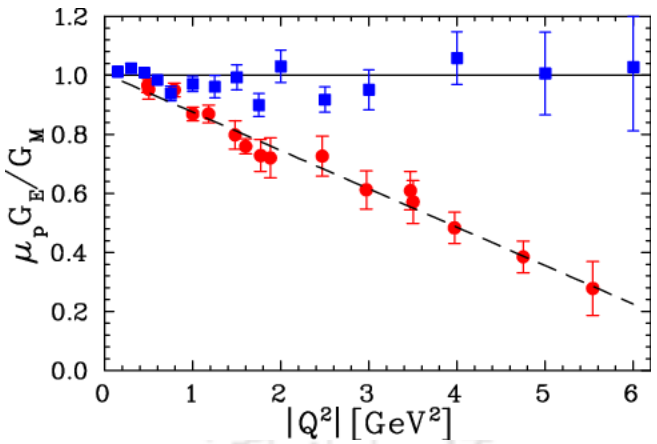

FIGURE 1.2: The ratio of proton's electric (G_E^p) to magnetic (G_M^p) form factors as extracted using Rosenbluth Separation (blue square) and Polarization Transfer (red circle) techniques. This figure is adopted from Ref. [66].

the contributions has the correct magnitude and sign to explain the bulk of the discrepancy [67, 68]. It was in fact noted that the interference terms between the one-photon and two-photon exchange diagrams can considerably affect the un-polarized cross-section used to extract G_E^p using the LT separation technique but has almost inconsequential impact on the PT extraction of the form factor ratio. Consequently, incorporating the TPE corrections, the ratio extracted by using the Rosenbluth separation moves closer to the corresponding ratio obtained via the PT method, as clearly seen in the plot displayed in Fig.[1.3] adopted from Ref. [22]. For more details on the impact of the TPE contributions on the form factors and other observables, we refer to some of the recent review articles [22, 69–71]).

1.2 Proton Radius Puzzle

Analogous to form factor discrepancy, the proton radius puzzle ostensibly reflects a disagreement between results for the proton's charge radius extracted using different approaches. The following section addresses the different methods that have been used till date for proton's radius measurements before discussing the details of the resulting radius discrepancy.

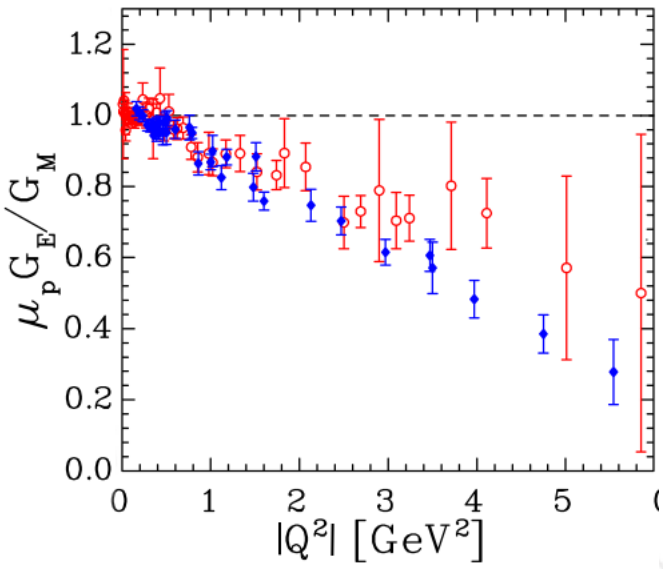

FIGURE 1.3: Comparison of Polarization Transfer (PT) measurements (filled diamonds) and Rosenbluth (LT) separations (open circles) with TPE corrections to the ratio of the electric (G_E^p) to magnetic (G_M^p) form factors. This figure is adopted from [22].

1.2.1 Elastic electron proton scattering

This is the oldest technique to measure size of proton initiated by the pioneering work of Robert Hofstadter in 1954 [7–9, 72, 73]. There the proton's *root-mean-square* (rms) charge radius (r_E^p) was extracted using the proton's electric form factor G_E^p determined from un-polarized ep elastic cross section using the Rosenbluth separation method. If the proton's electric charge distribution is $\rho(r)$, then

$$G_E^p(Q^2) = \int \mathrm{d}^3\vec{r}\,\rho(\vec{r})e^{i\vec{Q}\cdot\vec{r}} = 1 + \frac{1}{6}(r_E^p)^2Q^2 + \cdots, \tag{1.6}$$

where $\vec{Q}$ is the three-momentum transferred to the proton and r_E^p can be defined in terms of the slope of G_E^p at $Q^2 = 0$, namely,

$$(r_E^p)^2 = 6\left(\frac{\mathrm{d}G_E^p(Q^2)}{\mathrm{d}Q^2}\right)_{Q^2=0}. \tag{1.7}$$

Here we wish to emphasize again that in a scattering experiment G_E^p can be measured only at a finite non-zero Q^2, which is then extrapolated to $Q^2 = 0$ using some fitting algorithm before evaluating the radius from the slope.

1.2.2 Atomic Hydrogen Spectroscopy

The finite size of proton affects the energy levels of the hydrogen atom which can be measured in one of the the lower s-state. The size-dependent corrections were originally evaluated in Ref. [74] in the context of non-relativistic quantum mechanics where it was shown that the result only depended on the square of proton rms radius. Evidently, QED yields the correct fine structure of hydrogenic energy levels with great accuracy in terms of the Rydberg constant R_∞ and the proton's rms radius r_E^p [75, 76] as,[1]

$$E_{njl} = -\left[\frac{1}{n^2} + F_{n,j,l}\left(\alpha, \frac{m_e}{M}\right)\right] \frac{R_\infty}{1+\frac{m_e}{M}} + \delta_{l0}\frac{8\pi^2}{3}\frac{m_r^3\alpha^4}{n^3}(r_E^p)^2\,; \qquad m_r = \frac{m_e M}{m_e + M}\,. \quad (1.8)$$

In this formula, the first term can be obtained from the simple Bohr Model, viz, solving Schrödinger's equation and the second term $F_{n,j,l}$ collects all relativistic corrections, proton recoil effects and QED radiative corrections [78, 79]. Now trusting the correctness of the QED calculations, precise experimental measurements of hydrogenic energy levels can be used to extract the proton's radius. In particular, for small splittings like the 2s-2p Lamb shift [80, 81], the proton's radius can be obtained directly by using the accurately known value of R_∞ from other sources. However, in a variant approach to reduce systematic errors without having to rely on the existing value of R_∞, one can independently extract both r_E^p and R_∞ by measuring two different transitions, one being the most precise 1s-2s transition [82] and the second one between the 2s state and a higher level state such as 8s or 8d [83, 84].

1.2.3 Muonic Hydrogen Spectroscopy

Exotic atoms are systems where one or more sub-atomic particles may be replaced by heavier particles of the same charge and bound to a nucleus primarily though Coulomb attraction. For example, in muonic atoms the electrons are replaced by their heavier negatively charged partners, namely, the muons, which provide a unique testing ground to study nuclear properties at low-energies [85, 86]. In particular, muonic hydrogen (μH) is one such an exotic atom which can be formed by stopping low-energy muons in hydrogen

[1] For more details see e.g., Ref. [77].

gas. Because of muon's 200 times heavier mass than the electron, its Bohr radius is 200 times smaller such that it spends a considerable amount of time in close proximity to the proton. As a result, the muonic atom energy levels are considerably more sensitive to the proton's size effects and thereby amenable to the extraction of the proton's radius using the same techniques as in the case of atomic hydrogen, albeit with much more precision. Muonic hydrogen was already considered for Lamb shift measurements in the late 60's [87] for precision QED tests. Although X-rays transitions from muonic hydrogen level states were observed successfully by the 70's [88], failure to observe the metastable 2s state of μH [89–91] stopped any progress in the Lamb shift measurements. Eventually, the long-lived 2s state was discovered around 2000 [92–95], which finally led to the proposal of precision determination of the proton's rms radius from μH Lamb shift measurements using laser resonance spectroscopy by the CREMA Collaboration at PSI [96, 97].

The puzzle: Prior to 2010 the value of the proton's radius officially published by the Committee on Data for Science and Technology (CODATA) was fixed at 0.8768(69) fm in their 2006 publication [79] which was predominantly based on atomic hydrogen results [98, 99] along with some electron scattering measurements [100]. In 2010, CREMA collaboration published their first result of Lamb shift measurement in μH atom and reported their extracted value as

$$(r_E^p)_{\text{CREMA}'10} = 0.84184 \pm 0.00067 \text{ fm}\,.$$

which was about 4% smaller and 5σ off compared to the CODATA-2006 value [79]. This experiment was again repeated in 2013 by CREMA, with the measurement of a second splitting and a slightly improved analysis than the first, and reported the result

$$(r_E^p)_{\text{CREMA}'13} = 0.84087 \pm 0.00039 \text{ fm}\,.$$

CODATA which also updates their values every four years, included the MAMI electron scattering result which appeared in 2010 [35] to their previous CODATA-2006 average value and reported their modified value of the proton's radius as

$$(r_E^p)_{\text{CODATA}'14} = 0.8775 \pm 0.0051 \text{ fm}$$

in their 2014 publication [101]. The result was a staggering $\sim 7\sigma$ off compared to the μH result published by CREMA in 2013. This conundrum has come to be popularly regarded as the *Proton Radius Puzzle*. Fig.[1.4] elucidates the proton radius situation, which we have adopted from Ref. [102]. Furthermore, the deuteron rms charge radius extracted

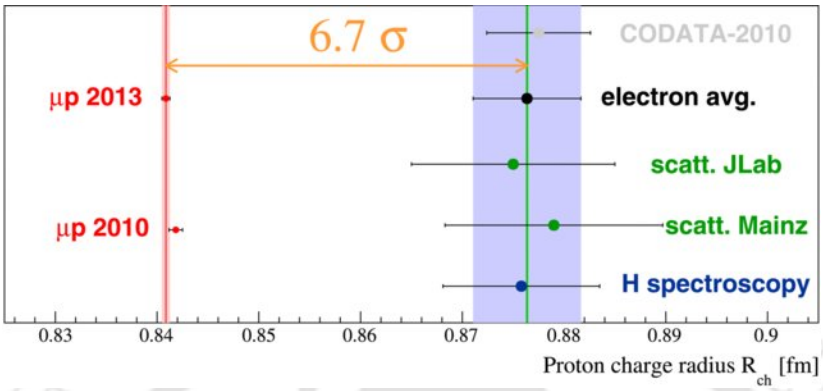

FIGURE 1.4: Proton's charge radius ($R_{ch} \equiv r_E^p$) predicted from the muonic hydrogen spectroscopic measurements [21, 103], atomic hydrogen spectroscopic measurements [101], electron scattering measurements at MAMI [35], and a global fit analysis of earlier world data [104]. The CODATA-2010 recommended value [101] is also included for comparison. We have adopted this figure from Ref. [102].

from Lamb shift measurement in μD atom [95, 105, 106] showed similar deviations from the CODATA recommended value, extending the radius puzzle to deuteron as well. The deutron rms radius

$$(R_E^d)_{\text{exp.}} = 2.12562 \pm 0.00078 \text{ fm}\,,$$

as extracted from μD spectroscopy [95] is about 6.3σ at odds with the CODATA-2014 recommended value [107]

$$(R_E^d)_{\text{CODATA'14}} = 2.1413 \pm 0.0025 \text{ fm}\,.$$

Resolution: The emergence of the proton radius puzzle gave rise to a great impetus in the scientific community leading to an intensive activity both on the theoretical and experimental sides to seek a possible resolution to this puzzle throughout the last decade. Both spectroscopic and scattering methods of radius extraction has been scrutinized and intensely debated [24, 108–111], along with the proposals of new scattering experiments using electron [33, 34] and muon [41, 112], and hydrogen spectroscopy measurements [113, 114]. Unnatural structure affects, such as, unusually large value of the proton's third

Zemach moment was proposed as a potential solution [115–117] along with many others. There were neither shortage of exotic proposals of BSM scenarios of lepton universality violation through incorporation of novel interaction mediated via non-standard vector and scalar bosons [23, 25, 27, 29, 118–123]. But recent results from the PRad experiment and the 2019 Lamb shift measurements in hydrogen atom (cf. Table 1.1) might be after all hinting towards a less exciting resolution to the proton radius problem. [2] In this context it is interesting that *Dispersion Relations* based analyses of the older MAMI scattering data even prior to the radius puzzle have always predicted a smaller value of the proton's radius consistent with the μH CREMA prediction [124–127]. Incidentally, a recent analysis of space-like form factor world data [128] using a novel theoretical framework, so-called the *Dispersively Improved Chiral EFT* (DIχEFT) [129], have obtained a value of the charge radius, $(r_E^p)_{\text{DI}\chi\text{EFT}} = 0.844(7)$ fm, also consistent with the high-precision CREMA result. For a definitive resolution, to this end the final missing piece of the puzzle must come from an experiment involving the scattering of muons, *vis-a-vis*, the MUSE [130], whose results can be expected in the near future. A smaller value of the radius from MUSE could be the "final nail in the coffin" for the earlier larger value of proton radius.

e-p Scattering			H-Spectroscopy		
Q^2 (GeV/c)^2	Year	Radius (fm)	Transition	Year	Radius (fm)
0.001-0.017	2017	0.81 ± 0.08 [33]	2s-4p	2017	0.8335 ± 0.0095 [131]
0.00021-0.06	2019	0.831 ± 0.014 [32]	1s-3s	2018	0.877 ± 0.013 [132]
0.001-0.017	2019	0.836 ± 0.061 [39]	2s-2p	2019	0.833 ± 0.010 [31]

TABLE 1.1: Results for the proton's charge radius taken from most recent experiments.

[2] In light of the new experiments supporting the smaller radius hypothesis, the latest CODATA-2018 compilation recommends the proton's radius to be $r_E^p = 0.8414 \pm 0.0019$ fm (visit https://physics.nist.gov/cgi-bin/cuu/Value?rp) which is now well in agreement with the 2013 μH CREMA results.

1.3 The MUSE: A New Venture

The MUon proton Scattering Experiment (MUSE) planned at the Paul Scherrer Institute (PSI) [41] is an effort in the experimental front to address the radius discrepancy by bringing forth possibly new information with simultaneous measurement of proton's radius from elastic electron (positron) and muon (anti-muon) scattering on the proton for momentum transfers in the range $|Q^2| = 0.0016 - 0.08$ (GeV/c)^2 at sub-percent accuracy. Table 1.2 shows the kinematic coverage of MUSE.

Quantity	Kinematic Range
Beam momenta	0.115, 0.53, 0.210 GeV/c
Scattering angle	20° to 100°
$\|Q^2\|$ range for electrons	0.0016 (GeV/c)^2 to 0.0820 (GeV/c)^2
$\|Q^2\|$ range for muons	0.0016 (GeV/c)^2 to 0.0799 (GeV/c)^2

TABLE 1.2: Full kinematic range of the proposed MUSE Experiment at PSI.

Since the MUSE Collaboration plans to measure $\mu^{\pm}$p as well as $e^{\pm}$p cross-sections, they should be able to determine the TPE effects from the ratios $\sigma(\mu^-\text{p})$ to $\sigma(\mu^+\text{p})$ and $\sigma(e^-\text{p})$ to $\sigma(e^+\text{p})$. Briefly, the MUSE objectives are as follows:

1. To measure ℓp (with $\ell \equiv e^{\pm}$, $\mu^{\pm}$) scattering in the low-Q^2 region.
2. To extract the proton form factors and the corresponding radii from the measured cross-sections.
3. To perform precision tests of hadronic TPE contributions to the proton's radius extraction.
4. To perform precision tests of lepton universality hypothesis, and thereby extract possible BSM physics responsible of the radius discrepancy by comparing ep and μp scattering cross sections.

Experiment setup: MUSE uses a mixed secondary beam-line consisting of $e^{\pm}$, $\mu^{\pm}$ and $\pi^{\pm}$ produced from the primary proton beam which is transported through the πM1 channel and then identified by timing relative to the radio-frequency (RF) of the accelerator.

A Geant4 [133] simulation of the experimental set up is shown in Fig.[1.5] which we have taken from Ref. [134]. Along the beam-line are the following components enumerated:

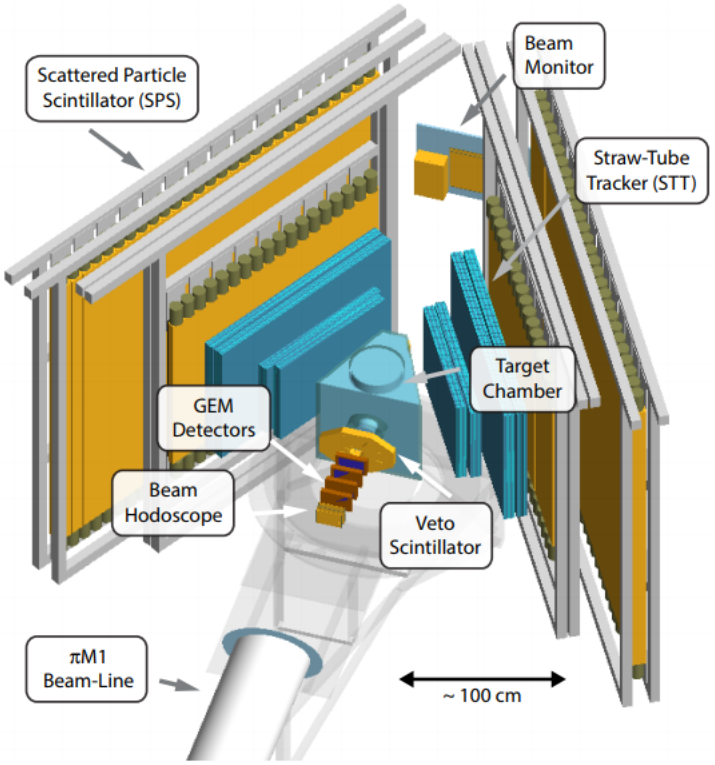

FIGURE 1.5: Geant4-based schematic view of the detector setup for the MUSE experiment. This figure is taken from Ref.[134].

1. *Beam hodoscope*: Identifies the beam particles using the Time Of Flight (TOF) and the Radio Frequency (RF) signal, which is required for triggering and analysis.

2. *GEM detector*: Tracks the trajectories of the particles into the liquid hydrogen target, which allows to determine the scattering angle and reaction vertices precisely.

3. *Veto Scintillators*: Used to veto events which are not arsing from beam particle hitting the target, thereby reducing the trigger rate from background events.

4. *Straw-tube tracker*: Tracks the scattered particles with high resolution ($< 150\mu m$) and efficiency ($> 99.8\%$).

5. *Scattered particle scintillator*: Helps in event triggering and reaction identification through TOF.

6. *Beam monitor*: Provides high-precision time measurements that determines the beam properties suppressing backgrounds from Moller and Bhabha scattering. It also helps in the precise muon and pion momentum determination.

For more information on the MUSE and its present status, we refer to the Refs. [41, 42, 130]. Notably, MUSE does not have a magnetic spectrometer to measure scattered particle momentum, nor will it be possible to detect the bremsstrahlung photons. In fact, MUSE is a single-arm experiment where only the lepton scattering angle would be detected in the angular range $20^\circ - 100^\circ$. Consequently, the MUSE data is expected to be contaminated by radiative events. This aspect highlights the need for considering radiative correction analysis for the future MUSE data in order to disentangle various backgrounds radiative tails effects, so-called the *radiative unfolding* procedure (cf. chapter 2) before making any meaningful extraction of observables, e.g., the proton's form factors or even its charge and magnetic radii. The work of this thesis is to address these radiative correction issues which may be necessary in the effort to reduce possible theoretical systematic uncertainties for the future analysis of MUSE data at the projected $\lesssim 1\%$ accuracy level.

1.4 Thesis Outline

This thesis is divided into seven chapters and four appendices. We briefly outline the work presented in each of the following chapters and the contents of the appendices:

- **Chapter 2:** Here we present an overview of the theoretical background on the radiative corrections in QED and survey some of the well-known previous works on radiative correction analysis involving the lepton-proton scattering process, ultimately motivating the work for this thesis.

- **Chapter 3:** This chapter motivates the basic idea and use of a low-energy EFT framework, which is used as the primary theoretical tool throughout the work presented in this thesis. After a brief discussion on chiral symmetry in low-energy QCD and its breaking, we discuss the framework of Chiral Perturbation Theory

(χPT) applied to the meson and baryon sectors. In particular, we consider the extreme non-relativistic limit of the relativistic formulation of Baryon χPT, namely, the Heavy Baryon Chiral Perturbation Theory (HBχPT) framework, which we pursued in all of our analyses included in this thesis. An essential component of an EFT analysis is the establishment of a consistent power counting scheme necessary to ensure a model independent approach and well-defined control over systematic uncertainties. The derivations and implications of the various, *Weinberg's chiral power counting* schemes in χPT are discussed in this chapter.

- **Chapter 4:** We carry out a prototype theoretical analysis using HBχPT for the cross-section of the lepton-proton bremsstrahlung process, namely, ℓ+p $\to$ ℓ+p+γ^*, which constitutes an undetected background process for the MUSE experiment, going up-to-and-including next-to-leading order (NLO) in chiral expansion. We show that the commonly used so-called *peaking approximation*, which is used to evaluate the *radiative tail* for the elastic cross section, is not applicable for muon-proton scattering at the low-energy MUSE kinematics. In addition, we point out an error in one of the theoretical derivations in the commonly cited work of Ref. [10]. Furthermore, we illuminate a certain pathology with the standard chiral power counting scheme associated with electron scattering, whereby the next-to-next-to-leading order (NNLO) contributions from the pion loop diagrams are arguably kinematically enhanced and numerically may be of the same magnitude as the NLO corrections.

- **Chapter 5:** In this chapter, we use HBχPT to evaluate the TPE corrections to the low-energy elastic lepton-proton scattering at NLO accuracy, including a non-zero lepton mass. We consider the elastic proton intermediate state in the TPE diagrams invoking the so-called soft photon approximation (SPA). The infrared singular contributions are projected out using dimensional regularization. The resulting infrared singularity-free TPE contribution is in good numerical agreement with existing predictions based on standard diagrammatic SPA evaluations. Notably, this kind of TPE analysis may be necessary for future analysis of experimental data from MUSE.

- **Chapter 6:** Here we present a complete radiative correction analysis to the ℓp elastic scattering process in HBχPT at NLO accuracy. The analysis includes the systematic evaluation of all corrections arising from the one-loop virtual diagrams along with the corresponding soft photon bremsstrahlung emission contributions to the elastic cross section. Using dimensional regularization we demonstrate the complete cancellation of infrared divergences between the loop and soft real photon emission process. In addition, dimensional regularization is also used in isolating the ultraviolet divergences in the loops which are eventually renormalized in a standard way using counterterms as done in QED. We show that by going to the sub-leading orders for the radiative and recoil corrections, the convergence of the chiral series up to NLO which was reasonably well for electron scattering, is significantly spoiled with contributions nearly becoming as large as NLO:LO=1:1, for muon scattering. This ostensibly indicates possible importance of including NNLO corrections for a robust analysis of the later process in MUSE.

- **Chapter 7:** In the last chapter we summarize all the works presented in the thesis with some concluding remarks. An outlook is finally included at the end for possible future extensions and scope of these research works.

- **Appendices:** The thesis includes a set of appendices containing supplementary details, like derivations and lengthy expressions, which were not essential in the context of the discussions presented in the above chapters. They are as follows:

  1. **Appendix A:** The LO and NLO HBχPT Lagrangian, specifically used in this thesis work is shown along with the relevant Feynman rules for the heavy nucleon propagators and the interaction vertices.

  2. **Appendix B:** The various partial amplitudes contributing to the NLO correction to the bremsstrahlung process $\ell + \mathrm{p} \to \ell + \mathrm{p} + \gamma^*$.

  3. **Appendix C:** The evaluation of the TPE *seagull* diagram.

  4. **Appendix D:** Derivation of the relation between the detector acceptance in the laboratory frame and the maximal photon energy in the S-frame.

Chapter 2

Radiative Corrections in Lepton-Proton Scattering: An Overview

Leptons such as electrons and muons can only interact with the nucleons via either electromagnetic interactions or weak interactions. Quantum Field Theory (QFT) suggests that while the electromagnetic interaction is mediated via the exchange of the massless gauge boson, the photon, the weak interaction can be mediated via the three types of massive vectors bosons, namely, the $W^{\pm}, W^{0}$ and the Z bosons. In the language of diagrammatic perturbation theory, the leading contributions should arise from the Born approximation diagrams, i.e., with a single gauge boson exchange. However, the Born diagrams associated with the weak interaction are very much suppressed at low-energies due to the large masses of the massive vector bosons leaving the *one-photon exchange* (OPE) Born diagram as the most dominant one, leading to the Born elastic cross-section, Eq. (1.1).

However, with the ever-increasing demand of pushing the frontiers of experimental accuracy, the analysis of high-precision data demands greater precision of theoretical estimations from QFT calculations than what is achievable through the naive Born cross-section analysis. Thus, one needs to incorporate sub-leading order diagrams in perturbation theory. In QED, this involves contributions from both real *soft* photon emission or *bremsstrahlung* and virtual *loop* processes with simultaneous emissions and absorption of virtual photons. These additional higher diagrams correspond to a bifurcation of lepton momenta, similar to the bifurcation of electric currents according to Kirchhoff's rules in circuit theory, to preserve the total four-momenta conservation with arbitrary momentum running along each line. That leads to subtle changes in the energy and angular distribution of the scattering leptons. This resulting difference between the measured and naive Born cross-section is regarded as the electromagnetic radiative correction. We now briefly discuss the higher-order radiative corrections.

2.1 Radiative Correction due to Virtual Photons

The *leading order* or the Born diagram contribution to elastic lepton-proton scattering process in QED counts at $\mathcal{O}(\alpha)$, where $\alpha = e^2/(4\pi)$ is the QED fine structure constant. All *subleading order* one-loop diagrams contributing at $\mathcal{O}(\alpha^2)$ are listed in Figure [2.1]. Along with Born diagram, all these diagrams contribute to $\mathcal{O}(\alpha^3)$ QED accuracy in the elastic cross section. The following $\mathcal{O}(\alpha)$ components of the radiatively corrected terms are:

- **Fermion Self-Energy Correction** ($\mathcal{M}_{\text{self}}$): Diagrams (A), (B), (C) and (D) in Fig.[2.1] are the lepton/proton self-energy diagrams which are the leading order correction to lepton/proton propagators. These self-energy contributions contain UV divergent terms which are absorbed via counterterms. In addition, these terms contain IR divergences as well. However, at the lowest order in the radiative corrections, these self-energy loops only occur in the external legs and the due to the condition for on-shellness of the leptons/protons these terms vanish, and hence these loop diagrams are not directly required at this order (see [135]). Nonetheless,

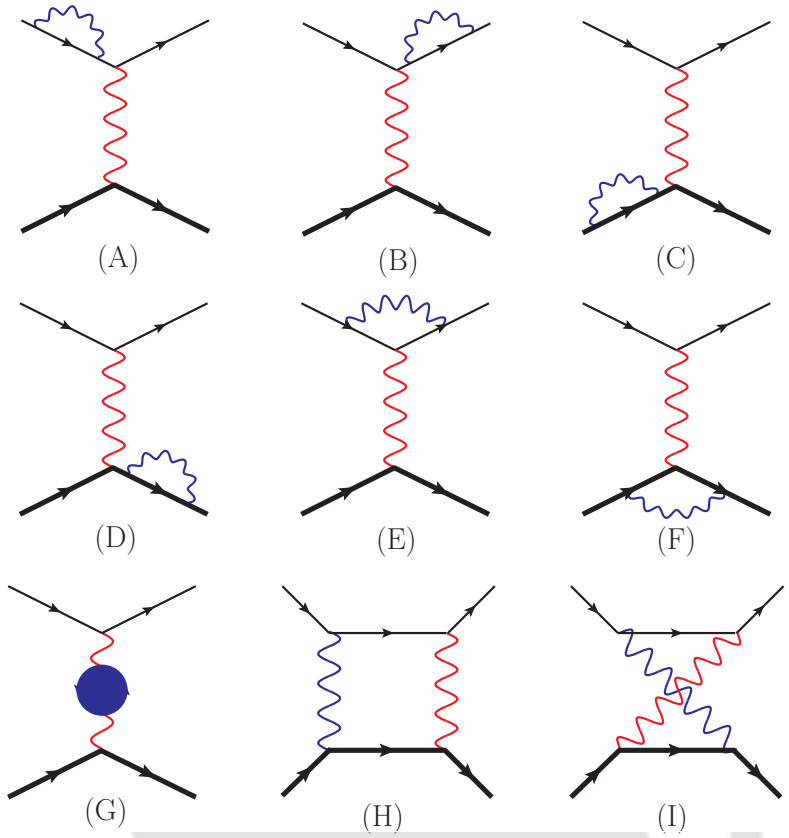

FIGURE 2.1: All virtual photon one-loop $\mathcal{O}(e^4)$ diagrams that contribute to elastic lepton-proton (ℓp$\to \ell$p) scattering cross section at $\mathcal{O}(\alpha^3)$. The thick (thin) lines denote proton (lepton) propagators and the wiggly lines denote the photon propagators. The filled blob in diagram (G) denotes the lowest order vacuum polarization corrections from the leptonic (e^+e^-, $\mu^+\mu^-$, $\tau^+\tau^-$) as well as hadronic ($q\bar{q}$, $\pi^+\pi^-$, $\cdots$) contributions.

their derivatives are needed to evaluate the wave function renormalization constants which by virtue of the *Ward-Takahashi* identity [136, 137] are guaranteed to obtain a renormalized result.

- **Lepton-Photon Vertex Correction** ($\mathcal{M}^l_{\rm vertex}$): The diagram (E) in Fig.[2.1] has been extensively studied in the literature (see [138]). Generally, this lepton-photon vertex is parametrized in terms of the two electromagnetic relativistic form factors, namely, the *Dirac* (F_1^l) and *Pauli* (F_2^l) form factors:

$$\Gamma^\mu_l(p,p') = \gamma^\mu F_1^l(Q^2) + \frac{i\sigma^{\mu\nu}Q_\nu}{2m_l}F_2^l(Q^2)\,, \quad Q_\mu = (p-p')_\mu\,,$$

where $p(p')$ is the incoming (outgoing) lepton four-momenta, $F_1^l(0) = 1$ at all orders in QED and $F_2^l(0) = \frac{\alpha}{2\pi}$, say, at one-loop order. Whereas the contribution of the

vertex correction diagram to F_2^l at non-zero Q^2 is finite at one-loop and contributes to the anomalous magnetic moment of the lepton, F_1^l contains both UV and IR divergences. The UV divergence can be subtracted via counterterms which leaves only the IR-divergent parts in the vertex contribution (cf. Chapter 6 for its expression and also appendix of Ref. [139]) for a detailed evaluation and renormalization using dimensional regularization). These loop IR divergences are systematically canceled by IR-divergent counterparts from soft photon emissions from the external lepton legs.

- **Proton-Photon Vertex Correction** ($\mathcal{M}^p_{\text{vertex}}$): Due to the finite size of the proton and the non-perturbative nature of the underlying hadronic interactions, the proton-photon vertex, diagram (F) in Fig.[2.1], is usually parametrized at low-energies or momentum transfers in terms of the two non-relativistic form factors, namely, the so-called *Sachs* electric (G_E^p) and magnetic (G_M^p) proton form factors, which in the *Heavy Baryon Chiral Perturbation Theory* (HBχPT) formalism (as used in this thesis) is expressed as [140]

$$\Lambda_p^\mu(P,P') = v^\mu G_E^p(Q^2) + \frac{[S^\mu,\, S\cdot Q]}{M} G_M^p(Q^2)\,, \quad Q_\mu = (P'-P)_\mu\,.$$

where $P(P')$ is the initial (final) proton four-momenta, $v^\mu \equiv (1,\mathbf{0})$ is the proton velocity four-vector and $S^\mu = (0,\sigma)$ is its spin four-vectors in the Breit frame. These Sachs form factors are related to the standard relativistic Dirac (F_1^p) and Pauli (F_2^p) form factors of the proton, namely,

$$G_E^p(Q^2) = F_1^p(Q^2) + \frac{Q^2}{4M^2}F_2^p(Q^2) \quad \text{and} \quad G_M^p(Q^2) = F_1^p(Q^2) + F_2^p(Q^2)\,,$$

such that at $Q^2 = 0$, $G_E(0) = 1$, and the proton's magnetic moment is defined through the relation $G_M^p(0) = \mu_p \equiv 1 + \kappa_p = 2.793$. These form factors can not be directly evaluated using standard QFT techniques. In literature, they are predominantly modeled via phenomenologically fixed form factors [10, 50], which parametrize all the UV physics that remain unresolved in the basic theory. The utility of this approach is that the expressions are guaranteed to be UV finite and do not require renormalization. However, in the context of a low-energy effective

theory of strong interactions, like *Chiral Perturbation Theory* (χPT), as described later in this thesis, the one-loop expressions for the form factors can be systematically derived from first principles using special Feynman rules for the fundamental point-like proton-photon vertices based on a *chiral power counting* scheme. In this case, these one-loop vertex corrections do contain both UV and IR-divergent terms which require renormalization. The UV divergences are absorbed by introducing counterterms or *low-energy constants* (LECs) while the IR terms are canceled by similar divergences arising from soft photon bremsstrahlung from external proton legs.

- **Vacuum Polarization Corrections** ($\mathcal{M}_{\text{v.p.}}$): The diagram (G) in Fig.[2.1] describes a process in which background electromagnetic field produces virtual lepton-anti-lepton and other possible light hardon pairs (depending on available phase-space) that basically change the charge and current distributions which generated the original electromagnetic field. In a basic classical picture, these paired charges themselves give rise to a vacuum dipole-like field leading to a partial *screening* of the original *bare charges* e_0 of the leptons or protons. This phenomenon is termed as *vacuum polarization* (see Chapter 6 and also, e.g., Ref. [141]). In QED, this simply accounts for the self-energy of the exchanged photon for the above diagram. The one-loop contribution to this diagram is IR-finite but contains UV divergences which must be absorbed using counterterms eventually leading to charge renormalization $e_0 \to e$, with e being the physical electromagnetic charge. The extent to which the screening effects renormalize the effective QED coupling is quantified through a four-momentum transfer dependent $\mathcal{O}(e^2)$ vacuum polarization tensor, $\Pi^{\mu\nu}(Q^2) = (Q^2 g^{\mu\nu} - Q^\mu Q^\nu)\,\Pi(Q^2)$, namely,

$$\alpha \equiv \alpha_{\text{eff}}(Q^2) = \frac{\alpha_0}{1 - [\Pi(Q^2) - \Pi(0)]}\,; \quad \Pi = \Pi_{\text{lepton}} + \Pi_{\text{hadron}}\,,$$

where $\alpha_0 = \frac{e_0^2}{4\pi}$ is the bare QED coupling and $\alpha = \frac{e^2}{4\pi}$ is the corresponding renormalized or physical coupling constant. The polarization tensor $\Pi_{\text{lepton}}(Q^2)$ receives contribution from the three leptonic favors/generations, $f = e,\, \mu,\, \tau$, which are obtained perturbatively in usual QED, while the corresponding hadronic contributions

Π_{hadron} could be obtained both perturbatively, e.g., $\pi^+\pi^-$ loop contribution can be evaluated using scalar QED [142, 143], as well as non-perturbatively using *dispersion relations* (see e.g., Refs. [144–146]). In Chapter 6 of this thesis, we shall discuss these corrections in more more details.

- **Two-Photon Exchange Contributions ($\mathcal{M}^{lp}_{\gamma\gamma;\,\text{TPE}}$):** Of all the one-loop contributions, the TPE diagrams (H) and (I) in Fig.[2.1] are the most subtle and elusive ones with profound physical implications. Over the last two decades, these one-loop contributions have been attracting a lot of attention and which has been sought after, mainly as a resolution to the form factor discrepancy followed by the proton radius puzzle [22, 147], as discussed in Chapter 1. However, a considerable degree of systematic uncertainties continues to beset the TPE evaluations. The inherent technical reason afflicting such theoretical evaluations is that there is no unique approach in estimating them as they receive contributions from a very wide range of scales, ranging from the deep-inelastic high-$|Q^2|$ regime to the low- and moderate-$|Q^2|$ domain. With no consistent model-independent theoretical framework to cover the entire spectrum of the strong dynamics, it becomes imperative to juxtapose a hierarchy of models and field theoretical techniques to tackle the respective contribution arising from the different energy domains with essentially no control over possible "double counting" in overlapping kinematic domains. In particular, at the sub-GeV $|Q^2|$ domain with limited statistic, the inelastic proton's *polarizability* contribution from all possible intermediate excitations and resonance states become a dominant source of uncertainty in comparison to the small magnitude of the low-$|Q^2|$ TPE effects. With the much larger TPE contributions and better data statistics, uncertainties at larger $|Q^2|$ are known to be considerably moderate. Nevertheless, the most dominant TPE contributions relevant to the low-energy MUSE kinematics arise from the elastic photon intermediate state. In this kind of single-particle approximation, the so-called *direct-box* and *crossed-box* diagrams (collectively referred to as *box* diagrams) are UV finite in standard QFT, although they are evidently IR-divergent. Additionally, in a low-energy EFT framework with heavy-fermion formalism, like in HBχPT, the non-relativistic treatment of the heavy proton leads

to the so-called *seagull* TPE diagram (not shown in Fig.[2.1], however, see Chapter 5), which, as evaluated in the Appendix C, also turns out to be both UV- and IR-finite. The Chapter 5 of this thesis deals with the detailed estimation of the TPE contributions, especially in the context of MUSE kinematics.

Radiative corrections in standard hardonic physics are categorized into the so-called *inner* and *outer* corrections. The former type corresponds to the short-distance electromagnetic effects which encode non-perturbative strong dynamics and are predominantly model dependent. The latter corresponds to long-distance corrections, which can be evaluated model-independently, and the QED corrections discussed above qualify for this type of contribution. Furthermore, we may categorize the virtual or emitted real photons into *soft photons* and *hard photons*. By soft photons, we mean photons for which the absolute value of the three-momentum $|\vec{k}|$ is smaller than a certain small but arbitrary energy, ΔE, i.e., $|\vec{k}| < \Delta E$. On the other hand by hard photons, we mean $|\vec{k}| > \Delta E$. Note that the terms soft and hard apply to both virtual and real photons. For elastically scattered leptons, if their energies are observed in an energy bin of width ΔE, then the maximal energy of the emitted soft real photon is also ΔE, neglecting of course proton recoil corrections. Furthermore, we note that these soft and hard assignments are meaningful only relative to a given frame of reference. As for each of the previously discussed one-loop amplitudes (after UV renormalization), they can be expressed as the sum of an IR-divergent *soft* part and a finite *hard* part. With the exception of F_2^l contribution and the TPE seagull diagram, all the one-loop amplitudes, namely, the self-energy, vertex, leptonic vacuum polarization and the TPE box diagram corrections can be shown to get factorized into a tree-order Born amplitude $\mathcal{M}_\gamma$ and constitute the dominant corrections to the unpolarized cross section (cf. Chapter 6). Whereas, the finite F_2^l and the seagull amplitudes which have much smaller contributions are often neglected in literature, especially in the context of ultra-relativistic approximation, $|Q^2| >> m_l^2$. Thus, the total virtual correction to the elastic scattering cross section is given as

$$\mathcal{M}_{\text{virtual}} = \mathcal{M}_{\text{self}} + \mathcal{M}^l_{\text{vertex}} + \mathcal{M}^p_{\text{vertex}} + \mathcal{M}_{\text{v.p.}} + \mathcal{M}^{lp}_{\gamma\gamma;\,\text{TPE}} \equiv \mathcal{M}^{\text{soft}}_{\gamma\gamma} + \mathcal{M}^{\text{hard}}_{\gamma\gamma}\,, \qquad (2.1)$$

where the factorisable soft part of the amplitude is

$$\mathcal{M}^{\rm soft}_{\gamma\gamma} = \frac{\alpha}{\pi}\Big[\mathbf{IR}^{l}_{\rm vertex} + \mathbf{IR}^{p}_{\rm vertex} + \mathbf{IR}^{lp}_{\rm TPE} + \delta^{\rm soft}_{\rm virtual}\Big]\mathcal{M}_{\gamma}\,. \tag{2.2}$$

As already noted, the lepton and proton self-energy corrections vanish, i.e., $\mathcal{M}_{\rm self} \to 0$ in the on-shell limit. The terms, $\mathbf{IR}^{l}_{\rm vertex}$, $\mathbf{IR}^{p}_{\rm vertex}$ and $\mathbf{IR}^{lp}_{\rm TPE}$ are IR-divergent amplitudes, and $\delta^{\rm soft}_{\rm virtual}$ collects finite terms that vanish as $Q^2 \to 0$. Whereas the amplitude $\mathcal{M}^{\rm hard}_{\gamma\gamma}$ contains non-factorisable terms, contributing to small but non-vanishing corrections as $Q^2 \to 0$ to the cross section. Hence, the net elastic differential cross section due to all the one-loop virtual diagrams, i.e., at $\mathcal{O}(\alpha^3)$, is given as

$$\left(\frac{{\rm d}\sigma_{el}}{{\rm d}\Omega'_l}\right)_{\gamma\gamma} = \frac{\alpha}{\pi} 2\,\mathcal{R}{\rm e}\Big[\mathbf{IR}^{l}_{\rm vertex} + \mathbf{IR}^{p}_{\rm vertex} + \mathbf{IR}^{lp}_{\rm TPE} + \delta^{\rm soft}_{\rm virtual}\Big]\left(\frac{{\rm d}\sigma_{el}}{{\rm d}\Omega'_l}\right)_{\gamma} + \left(\frac{{\rm d}\sigma_{el}}{{\rm d}\Omega'_l}\right)^{\rm hard}_{\gamma\gamma}. \tag{2.3}$$

The last term above includes small but finite terms that do not vanish as $Q^2 \to 0$ arising from the non-factorizable hard part $\mathcal{M}^{\rm hard}_{\gamma\gamma}$, which for convenience sake may be formally expressed in the "factorized form", namely,

$$\left(\frac{{\rm d}\sigma_{el}}{{\rm d}\Omega'_l}\right)^{\rm hard}_{\gamma\gamma} = \frac{\alpha}{\pi}\delta^{\rm hard}_{\rm virtual}\left(\frac{{\rm d}\sigma_{el}}{{\rm d}\Omega'_l}\right)_{\gamma}; \quad \frac{\alpha}{\pi}\delta^{\rm hard}_{\rm virtual} = \frac{2\sum_{spins}\mathcal{R}{\rm e}\left(\mathcal{M}^{\dagger}_{\gamma}\mathcal{M}^{\rm hard}_{\gamma\gamma}\right)}{\sum_{spins}|\mathcal{M}_{\gamma}|^2},$$

such that the finite part of the fractional contribution to the elastic differential cross section due to the $\mathcal{O}(\alpha)$ one-loop virtual corrections can be expressed as

$$\frac{\alpha}{\pi}\delta_{\rm virtual} = \frac{\alpha}{\pi}\left[2\,\mathcal{R}{\rm e}\left(\delta^{\rm soft}_{\rm virtual}\right) + \delta^{\rm hard}_{\rm virtual}\right]. \tag{2.4}$$

2.2 Radiative Correction due to Real Photon Emission

In any practical experiment involving the retardation of charged particles, electromagnetic radiations are copiously emitted as a result of kinetic energies of the particles being converted into radiation, a process termed as the "bremsstrahlung" or *breaking* radiation [148]. Since the photon number is not a conserved quantity, associated with the

elastic or real *hard* photon emission radiative process, there is always a propensity of the scattered leptons to emit an indefinite number of associated *soft* photons. The distinction between the soft and the hard photons is, however, entirely subject to the sensitivity with which the photons can be detected in a given experiment. In fact, it is impossible to scatter a charged particle without emitting an infinite number of soft photons [149]. While hard photons are the ones that are typically observed (with energies above the detector resolution), soft photons have energies much smaller than the energies of the particles participating in a particular scattering process. Even though the soft photons are not detected, taking them into account in calculations of the scattering cross sections forms a crucial part of the radiative corrections. The net effect of these soft photons is to multiply the rate of a given process by a factor that approaches zero, although the rate itself goes to infinity, leading to an IR divergence. However, there exist simultaneous IR-divergent contributions to the scattering rate related to virtual soft photons that exactly cancel the IR-divergent soft bremsstrahlung rate. Hence, this kind of cancellation ensures the net cross-section to be finite at each order in perturbation theory. In fact, Jauch [150] showed that these cancellations are manifest at all orders in QED.

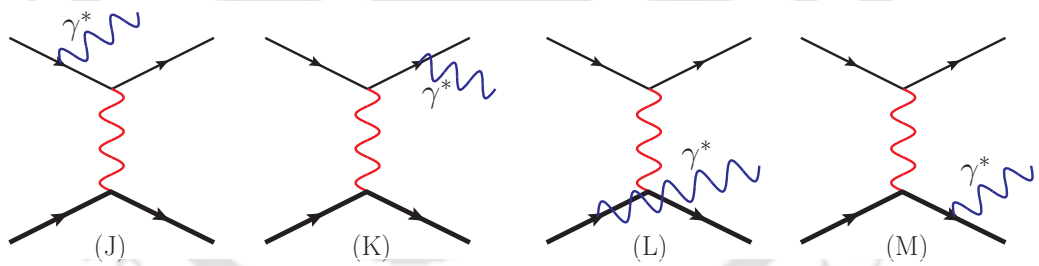

FIGURE 2.2: All bremsstrahlung $\mathcal{O}(e^3)$ diagrams that contribute to the radiative corrections to the elastic ℓ-p scattering cross section at $\mathcal{O}(\alpha^3)$. The thick (thin) lines denote proton (lepton) propagators and the wiggly lines denote real photon emissions (γ^*).

All $\mathcal{O}(e^3)$ bremsstrahlung diagrams are listed in Fig.[2.2]. The squared modulus of the corresponding amplitude that contributes to the cross section at $\mathcal{O}(\alpha^3)$ is obtained as[1]

$$|\mathcal{M}_{\rm brem}|^2 = |\mathcal{M}^l_{\gamma\gamma^*}|^2 + |\mathcal{M}^p_{\gamma\gamma^*}|^2 + 2\mathcal{R}{\rm e}\left(\mathcal{M}^{l\dagger}_{\gamma\gamma^*}\mathcal{M}^p_{\gamma\gamma^*}\right) , \tag{2.5}$$

[1]The sign "*" in γ^* is used here to denote a real photon, as distinct from a virtual photon denoted by γ.

where $\mathcal{M}^{l}_{\gamma\gamma^*}$ is the amplitude with the external lepton propagators radiating, whereas $\mathcal{M}^{p}_{\gamma\gamma^*}$ is the amplitude with the external proton propagators radiating. These contributions are IR-divergent in the limit of the photon momentum going to zero. These divergences are extracted by separating photon phase space into soft and hard parts relative to some arbitrary small value of the scattered lepton (bin width) energy ΔE, which could be related to the *detector acceptance* Δ^*_γ. For soft photons, $|\vec{k}| < \Delta^*_\gamma$, and for hard photons, $|\vec{k}| > \Delta^*_\gamma$. All the IR divergences will be contained within the soft terms, which can further be shown to be factorisable into the ℓp elastic Born cross section in the, so-called *Soft Photon Approximation* (SPA) [47, 151] with the photon four-momenta from the numerator of lepton propagators being neglected, whereby such soft photon emission will have no effect on the elastic kinematics. The differential cross section for the soft photon bremsstrahlung process, $\ell + \mathrm{p} \to \ell + \mathrm{p} + \gamma^*_{\mathrm{soft}}$, is then given as

$$\left(\frac{\mathrm{d}\sigma_{br}}{\mathrm{d}\Omega'_l}\right)_{\gamma\gamma^*_{\mathrm{soft}}} = \frac{\alpha}{\pi}\Big[\mathbf{IR}^{l} + \mathbf{IR}^{p} + \mathcal{R}\mathrm{e}\left\{2(\mathbf{IR}^{lp}) + \delta^{\mathrm{soft}}_{\mathrm{brem}}(\Delta^*_\gamma)\right\}\Big]\left(\frac{\mathrm{d}\sigma_{el}}{\mathrm{d}\Omega'_l}\right)_{\gamma}, \tag{2.6}$$

where $\delta^{\mathrm{soft}}_{\mathrm{brem}}(\Delta^*_\gamma)$ represents the extracted finite part of the cross section, while $\mathbf{IR}^{l}$, $\mathbf{IR}^{p}$ and $\mathbf{IR}^{lp}$ are the IR-divergent terms arising from lepton bremsstrahlung, proton bremsstrahlung and the interference of lepton and proton bremsstrahlung contributions, respectively, corresponding to the terms on the right hand side of Eq. (2.5). It is crucial to demonstrate the correspondence, namely,

$$\begin{aligned}
\mathbf{IR}^{l} &= -2\mathcal{R}\mathrm{e}(\mathbf{IR}^{l}_{\mathrm{vertex}}),\\
\mathbf{IR}^{p} &= -2\mathcal{R}\mathrm{e}(\mathbf{IR}^{p}_{\mathrm{vertex}}),\\
\mathbf{IR}^{lp} &= -\mathbf{IR}^{lp}_{\mathrm{TPE}},
\end{aligned} \tag{2.7}$$

at each order in perturbation theory to ensure a IR-finite result for the total elastic differential cross section:

$$\left(\frac{\mathrm{d}\sigma_{el}}{\mathrm{d}\Omega'_l}\right)_{2\gamma} = \left(\frac{\mathrm{d}\sigma_{el}}{\mathrm{d}\Omega'_l}\right)_{\gamma} + \left(\frac{\mathrm{d}\sigma_{el}}{\mathrm{d}\Omega'_l}\right)_{\gamma\gamma} + \left(\frac{\mathrm{d}\sigma_{br}}{\mathrm{d}\Omega'}\right)_{\gamma\gamma^*_{\mathrm{soft}}} \tag{2.8}$$

$$= \left(\frac{\mathrm{d}\sigma_{el}}{\mathrm{d}\Omega'_l}\right)_{\gamma}\left[1 + \frac{\alpha}{\pi}\left(\delta_{\mathrm{virtual}} + \delta^{\mathrm{soft}}_{\mathrm{real}}\right)\right], \tag{2.9}$$

where $\delta^{\rm soft}_{\rm real} = \mathcal{R}{\rm e}\,\delta^{\rm soft}_{\rm brem}(\Delta^*_\gamma)$ collects the finite terms that depend on the detector resolution Δ^*_γ, and vanish as $Q^2 \to 0$. On the other hand, the differential cross section for the real one-hard photon emission process, i.e., ℓ+p$\to$ ℓ+p+$\gamma^*_{\rm hard}$, is expressed in terms of the double differential cross section $\left(\frac{{\rm d}^2\sigma_{br}}{{\rm d}\Omega'_l {\rm d}E'}\right)$, with photon energies integrated from the detector threshold value, $E^{\rm min}_{\gamma^*} = |\vec{k}_{\rm thr}| = \Delta^*_\gamma$, to the maximal kinematically allowed value, $E^{\rm max}_{\gamma^*} = E - m_l$, depending on the incident lepton energy E. This also translates to the corresponding detector resolved kinematical spectrum of the inelastically scattered lepton with the upper energy limit as $(E')_{\rm max} = E'^{el} - \Delta^*_\gamma$, and the lower limit as $(E')_{\rm min} = m_l$, where

$$E'^{el}(\theta) = \frac{E}{\eta} = \frac{E}{1 + (2E/M)\sin^2(\theta/2)}\,, \tag{2.10}$$

is the lepton scattering angle θ dependent energy for an elastically scattered lepton, i.e., without inelastic radiative processes. Hence, the observed cross sections in a typical scattering experiment are the sum of the contribution from the basic OPE elastic Born cross sections along with the three other processes, namely, virtual photon exchange process, real soft photon emission process and real hard photon emission process or the so-called *elastic radiative tail* contribution, i.e.,

$$\left(\frac{{\rm d}\sigma_{tot}}{{\rm d}\Omega'_l}\right)_{\rm obs} = \left(\frac{{\rm d}\sigma_{el}}{{\rm d}\Omega'_l}\right)_\gamma \left[1 + \frac{\alpha}{\pi}\left(\delta_{\rm virtual} + \delta^{\rm soft}_{\rm real}\right)\right] + \int_{m_l}^{E'^{el} - \Delta^*_\gamma} \left(\frac{{\rm d}\sigma_{br}}{{\rm d}\Omega'_l\,{\rm d}E'}\right) {\rm d}E'\,. \tag{2.11}$$

2.2.1 Radiative Corrections and Radiative Tails

Before we proceed to demonstrate a prototype radiative analysis for the lepton-proton scattering, it may be worth noting that in the radiative background that accompanies the lepton scattering, it is useful to distinguish two principal mechanisms by which the scattered lepton loses energy in the target medium, namely, bremsstrahlung in the field of the target proton, and the so-called *Landau straggling* [152], i.e., bremsstrahlung in the field of a neighboring nucleon/nucleus accompanied with ionization, other than the target proton. In the context of the former mechanism, a clear distinction between the frequently used terminologies, namely, "radiative corrections" and "radiative tails" should be made here. Although this distinction is often vaguely made in the literature, the

review article by Maximon in Ref. [48] aptly clarifies the difference: the term "radiative corrections", as described earlier, refers to the corrections to the basic scattering cross-section due to virtual loops or real soft photons emission, with $E_\gamma \leq \Delta^*_\gamma$, and the term "elastic radiative tail" represents the background to the basic scattering process, where the lepton loses energy by real hard photon emission, with $E_\gamma > \Delta^*_\gamma$. Mathematically, the radiative tail distribution is nothing more than the derivative with respect to the photon three-momentum $|\vec{k}|$ of the basic cross-section plus its radiative corrections integrated to include real soft photon emission with total energy $\leq |\vec{k}|$, essentially leading to Eq. (2.11) using the energy conservation delta-function. Hence, the first term on the left-hand side of Eq. (2.11) involving the radiative correction factor, $\delta_{2\gamma} = \delta_{\text{virtual}} + \delta^{\text{soft}}_{\text{brem}}(\Delta^*_\gamma)$ is an *integrated* cross-section, while the second term which is an integral over a *differential distribution* is considered as the "elastic radiative tail" contribution.

Fig.[2.3] shows a schematic of a typical elastic tail for a scattered lepton for fixed scattering angle and incoming momentum. The plot shows three distinct regions:

1. the elastic region emerging from the dominant delta-function-like elastic peak at the right end of the plot,
2. the resonance region associated with protuberances on radiative tail representing the intermediate discrete inelastic levels, and finally,
3. the smooth inelastic continuum region on the left of the plot.

From an experimental point of view, radiative corrections must be applied to the primary elastic peak in order to extract the elastic form factors, charge and magnetic radii, etc. While the elastic radiative tail, which is an extension of the elastic peak, should be subtracted from the observed spectrum [49] in order to isolate the true contribution of the elastic peak. Similarly, there also exist "background inelastic radiative tails" (not shown in the figure), emerging from the inelastic peaks, which should also be subtracted along with the elastic tail to extract the true resonance contribution. Thus, in order to calculate the radiative correction to the elastic peak, one needs to consider all the virtual loops diagrams in Fig.[2.1], as well as the bremsstrahlung diagrams in Fig.[2.2] with the real photon three-momenta smaller than the minimum energy Δ^*_γ. Whereas

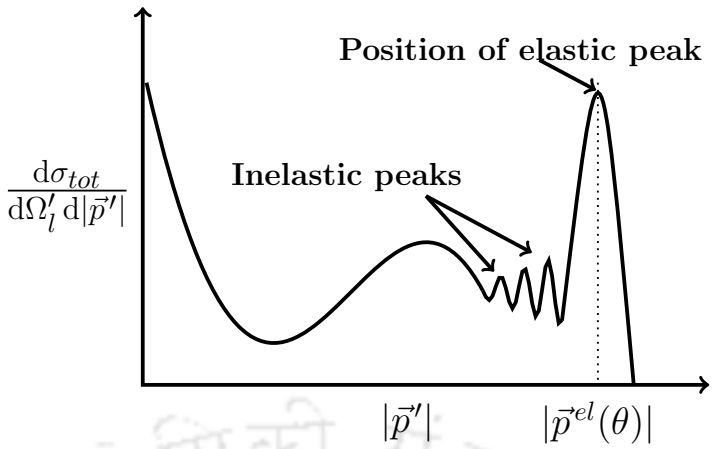

FIGURE 2.3: Schematic of a typical elastic radiative tail spectrum for a scattered lepton with momentum $\vec{p}'$ for fixed scattering angle θ and incoming lepton momentum $\vec{p}$, with $\vec{p}^{\,el}$ being the upper limit of $\vec{p}'(\theta)$.

to calculate the elastic radiative tail, one only needs to consider the bremsstrahlung diagrams in which photon three-momentum is greater than Δ^*_γ. Chapter 4 of this thesis primarily deals with the analysis of the elastic tail spectrum for ℓp scattering, whereas the corresponding calculations of the radiative corrections are detailed in Chapter 6. On the other hand, the radiative analysis of inelastic resonances and continua is a topic which is beyond the scope of this thesis.

2.3 A Prototype Radiative Analysis

Calculations based on radiative analysis are critically influenced by experimental conditions. Calculations for coincidence experiments [153, 154], where both the scattered particle and the recoil target are detected, are different from those in which only the scattered particle is detected. Again, there are other specialized calculations for analysis of polarized scattering [155–157]. In view of the fact that the work in this thesis is motivated by the experimental conditions, originally that of Refs. [7, 72, 73], for experimental studies conducted at SLAC and also in connection with the proposed arrangements for the MUSE facility at PSI, here we shall only discuss the radiative corrections relevant to the precision calculation of the unpolarized cross section for elastic ℓ-p scattering. As discussed in Chapter 1, the recoil target is not detected in this case but instead only the scattered lepton kinematics (momenta and scattering angle) are analyzed. We now

describe a prototype radiative analysis based on the original work of Tsai [47] which was later used and improved in subsequent analyses [10, 11, 50, 158–160]. The same methodology is adopted in this thesis in the context of a systematic model-independent EFT treatment of hadronic sector in contrast to previous *ad hoc* model assumptions. It must be noted that the treatment of Tsai [47] considered a lot of approximations since the primary motivation of that work was not to focus on a precision calculation but rather on demonstrating the procedure of projecting out the IR singular structures and their eventual cancellations. In particular, the finite terms being much smaller were predominantly neglected.

Beginning with the pioneering work on radiative correction due to electron scattering from a static Coulomb potential [13] of the proton, Schwinger showed that the Born cross section gets modified by a factor $1+\delta_2$ considering corrections to the current operator in covariant canonical perturbation theory using the second Born approximation. The factor δ_2 effectively includes effects of virtual photon loops (electron self-energy and electron-photon vertex corrections), vacuum polarization and bremsstrahlung of soft photons from the incoming and outgoing electrons and given by [13]

$$\begin{aligned}\delta_2(\Delta E \ll E,\theta) &= -2\left[\ln\left(\frac{E}{\Delta E}\right)-\frac{13}{12}\right]\left[\ln\left(\frac{-Q^2}{m_e^2}\right)-1\right]-\frac{17}{18}-f(\theta)\,;\\ f(\theta) &= \ln\left(\sin^2\frac{\theta}{2}\right)\ln\left(\cos^2\frac{\theta}{2}\right)-\mathrm{Sp}\left[-\sin^2\frac{\theta}{2}\right],\end{aligned} \tag{2.12}$$

where the $\mathrm{Sp}(x<1)$ is the *Spence* function defined by

$$\mathrm{Sp}(x)=\int_0^x\frac{\ln|1-t|}{t}\,\mathrm{d}t\,. \tag{2.13}$$

In this case of static potential scattering, the incoming lepton energy is same as the scattered energy, namely, $E'=E$ in the above equations, and ΔE represents the maximum energy loss by the electron by soft photon emissions. Later Tsai for the first time included proton recoil effects on the radiations emitted from the proton [47] missing in the work by Schwinger. To analytically cancel the IR-divergent terms coming from the proton current, utilizing soft photon approximation, Tsai evaluated the TPE box diagrams and the proton-photon vertex correction in the single-particle approximation of keeping only the

proton as the intermediate state. To demonstrate Tsai's analysis following the general framework developed in the seminal work of Yennie, Frautschi and Suura [151] applicable in the relativistic limit $-Q^2 \gg m_l^2$ and $m_l \ll M, E, E'$, let us first consider the TPE box diagrams (H) in Fig.[2.1]:

$$\mathfrak{M}_{\gamma\gamma;\,\mathrm{TPE}} = \frac{e^4}{(2\pi)^6}\int \mathrm{d}^4k \left[\bar{u}_l(p')\gamma_\mu \frac{(\not{p}-\not{k}+m_l)}{(p-k)^2-m_l^2+i0}\gamma_\nu u_l(p)\right]\frac{1}{k^2}\cdot\frac{1}{(Q-k)^2} \times\left[\bar{\mathcal{U}}_p(P')\,\Gamma_p^\mu[(Q-k)^2]\,\frac{(\not{P}+\not{k}+M)}{(P+k)^2-M^2+i0}\,\Gamma_p^\nu[k^2]\,\mathcal{U}_p(P)\right], \tag{2.14}$$

where $Q = p - p' = P' - P$ is the four-momentum transferred to the proton, and the standard relativistic proton-photon vertex factor is given as

$$\Gamma_p^\mu[Q^2] = F_1^p(Q^2)\gamma^\mu + \frac{i\kappa_p}{2M}F_2^p(Q^2)\sigma^{\mu\nu}Q_\nu\,. \tag{2.15}$$

The TPE matrix element Eq. (2.14) diverges either as the soft photon momentum $k \to 0$, or as $Q - k \to 0$. To extract the divergent contribution from the $\mathfrak{M}_{2\gamma}$ as $k \to 0$ we use Tsai's SPA trick [47]: we first set $\Gamma_p^\nu \to \gamma^\nu$ in Eq. (2.14) and then neglect k from the numerator of the lepton propagator and the $(Q-k)^2$ term in the denominator arising from the soft photon propagator, such that for $-Q^2 \gg m_l^2$, we have

$$\mathfrak{M}'_{\gamma\gamma_{\mathrm{soft}}} = -\frac{\alpha}{2\pi}K(P,-p)\mathfrak{M}_0\,, \tag{2.16}$$

where $\mathfrak{M}_0$ is the one-photon exchange amplitude (Born term) given by

$$\mathfrak{M}_0 = -\frac{e^2}{Q^2}\left[\bar{u}_l(p')\gamma^\mu u_l(p)\right]\left[\bar{\mathcal{U}}_p(P')\,\Gamma_\mu^p[Q^2]\,\mathcal{U}_p(P)\right], \tag{2.17}$$

and $K(P,-p)$ is a three-point function given by

$$\begin{aligned} K(p_i,p_j) &= -\frac{2(p_i\cdot p_j)}{i\pi^2}\int \mathrm{d}^4k \frac{1}{(k^2-2p_i\cdot k)(k^2-2p_j\cdot k)(k^2-\lambda^2)} \\ &= (p_i\cdot p_j)\int_0^1 \mathrm{d}y \frac{1}{p_y^2}\ln\frac{p_y^2}{\lambda^2}\,, \end{aligned} \tag{2.18}$$

where $p_y = p_i y + p_j(1-y)$ and λ is a fictitious photon mass introduced to regularize

the IR divergence [161]. Notably, it is found here that the rather complicated four-point function that arises from the TPE integral Eq. (2.14) in the SPA gets reduced to the above three-point function which is much more standard to evaluate and has been discussed extensively in the literature. For its evaluation we refer to the book, *Quantum Electrodynamics* by A. I. Akhiezer and V. B. Berestetskii [162]. Terms of this kind are typically IR singular which get cancel out completely when the elastic and inelastic (radiative) cross sections are added together. Similarly, to extract the divergent contribution as $(Q-k)\to 0$, Γ^μ is first replaced by γ^μ, and then setting $k=Q$ in the numerator and $k^2=Q^2$ in the denominator, one again obtains for $-Q^2 \gg m_l^2$

$$\mathfrak{M}''_{\gamma\gamma_{\rm soft}} = -\frac{\alpha}{2\pi} K(P',-p')\mathfrak{M}_0\,. \tag{2.19}$$

Adding both these contributions together yields the TPE box amplitude in SPA given by

$$\mathfrak{M}_{\gamma\gamma;\,\rm TPE} \overset{\gamma_{\rm soft}}{\rightsquigarrow} \mathfrak{M}'_{\gamma\gamma_{\rm soft}} + \mathfrak{M}''_{\gamma\gamma_{\rm soft}} = -\frac{\alpha}{2\pi}[K(P,-p)+K(P',-p')]\mathfrak{M}_0\,. \tag{2.20}$$

A similar expression can subsequently be obtained for the TPE crossed-box diagram (H) in Fig.[2.1], namely,

$$\mathfrak{M}^{\otimes}_{\gamma\gamma;\,\rm TPE} \overset{\gamma_{\rm soft}}{\rightsquigarrow} \frac{\alpha}{2\pi}[K(P,p')+K(P',p)]\mathfrak{M}_0\,, \tag{2.21}$$

leading to the total TPE contribution

$$\mathfrak{M}^{lp}_{\gamma\gamma;\,\rm TPE} = \mathfrak{M}_{\gamma\gamma;\,\rm TPE} + \mathfrak{M}^{\otimes}_{\gamma\gamma;\,\rm TPE}\,. \tag{2.22}$$

Since for obtaining unpolarized lepton-proton elastic cross sections, only the real parts of the amplitudes are relevant, $K(P,-p)$ and $K(P',-p')$ in the above amplitudes being complex, in Tsai's treatment they are approximated by their corresponding real parts, namely, $\mathcal{R}\mathrm{e}\,[K(P,-p)]\approx K(P,p)$ and $\mathcal{R}\mathrm{e}\,[K(P',-p')]\approx K(P',p')$, to analytically obtain the IR singular parts of the TPE contributions. For a justification and the extent of validity of this kind of approximation used by Tsai, see e.g., Ref [163].

Next, in Tsai's treatment of the lepton-photon and proton-photon vertex corrections,

again neglecting the soft photon momenta in the numerator of the fermion propagators in the one-loop amplitudes amplitudes, yield the following results with $-Q^2 \gg m_l^2$, namely,

$$\begin{aligned}\mathfrak{M}^{l}_{\rm vertex} &= -\frac{\alpha}{2\pi}\left[K(p,p') - K(p,p) - \frac{3}{2}\ln\left(\frac{-Q^2}{m_l^2}\right) + 2\right]\mathfrak{M}_0\,,\\ \mathfrak{M}^{p}_{\rm vertex} &= -\frac{\alpha}{2\pi}\left[K(P,P') - K(P,P)\right]\mathfrak{M}_0\,,\end{aligned} \tag{2.23}$$

with the total vertex contribution being

$$\mathfrak{M}^{l+p}_{\rm vertex} = \mathfrak{M}^{l}_{\rm vertex} + \mathfrak{M}^{p}_{\rm vertex}\,. \tag{2.24}$$

As for the vacuum polarization corrections, only the loop contribution from a single lepton-anti-lepton flavor was incorporated while the hadronic contributions could not be taken into account from first principles, namely,

$$\mathfrak{M}_{\rm v.p.} = \frac{\alpha}{2\pi}\left[-\frac{10}{9} + \frac{2}{3}\ln\left(\frac{-Q^2}{m_l^2}\right)\right]\mathfrak{M}_0\,. \tag{2.25}$$

Adding up all the above contributions, we obtain the elastic differential cross section via the formula

$$\begin{aligned}[{\rm d}\sigma_{el}]_{\gamma\gamma} = &\frac{1}{4\sqrt{(P\cdot p)^2 - m_l^2 M^2}}(2\pi)^4\delta^4\left(p' + P' - p - P\right)\frac{{\rm d}^3\vec{p}\,'}{(2\pi)^3 2E'}\,\frac{{\rm d}^3\vec{P}\,'}{(2\pi)^3 2E'_p}\\ &\times\frac{1}{4}\sum_{spins}\left[\mathfrak{M}_0^\dagger\mathfrak{M}_0 + 2\mathcal{R}{\rm e}\;\mathfrak{M}_0^\dagger\left(\mathfrak{M}^{lp}_{\gamma\gamma;\,\rm TPE} + \mathfrak{M}^{l+p}_{\rm vertex} + \mathfrak{M}_{\rm v.p.}\right)\right],\end{aligned} \tag{2.26}$$

which under relativistic approximations, i.e., for $-Q^2 \gg m_l^2$ and $m_l \ll M, E$, leads to a correction to the tree-level result, namely,

$$\left[\frac{{\rm d}\sigma_{el}(Q^2)}{{\rm d}\Omega'_l}\right]_{\gamma\gamma} = \left(\frac{{\rm d}\sigma_{el}(Q^2)}{{\rm d}\Omega'_l}\right)_{\rm Rosenbluth}\left[1 + \frac{\alpha}{\pi}\delta_{1-{\rm loop}}(Q^2)\right]\,, \tag{2.27}$$

where the IR-divergent $\mathcal{O}(\alpha)$ fractional elastic contribution proportional to the term obtained by Tsai is [47]

$$\begin{aligned}\delta_{1-\text{loop}}(Q^2) &= K(P,P) + K(P',p) + K(P,p') + K(p,p) - K(P,P') \\ &\quad - K(P,p) - K(P',p') - K(p,p') + \frac{13}{6}\ln\left(\frac{-Q^2}{m_l^2}\right) - \frac{28}{9} \\ &= \left[1 - \ln\left(\frac{-Q^2}{m_l^2}\right)\right]\ln\left(\frac{m_l^2}{\lambda^2}\right) - 2\ln\eta\ln\left(\frac{-Q^2}{\lambda^2}\right) \\ &\quad + \left[1 - \frac{E'_p}{|\vec{P}'|}\ln\left(\frac{E'_p + |\vec{P}'|}{M}\right)\right]\ln\left(\frac{M^2}{\lambda^2}\right) + \delta_{\text{virtual}}(Q^2)\,, \end{aligned} \tag{2.28}$$

with $E'_p = M - Q^2/(2M)$, and δ_{virtual} collects all IR-free (independent of the regulator λ) finite contributions (see Ref. [163] for their evaluation) adding to the $\mathcal{O}(\alpha)$ radiative corrections. Finally, the so-called *Rosenbluth* cross section is given by

$$\begin{aligned}\left(\frac{\mathrm{d}\sigma_{el}(Q^2)}{\mathrm{d}\Omega'_l}\right)_{\text{Rosenbluth}} &= \frac{\alpha}{4E^2\eta}\frac{\cos^2(\theta/2)}{\sin^4(\theta/2)} \\ &\quad \times \left\{\left[(F_1^p)^2 + \tau\kappa_p^2(F_2^p)^2\right] + 2\tau(F_1^p + \kappa_p F_2^p)^2\tan^2(\theta/2)\right\}, \end{aligned} \tag{2.29}$$

where $\tau = -Q^2/(4M^2)$, which takes into account the proton recoil factor, $\eta = E/E'^{el} = 1 + (2E/M)\sin^2(\theta/2)$.

Next, we need to determine the differential cross section for the soft bremsstrahlung process, ℓ+p$\rightarrow$ ℓ+p+γ^*. In SPA, we assume that the soft emissions do not alter the elastic kinematics, with the effect that the amplitude factorizes into the Born amplitude $\mathfrak{M}_0$, namely,

$$\mathfrak{M}^l_{\gamma\gamma^*} + \mathfrak{M}^p_{\gamma\gamma^*} = ie\left[\frac{p'\cdot\epsilon^*}{p'\cdot k} - \frac{p\cdot\epsilon^*}{p\cdot k} + \frac{P\cdot\epsilon^*}{P\cdot k} - \frac{P'\cdot\epsilon^*}{P'\cdot k}\right]\mathfrak{M}_0\,, \tag{2.30}$$

where ϵ_μ is the photon polarization four-vector. To this end, the inelastic differential cross section is calculated via the formula

$$\begin{aligned}[\mathrm{d}\sigma_{br}]_{\gamma\gamma^*} &= \frac{1}{4\sqrt{(P\cdot p)^2 - m_l^2M^2}}\frac{\mathrm{d}^3\vec{p}'}{(2\pi)^3 2E'}\frac{\mathrm{d}^3\vec{P}'}{(2\pi)^3 2E'_p}\frac{\mathrm{d}^3\vec{k}}{(2\pi)^3 2E_{\gamma^*}} \\ &\quad \times (2\pi)^4\delta^4\left(p' + P' + k - p - P\right)\frac{1}{4}\sum_{spins}|\mathfrak{M}^l_{\gamma\gamma^*} + \mathfrak{M}^p_{\gamma\gamma^*}|^2. \end{aligned} \tag{2.31}$$

In a typical single arm experimental arrangement, the recoil proton remains undetected. Thus, it makes sense to eliminate the three-momentum vector $\vec{P}'$ using the delta function, which yields

$$
\begin{aligned}
[\widetilde{\mathrm{d}\sigma_{br}}]_{\gamma\gamma^*} = & -\frac{e^2}{4\sqrt{(P\cdot p)^2 - m_l^2 M^2}} \frac{\mathrm{d}^3\vec{p}'}{(2\pi)^3 2E'} \frac{1}{2E'_p} \frac{\mathrm{d}^3\vec{k}}{(2\pi)^3 2E_{\gamma^*}} \\
& \times (2\pi)\delta\Big(E' + \sqrt{\left(\vec{p} + \vec{P} - \vec{p}' - \vec{k}\right)^2 + M^2} + E_{\gamma^*} - E - E_p\Big) \\
& \times \frac{1}{4}\sum_{spins} |\mathfrak{M}_0|^2 \left[\frac{p'}{p'\cdot k} - \frac{p}{p\cdot k} + \frac{P}{P\cdot k} - \frac{P'}{P'\cdot k}\right]^2 . \qquad (2.32)
\end{aligned}
$$

Now due to the presence of the recoil proton energy E'_p inside the energy conserving delta function, the emitted photon radiation spectrum is highly anisotropic. In other words, the maximum photon energy that may be emitted in the forward direction can be significantly larger than that emitted in the backward direction, especially in the case of large recoils at ultra-relativistic energies. Consequently, in the laboratory (*lab*) frame, one has to perform a complicated phase-space integration over a very elongated ellipsoidal volume. To avoid this complication, Tsai introduced a special Lorentz frame, so-called the *S-frame*, [2] corresponding to the center-of-mass system of the recoiling proton and the emitted photon in which $\vec{p} + \vec{P} - \vec{p}' = \vec{P}' + \vec{k} = \vec{0}$. The advantage of transforming to this frame is that the energy conserving delta function becomes independent of photon emission angles such that the ellipsoidal $|\vec{k}|$ integration reduces to a spherical integration. Furthermore, the maximum energy of the soft photon Δ_S in this special frame is also considered smaller than any other energy of the system, and thus using SPA, one can neglects the photon energy $E^S_{\gamma^*}$ within the delta function. Thus, the differential cross section in the S-frame is given as

$$
\begin{aligned}
\left[\frac{\widetilde{\mathrm{d}\sigma_{br}}}{\mathrm{d}\Omega'_l}\right]^S_{\gamma\gamma^*} = & -\frac{\alpha}{16(2\pi)^4}\sqrt{\frac{{E'_S}^2 - m_l^2}{(P_S\cdot p_S)^2 - m_l^2 M^2}} \\
& \times \delta\left(E'_S + {E'_p}^S - E_S - E^S_p\right) \frac{\mathrm{d}E'_S}{{E'_p}^S} \frac{\mathrm{d}^3\vec{k}_S}{E^S_{\gamma^*}} \\
& \times \frac{1}{4}\sum_{spins} |\mathfrak{M}_0|^2 \left[\frac{p'_S}{p'\cdot k_S} - \frac{p_S}{p\cdot k_S} + \frac{P_S}{P_S\cdot k_S} - \frac{P'_S}{P'_S\cdot k_S}\right]^2 , \qquad (2.33)
\end{aligned}
$$

where in terms of *lab*-frame energies we have, $E_S = E'^{el} = E/\eta$, $E^S_p = E + M - E'^{el}$, $E'_S = E$, and ${E'_p}^S = M$ in the SPA. Now using the delta function, we can eliminate the lepton momentum $|\vec{p}'_S|$ by integration to obtain a differential cross section formula

[2] This frame is also termed in the literature as the *R-frame*.

quite similar to the elastic one (but with reversed kinematics), albeit the integration over the photon momentum $\vec{k}_S$. In fact the resulting differential cross section under relativistic approximations, i.e., for $-Q^2 \gg m_l^2$ and $m_l \ll M, E_S, E'_S$, factorizes into the Rosenbluth differential cross section, namely,

$$\left[\frac{\mathrm{d}\sigma_{br}}{\mathrm{d}\Omega'_l}\right]^S_{\gamma\gamma^*} = -\frac{\alpha}{(2\pi)^2}\left(\frac{\mathrm{d}\sigma_{el}(Q^2)}{\mathrm{d}\Omega'_l}\right)^S_{\text{Rosenbluth}} \times \int_\lambda^{\Delta_S} |\vec{k}_S|\,\mathrm{d}E^S_{\gamma^*}\,\Theta\Big(\eta\Delta^*_\gamma - \Delta_S\Big) \oiint \mathrm{d}\Omega^S_k \times \left[\frac{p'_S}{p'_S\cdot k_S} - \frac{p_S}{p_S\cdot k_S} + \frac{P_S}{P_S\cdot k_S} - \frac{P'_S}{P'\cdot k_S}\right]^2 . \tag{2.34}$$

In particular, the upper limit of the photon energy integration $\Delta_S \ll M$ in the S-frame can be related to the lepton detector acceptance, $\Delta^*_\gamma = E'^{el} - (E')_{\max}$, [3] and the proton recoil factor, $\eta = E/E'^{el}$, in the *lab*-frame as $\Delta_S \leq \eta\Delta^*_\gamma$ (cf. Appendix B). Notably with the Θ-function being free of the photon emission angles, the angular integration can be easily performed. Finally, transforming back to *lab*-frame we have the result for the inelastic differential cross section

$$\left[\frac{\mathrm{d}\sigma_{el}(Q^2)}{\mathrm{d}\Omega'_l}\right]_{\gamma\gamma^*} = \frac{\alpha}{\pi}\left(\frac{\mathrm{d}\sigma_{el}(Q^2)}{\mathrm{d}\Omega'_l}\right)_{\text{Rosenbluth}} \delta_{\text{brem}}(Q^2)\,, \tag{2.35}$$

where

$$\delta_{\text{brem}}(Q^2) = \left[\ln\left(\frac{-Q^2}{m_l^2}\right) - 1\right]\ln\left(\frac{(m_l\eta\Delta^*_\gamma)^2}{EE'\lambda^2}\right) + 2\ln\eta\ln\left(\frac{M(2\eta\Delta^*_\gamma)^2}{(E'_p + |\vec{P}'|)\lambda^2}\right) - \left[1 - \frac{E'_p}{|\vec{P}'|}\ln\left(\frac{E'_p + |\vec{P}'|}{M}\right)\right]\ln\left(\frac{(2\eta\Delta^*_\gamma)^2}{\lambda^2}\right) + \delta_{\text{real}}(Q^2;\Delta^*_\gamma)\,, \tag{2.36}$$

with $E'_p = M - Q^2/(2M)$, and δ_{real} collects the detector resolution dependent IR-finite terms (see Ref. [163] for their evaluation) that contribute to the $\mathcal{O}(\alpha)$ radiative corrections. Note that the all IR-divergent terms $\propto \ln(\lambda^2)$ in the above expression are exactly opposite in sign to those in $\delta_{1-\text{loop}}$ Eq. (2.28). Consequently, when the inelastic soft

[3] Here we note that $E' = (E')_{\max}$ is the maximum value of the inelastically scattered lepton energy beyond which the detector can not distinguish the scattered lepton energy E' from the corresponding elastic limit E'^{el}, amounting to unobservable radiation loss.

bremsstrahlung contributions are added to the elastic contributions the resulting differential cross sections, namely,

$$\begin{aligned}\left[\frac{\mathrm{d}\sigma_{el}}{\mathrm{d}\Omega_l'}\right]_{2\gamma} &= \left[\frac{\mathrm{d}\sigma_{el}}{\mathrm{d}\Omega_l'}\right]_{\gamma\gamma} + \left[\frac{\mathrm{d}\sigma_{br}}{\mathrm{d}\Omega'}\right]_{\gamma\gamma^*} \\ &= \left(\frac{\mathrm{d}\sigma_{el}}{\mathrm{d}\Omega_l'}\right)_{\text{Rosenbluth}} \left[1 + \frac{\alpha}{\pi}\left\{\delta_{\text{virtual}} + \delta_{\text{real}}(\Delta_\gamma^*)\right\}\right] , \end{aligned} \tag{2.37}$$

is IR-finite whose expression being somewhat elaborate is left out for the sake of brevity. We instead refer to Tsai's original work, Ref. [47] [see Eq. (III.23) of this reference] for the complete analytical expression. This completes a typical radiative correction analysis of the ℓ-p elastic scattering process especially valid at relativistic lepton energies. However, in the pretext of high-precision radiative analyses typically needed for low and intermediate energy scattering data, many of the approximations used in Tsai's analysis become invalid and are potential sources of large systematic errors. This motivates a reconsideration of the complete radiative correction procedure in a modern field theoretical framework to effectively tackle hadronic effects in a model independent approach.

2.4 Motivation of Thesis Work

Although a lot of improvements to the approximations used in Tsai's were suggested over the years, still such analyses were inherently afflicted with large theoretical uncertainties in the context of a proper description of the proton-photon interactions due to the "non-Dirac-like" extended proton structure and complexities arising due to the underlying non-perturbative nature of strong interactions at low energies.

As discussed in the last section, hadronic effects have been traditionally handled in the literature through phenomenological modeling of the *off-shell* hadron vertices using *ad hoc on-shell* form factors which invariably give rise to uncontrollable errors. Moreover, off-shell for factors are complicated objects requiring the introduction of composite operators with the requirement of additional parameters in the theory. What is ideally needed in this case is a microscopic dynamical perturbative description of low-energy QCD, from

which one can derive both on-shell and off-shell properties of the nucleon, including observables such as charge or magnetic radii from first principles, *vis-a-vis* a low-energy EFT treatment. Thus, the primary objective of this thesis is to provide a model-independent EFT assessment of radiative corrections to the basic lepton-proton elastic scattering process as well as its inelastic background, viz, the radiative tail. Particular emphasis is given to the inclusion of vital recoil effects of not only the proton but also for the lepton, keeping in mind the low-energy kinematics of the proposed MUSE Experiment. A particular concern is degree of robustness of standard radiative analysis in high-energy electron-proton scattering data which may be questionable in the context of low-energy muon-proton scattering where muon recoil *de facto* leads to significant modifications to the radiative tail spectrum in comparison to electron scattering. Furthermore, the work of the thesis investigates novel systematic radiative recoil effects especially in the context of the TPE evaluation using HBχPT, which to our knowledge has not been pursued till date.

In the next chapter, we present an EFT description of the low-energy QCD based on the guiding principles of chiral symmetry, leading to the construction of χPT, and in particular, its 'extreme' non-relativistic extension to the baryon sector, the HBχPT.

Chapter 3

Methodology: Low-Energy EFT

3.1 Introduction

In this chapter, we will describe our *modus operandi*, namely, Chiral Perturbation Theory (χPT) which is low-energy Effective Field Theory (EFT) of strong interactions, and in particular, the SU(2) version of Baryon Chiral Perturbation Theory (BχPT) which is a version of χPT ideal for the studying the low-energy dynamics of mesons and nucleons, or even considering its extreme non-relativistic limit to include nucleon recoil effects, namely, the Heavy Baryon Chiral Perturbation Theory (HBχPT). Even before the advent of the gauge theory of strong interactions, namely, Quantum Chromodynamics (QCD) [164], which is the currently accepted underlying microscopic theory of strong interactions, the existence of chiral symmetry was known to people from phenomenological studies based on conservation of vector and axial-vector currents in nuclear beta decay [165, 166]. However, a field theoretical framework, capturing this symmetry, did not materialize until the late 70's due to the inherent non-perturbative nature of the problem and the lack of renormalizability of local interactions, which plagued many of these low-energy theories. But this scenario got radically altered, when Steven Weinberg through one of his seminal papers in 1979 [167] argued that a non-renormalizable theory was not altogether meaningless and may still be made useful and *effectively renormalizable*, provided one considers all possible terms in the Lagrangian allowed by low-energy symmetry constraints (other

than chiral symmetry) like parity, charge conjugation, and time-reversal invariances, etc., consistent with the underlying parent theory. In general, this meant that there could be an infinite number of terms (operators) which meets this requirement. However, a *power counting scheme*, which re-organizes such terms by some pre-determined degree of importance, ensured the predictability of the theory. In this way, one could simply deal with a small number of terms relevant at the desired level of accuracy. This path-breaking idea marked the beginning of a new era in Quantum Field theory (QFT), which led to the emergence of EFT [168] as a versatile dynamical framework capable of tackling non-perturbative particle dynamics, especially in the context of a hierarchy different energy scale. χPT is one such EFT which exploits the chiral symmetry and its breaking pattern to describe strong interaction at low energies $\lesssim 1$ GeV where the standard perturbative QCD is invalid.

3.2 Effective Field Theory

The underlying philosophy of EFT is that low-energy or long-distance physics does not depend on the details of high energy or short distance physics [169]. One can do a consistent field theoretical calculation considering only the relevant degrees of freedom available at that energy scale, ignoring additional degrees of freedom that may be manifest at high energies. The idea though straightforward, to put into practice, maybe quite involved. The essential prescription of an EFT materializes from an "unproven theorem", viz, a conjecture put forward by Weinberg [167], popularly regarded as the *Weinberg's Folk Theorem* [170], as coined by Arthur Wightman. It postulated that *a perturbative description in terms of the most general effective Lagrangian containing all terms compatible with the assumed symmetries yields the most general S-matrix elements consistent with analyticity, perturbative unitarity, cluster decomposition and the underlying symmetry principles of quantum field theory.*

The following points below briefly summarize the basic tenets and requirements involved in the formulation of an EFT prescription:

- **Approximate theory:** Unlike a renormalizable QFT which is in principle valid to infinitely high range of energies/momentum scales, an EFT is an approximate version of the parent QFT with a limited range of validity where there exists a well-defined scale hierarchy in the underlying dynamics.

- **Non-renormalizability:** The most general EFT Lagrangian which is constructed utilizing all possible available low-energy symmetries have in effect an infinite number of unknown parameters or couplings c_n, so-called the *Low-Energy Constants* (LECs), and higher dimensional ($D > 4$) local operators $\mathcal{O}_n$ of diminishing importance having the generic form:

$$\mathcal{L}_{\rm EFT}^{(\Lambda)}(x,\partial) \;=\; \underbrace{\mathcal{L}_{\leq D}}_{\text{renormalizable}} + \underbrace{\frac{1}{\Lambda}\mathcal{L}_{D+1} + \frac{1}{\Lambda^2}\mathcal{L}_{D+2} + \cdots}_{\text{non-renormalizable}} \equiv \sum_{n=0}^{\infty} \frac{c_n}{\Lambda^n}\mathcal{O}_n(x,\partial)\,. \tag{3.1}$$

- **Hard scale:** Existence of a well-defined *breakdown* Λ_H separating the energy domain into low- and high-energy (ultraviolet) regimes. All physical dynamics above Λ_H are considered perturbative while those below are inherently nonperturbative.

- **Integrating-out heavy modes:** Identification of the high-energy degrees of freedom which get frozen or decoupled from the spectrum as the relevant energies are insufficient to activate or excite them. However, in the the remaining theory with the relevant low-energy effective degree of freedom, the information of such high energy modes are not lost but remain implicitly embodied in the couplings of operator terms in the Lagrangian. This very idea, of course, stems from the well-known *Decoupling Theorem* by Appelquist and Carrazone [171]: *the effects of heavy particles go into local terms in a field theory, either as renormalizable couplings or in non-renormalizable local interactions suppressed by powers of the heavy mass scale.*

- **Low-energy constants (LECs):** The coupling parameters c_n symbolize all the ultraviolet (UV) physics that remain unresolved in the effective theory and are often used as counterterm to renormalize UV divergences arising in lower-dimensional operators. These LECs are *a priori* undetermined from the symmetry principles of

the effective theory itself and are needed to be fixed either phenomenologically, i.e., using data from experiments or Lattice QCD, or through "matching".

- **Matching:** In cases where either the underlying UV complete theory is completely known or empirical information is unavailable, the unknown coefficients of the local effective operators can be fixed by comparing the same Green's functions calculated in the full theory and the effective theory at a certain kinematic scale.

- **Universality and predictability:** The LECs ensure universality of the EFT in the sense that once they are estimated for a given process, they can be used in other processes involving the same the local operators to make predictions.

- **Power-counting:** This is used to establish an effective perturbative expansion of organizing the local operators in a way that at a given order (depending on the desired level of accuracy) only a finite number of terms in the Lagrangian can contribute. Being based on dimensional analysis scheme the procedure keeps track of systematic uncertainties in a controlled way, which is also necessary to ensure the predictive power of the EFT.

- **Momentum expansion:** Unlike a renormalizable QFT with a perturbative expansion in terms of a dimensional coupling, an EFT expansion scheme organizes the Feynman amplitudes (i.e., S-matrix elements) $\mathcal{M}$ for a given process in a generic expansion in powers of the typical small momentum $p \ll \Lambda_H$, namely,

$$\mathcal{M} \sim \sum_{n=0}^{\infty} \mathcal{K}_n \left(\frac{p}{\Lambda_H}\right)^n , \tag{3.2}$$

where $\mathcal{K}_n$ denote expressions containing masses of particles and other kinematical factors.

The motivation behind the formulation of an EFT for a particular dynamical system is based on one of two scenarios: (1) "UV completion" or the so-called *bottom-up approach* which assumes that the full known underlying high-energy dynamics is either not known or solvable at low-energies, and (2) "IR completion" or the so-called *top-down approach* which is based on the assumption that even if the full underlying theory is known or

solvable; it is more efficient and simpler to work with an effective low-energy theory with lesser degrees of freedom upon integrating out the heavy modes from the Lagrangian. The former idea of UV completion, on the one hand, motivated the development of χPT as a low-energy EFT of QCD, since the asymptotically free nature of strong coupling, invalidates the use of standard perturbative QFT framework. The latter IR completion scenario, on the other hand, motivated the development of the heavy baryon formulation, namely, HBχPT [172] which is a low-energy non-relativistic EFT of the Lorentz invariant χPT extended to include baryons, namely, BχPT. The recipe to integrate-out the heavy dynamics is elucidated very clearly in Ref. [173] in the context of a toy scalar model with a heavy field H of mass m_H that linearly couples to some combination of light fields J. For the sake of completeness we repeat the essential steps below. The Lagrangian is given as

$$\mathcal{L} = \frac{1}{2}(\partial_\mu H \partial^\mu H - m_H^2 H^2) + JH\,. \tag{3.3}$$

The following sequence of steps executes the procedure:

- Identification of a hard scale Λ_H with respect to which H is regarded as the heavy degree of freedom and J corresponding to a collection of light fields.

- Obtaining the effective action in terms of the light fields J after integrating out the heavy field H either using the heavy field's equation of motion [174] or in a path integral formalism [173, 175]. In the path integral approach the action $\mathcal{S}$ is first integrated by parts, whereby the surface term drops out at sufficiently large distances, leading to

$$\begin{aligned}\mathcal{S}[H,J] &= \int d^4x\, \mathcal{L}[H,J] \\ &= \int d^4x \Big[-\frac{1}{2} H\, \mathbb{D}\, H + JH \Big] \\ &= -\frac{1}{2}\int d^4x \Big[\frac{1}{2} H'\, \mathbb{D}\, H' - J\, \mathbb{D}^{-1} J \Big]\,, \end{aligned} \tag{3.4}$$

  where $\mathbb{D} = \Box + m_H^2$, following a change of variable, $H(x) \to H'(x) = H^0(x) + H(x)$, where

$$H^0(x) = \int d^4y\, \Delta_H(x-y) J(y) = -\mathbb{D}^{-1} J(x), \tag{3.5}$$

noting that

$$\begin{aligned}
[\mathscr{D}H] &= [\mathscr{D}H'] \\
\mathbb{D}_x\Delta(x-y) &= -\delta^4(x-y)\,, \\
\mathbb{D}_x H^0(x) &= \int d^4y\,\mathbb{D}_x\Delta_H(x-y)J(y) = -\int d^4y\,\delta^4(x-y)J(y) = -J(x)\,,
\end{aligned}$$

such that the generating functional remains invariant:

$$Z[0] = \int [\mathscr{D}H] e^{i\int d^4x\,\mathcal{L}[H,0]} = \int [\mathscr{D}H'] e^{i\int d^4x\,\mathcal{L}[H',0]}\,. \tag{3.6}$$

Equation (3.4) may be easily verified as follows:

$$\begin{aligned}
\int d^4x\,\Big[-\frac{1}{2}H\,\mathbb{D}\,H + JH\Big] &= \int d^4x\Big[-\frac{1}{2}(H'-H^0)\,\mathbb{D}\,(H'-H^0) + J(H'-H^0)\Big] \\
&= -\frac{1}{2}\int d^4x\Big[H'\,\mathbb{D}\,H' - H^0\,\mathbb{D}\,H' - JH' + JH^0\Big] \\
&= -\frac{1}{2}\int d^4x\Big[H'\,\mathbb{D}\,H' + JH^0\Big]
\end{aligned} \tag{3.7}$$

where through repeated integration by parts it may be shown that the second and third terms on the right hand side of the above integral cancel, namely,

$$\int d^4x H^0\,\mathbb{D}\,H' = \int d^4x\,H'\,\mathbb{D}H^0 = -\int d^4x\,JH'\,, \tag{3.8}$$

where $J = -\mathbb{D}H^0$. Thus, the effective generating functional is

$$\begin{aligned}
W_{eff}[J] = e^{i\mathcal{S}_{eff}[J]} &= \frac{\int[\mathscr{D}H]e^{i\int d^4x\,\mathcal{L}[H,J]}}{\int[\mathscr{D}H]e^{i\int d^4x\,\mathcal{L}[H,0]}} \\
&= \frac{\int[\mathscr{D}H']e^{i\int d^4x\Big[-\frac{1}{2}(H'\,\mathbb{D}\,H'+JH^0)\Big]}}{\int[\mathscr{D}H]e^{i\int d^4x\Big[-\frac{1}{2}(H\,\mathbb{D}H)\Big]}} \\
&= \frac{\int[\mathscr{D}H']e^{i\int d^4x\Big[-\frac{1}{2}(H'\,\mathbb{D}\,H'-JH^0)\Big]}}{\int[\mathscr{D}H']e^{i\int d^4x\Big[-\frac{1}{2}(H'\,\mathbb{D}\,H')\Big]}} \\
&= e^{-\frac{i}{2}\int \mathrm{d}^4x JH^0}\,,
\end{aligned} \tag{3.9}$$

and thereby the effective action could be directly read off, namely,

$$\mathcal{S}_{eff}[J] = -\frac{1}{2}\int \mathrm{d}^4x\, J(x)H^0(x) = -\frac{1}{2}\int d^4x\, d^4y\, J(x)\Delta_H(x-y)J(y)\,. \tag{3.10}$$

- Integrating out the heavy field H leaves the effective action $\mathcal{S}_{eff}$ with only the light fields J convoluted by the non-local operator $\Delta_H(x-y)$. However, to facilitate local interactions between light fields, the non-local effective action must be expanded in terms of local operators. To obtain local interactions $J(y)$ is Taylor expanded in x

$$J(y) = J(x) + (y-x)\frac{\partial J(y)}{\partial y}\Big|_{y=x} + \cdots\,. \tag{3.11}$$

Keeping only the first term in the expansion and using the result

$$\int \mathrm{d}^4y\, \Delta_H(x-y) = \int \mathrm{d}^4y \int \frac{d^4p}{(2\pi)^4}\frac{e^{-ip(x-y)}}{p^2 - m_H^2 + i\eta} = -\frac{1}{m_H^2} + \mathcal{O}\left(\frac{1}{m_H^4}\right)\,, \tag{3.12}$$

finally yields a local effective action

$$\mathcal{S}_{eff}[J] = \int d^4x \frac{1}{2m_H^2} J(x)J(x) + \cdots \tag{3.13}$$

where the ellipses denote additional terms suppressed by higher powers of heavy particle mass m_H. This action correctly describes the physics of low-energy modes at scales $E \ll m_H$. The essential point to realize here that to any given order in $1/m_H$ expansion there are only a *finite* number of effective operators.

3.3 Chiral Symmetry in QCD and its Breaking

Chiral symmetry is one of the important low-energy global symmetries of strong interaction [176] in the light quark sector. The QCD Lagrangian written in terms of the current quark fields $q(x)$ with flavors, namely, the "up" u, "down" d and the "strange" s, and

the eight independent color gauge fields, namely, the gluons $\mathcal{A}^a_\mu(x)$ $(a = 1, \cdots, 8)$ is [1]

$$\mathcal{L}_{\rm QCD} \;=\; \bar{q}(x)[i\not{D} + \mathcal{M}_q]q(x) - \frac{1}{2}{\rm Tr}_c\left[\mathcal{G}_{\mu\nu}(x)\mathcal{G}^{\mu\nu}(x)\right] \tag{3.14}$$

where, the gluon field strength tensor is $\mathcal{G}^a_{\mu\nu} = \partial_\mu\mathcal{A}^a_\nu - \partial_\nu\mathcal{A}^a_\mu + gf^{abc}\mathcal{A}^b_\mu\mathcal{A}^c_\nu$ with strong coupling g and *structure constant* f_{abc}. The quark fields transforming according to the fundamental representation of the flavor ${\rm SU}(3)_f$ symmetry is

$$q = \begin{pmatrix} u \\ d \\ s \end{pmatrix}, \text{ and } \mathcal{M}_q = \begin{pmatrix} m_u & 0 & 0 \\ 0 & m_d & 0 \\ 0 & 0 & m_s \end{pmatrix}$$

being the quark mass matrix. The QCD Lagrangian at a classical level is invariant under the full global symmetry transformation group:

$$\mathcal{G} = {\rm SU}(3)_L \otimes {\rm SU}(3)_R \otimes {\rm U}(1)_V \otimes {\rm U}(1)_A\,.$$

However at the quantum loop level the singlet ${\rm U}(1)_A$ global symmetry transformations, namely, $q \mapsto \exp(-i\gamma_5\alpha)q\,, \alpha \in \mathbb{R}$, of the axial-vector current $A_\mu(x) = \bar{q}(x)\gamma_\mu\gamma_5 q(x)$ develops the so-called *chiral anomaly* [177, 178] which explicitly breaks the above symmetry, i.e., in group-theoretical terms

$$\mathcal{G} \Rightarrow \tilde{\mathcal{G}} = {\rm SU}(3)_L \otimes {\rm SU}(3)_R \otimes {\rm U}(1)_V\,.$$

Special gluonic field configurations, so-called the *instantons* [179], are believed to induce such anomalous symmetry breaking. It is worth noting that the QCD Lagrangian remains invariant under the singlet ${\rm U}(1)_V$ global symmetry transformations, namely, $q \mapsto \exp(-i\beta)q\,, \beta \in \mathbb{R}$, resulting in the conserved singlet vector current, $V_\mu(x) = \bar{q}(x)\gamma_\mu q(x)$. This unbroken symmetry is connected with conserved baryon numbers, $B = \pm 1/3$ of the light quarks and anti-quarks.

[1] Note that for each flavor of quark field, there is an associated color triplet, e.g., $u \equiv (u_r, u_g, u_b)$, with subscripts "r", "g" and "b" standing for "red", "green" and "blue", respectively, transforming according to the fundamental representation of color ${\rm SU}(3)_c$ symmetry. Also notable is that the covariant derivative $\not{D}$ acts only in color and Dirac spaces but not in the flavor space.

At this point, one can decompose the quarks field into its left handed q_L and right handed q_R chiral components as

$$q_L = \frac{1}{2}(1-\gamma_5)q \quad \text{and} \quad q_R = \frac{1}{2}(1+\gamma_5)q\,, \tag{3.15}$$

in terms of which the QCD Lagrangian Eq. (3.14) becomes

$$\begin{aligned}\mathcal{L}_{\rm QCD} &= \bar{q}_R[i\not{D}]q_R + \bar{q}_L[i\not{D}]q_L - \frac{1}{2}{\rm Tr}_c(\mathcal{G}_{\mu\nu}\mathcal{G}^{\mu\nu}) - \bar{q}_L\mathcal{M}_q q_R - \bar{q}_R\mathcal{M}_q^\dagger q_L \\ &= \mathcal{L}^0_{QCD} - \delta\mathcal{L}^m_{QCD}\,. \end{aligned} \tag{3.16}$$

In the last line of the above equation, we have separated the QCD Lagrangian into a massless part $\mathcal{L}^0_{QCD}$ and a quark mass dependent term $\delta\mathcal{L}^m_{QCD}$. We have

$$\mathcal{M}_q = \begin{pmatrix} m_u = 0.005\,{\rm GeV} & 0 & 0 \\ 0 & m_d = 0.009\,{\rm GeV} & 0 \\ 0 & 0 & m_s = 0.175\,{\rm GeV} \end{pmatrix} \ll \Lambda_\chi \approx 1\,{\rm GeV}$$

where the mass scale of 1 GeV is the scale of chiral symmetry breaking, i.e., the scale usually associated with the mass of the ρ vector-meson[2] which is one of the lightest hadrons composed of the current quarks which can not be one of the Goldstone bosons of chiral symmetry breaking. As long as the current quark masses are considerably smaller than this scale, chiral symmetry is approximately realized where the mass dependent Lagrangian term has little influence on the QCD spectrum. In this case, it can be easily seen that the $\mathcal{L}^0_{QCD}$ is invariant under the following independent transformation of the left-handed and right-handed quark field:

$$q_R \mapsto R\,q_R, \quad q_L \mapsto L\,q_L, \quad \text{where } R, L = \exp\left[-i\sum_{a=1}^{8}\Theta_a^{L,R}\frac{\lambda^a}{2}\right] \in {\rm SU}(3)_{L,R}$$

[2]In many processes involving nucleons, e.g., in the low-energy Compton scattering process, the spin-3/2 resonances $\Delta(1232)$ play special role in setting the hard scale of χPT, as the mass difference, $M_\Delta - M_N \approx 300$ MeV, is much snaller then the ρ meson mass [180].

where $\Theta_a^{L,R}$ $(a = 1, \cdots, 8)$ are real-valued parameters and λ^a are the Gell-Mann SU(3) matrices. So in group-theoretical terms, we can say that the QCD Lagrangian has the global $G = \mathrm{SU}(3)_L \otimes \mathrm{SU}(3)_R$ symmetry in the limit of vanishing quark masses (chiral limit). This group G is commonly termed as the *chiral symmetry group*. Noether's theorem [181], suggests that es corresponding to this global symmetry group G one can expect $2(3^2 - 1) = 16$ conserved currents, namely, the left-handed and right-handed currents,

$$\begin{aligned} \mathcal{L}_\mu^a(x) &= \bar{q}_L(x)\gamma_\mu \frac{\lambda^a}{2} q_L(x)\,, \\ \mathcal{R}_\mu^a(x) &= \bar{q}_R(x)\gamma_\mu \frac{\lambda^a}{2} q_R(x), \quad a = 1, ..., 8\,. \end{aligned} \tag{3.17}$$

Equivalently the chiral group may be expressed as $G = \mathrm{SU}(3)_V \otimes \mathrm{SU}(3)_A$, and hence associated with sixteen conserved vector $\mathcal{V}_\mu^a$ and axial-vector $\mathcal{A}_\mu^a$ currents, which arise by taking the following linear combinations of the above chiral currents:

$$\begin{aligned} \mathcal{V}_\mu^a(x) &= \mathcal{R}_\mu^a(x) + \mathcal{L}_\mu^a(x) = \bar{q}(x)\gamma_\mu \frac{\lambda^a}{2} q(x); \quad \partial^\mu \mathcal{V}_\mu^a(x) = 0\,, \\ \mathcal{A}_\mu^a &= \mathcal{R}_\mu^a(x) - \mathcal{L}_\mu^a(x) = \bar{q}(x)\gamma_\mu\gamma_5 \frac{\lambda^a}{2} q(x); \quad \partial^\mu \mathcal{A}_\mu^a(x) = 0\,. \end{aligned} \tag{3.18}$$

Symmetries in QFT are realized in two different ways depending on the response of the ground state to these symmetries, viz.,

- **Wigner-Weyl mode:** Ordinary realization of symmetries, in which a the symmetry of the Hamiltonian/Lagrangian is reflected in the symmetry of the spectrum leading to degeneracies that are especially respected in the ground (vacuum) states [182, 183].

- **Nambu-Goldstone mode:** Non-trivial way of realization of symmetries, in which a symmetry of the ground state becomes different or hidden from the apparent symmetry pattern of the Hamiltonian/Lagrangian leading to a *spontaneously* or *dynamically* broken symmetry [165, 166, 184, 185].

Now according to the *Vafa-Witten Theorem* [186]: *vector-like global symmetries, such as strangeness, flavor, isospin, baryon number, etc., in vector-like gauge theories, e.g., QCD can not be spontaneously broken as long as the vacuum theta-angle is zero (or nearly zero).* This should mean that such vector-like symmetries must be realized in the Wigner-Weyl mode and consequently, the vector charges Q_V^a annihilates the ground state, i.e.,

$$Q_V^a|0\rangle = 0, \quad Q_V^a = \int d^3x\, \mathcal{V}_0^a(x)$$

leading to a QCD spectrum of degenerate multiplets, *vis-a-vis*, the baryon octets belonging the vector subgroup $H = SU(3)_V$ of the chiral group G. However, the fact that the observed baryon octet masses are not the same and in contrary vary substantially, suggests that symmetry breaking pattern in the Wigner-Weyl mode involves explicitly broken symmetries. In this case, the considerable difference of the physical s-quark mass from that of the u, d-quark explicitly breaks the flavor $\mathrm{SU}(3)_V$ symmetry. It may be notable that although $\mathrm{SU}(3)_V$ is a "badly" broken symmetry, the isospin subgroup $\mathrm{SU}(2)_V$ is a fairly good symmetry of the QCD spectrum as evident from the almost equal masses of the baryon charge multiplets for a given strangeness.

Proceeding in the same line of arguments, the axial-vector symmetry is also expected to be realized in the same mode with the axial charge annihilating the vacuum, i.e.,

$$Q_A^a|0\rangle = 0, \quad Q_A^a = \int d^3x\, \mathcal{A}_0^a(x)\,.$$

This leads to the so-called *parity doubling* of the QCD spectrum with the expected appearance of degenerate negative parity baryons that contradicts with observed spectrum. In their absence, one concludes that the axial charges do not annihilate the ground state, $Q_A^a|0\rangle \neq 0$. Does this mean that axial symmetry is not good symmetry? There are plenty of evidence to suggest that this symmetry is somehow manifest. For example, the weak decay of a pion is consistent with the Partially Conserved Axial-vector Current (PCAC) hypothesis [166], along with the success of Goldberger-Treiman relation [187], indicates that underlying strong interaction mechanisms respect axial symmetry, albeit indirectly. Hence, the axial symmetry must be realized in the Nambu-Goldstone mode [184, 185], i.e., the ground state does not preserve the full symmetry group of the Hamiltonian, in

which case the chiral symmetry group G spontaneously breaks into the diagonal subgroup H (or the "little group") of flavor symmetries, i.e.,

$$\mathrm{SU}(3)_L \otimes \mathrm{SU}(3)_R \equiv \mathrm{SU}(3)_{V=L+R} \otimes \mathrm{SU}(3)_{A=L-R} \Rightarrow \mathrm{SU}(3)_V .$$

Now according to *Goldstone's Theorem: for every spontaneously broken symmetry, there corresponds a massless particle whose quantum numbers are the same as that symmetry's Noether Charge*. This means that corresponding to the eight axial generators Q_A^a that do not annihilate the vacuum and commute with the Hamiltonian, there should appear an octet of massless *Nambu-Goldstone* (NG) bosons under the same flavor subgroup $H \subset G$ but with negative parities and baryon number $B = 0$. Indeed the lightest particles in the hadron spectrum, namely, the pseudoscalar octet of mesons, $\pi^{\pm}$, π^0, $K^{\pm}$, K^0, $\bar{K}^0$, and η, may be identified as the NG bosons of spontaneous broken chiral symmetry group G. In reality, these octet mesons are *pseudo*-NG bosons by nature due to their small masses (compared to the chiral symmetry breaking scale) that originate from the non-zero quark mass term $\delta\mathcal{L}_{QCD}^m$ of the QCD Lagrangian explicitly breaking the chiral symmetry. With chiral symmetry being an approximate symmetry of strong interaction, the conservation of the axial current $\mathcal{A}_\mu^a$ is only approximately realized, leading to the well-known PCAC relation,

$$\langle 0|\partial^\mu \mathcal{A}_\mu^a(x)|\pi^b(x)\rangle = \delta^{ab} m_\pi^2 f_\pi \,, \quad (a, b = 1, 2, 3) \tag{3.19}$$

valid in the SU(2) limit, where f_π is the pion decay constant. This "softness" of this symmetry breaking effects can be best described in a perturbative *spurion analysis*, as long as $\delta\mathcal{L}_{QCD}^m$ terms are small compared to some relevant hadronic scale, e.g., the chiral symmetry breaking scale $\Lambda_\chi \sim 1$ GeV. This is what is done in χPT, which describes the interactions of NG bosons among themselves and with external fields in perturbative S-matrix expansion in terms of quark mass and momenta.

To this end, a spurion analysis can be easily described in QFT, e.g., using complex scalar fields. The following sequence of steps executes the procedure:

- *Introduction of a complex spurion field for the explicit symmetry breaking quantity, (e.g., quark mass, electric charge, etc.) pretending it to transform in a way that the symmetry breaking terms are invariant under the full symmetry.*

- *Construction of the effective Lagrangian with invariant operators in terms of the spurion field.*

- *Restoring the true value of the symmetry breaking quantity as a vacuum expectation value (vev) of the spurion field which finally breaks the symmetry spontaneously with the spurion not transforming under the full symmetry.*

As a simple demonstration of this formalism, let us consider the following example, taken from Ref. [188], of a complex scalar Lagrangian with the perturbation $\mathscr{L}_{sb}$ which explicitly breaks the $\phi(x) \mapsto \phi'(x) = e^{i\alpha}\phi(x)$ global U(1) symmetry:

$$\begin{aligned} \mathcal{L}_0[\phi] &= (\partial_\mu \phi^*)(\partial^\mu \phi) - m^2|\phi|^2 - \lambda|\phi|^4 + \mathscr{L}_{sb}[\phi]\,, \\ \mathscr{L}_{sb}[\phi] &= \mu^2\phi^*\phi + c.c.\,, \end{aligned} \tag{3.20}$$

where μ^2 is a real constant which is considered small compared to any scale in the unbroken part of the Lagrangian. As a result of the symmetry transformation, the symmetry broken part of the Lagrangian becomes

$$\mathscr{L}_{sb}[\phi'] = \mu^2\phi'^*\phi' = e^{2i\alpha}\mu^2\phi^*\phi.$$

This is not invariant unless the parameter μ is promoted to behave like a complex scalar *spurion field* $\hat{\mu}$ that transformed as $\hat{\mu}^2 \mapsto e^{-2i\alpha}\hat{\mu}^2$. In this case the full Lagrangian $\mathcal{L}_0[\phi, \hat{\mu}]$ with the new "spurious" field is now invariant under the U(1) transformation. Using the spurion field one may proceed to construct an effective Lagrangian with the most general U(1) invariant operators of the form $\hat{\mu}^{2a}\phi^b\phi^{*c}\,, a, b, c \in \mathbb{Z}$, and $b > c$ such that

$$\hat{\mu}^{2a}\phi^b\phi^{*c} \overset{\mathrm{U}(1)}{\longmapsto} e^{i(-2a+b-c)\alpha}\hat{\mu}^{2a}\phi^b\phi^{*c}\,, \qquad \text{provided} \quad a = \frac{b-c}{2}\,. \tag{3.21}$$

Since μ is only a constant and not a field (real degree of freedom), at the end of the analysis the U(1) symmetry is again broken, but now "spontaneously" instead of "explicitly", by assigning μ the vev of the spurion field, namely, the *Dashen condition:* $\mu = \langle 0|\hat{\mu}|0\rangle > 0$. This facilitates a power series expansion in the perturbation parameter μ in the resulting

EFT. Thus, the spurion formalism in effect converts a theory with explicitly broken symmetry to mimic a spontaneously broken perturbative theory.

3.4 Chiral Perturbation Theory

In the long pursuit of developing a low-energy effective chiral theory of QCD incorporating spontaneous chiral symmetry breaking, it emerged that an effective decoupling of high-energy modes would not be manifest unless the NG bosons were realized in a non-linear way incorporating derivative interactions to be consistent with low-energy theorems. This would not only decouple short distance effects of quarks and gluons but also effects due to the presence of heavy mesons and other resonances, such as $\rho(770)$, in the hadron spectrum close to the hard scale and not appear explicitly in the chiral Lagrangian. Based on this fundamental tenet, Chiral Perturbation Theory (χPT) was established as an effective field theory of QCD which exploits the usual low-energy symmetries, like the P, C, and T invariances, as well as the spontaneously broken chiral symmetry to provide a systematic description of strong interaction at energy scales well below its breakdown scale, $\Lambda_\chi \sim 1$ GeV. Since the theory assumes chiral symmetry, its applications are restricted to the light quark sector and can not describe the dynamics of heavy quarks. In the meson sector, it describes the interactions among the pseudo-NG bosons as well as with the non-linearly coupled external fields in a perturbative NG boson momentum or quark mass expansion of the S-matrix elements, in contrast to the usual coupling constant expansion. When χPT is extended to incorporate the low-energy dynamics of baryons, we deal with Baryon Chiral Perturbation Theory (BχPT), and often its non-relativistic counterpart, Heavy Baryon Chiral Perturbation Theory (HBχPT) as used in the later chapters of this thesis. From here on we shall restrict our discussions only to the $N_f = 2$ flavor version of χPT with chiral group, $G = \mathrm{SU}(2)_L \otimes \mathrm{SU}(2)_R$, which spontaneously breaks into the diagonal "isospin" subgroup, $H = \mathrm{SU}(2)_{V=I}$, and describing the dynamics of nucleon $N = (p, n)$ and pion (π^+, π^0, π^-) fields only.

Since QCD can not be solved at low-energies, the effective Lagrangian expressed in terms of NG bosons is achieved as a bottom-up approach [189]. Here we briefly review the meson χPT following the nice exposition presented in Ref. [190]. The theoretical foundations of

χPT rely on the methodology proposed by Callan, Coleman, Wess, and Zumino (CCWZ formalism) [191, 192], of constructing an effective Lagrangian in the presence of spontaneously broken symmetry based on the well-known non-linear σ-model parametrization. Nevertheless, the formalism is truly general in the sense that the underlying physics can be shown to be independent of any choice of coordinate parametrization of the NG fields, provided that the parametrization is non-linear to facilitate the decoupling of heavy modes. In other words, the S-matrix elements are invariant under reparametrization, and thus, the low-energy physics should only depend on the structures of G and H. According to the *CCWZ formalism: If a theory invariant under the Lie Group manifold G with dimensionality $n_G = \dim G$ gets spontaneously broken to a Lie Group submanifold $H \subset G$ with dimensionality $n_H = \dim H$, then the resulting $n = n_G - n_H$ broken generators, namely, the NG bosons, would constitute the left coset or quotient space $K = G/H$ of H whose dimension is $n = \dim K$.*

3.4.1 SU($N_f = 2$) Meson Chiral Perturbation Theory

Along the lines of the CCWZ construction of group elements, the spontaneously broken chiral symmetry group can be written as

$$G = \mathrm{SU}(2)_L \otimes \mathrm{SU}(2)_R = \{(L, R) |\ L \in \mathrm{SU}(2)_L,\ R \in \mathrm{SU}(2)_R\}\,,$$

and that of the unbroken diagonal flavor subgroup can be written as

$$H = \mathrm{SU}(2)_V = \{V \equiv (V, V) |\ V \in \mathrm{SU}(2)_V\} \subset G.$$

The NG pions then belong to the coset space or quotient given by

$$K = G/H = \mathrm{SU}(2)_L \otimes \mathrm{SU}(2)_R / \mathrm{SU}(2)_\mathrm{V} \sim SU(2)_A.$$

Now, if $g_1 = (L_1, R_1)$, $g_2 = (L_2, R_2) \in G$, then using the group composition law of G, namely, $g_1 g_2 = (L_1, R_1)(L_2, R_2) = (L_1 L_2, R_1 R_2)$, it can be shown that the left coset $gH \in K$ of any element $g \in G$ has the representation, $gH = (LR^\dagger, \mathbb{I})H$:

Proof: If $h = (V, V) \in H$, and

$$gH = (L, R)H = \{(LV, RV)|\ V \in \mathrm{SU}(2)_V\}\ ,$$

then

$$\begin{aligned} gh = (L, R)(V, V) &= (LV, RV) = (LR^\dagger RV, RV) \\ &= (LR^\dagger, \mathbb{I})(RV, RV) = (LR^\dagger, \mathbb{I})(V', V')\,, \\ &= (LR^\dagger, \mathbb{I})h' \end{aligned} \tag{3.22}$$

where $\mathbb{I}_{2\times 2}$ is the SU(2) identity element and $h' \in H$ is the so-called *compensator* element. Then it implies the coset decomposition, $gH = (LR^\dagger, \mathbb{I})H$.

Thus, there is arbitrary choice in parameterizing the left coset gH of H by a single representative element, $U = LR^\dagger$, i.e., $gH = (U, \mathbb{I})H$. By virtue of invariance under reparametrization, in order to introduce the space-time coordinate x dependence of the left coset elements, U can be chosen as an element of the local SU(2) group, namely $g(x)H = (U(x), \mathbb{I})H$, where

$$U(x) = L(x)R^\dagger(x) = \exp\left(i\frac{\phi(x)}{f_\pi}\right) \in \mathrm{SU}(2)_{\mathrm{local}} \tag{3.23}$$

where $f_\pi \simeq 92$ MeV is the pion decay constant in the chiral limit, and $\phi(x)$ constitutes the triplet of pion fields, $\pi^a \equiv (\pi^1, \pi^2, \pi^2)$, which may be expressed in terms of the Pauli matrices, $\tau^a \equiv (\tau^1, \tau^2, \tau^1)$, in the physical "charge" basis as

$$\phi(x) = \sum_{a=1}^{3} \tau_a \phi_a(x) = \begin{pmatrix} \pi^0 & \sqrt{2}\pi^+ \\ \sqrt{2}\pi^- & -\pi^0\,. \end{pmatrix} \tag{3.24}$$

It is important to note that although the coset space elements are now isomorphic to SU(2) elements, it is not a group in general. Also note that the chiral transformations of the NG pion fields $\phi(x)$ in contrast to the field $U(x)$ are highly non-linear of the general

form

$$\pi^a(x) \mapsto \pi'^a(x) = \pi^a(x) + \sum_{p_1+p_2+p_3\geq 2,\, p_i\geq 0} f^a_{p_1p_2p_3}[\pi^1(x)]^{p_1}[\pi^2(x)]^{p_2}[\pi^3(x)]^{p_3}\,, \tag{3.25}$$

where the second terms on the right hand side represent the non-linearity of such transformations. In group theoretical language the above transformation can be represented in terms of the transformation of the square root of the $U(x)$ matrix field, i.e., $u^2(x) = U(x)$, namely, if $g \in G$, then

$$u(x) \overset{g}{\mapsto} u'(x) = \sqrt{LU(x)R^\dagger} = Lu(x)h^\dagger(L,R,\phi) = h(L,R,\phi)u(x)R^\dagger\,,$$

where $h(L,R,\phi) \in H$ is called the *compensator field*. This evidently reflects the fact that the $\mathrm{SU}(2)_{\mathrm{local}}$ parametrized [c.f Eq. (3.24)] coset elements are not necessarily preserved under the group action G. However, with the same $\mathrm{SU}(2)_{\mathrm{local}}$ parametrization, this kind of complicated *non-linear realization* of the pion fields can be reduced to a much more simpler transformation under the action of G, namely,

$$U(x) \overset{g}{\mapsto} U'(x) = LU(x)R^\dagger\,,$$

i.e., $U(x)$ now transforms *linearly* under G. To see this, consider the global action of the element $g \in G$ on the locally parameterized left coset of H, say, $\tilde{g}(x)H = (\tilde{U}(x), \mathbb{I})H$.

Proof: If $g = (L,R),\ \tilde{g} = (\tilde{L},\tilde{R}) \in G$, then

$$\begin{aligned} g\{\tilde{g}(x)H\} &= g\left\{(\tilde{L}\tilde{R}^\dagger(x),\mathbb{I})H\right\} = (L,R)(\tilde{L}\tilde{R}^\dagger(x),\mathbb{I})H = (L\tilde{L}\tilde{R}^\dagger(x),R)H \\ &= (L\tilde{L}\tilde{R}^\dagger(x)R^\dagger R,R)H = \left(L[\tilde{L}\tilde{R}^\dagger(x)]R^\dagger,\mathbb{I}\right)(R,R)H \\ &= (L\tilde{U}(x)R^\dagger,\mathbb{I})H\,. \end{aligned}$$

One can now proceed to construct the most general effective Lagrangian using the low-energy symmetry properties of the $U(x)$ field, which can be organized in increasing powers of pion momenta and quark mass; the momentum expansion amounts to expansion in derivative over pion fields. The matrix representation of $U(x)$ is a 2×2 matrix in the

flavor space which transforms linearly under chiral transformations such that

$$U^\dagger U = \mathbb{I}_{2\times 2}\ , \quad \det(U) = 1\,.$$

We have

$$\mathscr{L}^{\rm eff}_{\pi\pi} = \mathscr{L}^{(2)}_{\pi} + \mathscr{L}^{(4)}_{\pi} + \mathscr{L}^{(6)}_{\pi} + \cdots\ , \tag{3.26}$$

where the superscripts, $n = 2, 4, 6, ...$, indicates number of derivatives or powers of the quark masses. [3] It is notable that in the mesonic case invariance under parity and Lorentz symmetry restricts terms in the Lagrangian with only even number of derivatives or pion momenta, i.e., term of the form $\mathcal{O}(p^{2n})$ can only contribute. To this end, we only display the lowest chiral order Lorentz invariant Lagrangian respecting chiral symmetry, parity, time-reversal, G-parity and charge conjugation invariance, namely,

$$\mathscr{L}^{(2)}_{\pi} = \frac{f_\pi^2}{4}\left({\rm Tr}[D_\mu U (D^\mu U)^\dagger] + {\rm Tr}[\chi U^\dagger + U\chi^\dagger]\right), \tag{3.27}$$

where "Tr" is the trace over the 2×2 flavor space. An vital aspect is that the above Lagrangian has a *local* $\mathrm{SU}(2)_L \otimes \mathrm{SU}(2)_R$ symmetry. This issue has profound consequences in the realization of the underlying low-energy symmetries of QCD Green's functions on which χPT is based on. As a plausibility argument to the Weinberg's Folk Theorem by *Heiri Leutwyler* [193, 194]: *in the absence of anomalies the manifestly Lorentz invariant chiral Ward-Identities satisfied by QCD Green's functions of the symmetry currents are equivalent to the invariance of the Lagrangian, vis-a-vis the effective action, under local chiral transformations.* Thus, to correctly capture the low-energy structure à la off-shell effects, one needs to consider *locally invariant* Lagrangian although the basic underlying symmetry is global. The use of local transformations can systematically generate the effect of Ward Identities in the generating functionals by considering 4-divergences of Green's functions without explicitly working out the *current algebras*. To consider the effect of external sources directly in the QCD effective action $\mathcal{S}_{\rm QCD}$, we may write

$$\begin{aligned} e^{i\mathcal{S}_{\rm QCD}[l_\mu, r_\mu, s, p]} &= \int [\mathscr{D}q][\mathscr{D}\bar{q}][\mathscr{D}\mathcal{A}^a_\mu] e^{i\int d^4x\, \mathcal{L}_{\rm QCD}[q,\bar{q},\mathcal{A}^a_\mu, l_\mu, r_\mu, s, p]} \\ &\to \int [\mathscr{D}U] e^{i\int d^4x\, \mathscr{L}^{\rm eff}_{\pi\pi}[U, l_\mu, r_\mu, s, p]} \end{aligned} \tag{3.28}$$

[3] since one power of quark mass counts as two order of derivatives

where the massless $N_f = 2$ flavor QCD Lagrangian $\mathcal{L}^0_{\rm QCD}$ with the iso-doublet quark field spinor, $q = (u \quad d)^T$, includes the additional source terms, i.e.,

$$\mathcal{L}_{\rm source} = -\bar{q}(x)\left\{\not{l}(x)\left[\frac{1+\gamma_5}{2}\right] - \not{r}(x)\left[\frac{1-\gamma_5}{2}\right] - [s(x) - i\gamma_5 p(x)]\right\} q(x)\,, \tag{3.29}$$

where,

$$\begin{aligned} l_\mu(x) &= \frac{1}{2}\left[\mathbb{I}\, l^0_\mu(x) + \tau^a l^a_\mu(x)\right] \quad \text{(left-handed)}\,, \\ r_\mu(x) &= \frac{1}{2}\left[\mathbb{I}\, r^0_\mu(x) + \tau^a r^a_\mu(x)\right] \quad \text{(right-handed)}\,, \\ s(x) &= \frac{1}{2}\left[\mathbb{I}\, s^0_\mu(x) + \tau^a s^a(x)\right] \quad \text{(scalar)}\,, \\ p(x) &= \frac{1}{2}\left[\mathbb{I}\, p^0(x) + \tau^a p^a(x)\right] \quad \text{(pseudoscalar)} \end{aligned} \tag{3.30}$$

are 2×2 flavor space Hermitian source (matrix) fields. It is notable that the quark mass term $\mathscr{M}_q$ is included as an iso-singlet scalar source field

$$s^0 = \mathscr{M}_q = \begin{pmatrix} m_u & 0 \\ 0 & m_d \end{pmatrix}.$$

Moveover, the scalar and pseudoscalar sources are related to the chiral quark condensates which also break chiral symmetry explicitly as well as dynamically. Their contributions are systematically included in the chiral Lagrangian through the χ field, namely,

$$\chi(x) = 2B_0\left[s(x) + ip(x)\right]\,, \tag{3.31}$$

where the parameter B_0 is related to the chiral quark condensate $\langle 0|q\bar{q}|0\rangle$ which is the order parameter for a dynamically broken chiral symmetry and given as

$$B_0 = -\frac{\langle 0|q\bar{q}|0\rangle}{2f_\pi^2}\,. \tag{3.32}$$

The above methodology of including external source fields in fact readily allows the scalar and pseudoscalar sources to be expressed as spurion fields so that they transform under chiral transformations. This facilitates easy contraction of local operators in the effective Lagrangian using the χ field that break chiral symmetry. The second term in $\mathscr{L}^{(2)}_\pi$ proportional to the flavor trace, $\langle \chi U^\dagger + U\chi^\dagger\rangle$, is just the leading chiral order

term. Furthermore, all underlying QCD symmetries can be systematically incorporated in the local operators of the effective chiral Lagrangian. To facilitate couplings of pions to the external sources, the ordinary derivatives ∂_μ are promoted to the so-called *chiral covariant derivatives*, $\partial_\mu \to D_\mu$ which include the vector $v^\mu = \frac{1}{2}(l^\mu + r^\mu)$ and axial-vector $a^\mu = \frac{1}{2}(r^\mu - l^\mu)$ source fields as

$$\begin{aligned} D^\mu U &= \partial^\mu U - i(v^\mu + a^\mu)U + iU(v^\mu - a^\mu) \\ D^\mu U^\dagger &= \partial^\mu U + iU^\dagger(v^\mu + a^\mu) - i(v^\mu - a^\mu)U^\dagger \,. \end{aligned} \tag{3.33}$$

Finally the responses of the different components of the chiral Lagrangian under local chiral transformations are as follows:

$$\begin{aligned} U &\mapsto L(x)UR^\dagger(x)\,, \\ U^\dagger &\mapsto R(x)U^\dagger L^\dagger(x)\,, \\ D_\mu U &\mapsto L(x)D_\mu U R^\dagger(x)\,, \\ v_\mu + a_\mu &\mapsto R(x)(v_\mu + a_\mu)R^\dagger(x) + iR(x)\partial_\mu R^\dagger(x)\,, \\ v_\mu - a_\mu &\mapsto L(x)(v_\mu - a_\mu)L^\dagger(x) + iL(x)\partial_\mu L^\dagger(x)\,, \\ s + ip &\mapsto L(x)(s + ip)R^\dagger(x)\,, \\ s - ip &\mapsto R(x)(s - ip)L^\dagger(x)\,. \end{aligned} \tag{3.34}$$

As an important application of the leading chiral order Lagrangian, by setting $l_\mu = r_\mu = p = 0$ and $s = \mathscr{M}_q$ and then expanding $U(x)$ in the symmetry broken part up to quadratic terms in the pion fields, i.e., to $\mathcal{O}\left[\phi^2(x)\right]$, yields one of the celebrated expressions of the Gell-Mann-Oaks-Renner relations, namely, the one that relates the physical pion masses, i.e., $m^2_{\pi^\pm} = m^2_{\pi^0} = (m_u + m_d)B_0$. The relation can be systematically improved by considering contributions from sub-leading chiral order operators, (i.e., of $\mathcal{O}(p^4)$ or above) in the effective chiral Lagrangian. A wide range of applications of sub-leading order analyses in $N_f = 2$ flavor χPT exist in the literature, e.g., determination of higher order corrections to the π-π scattering processes, pion Compton scattering, accurate predictions of electromagnetic pion form factors and polarizabilities, radiative correction to π-β decays, etc., and anomalous pion decays. These topics however not being relevant

and beyond the scope of the thesis work will not be discussed here.

3.4.2 Weinberg's Power Counting Scheme for χPT

Since the effective Lagrangian by construction contains an infinite number of local operators, one needs an organizing scheme that prioritizes terms by order of relevance starting from the most dominant terms, viz., the leading order. The scheme also addresses how quantum loops and quark masses should appear order-by-order in a diagrammatic perturbative S-matrix expansion, such that at every order, one needs to evaluate only a finite number of diagrams with a small number of loops. This is ensured by the *Weinberg's power counting scheme* [167].

To organize term in an expansion over the small generic four-momentum p of the NG pions (or their derivatives ∂_μ) the following chiral powers are assigned to the basic components of the chiral Lagrangian:

$$\begin{aligned} U(x),\ U^\dagger(x) &\ \rightarrow\ \mathcal{O}(p^0) \\ \partial_\mu U(x),\ v_\mu(x),\ a_\mu(x),\ D_\mu U(x) &\ \rightarrow\ \mathcal{O}(p) \\ s(x),\ p(x),\ \chi(x),\ m_\pi^2 &\ \rightarrow\ \mathcal{O}(p^2)\,. \end{aligned} \tag{3.35}$$

With these chiral counting a simple assessment of the chiral behavior of amplitudes (contributions to the n-point Green's functions) is possible using a Naive Dimensional Analysis (NDA). To this end a linear re-scaling of the external momenta, namely, $p \mapsto tp$, and a quadratic re-scaling of the current quark masses, $\mathscr{M}_q \mapsto t^2\mathscr{M}_q$ amounts to re-scaling the S-matrix elements, $S_{fi} \sim \delta^4(P_f - P_i)\mathcal{A}$ as $S_{fi} \mapsto t^{D-4}S$, where the Feynman amplitudes scale as $\mathcal{A}(p, \mathscr{M}_q) \mapsto \mathcal{A}(tp, t^2\mathscr{M}_q) = t^D\mathcal{A}(p, \mathscr{M}_q)$ with D being the so-called *chiral dimension* of a diagram determined by its topology. This is easily demonstrated by considering a Feynman graph in the generic dimensional form

$$\mathcal{A}(p, \mathscr{M}_q) \sim \int [d^4p]^L \frac{1}{[p^2]^I} \prod_{n=2;\,\text{Even}}^{\infty} [p^n]^{\mathcal{V}_n} \tag{3.36}$$

with $\mathcal{V}_n$ number of vertex insertions from $\mathscr{L}_\pi^{(n)}$ Eq. (3.26), L number of loops, and I number of internal lines, the above momentum and quark mass scalings result in the following scaling of the full graph:

$$\begin{aligned}\mathcal{A}(tp, t^2\mathscr{M}_q) &\sim \int [d^4(tp)]^L \frac{1}{[(tp)^2]^I} \prod_{n=2;\,\text{Even}}^{\infty} [(tp)^n]^{\mathcal{V}_n} \\ &= t^{4L-2I+\sum_n n\mathcal{V}_n} \int [d^4p]^L \frac{1}{[p^2]^I} \prod_{n=2;\,\text{Even}}^{\infty} [p^n]^{\mathcal{V}_n} \\ &= t^D \mathcal{A}(p, \mathscr{M}_q)\,, \end{aligned} \tag{3.37}$$

where $D = 4L - 2I + \sum_n n\mathcal{V}_n$. Moreover, for any graph we may use the topological identity, $V - I + L = 1$, where $V = \sum_n \mathcal{V}_n$ is the total number vertices. This yields the scaling dimension D of graph which is necessarily an even integer, namely,

$$D = 2 + 2L + \sum_{n=2;\,\text{Even}}^{\infty} (n-2)\mathcal{V}_n\,. \tag{3.38}$$

The chiral Lagrangian starts at $\mathcal{O}(p^2)$, so that with $n \geq 2$ we must also have $D \geq 2$. Graphs with $D = 2$ do not contain any loops ($L = 0$), one-loop ($L = 1$) graphs start with $D = 4$, two-loop graphs with $D = 4$, and L-loop graphs with $D = 2 + 2L$. Consequently, up to a given chiral dimension D only a small number of loop diagrams ($L < D$) are needed to be evaluated, and more importantly, the UV divergences appearing from loops can always be renormalized with counterterm diagrams with the same chiral dimension. This feature effectively makes χPT act as a renormalizable field theory. For example, in pion-pion scattering computations at the lowest chiral order, i.e., $D = 2$, only tree level diagrams contribute. The resulting real-valued amplitude, namely,

$$\mathcal{A}(s) \sim \frac{s - m_\pi^2}{f_\pi^2}\,, \tag{3.39}$$

is a rather good estimate near threshold, but unfortunately violates perturbative unitarity growing monotonically large as $s \to \infty$. This necessitates the inclusion of diagrams with at least chiral dimension $D = 4$ which include one-loop ($L = 1$) diagrams with vertices from $\mathscr{L}_\pi^{(2)}$ and tree order ($L = 0$) counterterm diagrams with a single insertion of $\mathscr{L}_\pi^{(4)}$ vertex. No further diagrams with $\mathscr{L}_\pi^{(n>4)}$ vertices are needed. Thus, in meson

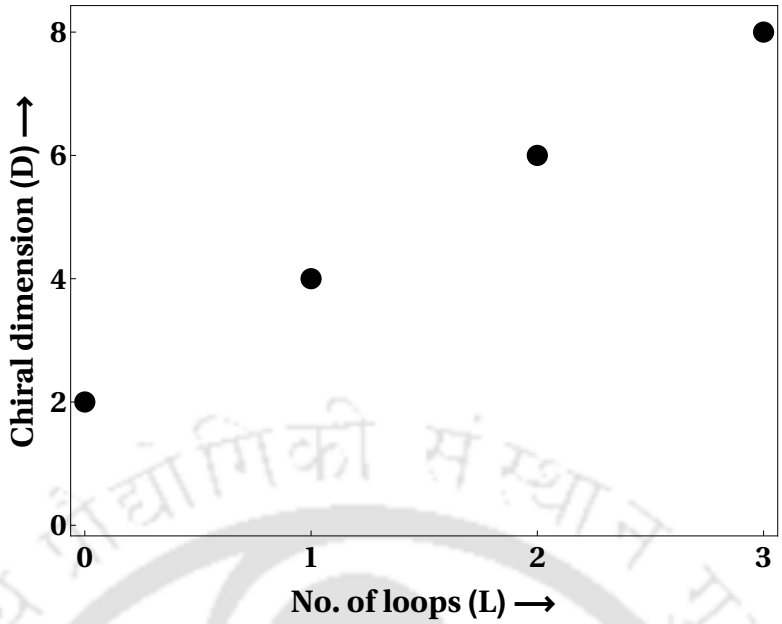

FIGURE 3.1: Power counting scheme for determining the elastic π-π scattering amplitude, $\mathcal{A}_{\pi\pi} \sim p^D$, with generic pion momentum p. A one-to-one correspondence of loop and small momentum expansion is always manifest in meson χPT. The figure is adopted from Ref. [195].

χPT amplitudes of various processes employ the NDA counting rule with a *one-to-one correspondence* between loop and small momentum expansion. This low-energy structure of chiral expansion of the elastic π-π scattering amplitude is schematically depicted in Figure [3.1].

3.4.3 SU($N_f = 2$) Baryon Chiral Perturbation Theory

The $N_f = 2$ flavor meson χPT formalism can be extended to the baryon sector, which is most systematically spelled out in the seminal work of Gasser, Sainio and Švarc [195], to describe the dynamics of nucleons interacting with pions and external fields. Again one utilizes the basic CCWZ prescription for the spontaneous breakdown of the chiral symmetry group $G = \mathrm{SU}(2)_L \otimes \mathrm{SU}(2)_R$ to the diagonal "isospin" subgroup $H = \mathrm{SU}(2)_{V=I}$, with the iso-doublet nucleons belonging to its fundamental representation denoted as

$$\Psi = \begin{pmatrix} p \\ n \end{pmatrix}$$

where p and n are each four-component Dirac spinors representing the proton and neutron, respectively. The nucleon field transforms linearly (Wigner-Wely mode) under $H \subset G$, namely, $\Psi \mapsto \Psi' = V\Psi V^\dagger$ with $V \in H$. While the triplet of pseudo-NG pions belong to the adjoint representation of the SU(2) parametrized coset space G/H. The pions fields $U(x)$ are realized non-linearly (Nambu-Goldstone mode) under the local chiral transformations G as defined by the mapping $U(x) \mapsto L(x)U(x)R^\dagger(x)$. This feature is essential to ensure vanishing of their self-interactions in the limit of zero momentum. Under the action of a local chiral transformations $g \in G$, the nucleons transform in a highly non-linear manner similar to the original NG fields $\phi(x)$ [c.f Eq. (3.25)], namely,

$$\Psi(x) \overset{g}{\mapsto} K[L(x), R(x), \phi(x)]\Psi(x) \ , \ \text{with} \ \ L(x), R(x) \in \mathrm{SU}(2)_{L,R;\mathrm{local}} \, , \tag{3.40}$$

where $K(L, R, \phi)$ is the local $\mathrm{SU}(2)_I$ valued compensator element which is implicitly dependent on the space-time coordinate x and as before defined by the transformation of the "square root" matrix field,

$$u(x) = \sqrt{U(x)} = \exp\left(i\frac{\phi(x)}{2f_\pi}\right) \, , \tag{3.41}$$

namely,

$$\begin{aligned} u(x) \overset{g}{\mapsto} u'(x) &= \sqrt{L(x)U(x)R^\dagger(x)} \\ &= L(x)u(x)K^\dagger[L(x), R(x), \phi(x)] \\ &= K[L(x), R(x), \phi(x)]u(x)R^\dagger(x) \end{aligned} \tag{3.42}$$

such that the compensator has the following representation:

$$K[L(x), R(x), \phi(x)] = \left(\sqrt{L(x)U(x)R^\dagger(x)}\right)^\dagger L(x)\sqrt{U(x)} \, . \tag{3.43}$$

In particular if, $L(x) = R(x) = K[V(x), V(x)\phi(x)]$, we have

$$u' = \sqrt{Ku^2K^\dagger} = \sqrt{KuK^\dagger KuK^\dagger} = KuK^\dagger \, ,$$

which on comparison with the last line of Eq. (3.42) yields $K[V(x), V(x), \phi(x)] = V(x)$, which is consistent with the fact that $K \in H$. In other words, Ψ transforms linearly as an isospin doublet under H.

The local character of chiral transformations requires us to introduce a chiral covariant derivative $\mathcal{D}_\mu$ which transform as $\mathcal{D}_\mu \mapsto K\mathcal{D}_\mu K^\dagger$ where

$$\mathcal{D}_\mu = \partial_\mu + \Gamma_\mu \,, \tag{3.44}$$

and Γ_μ is the so-called *chiral connection*, i.e., the gauge field for the local chiral transformations,

$$\Gamma_\mu \mapsto K\Gamma_\mu K^\dagger - K\partial_\mu K^\dagger \,, \tag{3.45}$$

which includes the response to the external vector and axial-vector gauge fields, namely,

$$\Gamma_\mu = \frac{1}{2}[u^\dagger\{\partial_\mu - i(v_\mu + a_\mu)\}u + u\{\partial_\mu - i(v_\mu - a_\mu)u^\dagger\}] \,. \tag{3.46}$$

In BχPT Lagrangian, there is another Hermitian building block u_μ, so-called the *chiral vielbein*, having an axial-vector like structure and transforming as $u_\mu \mapsto K u_\mu K^\dagger$:

$$u_\mu = i[u^\dagger\{\partial_\mu - i(v_\mu + a_\mu)\}u - u\{\partial_\mu - i(v_\mu - a_\mu)u^\dagger\}] \,. \tag{3.47}$$

Utilizing all the above discussed building blocks, the most general effective pion-nucleon Lagrangian can be constructed with one nucleon in the initial and final states having minimum number of derivatives, namely,

$$\mathcal{L}^{(1)}_{\pi N} = \bar{\Psi}\left(i\not{\mathcal{D}} - M_0 + \frac{g_A}{2}\not{u}\gamma_5\right)\Psi \,, \tag{3.48}$$

where $g_A \simeq 1.26$ is the axial-vector coupling constant and M_0 is the nucleon mass, respectively, in the chiral limit. A notable difference between nucleons and the NG pions is that the nucleon masses do not vanish in the chiral limit even with zero quark masses

which complicates matters. This mean that a new power counting scheme must be addressed in the nucleon sector preserving the power counting scheme addressed earlier in the pion sector. Moreover, Lorentz symmetry demands that the sixteen independent bilinears $\bar{\Psi}\Gamma\Psi$ components in the Dirac space must also transform under the chiral transformations. Here an expansion scheme in the nucleon sector in terms of the generic *small* three-momentum p_N of the "heavy" nucleon may be considered as the counterpart to the counting in terms of the generic four-momentum p of the pions in meson χPT. To this end a systematic expansion in term of powers of $p \sim \mathcal{O}(p_N)$ is incorporated with the chiral powers of the basic elements of the baryonic sector assigned as:

$$\begin{aligned} M_0,\ \Psi(x),\ \bar{\Psi}(x),\ \mathcal{D}_\mu\Psi(x),\ \bar{\Psi}(x)\Psi(x),\ \bar{\Psi}(x)\gamma_\mu\Psi(x) &\rightarrow \mathcal{O}(p^0) \\ \bar{\Psi}(x)\gamma_\mu\gamma_5\Psi(x),\ \Gamma_\mu,\ u_\mu,\ \bar{\Psi}(x)\sigma^{\mu\nu}\Psi(x),\ \bar{\Psi}(x)\sigma^{\mu\nu}\gamma_5\Psi(x) &\rightarrow \mathcal{O}(p^0) \\ p_N,\ (i\not{\mathcal{D}} - m_N)\Psi(x),\ \bar{\Psi}(x)\gamma_5\Psi(x) &\rightarrow \mathcal{O}(p)\,. \end{aligned} \tag{3.49}$$

As seen from the above, unlike in meson sector, the components in the nucleon sector can come in odd powers of p or derivatives of the nucleon fields due to additional possibility of contraction with Dirac gamma matrices γ_μ. Consequently, the effective Lagrangian has term of both even and odd chiral powers:

$$\begin{aligned} \mathcal{L}_{\text{eff}} &= \mathcal{L}^{\text{eff}}_{\pi N} + \mathscr{L}^{\text{eff}}_{\pi\pi} \\ \mathcal{L}^{\text{eff}}_{\pi N} &= \Delta\mathcal{L}^{(0)}_{\pi N} + \mathcal{L}^{(1)}_{\pi N} + \mathcal{L}^{(2)}_{\pi N} + \mathcal{L}^{(3)}_{\pi N} + \cdots\,. \end{aligned} \tag{3.50}$$

It is notable that the UV divergences due to pion loops require additional counterterms for renormalization which often lead to the generation of different chiral dimensions, e.g., one requires the counterterm

$$\Delta\mathcal{L}^{(0)}_{\pi N} = \Delta M_0 \left(\frac{M_0}{f_\pi}\right)^2 \bar{\Psi}\Psi\,, \tag{3.51}$$

expressed in terms of the lowest order nucleon self-energy correction ΔM_0. This counterterm which counts as $D = 0$, i.e., $\mathcal{O}(1)$, is not originally present in the πN effective Lagrangian but rather needs to be added "by hand" to avoid shifting of M_0 at the "canonical" leading chiral order, namely, $\mathcal{O}(p)$. Thus, in contrary to meson χPT, the

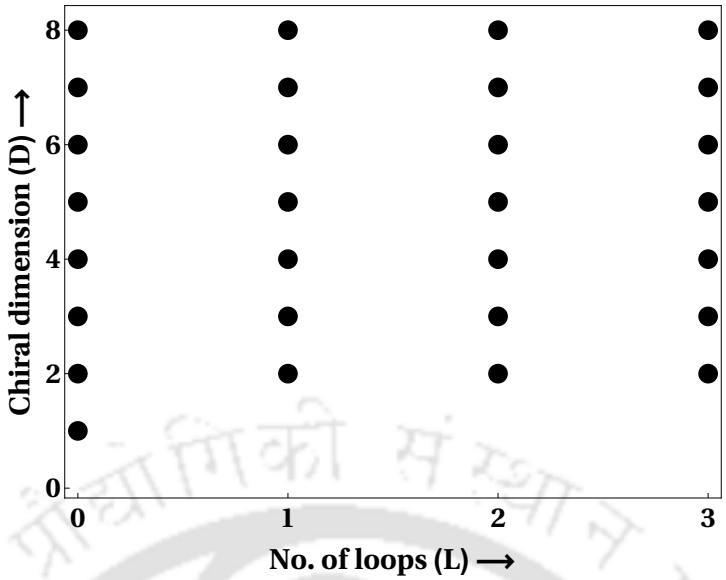

FIGURE 3.2: Chiral expansion in BχPT used in the calculation of πN scattering amplitude, $\mathcal{A}_{\pi N} \sim p^D$, with generic nucleon three-momentum or modulus of the pion four-momentum p. The schematic shows the lack of corresponding between loop expansion and chiral dimension of contributing Feynman graphs using standard dimensional regularization to compute loops. The figure is adopted from Ref. [195].

BχPT power counting gets hampered by quantum-loop corrections and the basic reason for this complication is the non-vanishing chiral limit mass of the nucleon adding a dimensionful parameter in the theory. Using standard dimensional regularization (DR) scheme, it may be shown that pion loop effects contribute to large non-analytic terms of order $(M_0/4\pi f_\pi)^2 \sim 1$, and consequently, diagrams with higher and higher number of loops are needed to renormalize coupling constants at every chiral order thereby spoiling the one-to-one correspondence between loop expansion and chiral dimensions of Feynman diagrams [195]. Therefore, many calculations existing in the literature that truncate up to one-loop approximation, evidently casts doubts regarding the robustness of those results. Fig.[3.2] schematically depicts this messy situation one encounters while evaluating the πN scattering amplitude. At the leading chiral order, $D = 1$, there are only tree level diagrams. However, even going to the very next order, $D = 2$, an indefinite number of loops begin to contribute. As a simple demonstration of the tree order application of BχPT, we now set the external sources, $a_\mu = v_\mu = 0$, and expand the fields u and $u^\dagger$, as well as the vielbein u_μ and connection Γ_μ, up to the respective leading contribution in

the pion fields, namely,

$$\begin{aligned} u(x) &= \mathbb{I}_{2\times 2} + i\frac{\boldsymbol{\tau}\cdot\boldsymbol{\pi}(x)}{2f_\pi} + \mathcal{O}(\pi^2)\,, \\ u^\dagger(x) &= \mathbb{I}_{2\times 2} - i\frac{\boldsymbol{\tau}\cdot\boldsymbol{\pi}(x)}{2f_\pi} + \mathcal{O}(\pi^2)\,, \\ u_\mu(x) &= -\frac{\boldsymbol{\tau}\cdot\partial_\mu\boldsymbol{\pi}(x)}{f_\pi} + \mathcal{O}(\pi^3)\,, \\ \Gamma_\mu(x) &= \frac{i}{4f_\pi}\boldsymbol{\tau}\cdot\boldsymbol{\pi}(x)\times\partial_\mu\boldsymbol{\pi}(x) + \mathcal{O}(\pi^4)\,. \end{aligned} \tag{3.52}$$

Then the canonical BχPT leading order Lagrangian yields the interaction terms,

$$\mathcal{L}^{(1)}_{\pi N;\text{int}} \to -\frac{g_A}{2f_\pi}\bar{\Psi}\gamma^\mu\gamma_5\,\boldsymbol{\tau}\cdot\partial_\mu\boldsymbol{\pi}\,\Psi - \frac{1}{4f_\pi^2}\bar{\Psi}\gamma^\mu\,\boldsymbol{\tau}\cdot\boldsymbol{\pi}\times\partial_\mu\boldsymbol{\pi}\,\Psi + \cdots\,. \tag{3.53}$$

In the same way, we also expand U and $U^\dagger$, namely,

$$\begin{aligned} U(x) &= \mathbb{I}_{2\times 2} + i\frac{\boldsymbol{\tau}\cdot\boldsymbol{\pi}(x)}{f_\pi} + \mathcal{O}(\pi^2)\,, \\ U^\dagger(x) &= \mathbb{I}_{2\times 2} - i\frac{\boldsymbol{\tau}\cdot\boldsymbol{\pi}(x)}{f_\pi} + \mathcal{O}(\pi^2)\,, \end{aligned} \tag{3.54}$$

such that the pertinent terms from the leading order pionic Lagrangian that only couples to an isovector pseudoscalar external source field $\mathbf{p}$, via the field, $\chi = 2B_0\,(\mathscr{M}_q + i\boldsymbol{\tau}\cdot\mathbf{p})$, yields

$$\begin{aligned} \mathscr{L}^{(2)}_{\pi;\text{ext}} &\to \frac{f_\pi^2 B_0}{2}\text{Tr}\left\{(\mathscr{M}_q + i\boldsymbol{\tau}\cdot\mathbf{p})U^\dagger - U(\mathscr{M}_q + i\boldsymbol{\tau}\cdot\mathbf{p})\right\} \\ &= -\frac{B_0}{2}\text{Tr}\left\{(\boldsymbol{\tau}\cdot\boldsymbol{\pi})^2\,\mathscr{M}_q\right\} + 2B_0 f_\pi\mathbf{p}\cdot\boldsymbol{\pi} + \cdots\,. \end{aligned} \tag{3.55}$$

The above terms may be used to exactly obtain the celebrated *Goldberger-Treiman relation* connecting the strong coupling $g_{\pi NN} \simeq 13.5$ and the axial couplings g_A of the pion-nucleon system:

$$f_\pi g_{\pi NN} = M_0 g_A\,. \tag{3.56}$$

Thus, in general, working out various tree order diagrams from the leading order πN Lagrangian (with and without including external source fields) yield several other well-known low-energy current algebra theorems, e.g., *Adler-Weisberger sum rule* [196–198],

Weinberg sum rule [199], *Weinberg-Tomozawa relation* [200, 201] and *Kroll-Ruderman relation* [202], to name a few. Furthermore, going beyond the leading chiral order, and also including isospin breaking and loop contributions, yield corrections to such current algebra relations, e.g., most prominently, the Goldberger-Treiman *discrepancy*:

$$\Delta_{\pi N} = 1 - \frac{M_0 g_A}{f_\pi g_{\pi NN}} \,. \tag{3.57}$$

Moreover, it goes without saying that the consideration of higher loop correction is certainly necessary to restore perturbative unitarity which is evidently violated by real-valued tree amplitudes. These corrections ultimately renormalize the chiral limit values of the the couplings and the nucleon mass.

As remedies to the aforementioned difficulties encountered in BχPT in incorporating loops corrections, two alternative techniques exist. Firstly, the one-to-one correspondence of loop and chiral expansions in a fully relativistic treatment of nucleons is manifest only with the non-analytic parts of amplitudes but not with the analytic parts. In the so-called, *Infrared Regularization Scheme* (IRχPT), advocated by Ellis, Tang, Becher and Leutwyler in Refs. [203–205], the loops evaluated with DR is split up in a specific way into a regular and an irregular part. With the regular part absorbed into the LECs, the one-to-one power counting can be restored with only the irregular part contributing to the amplitudes of diagrams. However, there exists a second more standardized approach, namely, HBχPT, initially advocated by Jenkins and Manohar [206] in the context of χPT, and constructed in close analogy to Heavy-Quark Effective Theory (HQET) developed by Grinstein and Georgi [207, 208]. Contrary to the full relativistic approach of IRχPT, the heavy baryon formalism considers the extreme non-relativistic limit of relativistic BχPT Lagrangian, amounts to a $1/M_N$ expansion in the heavy nucleon mass, $M_N = M_0 \left[1 + \mathcal{O}\left(\mathscr{M}_q\right)\right] \simeq 939$ MeV, that allows reshuffling of the nucleon mass dependence from their propagators to a series of the interaction vertices. The procedure effectively restores the direct correspondence between the loop and chiral expansion, as will be discussed in the next section. The methodology is especially suitable for dealing with nucleon recoil effects in a large number of processes involving real and virtual photons, which naturally motivates the study of the lepton-proton scattering process in the following chapters of

this thesis.

3.4.4 SU($N_f = 2$) Heavy Baryon Chiral Perturbation Theory

In this approach, the basic idea is to consider the nucleons as extremely heavy (static) sources surrounded by clouds of pions, an idea that was already conceived in the early seminal works of Gasser and Leutwyler [209, 210] for determining quark mass ratio from baryon spectrum. It was realized that in a fully relativistic treatment with NG pions and non-vanishing nucleon mass in the chiral limit, the cloud of pions surrounding the nucleon become long ranged inducing large non-analytical corrections and ruining the straightforward chiral counting. Since the square of the nucleon four-momentum, $P_N^2 = M_N^2$ (where the nucleon mass in the isospin limit is denoted as, $M_N = M_0 \left[1 + \mathcal{O}\left(\mathscr{M}_q\right)\right] \simeq$ 939 MeV), is a quantity as large as the square of the hard scale, $\Lambda_\chi \sim 4\pi f_\pi \simeq 1$ GeV, it is legitimate to devise a $1/M_N$ expansion scheme that will re-organize terms in the BχPT Lagrangian in such a way that the resulting string of interactions have no terms of $\mathcal{O}(M_N)$. Consequently, from NDA the resulting theory has loop corrections of the typical size, $p^2/16\pi^2 f_\pi^2 \sim (m_\pi/4\pi f_\pi)^2 \simeq 0.014$, which is a magnitude suppressed compared to the concomitant $1/M_N$ correction terms to the interaction vertices with typical size, $p/M_N \sim p/\Lambda_\chi \sim m_\pi/\Lambda_\chi \sim m_\pi/4\pi f_\pi \simeq 0.11$. Since the leading chiral order (LO) interactions appear at $\mathcal{O}(p)$, the $1/M_N$ terms in the Lagrangian represent $\mathcal{O}(p^2)$, i.e., *next-to-leading order* (NLO), while loop corrections are suppressed by two orders, appearing only at $\mathcal{O}(p^3)$, i.e., *next-to-next-to-leading order* (NNLO). This relative hierarchy is maintained at all sub-leading chiral order including a higher number of loops thereby restoring the one-to-one correspondence between loops and chiral expansion in the power counting.

Let us now discuss the essential steps involved in the considering the extreme non-relativistic limit of the BχPT πN Lagrangian leading to the above discussed structure of the heavy baryon theory. To this end, following the motivation from HQET, it amounts to decomposing the external nucleon four-momentum into a large piece close to its mass-shell and a small residual component as

$$P_N^\mu = M_N v^\mu + p_r^\mu \,, \tag{3.58}$$

where $v_\mu = (1, \mathbf{0})$ is the four-velocity vector satisfying $v^2 = 1$, while $p_r^\mu \sim p_N \sim \mathcal{O}(p)$ is a small off-shell *residual* nucleon four-momentum, with

$$v \cdot p_r = p_r^0 = P_N^0 - M_N = \frac{\mathbf{p}_N^2}{2M_N} \ll M_N \,. \tag{3.59}$$

Then can phase out the heavy mass as

$$\exp(iP_N \cdot x) = \exp(iM_N v \cdot x) \exp(ip_r \cdot x).$$

In what follows, we shall use velocity dependent "large" (upper) and "small" (lower) components of heavy nucleon field, namely, $N_v(x)$ and $l_v(x)$, respectively, instead of the previously defined Dirac field $\Psi(x)$, and related by, [4]

$$\begin{aligned} N_v(x) &= e^{iM_N v\cdot x}\, \mathbb{P}_v^+\, \Psi(x) \quad \text{with} \quad \not{v} N_v(x) = N_v(x)\,, \\ l_v(x) &= e^{iM_N v\cdot x}\, \mathbb{P}_v^-\, \Psi(x) \quad \text{with} \quad \not{v} l_v(x) = -l_v(x)\,, \end{aligned} \tag{3.60}$$

where the projection operators for the respective component of the nucleon Dirac field Ψ with a fixed velocity v are

$$\mathbb{P}_v^\pm = \frac{1 \pm \not{v}}{2} \,. \tag{3.61}$$

The action of the above projectors on the velocity dependent fields can be summarized as:

$$\begin{aligned} \mathbb{P}_v^+ N_v(x) = N_v(x) \quad &, \quad \mathbb{P}_v^- N_v(x) = 0 \,, \\ \mathbb{P}_v^+ l_v(x) = 0 \quad &, \quad \mathbb{P}_v^- l_v(x) = l_v(x) \,. \end{aligned} \tag{3.62}$$

[4] Equivalently, the upper or positive energy components $N_v(x)$ may be also regarded as the "light" degree of freedom while the lower or negative energy components may be regarded as the "heavy" degree of freedom, since antiparticle modes are effectively decoupled at small non-relativistic energies $E_N \ll M_N$.

Next the relativistic heavy nucleon propagator can be similarly transformed, namely,

$$\begin{aligned}\frac{i}{\not{P}_N - M_N + i\eta} = i\frac{\not{P}_N + M_N}{P_N^2 - M_N^2 + i\eta} &= i\frac{M_N\not{v} + \not{p}_r + M_N}{2M_N v\cdot p_r + p_r^2 + i\eta}\,, \quad \eta \to 0_+ \\ &= \left(\frac{1+\not{v}}{2}\right)\left(\frac{i}{v\cdot p_r + i\eta}\right) + \mathcal{O}\left(\frac{p_r}{M_N}\right) \\ &= \mathbb{P}_v^+\left(\frac{i}{v\cdot p_r + i\eta}\right) + \mathcal{O}\left(\frac{p_r}{M_N}\right). \qquad (3.63)\end{aligned}$$

Using the velocity four-vector we can also split the covariant derivative in the following way:

$$\not{\mathcal{D}} = \not{v}(v\cdot\mathcal{D}) + \gamma_\mu(g^{\mu\nu} - v^\mu v^\nu)\mathcal{D}_\nu = \not{\mathcal{D}}^{\parallel} + \not{\mathcal{D}}^{\perp}\,, \qquad (3.64)$$

where $\not{\mathcal{D}}^{\parallel} = \not{v}(v\cdot\mathcal{D})$ and $\not{\mathcal{D}}^{\perp} = \gamma_\mu(g^{\mu\nu} - v^\mu v^\nu)D_\nu$ are the longitudinal and transverse components of the covariant derivative, respectively, such that $\{\not{\mathcal{D}}^{\parallel}, \not{\mathcal{D}}^{\perp}\} = \{\not{v}, \not{\mathcal{D}}^{\perp}\} = 0$. We now define the spin-1/2 operator in terms of the four-velocity as

$$S_v^\mu = \frac{i}{2}\gamma_5\sigma^{\mu\nu}v_\nu = -\frac{1}{2}\gamma_5(\gamma^\mu\not{v} - v^\mu)\,, \qquad (3.65)$$

satisfying the following relations ($\epsilon_{0123} = 1$):

$$S\cdot v = 0,\;\; S^2 = -\frac{3}{4},\;\; \{S_\mu, S_\nu\} = \frac{1}{2}(v_\mu v_\nu - g_{\mu\nu}),\;\; [S_\mu, S_\nu] = i\epsilon_{\mu\nu\rho\sigma}v^\rho S^\sigma\,. \qquad (3.66)$$

The spin and velocity four-vectors allows to decompose all possible bilinears covariants associated with the large components, namely,

$$\begin{aligned}&\bar{N}_v\gamma_\mu N_v = v_\mu\bar{N}_v N_v \quad,\;\; \bar{N}_v\gamma_5 N_v = 0\,, \quad \bar{N}_v\gamma_\mu\gamma_5 N_v = 2\bar{N}_v S_\mu N_v\,, \\ &\bar{N}_v\sigma^{\mu\nu}N_v = 2\epsilon^{\mu\nu\rho\sigma}v_\rho\bar{N}_v S_\sigma N_v \quad,\;\; \bar{N}_v\gamma_5\sigma^{\mu\nu}N_v = 2i\left(v^\mu\bar{N}_v S^\nu N_v - v^\nu\bar{N}_v S^\mu N_v\right). \qquad (3.67)\end{aligned}$$

Next we wish to non-relativistically reduce the BχPT Lagrangian by integrating out the small component field l_v in order to obtain the effective heavy nucleon Lagrangian solely in terms of large component field N_v. One way is to eliminate the field l_v using the equation of motion which essentially amounts to a Foldy-Wouthuysen transformation [174], as described in details in the review, Ref. [190]. Below we consider the alternative and more

elegant path integral approach by Mannel *et al.*, as detailed in Ref. [175] (also see, e.g., Appendix A of Ref. [172]). To this end, the full generating functional corresponding the relativistic πN Lagrangian is written as

$$Z[\eta,\bar{\eta},v_\mu,a_\mu,s,p]=\int[\mathscr{D}\Psi][\mathscr{D}\bar{\Psi}][\mathscr{D}\phi]\exp\left\{\mathcal{S}_{\pi N}+\mathcal{S}_{\pi\pi}+\int d^4x\,(\bar{\eta}\Psi+\bar{\Psi}\eta)\right\} \tag{3.68}$$

with

$$\begin{aligned}\mathcal{S}_{\pi N}[\Psi,\bar{\Psi},u,v_\mu,a_\mu,s,p] &= \int d^4x\,\left\{\mathcal{L}^{(1)}_{\pi N}+\mathcal{L}^{(2)}_{\pi N}+\mathcal{L}^{(3)}_{\pi N}+\cdots\right\},\\ \mathcal{S}_{\pi\pi}[U,v_\mu,a_\mu,s,p] &= \int d^4x\,\left\{\mathscr{L}^{(2)}_{\pi}+\mathscr{L}^{(4)}_{\pi}+\mathscr{L}^{(6)}_{\pi}+\cdots\right\}.\end{aligned} \tag{3.69}$$

By writing, $\Psi=e^{-iMv\cdot x}(N_v+l_v)$, the above πN action can be expressed in the form

$$\mathcal{S}_{\pi N}=\int d^4x\,\left\{\bar{N}_v\mathcal{A}N_v+\bar{l}_v\mathcal{B}N_v+\bar{N}_v\gamma_0\mathcal{B}^\dagger\gamma_0 l_v-\bar{l}_v\mathcal{C}l_v\right\}, \tag{3.70}$$

where the matrices $\mathcal{A},\mathcal{B}$ and $\mathcal{C}$ can be expressed in a string of $\mathcal{O}(p^n)$ term upon expansion in $1/M_N$. Thus, we can write, $\mathcal{A}=\mathcal{A}^{(1)}+\mathcal{A}^{(2)}+\cdots$, and likewise for $\mathcal{B}$ and $\mathcal{C}$. Thus, e.g., expanding up to $\mathcal{O}(p^2)$ terms we get

$$\begin{aligned}\mathcal{A}^{(1)} &= i(v\cdot\mathcal{D})+g_A(u\cdot S),\\ \mathcal{A}^{(2)} &= c_1\langle\chi_+\rangle+\frac{c_2}{2}\langle(v\cdot u)^2\rangle+\frac{c_3}{2}\langle u^2\rangle+c_5\left(\chi_+-\frac{1}{2}\langle\chi_+\rangle\right)\\ &\quad -2i[S^\mu,S^\nu]\left(\frac{ic_4}{4}[u_\mu,u_\nu]+\frac{c_6}{8M_N}f^+_{\mu\nu}+\frac{c_7}{8M_N}\langle f^+_{\mu\nu}\rangle\right),\\ \mathcal{B}^{(1)} &= i\not{\mathcal{D}}^\perp-\frac{1}{2}g_A(v\cdot u)\gamma_5,\\ \mathcal{B}^{(2)} &= 2i\gamma_5(v^\mu S^\nu-v^\nu S^\mu)\left(\frac{ic_4}{4}[u_\mu,v_\nu]+\frac{c_6}{8M_N}f^+_{\mu\nu}+\frac{c_7}{8M_N}\langle f^+_{\mu\nu}\rangle\right),\\ \mathcal{C}^{(0)} &= 2M_N,\\ \mathcal{C}^{(1)} &= i(v\cdot\mathcal{D})+g_A(u\cdot S),\\ \mathcal{C}^{(2)} &= -\mathcal{A}^{(2)},\end{aligned} \tag{3.71}$$

where $\langle\cdots\rangle$ represents flavor trace, and

$$\begin{aligned}f^+_{\mu\nu} &= u^\dagger f^R_{\mu\nu}u+uf^L_{\mu\nu}u^\dagger,\\ f^r_{\mu\nu} &= \partial_\mu r_\nu-\partial_\nu r_\mu-i[r_\mu,r_\nu],\end{aligned}$$

$$
\begin{aligned}
f^L_{\mu\nu} &= \partial_\mu l_\nu - \partial_\nu l_\mu - i[l_\mu, l_\nu]\,, \\
r_\mu &= v_\mu + a_\mu\,, \quad l_\mu = v_\mu - a_\mu\,, \\
\chi_+ &= u\chi u + u^\dagger \chi u^\dagger\,,
\end{aligned} \tag{3.72}
$$

As seen above, $\mathcal{A}^{(2)}$, $\mathcal{B}^{(2)}$ and $\mathcal{B}^{(2)}$ contain the contributions of the *finite* LECs, $c_1, ..., c_7$, from the $\mathcal{O}(p^2)$ BχPT Lagrangian of the generic form

$$
\mathcal{L}^{(2)}_{\pi N} = \sum_{i=1}^{7} c_i \bar{\Psi} \mathbb{O}^{(2)}_i \Psi\,, \tag{3.73}
$$

where the 7 operators $\mathbb{O}^{(2)}_i$ can be found in Ref. [211], and will not be discussed henceforth.

It is notable that the source terms in the generating functional can be treated in same way by projecting out their large and small components, namely,

$$
\begin{aligned}
R_v(x) &= e^{iM_N v\cdot x}\, \mathbb{P}^+_v \eta(x) \\
\rho_v(x) &= e^{iM_N v\cdot x}\, \mathbb{P}^-_v \eta(x)\,,
\end{aligned} \tag{3.74}
$$

such that the source terms can be expressed as

$$
\int d^4x \left(\bar{\eta}\Psi + \bar{\Psi}\eta\right) = \int d^4x \left(\bar{R}_v N_v + \bar{N}_v R_v + \bar{\rho}_v l_v + \bar{l}_v \rho_v\right)\,. \tag{3.75}
$$

Returning to the expression for $\mathcal{S}_{\pi N}$, we now integrate out the field l_v to obtain the generating functional of the heavy nucleon effective theory in terms of N_v, namely,

$$
\begin{aligned}
W_{\pi N} &= e^{i\widehat{\mathcal{S}}_{\pi N}[v_\mu, a_\mu, s, p]} \\
&= \frac{\int [\mathscr{D}(N_v, \bar{N}_v)][\mathscr{D}(l_v, \bar{l}_v)][\mathscr{D}u] e^{i\int d^4x\, \mathcal{L}^{\rm eff}_{\pi N}[N_v(x), l_v(x), v_\mu, a_\mu, s, p]}}{\int [\mathscr{D}(l_v, \bar{l}_v)][\mathscr{D}u] e^{i\int d^4x\, \mathcal{L}^{\rm eff}_{\pi N}[l_v(x), v_\mu, a_\mu, s, p]}} \\
&= \frac{\int [\mathscr{D}(N_v, \bar{N}_v)][\mathscr{D}(l_v, \bar{l}_v)][\mathscr{D}u] e^{i\int d^4x \left\{\bar{N}_v \mathcal{A} N_v + \bar{l}_v \mathcal{B} N_v + \bar{N}_v \gamma_0 \mathcal{B}^\dagger \gamma_0 l_v - \bar{l}_v \mathcal{C} l_v\right\}}}{\int [\mathscr{D}(l_v, \bar{l}_v)][\mathscr{D}u] e^{i\int d^4x \left\{-\bar{l}_v \mathcal{C} l_v\right\}}}\,.
\end{aligned} \tag{3.76}
$$

To complete the square in the generating functional we use the following field re-definition, namely,

$$
l_v \to l'_v = l_v - \mathcal{C}^{-1}\mathcal{B} N_v\,, \tag{3.77}
$$

and the fact that the integration measure is independent of this transformation, i.e., $[\mathscr{D}(l_v,\bar{l}_v)]=[\mathscr{D}(l'_v,\bar{l}'_v)]$, we have

$$\begin{aligned} W_{\pi N} &= e^{i\widehat{\mathcal{S}}_{\pi N}[v_\mu,a_\mu,s,p]} \\ &= \frac{\int[\mathscr{D}(N_v,\bar{N}_v)][\mathscr{D}(l'_v,\bar{l}'_v)][\mathscr{D}u]e^{i\int d^4x\left\{\bar{N}_v\left[\mathcal{A}+(\gamma_0\mathcal{B}^\dagger\gamma_0)\mathcal{C}^{-1}\mathcal{B}\right]N_v-\bar{l}'_v\mathcal{C}l'_v\right\}}}{\int[\mathscr{D}(l'_v,\bar{l}'_v)][\mathscr{D}u]e^{i\int d^4x\left\{-\bar{l}'_v\mathcal{C}l'_v\right\}}} \\ &= \frac{e^{i\int d^4x\left\{\bar{N}_v\left[\mathcal{A}+(\gamma_0\mathcal{B}^\dagger\gamma_0)\mathcal{C}^{-1}\mathcal{B}\right]N_v\right\}}\int[\mathscr{D}(l'_v,\bar{l}'_v)][\mathscr{D}u]e^{i\int d^4x\left\{-\bar{l}'_v\mathcal{C}l'_v\right\}}}{\int[\mathscr{D}(l'_v,\bar{l}'_v)][\mathscr{D}u]e^{i\int d^4x\left\{-\bar{l}'_v\mathcal{C}l'_v\right\}}} \\ &= e^{i\int d^4x\left\{\bar{N}_v\left[\mathcal{A}+(\gamma_0\mathcal{B}^\dagger\gamma_0)\mathcal{C}^{-1}\mathcal{B}\right]N_v\right\}}\,. \end{aligned} \tag{3.78}$$

From the above equation we can directly read off the effective action involving only the large component field N_v, namely,

$$\widehat{\mathcal{S}}_{\pi N}[N_v,\bar{N}_v,u,v_\mu,a_\mu,s,p]=\int d^4x\left\{\bar{N}_v\left[\mathcal{A}+(\gamma_0\mathcal{B}^\dagger\gamma_0)\mathcal{C}^{-1}\mathcal{B}\right]N_v\right\}. \tag{3.79}$$

Note that when the source part of the action is included, to integrate away the lower component field l_v by completing the square we instead need the field re-definition, $l'_v=l_v-\mathcal{C}^{-1}(\mathcal{B}N_v+\rho_v)$. The full effective action then becomes

$$\begin{aligned} \mathcal{S}_{eff} &= \widehat{\mathcal{S}}_{\pi N}[N_n,\bar{N}_v,u,v_\mu,a_\mu,s,p]+\mathcal{S}_{\pi\pi}[U,v_\mu,a_\mu,s,p] \\ &\quad+\int d^4x\,\left(\bar{R}_vN_v+\bar{N}_vR_v\right)+\cdots\,, \end{aligned} \tag{3.80}$$

where the ellipses denote source term with ρ_v and $\bar{\rho}_v$.

In the resulting effective action $\widehat{\mathcal{S}}_{\pi N}$, we note that the operator $\mathcal{C}^{-1}$ still needs to be expanded in a power series in $1/M_N$, namely,

$$\begin{aligned} \mathcal{C}^{-1} &= \left(\mathcal{C}^{(0)}+\mathcal{C}^{(1)}+\mathcal{C}^{(2)}\cdots\right)^{-1}\equiv\mathcal{C}^{-1(0)}+\mathcal{C}^{-1(1)}+\cdots \\ &= \frac{1}{2M_N}-\frac{iv\cdot\mathcal{D}+g_Au\cdot S}{(2M_N)^2}-\frac{\mathcal{C}^{(2)}}{(2M_N)^2}+\frac{(iv\cdot\mathcal{D}+g_Au\cdot S)^2}{(2M_N)^2}+\mathcal{O}(p^3)\,. \end{aligned} \tag{3.81}$$

Of course, with higher order loop contributions that start appearing at $\mathcal{O}(p^3)$, many scale-dependent counterterms of $\mathcal{O}(p^3)$ will necessarily modify the matrices $\mathcal{A}$, $\mathcal{B}$ and $\mathcal{C}$, thereby also modifying the above expansion of the matrix $\mathcal{C}^{-1}$ with more $\mathcal{O}(p^3)$ terms.

Finally, with the $1/M_N$ power series expansion incorporated, the effective heavy nucleon Lagrangian up to $\mathcal{O}(q^3)$ can be given as

$$\begin{aligned}\widehat{\mathcal{L}}_{\pi N} &= \bar{N}_v\Big\{\mathcal{A}^{(1)}+\mathcal{A}^{(2)}+\frac{(\gamma_0\mathcal{B}^{(1)\dagger}\gamma_0)\mathcal{B}^{(1)}}{2M_N}\\ &\quad+\mathcal{A}^{(3)}+\frac{(\gamma_0\mathcal{B}^{(1)\dagger}\gamma_0)\mathcal{B}^{(2)}+(\gamma_0\mathcal{B}^{(2)\dagger}\gamma_0)\mathcal{B}^{(1)}}{2M_N}\\ &\quad-(\gamma_0\mathcal{B}^{(1)\dagger}\gamma_0)\frac{i(v\cdot D)+g_A(u\cdot S)}{(2M_N)^2}\mathcal{B}^{(1)}\Big\}N_v+\mathcal{O}(p^4)\,, \end{aligned} \tag{3.82}$$

where $\mathcal{A}^{(3)}$ contains the contribution of a large number of fixed LECs and scale dependent counterterms which can be found in Ref. [140] and will not be discussed here. The $\mathcal{O}(q^4)$ terms are either suppressed by powers of $1/M_N$ or $1/\Lambda_\chi$, both being treated at the same footing. In other words, HBχPT constitutes a simultaneous expansion in p/M_N and $p/\Lambda_\chi \sim p/(4\pi f_\pi)$ where p is a small external momentum. To this end, collating all the terms up to $\mathcal{O}(p^2)$, the effective πN Lagrangian at LO and NLO in HBχPT can be expressed as

$$\widehat{\mathcal{L}}^{(1)}_{\pi N} = \bar{N}_v\Big[i(v\cdot\mathcal{D})+g_A(u\cdot S)\Big]N_v\,, \tag{3.83}$$

$$\widehat{\mathcal{L}}^{(2)}_{\pi N} = \frac{1}{2M_N}\bar{N}_v\Big[(v\cdot\mathcal{D})^2-\mathcal{D}^2-ig_A\left\{S\cdot\mathcal{D},v\cdot u\right\}\Big]N_v+\sum_{i=1}^{7}\hat{c}_i\bar{N}_n\widehat{\mathbb{O}}^{(2)}_i N_v\,, \tag{3.84}$$

where the local dimension-2 operators $\widehat{\mathbb{O}}^{(2)}_i$ $(i=1,...,7)$ are as follows:

$$\begin{aligned}\widehat{\mathbb{O}}^{(2)}_1 &= \langle\chi_+\rangle\,,\\ \widehat{\mathbb{O}}^{(2)}_2 &= \frac{1}{2}\langle(v\cdot u)^2\rangle\,,\\ \widehat{\mathbb{O}}^{(2)}_3 &= \frac{1}{2}\langle u\cdot u\rangle\,,\\ \widehat{\mathbb{O}}^{(2)}_4 &= \frac{1}{2}[S^\mu,S^\nu][u_\mu,u_\nu]\,,\\ \widehat{\mathbb{O}}^{(2)}_5 &= \left(\chi_+-\frac{1}{2}\langle\chi_+\rangle\right)\,,\\ \widehat{\mathbb{O}}^{(2)}_6 &= -\frac{i}{4M_N}[S^\mu,S^\nu]f^+_{\mu\nu}\,,\\ \widehat{\mathbb{O}}^{(2)}_7 &= \frac{1}{4M_N}[S^\mu,S^\nu]\langle f^+_{\mu\nu}\rangle\,. \end{aligned} \tag{3.85}$$

It is notable that the LO HBχPT Lagrangian $\widehat{\mathcal{L}}^{(1)}_{\pi N}$ is completely free of the nucleon mass M_N terms.

3.4.5 HBχPT Power Counting Scheme

In close analogy to the previous discussion on power counting in the meson sector, let us assess the chiral behavior of a typical Feynman diagram containing both pions and nucleons. We linearly re-scale the external pion four-momenta or nucleon three-momenta as $p \mapsto tp$, and quadratically re-scale the quark masses as $\mathscr{M}_q \mapsto \mathscr{M}_q$. A generic graph in this case has the form

$$\mathcal{A}(p, \mathscr{M}_q) \sim \int [d^4p]^L \frac{1}{[p^2]^{I_\pi}} \frac{1}{[p]^{I_N}} \prod_{n=2;\,\text{Even}}^{\infty} [p^n]^{\mathcal{V}^\pi_n} \prod_{r=1}^{\infty} [p^r]^{\mathcal{V}^{\pi N}_r} \tag{3.86}$$

with $\mathcal{V}^\pi_n$ and $\mathcal{V}^{\pi N}_r$ number of dimension-n and dimension-r vertex insertions from $\mathscr{L}^{(n)}_\pi$ and $\widehat{\mathcal{L}}^{(r)}_{\pi N}$, respectively, L number of loops, and I_π (I_N) number of internal pion (nucleon) lines. Then the response of the graph to the re-scalings can be easily obtained:

$$\begin{aligned} \mathcal{A}(tp, t^2\mathscr{M}_q) &\sim \int [d^4(tp)]^L \frac{1}{[(tp)^2]^{I_\pi}} \frac{1}{[tp]^{I_N}} \prod_{n=2;\,\text{Even}}^{\infty} [(tp)^n]^{\mathcal{V}^\pi_n} \prod_{r=1}^{\infty} [(tp)^r]^{\mathcal{V}^{\pi N}_r} \\ &= t^{4L-2I_\pi-I_N+\sum_n n\mathcal{V}^\pi_n+\sum_r r\mathcal{V}^{\pi N}_r} \mathcal{A}(p, \mathscr{M}_q)\,. \end{aligned} \tag{3.87}$$

Consequently, the chiral dimension of the graph is

$$D = 4L - 2I_\pi - I_N + \sum_{n=2;\,\text{Even}}^{\infty} n\mathcal{V}^\pi_n + \sum_{r=1}^{\infty} r\mathcal{V}^{\pi N}_r\,. \tag{3.88}$$

Next we use the topological identity, namely, $V_\pi + V_{\pi N} - I_\pi - I_N + L = 1$, where $V_\pi = \sum_n \mathcal{V}^\pi_n$ and $V_{\pi N} = \sum_r \mathcal{V}^{\pi N}_r$ are the total numbers of $\pi\pi$ and πN vertices, respectively, to eliminate I_π from the above equation as

$$D = 2L + I_N + 2 + \sum_{n=2;\,\text{Even}}^{\infty} (n-2)\mathcal{V}^\pi_n + \sum_{r=1}^{\infty} (r-2)\mathcal{V}^{\pi N}_r\,. \tag{3.89}$$

Now it is notable that the fermionic determinant, $\Delta_l = \exp(\frac{1}{2}\text{Tr}\ln\mathcal{C})$, which one obtains from the generating functional after integrating out l_v, being a constant eventually drops

out of the effective action $\widehat{\mathcal{S}}_{\pi N}$. This implies that HB$\chi$PT is a *local theory* where all closed nucleon loops are *quenched*. Thus, processes with one initial and one final state nucleon must contain a single nucleon line running through any Feynman graph of the process connecting the initial and final states. In that case, we can always show that $V_N = I_N + 1$, and hence obtain

$$D = 2L + 1 + \sum_{n=2;\,\text{Even}}^{\infty} (n-2)\mathcal{V}_n^{\pi} + \sum_{r=1}^{\infty}(r-1)\mathcal{V}_r^{\pi N}\,. \tag{3.90}$$

Evidently, the chiral dimension formula now shows the restoration of the one-to-one correspondence between the loop and chiral expansion in HBχPT analogous to meson χPT. With $D \geq 2L+1$, we see that only tree diagrams can contribute below $D < 3$, which means that the parameters of $\widehat{\mathcal{L}}_{\pi N}^{(1)}$ and $\widehat{\mathcal{L}}_{\pi N}^{(2)}$ are protected from pion loop corrections at any order, and are, therefore, wholly finite and scale-independent. The pion loops contributions start at $D = 3$, and the above formula clearly suggests that the finite LECs $c_1, ..., c_7$ of $\widehat{\mathcal{L}}_{\pi N}^{(2)}$ are needed as counterterm to renormalize the UV divergences. Finally, each loop being suppressed by two chiral orders, two-loops correction contributes only at $D = 5$.

This concludes the topical review of the basic concepts in χPT. The next few chapters of this thesis deal with applications of HBχPT in calculating radiative correction to elastic lepton-proton scattering. Basically we will use this formalism to describe the proton photon interaction while lepton photon vertex will be described by well known QED as shown in Fig.[3.3][5]. The relevant pieces of Lagrangian used in these works along

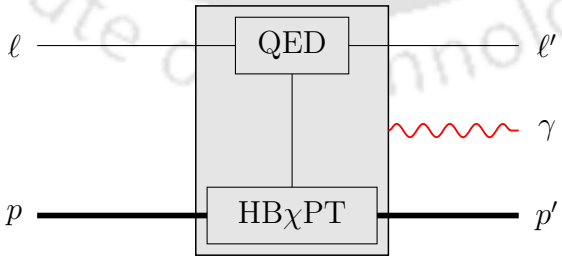

FIGURE 3.3: The ℓp scattering process and bremsstrahlung emission in EFT.

[5]It is worth mentioning here that such a factorization scenario assumed in Fig.[3.3] will not be applicable at higher orders in chiral counting, say, next-to-next-to-leading order (NNLO) on-wards, as explicit dependence on the proton structure (pion-loops and intermediate nucleon excited states) and isospin violation terms will arise, which necessitates the introduction of counter-terms and LEC insertions parametrizing the unresolved UV physics (e.g., contributions of high-momentum photons) in the EFT.

with the required Feynman rules can be found in Appendix A. We will start with the lepton-proton bremsstrahlung process in the next chapter, followed by TPE and complete radiative analyses in the subsequent chapters.

Chapter 4

Bremsstrahlung Scattering

4.1 Introduction

In this chapter we present a pedagogical and model independent prescription of the lepton-proton bremsstrahlung scattering process. Contents of this chapter is partly published in [212] and [213]. Bremsstrahlung photons constitute an integral part of the lepton-proton elastic scattering, and is one of the principal sources of uncertainties in the accurate measurement of the momentum transfers. As mentioned earlier in Chapter 1, in MUSE only the lepton scattering angle (θ) is detected. The final scattered lepton energy (E') is not measured, nor are the bremsstrahlung photons, hence their data analysis necessarily needs to correct for this radiation process.

The lepton beam momenta considered by MUSE are of the order of the muon mass [41] (also see MUSE specifications in Chapter 1). A particular concern is the standard radiative correction procedure, which makes use of the so-called *peaking approximation*, [see, e.g., Refs. [10, 47, 48, 50] for reviews]. This approximation assumes that the bremsstrahlung photons are emitted either along the incident beam direction, or in the direction of the scattered final lepton momentum. The validity of this approximation normally relies on elastic scattering of highly relativistic particles, like electrons. This is, however, questionable when either the particle energy is comparable to its mass, e.g., in the case of low-energy muon scattering in MUSE, or for inelastic scatterings with large

energy losses $\sim (30-40)\%$ from the incident projectiles due to bremsstrahlung [10]. The main purpose of this part of the work is to accurately assess the bremsstrahlung processes from electron and muon scattering off a proton at low energies in a model independent formalism. We show in a pedagogical manner the radical differences between the electron and muon angular bremsstrahlung spectra. We demonstrate how the lepton mass crucially influences the photon's angular distribution, and also discuss how the *radiative tail* cross section $\mathrm{d}\sigma_{br}/(\mathrm{d}p'\mathrm{d}\Omega')$ depends on the outgoing lepton momentum p' and its mass m_l. In particular the so-called *peaking approximation* is not applicable for muon scattering at MUSE momenta. In fact, our results corroborate the analysis in Ref. [153], where it was shown that the peaking approximation, which is predominantly valid in the zero-mass limit or for very high-momentum transfers, becomes questionable at lower energies and could lead to significant errors in estimating the low-energy radiative cross sections.

In this work we use the effective field theoretical (EFT) framework of heavy baryon chiral perturbation theory (HBχPT) in presenting a systematic evaluation of the bremsstrahlung process by including the *next-to-leading order* (NLO) chiral corrections involving the leading order (LO) or $1/M$ proton recoil correction effects. Furthermore, we provide a rough estimate of the *next-to-next-to-leading order* (NNLO) contributions from the proton's structure effects that arise from pion loop corrections to the LO proton-photon vertex. These NNLO pion loop contributions effectively introduce the proton's rms radius, the first momentum dependent term in the charge form factor of the proton. As we shall discuss, contrary to the expectations based on standard chiral power counting for this process, the NNLO pion loop contributions appear to be kinematically enhanced by the small electron mass and roughly of the same order as the NLO contributions. This interesting observation, that emerges from our analysis in the case of the electron scattering, is not manifested in the case of the muon scattering due to the much larger muon mass.[1] Finally, we have corrected an error/misprint in an important published theoretical result (cf. Eq. (B.5) of Ref.[10]) in the context of lepton-proton scattering process, which is incorporated in standard radiative corrections procedure applied during data processing of *raw* experimental data.

[1] By LO, we mean the correction terms that are leading order in chiral counting, which includes the leading kinematic recoil corrections [see Sec. 4.3 for clarification.]

The chapter is organized as follows: In Sec. 4.2, we present a brief description of the lepton-proton bremsstrahlung process and the associated kinematics in the context of χPT, which, in principle, allows an order by order perturbative evaluation of the radiative and proton recoil correction contributions. In Sec. 4.3, we define the coordinate system and discuss the kinematics that are used in our evaluations of the analytic expressions for the differential cross sections. In Sec. 4.4, we present the results for our systematic evaluation up to and including NLO in chiral power counting. We furthermore include an estimate of the NNLO pion loop corrections, and present a comparison of these NNLO results with our full NLO evaluations. Section 4.5, contains a discussion of our numerical results. Finally, a short summary is presented before giving some concluding remarks

4.2 Low-Energy Lepton-Proton Bremsstrahlung

In our evaluation the standard relativistic lepton-current [214] is given by the expression

$$J_l^\mu(Q) = e\bar{u}_l(p')\gamma^\mu u_l(p)\,, \tag{4.1}$$

where $e = \sqrt{4\pi\alpha}$, and the four-momentum transferred to the proton is $Q = p - p'$. The lepton mass is included in all our expressions, and we will show that the lepton mass plays a crucial role in determining the shape of the low-energy lepton-proton bremsstrahlung differential cross section. The hadronic current is derived from the χPT Lagrangian. In χPT it is assumed that the LO terms give the dominant contributions to the amplitude, while the higher chiral orders contribute smaller corrections to the LO amplitude. Note that in our evaluation the NLO (M^{-1}) corrections to the bremsstrahlung process have two different origin, namely, the *kinematic* phase-space corrections, as seen in Eqs. (4.3) and (4.4) below, and the *dynamical* M^{-1} NLO corrections that arise from the photon-proton interaction in $\widehat{\mathcal{L}}^{(2)}_{\pi N}$ (cf. Appendix A). In particular, it should be mentioned that in general the anomalous magnetic moments of the nucleons formally enter into the χPT calculations at NLO through $\widehat{\mathcal{L}}^{(2)}_{\pi N}$.

We first evaluate the LO contributions to the lepton-proton bremsstrahlung process shown in Figure [4.1], using the explicit expression for the LO Lagrangian $\widehat{\mathcal{L}}^{(1)}_{\pi N}$ (cf. Appendix A)

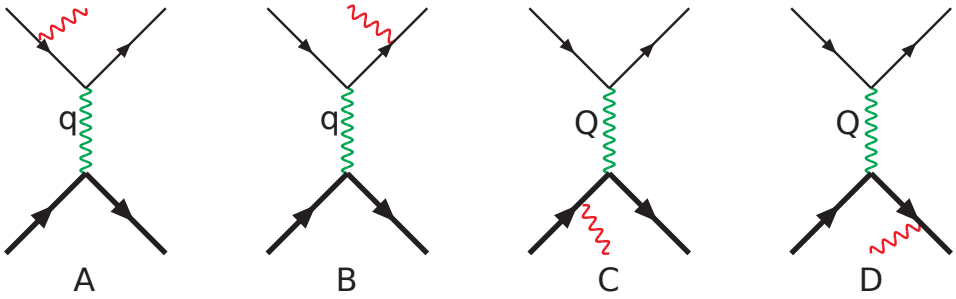

FIGURE 4.1: Feynman diagrams contributing to lepton-proton bremsstrahlung process. In the Coulomb gauge the proton radiation diagrams (C) and (D) do not contribute at the leading order in χPT.

relevant for the processes under study. We adopt the Coulomb gauge, i.e., $\epsilon \cdot v = 0$, where ϵ^μ is the outgoing photon polarization four-vector. This implies that in χPT the bremsstrahlung photon from the proton, diagrams (C) and (D) in Fig. [4.1], do not contribute to the bremsstrahlung process at LO (see Appendix A for the Feynman rules). The first non-trivial contribution of photon radiation from proton [Feynman diagrams (G) and (H) in Fig. [4.2] arises from the NLO interactions specified by $\widehat{\mathcal{L}}^{(2)}_{\pi N}$. Like diagrams (C) and (D) in Fig. [4.1], diagrams (I) and (J) in Fig. [4.2] do not contribute in the Coulomb gauge. Since the bremsstrahlung cross section is proportional to α/m^2 for a radiating particle of mass m, we expect the NLO contributions to be small compared to the LO due to the large proton mass.

In χPT we naively expect that the NNLO corrections are of order $(\mathscr{P}/\Lambda_\chi)^3 \ll 1$, where $\mathscr{P}$ denotes the generic four-momentum transfer for the process of the order of the pion mass (m_π). However, it turns out that the pion loop contributions are as important as the lower chiral order nucleon pole graph contributions. We will investigate the question regarding the magnitudes of the NNLO pion loop contributions in our process, i.e., we examine how well the usual chiral counting works for the lepton-proton bremsstrahlung process in Sec. 4.5. At NNLO the Lagrangian $\widehat{\mathcal{L}}^{(3)}_{\pi N}$, can be written as $\widehat{\mathcal{L}}^{(3)}_{\pi N} = \widehat{\mathscr{L}}^{(3),\text{fixed}}_{\pi N} + \widehat{\mathscr{L}}^{(3)}_{\pi N}$, where $\widehat{\mathscr{L}}^{(3),\text{fixed}}_{\pi N}$ contains M^{-2} recoil terms with known coefficients, while $\widehat{\mathscr{L}}^{(3)}_{\pi N}$ contains low-energy constants (LECs). The LECs regularize the ultra-violet (UV) contributions from the pion loop diagrams, which enter at NNLO order. The pion loops associated with the photon-proton vertex in diagrams (A) and (B) of Fig. [4.1] are illustrated in Fig. [4.3]. They contribute to the first momentum dependence of the proton form factors in χPT. In this work we will effectively make use of the NNLO proton electric form factor

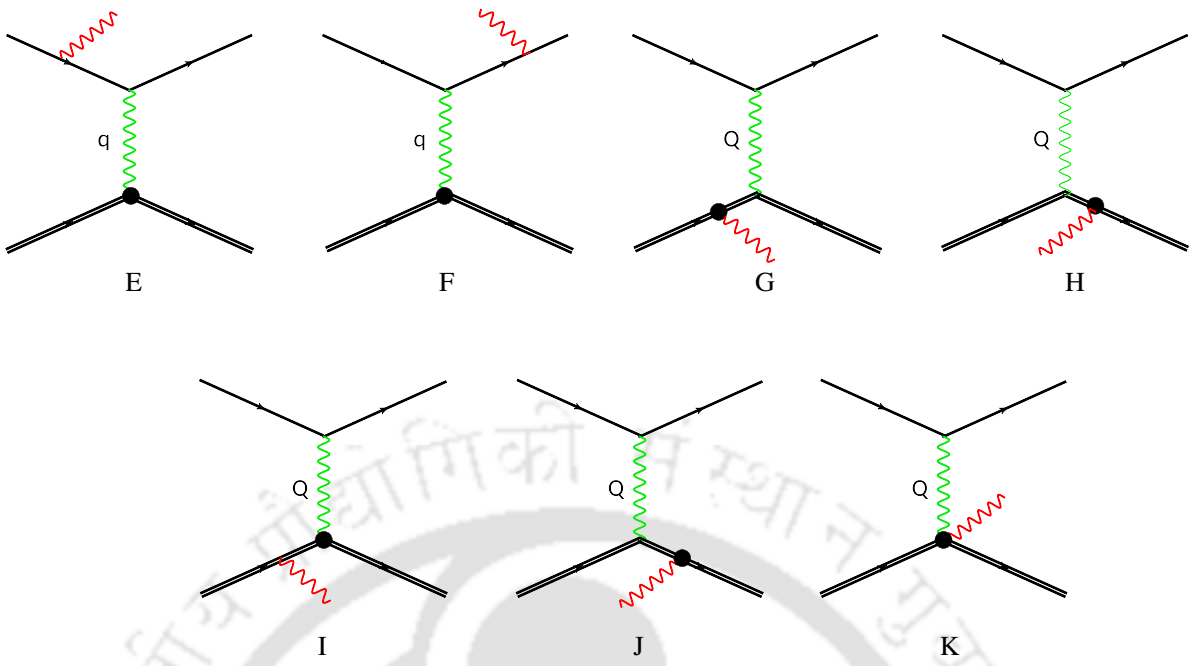

FIGURE 4.2: Feynman diagrams contributing to the lepton-proton bremsstrahlung process at NLO. The filled blobs represents insertion of proton-photon interaction terms from $\widehat{\mathcal{L}}^{(2)}_{\pi N}$. In the Coulomb gauge the proton radiation diagrams (I) and (J) do not contribute.

which along with the magnetic form factor was formally derived in Refs. [180, 215–217] using χPT. The explicit $\widehat{\mathcal{L}}^{(3)}_{\pi N}$ expression can also be found in those references. At this chiral order the measured rms charge and magnetic radii determine LECs in $\widehat{\mathcal{L}}^{(3)}_{\pi N}$ [216]. In essence, a measure of the NNLO contributions to our cross section is the following electric Sachs form factor G^p_E, expressed in terms of the corresponding iso-vector G^v_E and

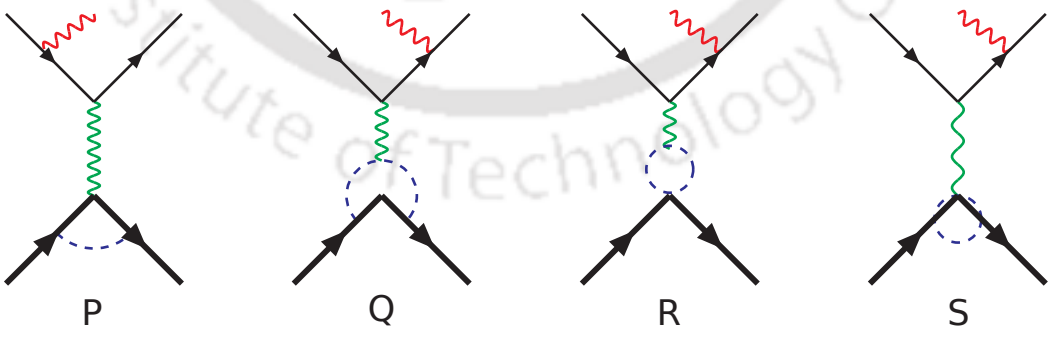

FIGURE 4.3: A subset of all NNLO Feynman diagrams of the lepton-proton bremsstrahlung process, where the pion loops, shown by the dashed (blue) propagator lines, contribute to the proton form factors. The vertices in the NNLO pion loop diagrams are all generated by $\widehat{\mathcal{L}}^{(1)}_{\pi N}$.

iso-scalar G_E^s form factors, namely

$$\begin{aligned} G_E^p(q^2) &= \frac{1}{2}\left[G_E^v(q^2) + G_E^s(q^2)\right] \\ &\approx 1 + \frac{q^2}{6}(r_E^p)^2 + \mathcal{O}(q^4)\,, \end{aligned} \tag{4.2}$$

where r_E^p is the electric radius of the proton.

In Sec. 4.5, our rough estimate of the NNLO contribution is obtained by folding the LO differential cross section results with G_E^p which include the "measured" rms radius as the phenomenological input. These should *effectively simulate* the NNLO χPT pion loop contributions.

4.3 The LO and NLO Cross Sections

At LO only the Feynman diagrams (A) and (B) in Fig. [4.1], contribute. We denote the incident and scattered lepton four-momenta as $p = (E, \vec{p})$ and $p' = (E', \vec{p}')$, respectively, where, e.g., $E = \sqrt{m_l^2 + \vec{p}^2}$. The corresponding proton four-momenta are $P = (E_p, \vec{P})$ and $P' = (E_p', \vec{P}')$, and the outgoing photon has the four-momentum $k = (E_\gamma, \vec{k})$. Furthermore, θ is the lepton scattering angle such that $\vec{p}\cdot\vec{p}' = |\vec{p}||\vec{p}'|\cos\theta$, and $q = (Q - k)$ is the four-momentum transferred to the proton when the lepton is radiating.

In χPT the non-relativistic heavy proton four-momentum satisfies re-parametrization invariance [172, 218], and takes the form $P_p^\mu = Mv^\mu + p_p^\mu$, where M is the proton mass, such that the square of its off-shell *residual* part is $p_p^2 \ll M^2$. This means that the incident proton kinetic energy to lowest order in M^{-1} becomes $v\cdot p_p = \frac{\vec{p}_p^{\,2}}{2M} + \cdots$, and similarly for the final recoiling proton. The bremsstrahlung differential cross section is given in the laboratory (*lab*) frame by the general expression

$$\mathrm{d}\sigma_{br} = \int \frac{\mathrm{d}^3\vec{p}'\;\mathrm{d}^3\vec{k}}{(2\pi)^5 8E'E_\gamma} \frac{\delta\left(E - E' - E_\gamma - \frac{(\vec{p}-\vec{p}'-\vec{k})^2}{2M} + \cdots\right)}{4ME\left(M + \frac{(\vec{p}-\vec{p}'-\vec{k})^2}{2M} + \cdots\right)} \frac{1}{4}\sum_{spins} |\mathcal{M}_{\gamma\gamma^*}|^2\,, \tag{4.3}$$

where in the phase-space expression (including the δ-function) we expand the recoil proton energy as[2]

$$E'_p \;=\; \sqrt{M^2+(\vec{p}\,'_p)^2} = M + \frac{(\vec{p}-\vec{p}\,'-\vec{k})^2}{2M} + \mathcal{O}\left(M^{-3}\right) . \tag{4.4}$$

A straightforward evaluation of the two Feynman diagrams (A) and (B), shown in Fig. [4.1] leads to the following LO expression for the bremsstrahlung amplitude squared:

$$\begin{aligned}
\frac{1}{4}\sum_{spins}|\mathcal{M}^{(0)}_{br}|^2 = \frac{1}{4}\sum|\mathcal{M}_A+\mathcal{M}_B|^2 &= \left(\frac{512\pi^3\alpha^3}{q^4}\right)(M+E_p)(M+E'_p) \\
\times\Bigg\{ &-\frac{1}{[(p'+k)^2-m_l^2]^2}\Big[m_l^4+m_l^2E'E+m_l^2EE_\gamma+m_l^2E'E_\gamma-EE'E_\gamma^2 \\
&\quad +m_l^2(\vec{k}\cdot\vec{p})-m_l^2(\vec{k}\cdot\vec{p}\,')+\ m_l^2(\vec{p}\cdot\vec{p}\,')+EE_\gamma(\vec{k}\cdot\vec{p}\,') \\
&\quad -E'E_\gamma(\vec{k}\cdot\vec{p})+(\vec{k}\cdot\vec{p}\,')(\vec{k}\cdot\vec{p})\Big] \\
&-\frac{1}{[(p-k)^2-m_l^2]^2}\Big[m_l^4-E_\gamma^2EE'+m_l^2EE'-m_l^2EE_\gamma-m_l^2E'E_\gamma \\
&\quad +m_l^2(\vec{p}\cdot\vec{k})+m_l^2(\vec{p}\cdot\vec{p}\,')-\ m_l^2(\vec{k}\cdot\vec{p}\,')-EE_\gamma(\vec{k}\cdot\vec{p}\,') \\
&\quad +E'E_\gamma(\vec{k}\cdot\vec{p})+(\vec{k}\cdot\vec{p}\,')(\vec{k}\cdot\vec{p})\Big] \\
&-\frac{2}{[(p'+k)^2-m_l^2]\,[(p-k)^2-m_l^2]}\Big[m_l^2E'E-m_l^2E_\gamma^2+E^2E'^2-m_l^2(\vec{p}\cdot\vec{p}\,') \\
&\quad +E^2(\vec{k}\cdot\vec{p}\,')-\ E'^2(\vec{k}\cdot\vec{p})-(\vec{p}\cdot\vec{p}\,')^2+(\vec{p}\cdot\vec{p}\,')(\vec{k}\cdot\vec{p}\,') \\
&\quad -(\vec{p}\cdot\vec{p}\,')(\vec{k}\cdot\vec{p})\Big]\Bigg\} .
\end{aligned} \tag{4.5}$$

To evaluate the cross section, it is convenient to define our reference frame such that the momentum transfer, $\vec{Q}=\vec{p}-\vec{p}\,'$ is directed along the z-axis [10], while the lepton momenta, $\vec{p}$ and $\vec{p}\,'$, lie in xz-plane as shown in Fig. [4.4]. The pertinent angles are defined as follows:

$$\begin{aligned}
\vec{k}\cdot\vec{p}\,' &= E_\gamma|\vec{p}\,'|(\cos\gamma\,\cos\alpha+\sin\alpha\,\sin\gamma\,\cos\phi_\gamma), \\
\vec{k}\cdot\vec{p} &= E_\gamma|\vec{p}\,|(\cos\zeta\,\cos\alpha+\sin\alpha\,\sin\zeta\,\cos\phi_\gamma) .
\end{aligned} \tag{4.6}$$

[2]For a χPT analysis for this process up to and including NNLO, it is sufficient to expand kinematic quantities up to $\mathcal{O}(M^{-2})$.

The lepton scattering angle in our coordinate system is given as $\theta = \gamma - \zeta$. When the lepton radiates a photon the squared four-momentum transferred to the proton is

$$\begin{aligned} q^2 &= (Q-k)^2 \\ &= 2\left[m_l^2 - EE' + |\vec{p}||\vec{p}'|\cos\theta - E_\gamma(E-E') + E_\gamma\cos\alpha\sqrt{|\vec{p}|^2+|\vec{p}'|^2-2|\vec{p}||\vec{p}'|\cos\theta}\right], \end{aligned} \tag{4.7}$$

which is independent of ϕ_γ in our reference frame as suggested in Ref. [10]. This choice of reference frame readily allows the analytical ϕ_γ integration.

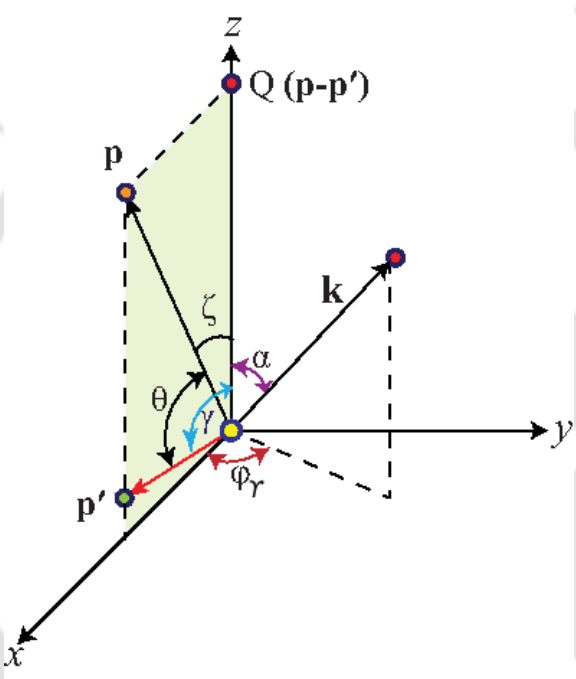

FIGURE 4.4: Reference coordinate system used in the evaluation of the differential cross section, such that $\vec{Q} = \vec{p} - \vec{p}'$ is taken along the z-axis, while $\vec{p}$ and $\vec{p}'$ lie in xz-plane. The different angles and three-momentum symbols are defined in the text.

To evaluate our LO expression for the differential cross section, $\mathrm{d}^3\sigma_{br}^{(\mathrm{LO})}/(\mathrm{d}|\vec{p}'|\,\mathrm{d}\Omega_l'\,\mathrm{dcos}\alpha)$ [see Eq. (4.15)], it is convenient to define two angle dependent parameters,

$$a = \frac{1-\beta'\cos\alpha\,\cos\gamma}{\beta'\sin\alpha\,\sin\gamma} \quad \text{and} \quad b = \frac{1-\beta\cos\alpha\,\cos\zeta}{\beta\sin\alpha\,\sin\zeta}\,. \tag{4.8}$$

Here $\beta = \frac{|\vec{p}|}{E}$ and $\beta' = \frac{|\vec{p}'|}{E'}$ are the incoming and outgoing lepton velocities, respectively. In this equation, we also define the magnitudes of the incoming and outgoing lepton three-momenta as $p = |\vec{p}|$ and $p' = |\vec{p}'|$, respectively. To obtain our final expression,

we integrate the cross section in Eq. (4.3) over the photon energies E_γ, which means that the infrared singularity will appear when the momentum p' is close to it's maximal allowed value. To account for the proton recoil corrections in the kinematics we include the M^{-1} terms in the photon energy E_γ given by the delta-function in Eq. (4.3). Defining $E_\gamma^0 = E - E'$, yields

$$E_\gamma = E_\gamma^0 - \frac{K}{M} + \mathcal{O}\left(M^{-3}\right) , \tag{4.9}$$

where,

$$K = \frac{1}{2}\left[|\vec{p}|^2 + |\vec{p}'|^2 - 2|\vec{p}||\vec{p}'|\cos\theta + (E_\gamma^0)^2 - 2E_\gamma^0\cos\alpha\sqrt{|\vec{p}|^2 + |\vec{p}'|^2 - 2|\vec{p}||\vec{p}'|\cos\theta}\right] \tag{4.10}$$

When integrating over E_γ, the expression in the delta-function also introduces a factor $\left(1 - \frac{Z}{M}\right)$ in the phase-space to lowest order in M^{-1} needed in our analysis, where

$$Z = E_\gamma^0 - \cos\alpha\,\sqrt{|\vec{p}|^2 + |\vec{p}'|^2 - 2|\vec{p}||\vec{p}'|\cos\theta}. \tag{4.11}$$

Furthermore, the M^{-1} correction in the photon energy affects the expression for the four-momentum transfer q^2, which can be written as

$$q^2 = (q^0)^2 + \frac{\kappa}{M} + \mathcal{O}\left(m_p^{-3}\right) , \tag{4.12}$$

where

$$(q^0)^2 = 2\left[m_l^2 - EE' + |\vec{p}||\vec{p}'|\cos\theta - E_\gamma^0(E - E') + E_\gamma^0\cos\alpha\sqrt{|\vec{p}|^2 + |\vec{p}'|^2 - 2|\vec{p}||\vec{p}'|\cos\theta}\right],$$

and

$$\kappa = 2K\left[E - E' - \cos\alpha\sqrt{|\vec{p}|^2 + |\vec{p}'|^2 - 2|\vec{p}||\vec{p}'|\cos\theta}\right] . \tag{4.13}$$

In the process of evaluation of the cross section up to NNLO, we will only need the M^{-1} kinematic terms, i.e., we include the M^{-1} corrections for E_γ, q^2, as well as in the above given phase-space factor.

As a pedagogical survey of the bremsstrahlung process at energies not much larger than the muon mass, we initially consider the most simplest and rather qualitative case of the static proton limit ($M \to \infty$). We shall then compare these qualitative results with the improved ones obtained by, first, including the kinematical M^{-1} recoil corrections

in the phase space factor and the delta-function expression in Eq. (4.3), and second, by including the dynamical M^{-1} recoil corrections in the matrix element at NLO.

As a first step, we may want to evaluate the LO cross section in the static proton limit ($M \to \infty$), which is expressed as

$$\mathrm{d}\sigma^{(\mathrm{LO})}_{br;\,\mathrm{static}} = \int \frac{\mathrm{d}^3\vec{p}\,'\,\mathrm{d}^3\vec{k}}{(2\pi)^5 32E'E^0_\gamma M^2 E}\delta\left(E - E' - E^0_\gamma\right)\left(\frac{1}{4}\sum_{spin}|\mathcal{M}^{(0);\,\mathrm{static}}_{\gamma\gamma^*}|^2\right). \quad (4.14)$$

$\mathcal{M}^{(0);\,\mathrm{static}}_{\gamma\gamma^*}$ in Eq. (4.14) is obtained from the LO matrix element, namely, $\mathcal{M}^{(0)}_{\gamma\gamma^*} = \mathcal{M}_A + \mathcal{M}_B$, in the static proton limit ($M \to \infty$). In other words, we must set K, κ and Z all equal zero after obtaining the square of the LO matrix element $|\mathcal{M}^{(0)}_{\gamma\gamma^*}|^2$. Next we present our corresponding *non-static* LO result for bremsstrahlung 'triple' differential cross section, which incorporates the M^{-1} recoil effects only from the phase space [including the energy-delta function in Eq. (4.3)] but the matrix element is derived from the leading chiral order Lagrangian $\widehat{\mathcal{L}}^{(1)}_{\pi N}$, namely

$$\begin{aligned}
\frac{\mathrm{d}^3\sigma^{(\mathrm{LO})}_{br}}{\mathrm{d}p'\,\mathrm{d}\Omega'_l\,\mathrm{d}\cos\alpha} &= \left(\frac{\alpha^3\beta'^2}{2\pi^2 q^4}\right)\left(1 - \frac{Z}{M}\right)E_\gamma\left\{-\int_0^{2\pi}\mathrm{d}\phi_\gamma\frac{1}{(a-\cos\phi_\gamma)^2}\left(\frac{1}{EE'E^2_\gamma(\beta'\sin\alpha\sin\gamma)^2}\right)\right.\\
&\times\Big[m_l^4 - EE'E^2_\gamma + m_l^2E'E_\gamma + m_l^2EE' + m_l^2EE_\gamma + m_l^2pp'\cos\theta\\
&- m_l^2p'E_\gamma\left(\cos\alpha\cos\gamma + \sin\alpha\sin\gamma\cos\phi_\gamma\right) + p'EE^2_\gamma\left(\cos\alpha\cos\gamma + \sin\alpha\sin\gamma\cos\phi_\gamma\right)\\
&+ m_l^2pE_\gamma\left(\cos\alpha\cos\zeta + \sin\alpha\sin\zeta\cos\phi_\gamma\right) - pE'E^2_\gamma\left(\cos\alpha\cos\zeta + \sin\alpha\sin\zeta\cos\phi_\gamma\right)\\
&+ pp'E^2_\gamma\Big(\cos^2\alpha\cos\gamma\cos\zeta + \cos\alpha\cos\gamma\sin\alpha\sin\zeta\cos\phi_\gamma + \sin\alpha\sin\gamma\cos\alpha\cos\zeta\cos\phi_\gamma\\
&+ \sin^2\alpha\sin\gamma\sin\zeta\cos^2\phi_\gamma\Big)\Big]_{\mathrm{dir}(\gamma)}\\
&- \int_0^{2\pi}\mathrm{d}\phi_\gamma\frac{1}{(b-\cos\phi_\gamma)^2}\left(\frac{E'}{E^3E^2_\gamma(\beta\sin\alpha\sin\zeta)^2}\right)\\
&\times\Big[m_l^4 - EE'E^2_\gamma - m_l^2E'E_\gamma + m_l^2EE' - m_l^2EE_\gamma + m_l^2pp'\cos\theta\\
&- m_l^2p'E_\gamma\left(\cos\alpha\cos\gamma + \sin\alpha\sin\gamma\cos\phi_\gamma\right) - p'EE^2_\gamma\left(\cos\alpha\cos\gamma + \sin\alpha\sin\gamma\cos\phi_\gamma\right)\\
&+ m_l^2pE_\gamma\left(\cos\alpha\cos\zeta + \sin\alpha\sin\zeta\cos\phi_\gamma\right) + pE'E^2_\gamma\left(\cos\alpha\cos\zeta + \sin\alpha\sin\zeta\cos\phi_\gamma\right)\\
&+ pp'E^2_\gamma\Big(\cos^2\alpha\cos\gamma\cos\zeta + \cos\alpha\cos\gamma\sin\alpha\sin\zeta\cos\phi_\gamma + \sin\alpha\sin\gamma\cos\alpha\cos\zeta\cos\phi_\gamma\\
&+ \sin^2\alpha\sin\gamma\sin\zeta\cos^2\phi_\gamma\Big)\Big]_{\mathrm{dir}(\zeta)}
\end{aligned}$$

$$
\begin{aligned}
&+\int_0^{2\pi}\mathrm{d}\phi_\gamma\frac{1}{(a-\cos\phi_\gamma)(b-\cos\phi_\gamma)}\left(\frac{2}{E^2E_\gamma^2(\beta\beta'\sin^2\alpha\sin\gamma\sin\zeta)}\right)\\
&\times\Big[m_l^2EE'+E^2E'^2-m_l^2E_\gamma^2-\,m_l^2pp'\cos\theta-p^2p'^2\cos^2\theta\\
&+p'E^2E_\gamma\Big(\cos\alpha\cos\gamma+\,\sin\alpha\sin\gamma\cos\phi_\gamma\Big)+\,pp'^2E_\gamma\cos\theta\Big(\cos\alpha\cos\gamma\\
&+\sin\alpha\sin\gamma\cos\phi_\gamma\Big)-\,pE'^2E_\gamma\Big(\cos\alpha\cos\zeta+\,\sin\alpha\sin\zeta\cos\phi_\gamma\Big)\\
&-p^2p'E_\gamma\cos\theta\Big(\cos\alpha\cos\zeta+\,\sin\alpha\sin\zeta\cos\phi_\gamma\Big)\Big]_{\rm int}\Big\}\,. \qquad (4.15)
\end{aligned}
$$

The terms within the first and second square brackets, i.e., $[\cdots]_{\rm dir(\gamma)}$ and $[\cdots]_{\rm dir(\zeta)}$, represent the contributions from the "direct" terms (matrix element squared of diagram (B) and (A), respectively) of real photon emissions from the outgoing and incoming leptons, respectively. The third square bracket $[\cdots]_{\rm int}$, represents the "interference" contribution of diagrams (A) and (B).

Next including the $\mathcal{O}(M^{-1})$ dynamical corrections in the matrix elements due to the interactions in $\widehat{\mathcal{L}}^{(2)}_{\pi N}$, i.e., with

$$
\sum_{spins}\left|\mathcal{M}^{(1)}_{\gamma\gamma^*}\right|^2\;\rightarrow\;2\,\mathcal{R}\mathrm{e}\sum_{spins}\left(\mathcal{M}_{\rm A}+\mathcal{M}_{\rm B}\right)^\dagger\left(\mathcal{M}_{\rm E}+\mathcal{M}_{\rm F}+\mathcal{M}_{\rm G}+\mathcal{M}_{\rm H}+\mathcal{M}_{\rm K}\right), \qquad (4.16)
$$

yields the complete NLO expression to the bremsstrahlung differential cross section which is expressed as

$$
\frac{\mathrm{d}^3\sigma_{br}}{\mathrm{d}p'\,\mathrm{d}\Omega'_l\,\mathrm{d}\cos\alpha}\;=\;\frac{\mathrm{d}^3\sigma^{(\rm LO)}_{br}}{\mathrm{d}p'\,\mathrm{d}\Omega'_l\,\mathrm{d}\cos\alpha}+\Delta\left[\frac{\mathrm{d}^3\sigma^{(\rm NLO)}_{br}}{\mathrm{d}p'\,\mathrm{d}\Omega'_l\,\mathrm{d}\cos\alpha}\right], \qquad (4.17)
$$

where the $\mathcal{O}(M^{-1})$ NLO correction term above is

$$
\begin{aligned}
\Delta\left[\frac{\mathrm{d}^3\sigma^{(\rm NLO)}_{br}}{\mathrm{d}p'\,\mathrm{d}\Omega'_l\,\mathrm{d}\cos\alpha}\right]&=\left(\frac{\alpha^3\beta'^2}{2\pi^2(q^0)^4}\right)\frac{2E^0_\gamma}{M}\int_0^{2\pi}\mathrm{d}\phi_\gamma\\
&\times\Bigg[-\frac{1}{(a-\cos\phi_\gamma)^2}\left(\frac{W_{\rm BF}}{EE'(E^0_\gamma)^2(\beta'\,\sin\alpha\,\sin\gamma)^2}\right)\\
&\quad-\frac{1}{(b-\cos\phi_\gamma)^2}\left(\frac{E'W_{\rm AE}}{E^3(E^0_\gamma)^2(\beta\,\sin\alpha\,\sin\zeta)^2}\right)
\end{aligned}
$$

$$- \frac{1}{(a-\cos\phi_\gamma)(b-\cos\phi_\gamma)} \left(\frac{W_{\rm AF}+W_{\rm BE}}{E^2(E^0_\gamma)^2(\beta\beta'\sin^2\alpha\,\sin\gamma\,\sin\zeta)} \right)$$
$$+ \frac{(q^0)^2}{Q^2} \Bigg\{ \frac{1}{(a-\cos\phi_\gamma)} \left(\frac{W_{\rm BG}-W_{\rm BH}-W_{\rm BK}}{EE'(E^0_\gamma)^2(\beta'\,\sin\alpha\,\sin\gamma)} \right)$$
$$- \frac{1}{(b-\cos\phi_\gamma)} \left(\frac{E'(W_{\rm AG}+W_{\rm AH}-W_{\rm AK})}{E^3(E^0_\gamma)^2(\beta\,\sin\alpha\,\sin\zeta)} \right) \Bigg\} \Bigg] . \tag{4.18}$$

Notice that in all our NLO corrected expressions presented above we use the $\mathcal{O}(M^0) = \mathcal{O}(1)$ expressions, $E^0_\gamma = E - E'$ and $(q^0)^2$, already defined earlier in Eq. (4.9) and (4.8), respectively. The explicit expressions for the partial amplitudes of $\mathcal{O}(M^0)$, namely $W_{\rm AE}, W_{\rm AF}, W_{\rm AG}, W_{\rm AH}, W_{\rm AK}$ and $W_{\rm BE}, W_{\rm BF}, W_{\rm BG}, W_{\rm BH}, W_{\rm BK}$,[3] are rather lengthy and relegated to the Appendix B. As evident from the subscripts, these contributions arise from the interference of the diagrams in Fig. [4.1] with those in Fig. [4.2].

4.4 LO and NLO Results

The MUSE collaboration [41] proposes the scattering of lepton off proton at the following three beam momenta, $p = 115$, 153 and 210 MeV/c. As discussed, MUSE is designed to count the number of scattered leptons at a fixed scattering angle θ for any value of the scattered lepton momentum $|\vec{p}'|$ larger than a certain minimum value. We shall discuss the dependence of the cross section on the photon angle α and the lepton momentum $|\vec{p}'|$. First, however, we analyze the q^2 dependence of the bremsstrahlung process.

In order to extract a precise value for the proton rms radius, one needs to know accurately the Q^2 dependence of the proton form factor. To LO in χPT the four-momentum transferred to the proton is $q = (Q - k)$, since the proton do not radiate. At NLO, however, the momentum transfer can be either Q or q depending on whether the proton radiates or not. For a given scattering angle θ, Eq. (4.8) shows that q^2 is a function of the outgoing lepton momentum $|\vec{p}'|$, the lepton scattering angle θ, and the photon polar angle α. Although the bremsstrahlung process for muon scattering at a given angle θ, constitutes

[3]Note that amplitudes $W_{\rm AK}$ and $W_{\rm BK}$ originating due to the diagram K has negligible contribution to the cross section and were not considered in Ref.[212].

a small correction to the elastic cross section, the process introduces a non-negligible q^2 value uncertainty. Thus, we find it important to examine the q^2 dependence on $|\vec{p}\,'|$ and α in order to guesstimate the uncertainty given by the bremsstrahlung process.

First, it is inferred from Eq. (4.8) that for a given lepton mass m_l and very small $|\vec{p}\,'| = p'$, as the angle $\alpha \to 0$, the θ angular dependence of the squared momentum transfer $-q^2$ becomes practically negligible. This means that the photon emission direction $\vec{k}$ is (almost) *collinear* with the incident lepton direction $\vec{p}$. On the other hand, when p' tends toward its maximal limit for fixed θ, i.e., $p' \to p'_{elastic}(\theta)$, the α dependence plays a complex role in determining the resulting $-q^2$ behavior. Fig. [4.5] depicts the $-q^2$ behavior of the outgoing lepton momentum p', for a fixed incident lepton momentum $p = |\vec{p}|$, forward scattering angle θ, and a small polar angle α. Both plots exhibit a quadratic behavior of $-q^2$ versus p', with a minimum at a certain p' value. In general, the minimum depends on p, θ, α and the lepton mass m_l. Even in the massless ($m_l \to 0$) case, a minimum of $-q^2$ at a non-zero value of p' is obtained as long as θ or α is non-zero. For example, in the given figure the minimum occurs for $p' \lesssim 5$ MeV/c for the electron and $p' \lesssim 100$ MeV/c for the muon. Furthermore, we find that for given fixed angles (θ, α), and lepton mass $p' \ll m_l \leq p'_{elastic}$, the square momentum transfer $-q^2$ becomes linear in $|\vec{p}\,'|$ with a negative slope for forward scattering angles $\theta < \pi/2$. This behavior can be seen in each plot in Fig. [4.5] for the small p' region, though in case of the electron plot the negative slope of the hardly discernible. However, the inserted zoomed plot clearly shows this behavior. Thus, we can expect that the small q^2 dependence on p' in the low-momentum region below 100 MeV/c, that is relevant to MUSE, will produce significant effects on the differential cross section $\mathrm{d}\sigma/(\mathrm{d}p'\mathrm{d}\Omega')$. Note that the MUSE collaboration is expected to detect electrons and muons with momenta p' in a range down to about $50 - 20$ MeV/c.

Second, we note that the bremsstrahlung cross section is directly proportional to $1/q^4$, Eq. (4.15). In Fig. [4.6] we display the behavior of $1/q^4$ as a simultaneous function of p' and $\cos\alpha$. In the electron case, the figure clearly shows a large *collinear enhancement* of $1/q^4$ as $\alpha \to 0$ and p' is taken very small. This enhancement falls off sharply with the increasing values of both $\cos\alpha$ and p'. In contrast, for the muons no such enhancement in $1/q^4$ is apparent for small p'.

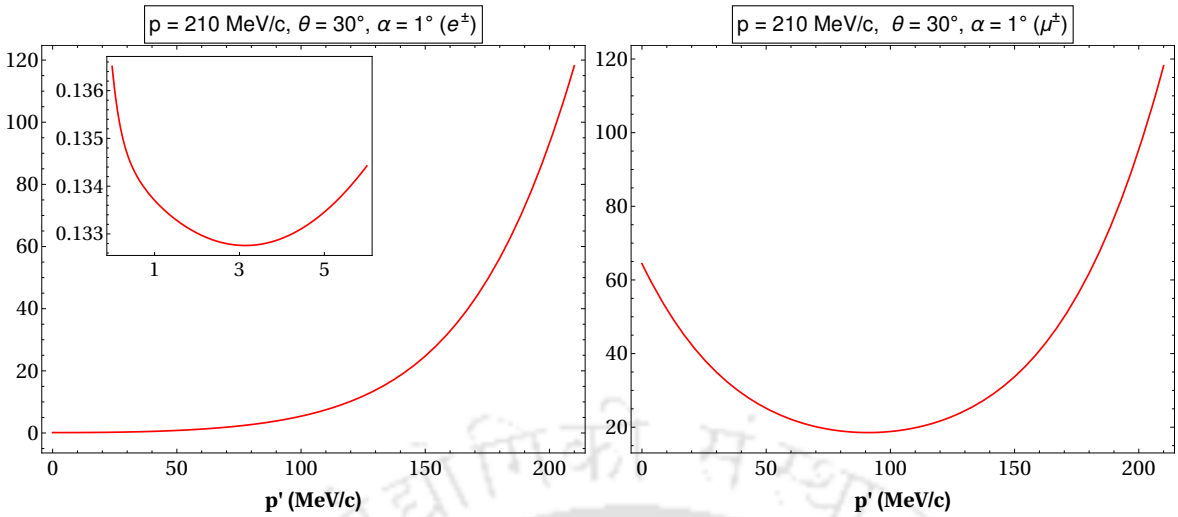

FIGURE 4.5: Behavior of the squared momentum transfer $-q^2$ (in units of 10^2 MeV$^2/c^2$), as a function of the outgoing lepton momentum, $p' = |\vec{p}'|$, for a fixed incident lepton momenta, $p = |\vec{p}| = 210$ MeV/c, scattering angle, $\theta = 30°$ and $\alpha = 1°$. When $p' \ll m_e, |\vec{p}|$, we have near collinear photon emission with $\vec{p}$. In the case of electron scattering (left plot), the inset plot clearly displays the minimum of $-q^2$.

In Fig. [4.7], we display the result for the total differential cross section up to and including NLO in χPT, Eq. (4.17), versus the cosine of the outgoing photon angle α, for three MUSE specified incoming momenta, $p = |\vec{p}| = 210, 153, 115$ MeV/c. For the bremsstrahlung process the outgoing lepton momentum can be chosen arbitrarily in the range $0 \leq p' \leq p'_{elastic}(\theta)$, with $p_{elastic}(\theta) < p$ for a given scattering angle θ. We only display the results for the MUSE specified kinematics with $p' = 30, 100$ and 200 MeV/c and for three forward angles: $\theta = 15°, 30°$ and $60°$. We also present a comparison of our NLO results with those of the LO (static and with recoil), as well as with the results obtained by using the corrected expression for Eq. (B.5) in Ref. [10] (see clarification towards the end of this section). The differential cross section shows that the commonly used peaking approximation [10, 47] is very well satisfied for the electron even at these low electron momenta p and p'. The double-peak structure is a distinctive feature of the angular radiative spectrum for ultra-relativistic particles.

The prominent double peaks occur for photon angle α close to the angle ζ (the ζ-peak) for the incoming electron momentum, and the angle γ (the γ-peak) for the outgoing electron momentum, as defined in Fig. [4.4]. Moreover, it may be noted in the figure that for $\theta = 15^o$ for both the lower plots (as well as for $\theta = 30^o$ and 60^o in the lower right plot) three peaks are generated with the ζ-peak being the dominant one. In each case the

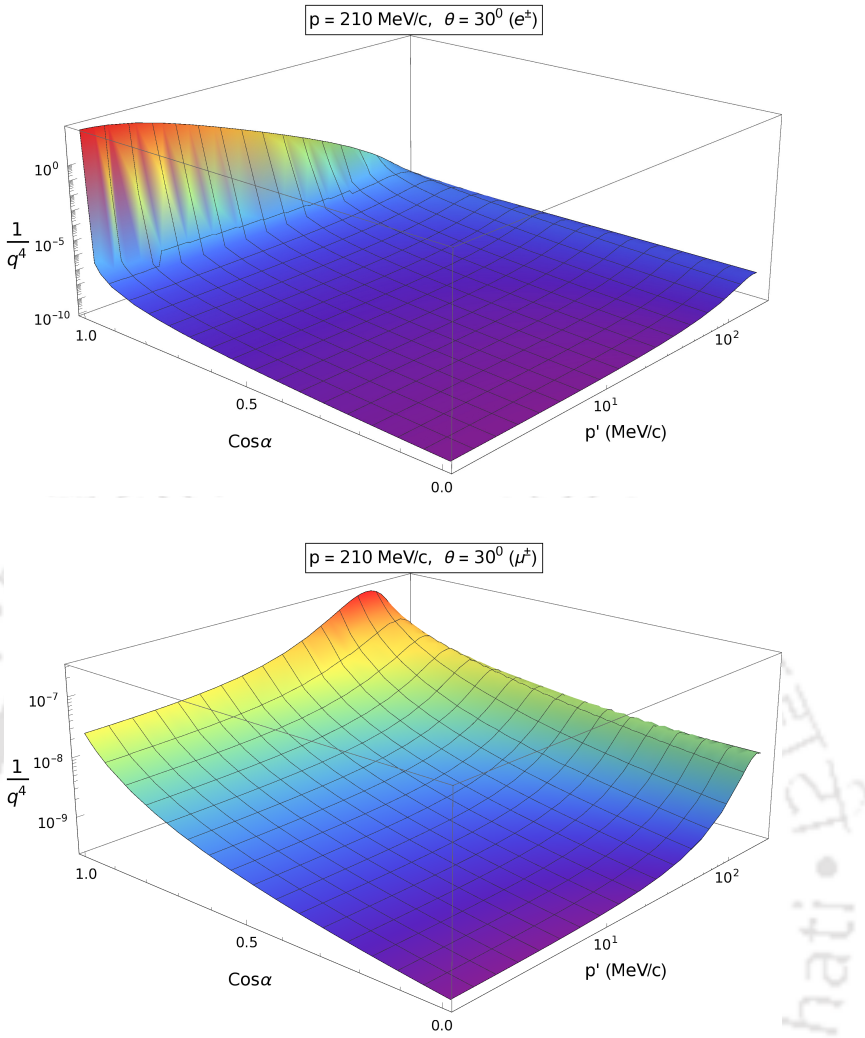

FIGURE 4.6: Behavior of q^{-4} [in $(\mathrm{MeV/c})^{-4}$] as a simultaneous function of the outgoing lepton momenta p' and $0 \leq \cos\alpha \leq 1$. The left plot is for the electron case and the right plot gives the muon results. In each case, the incident lepton momentum is $p = 210$ MeV/c and the scattering angle is $\theta = 30°$. In case of electron, there is a very large collinear enhancement for $p' \to 0$ and $\alpha \to 0$ and manifests as a local maximum at small p' in Fig. [4.10]. This phenomenon is not noticeable in the muon spectrum.

rightmost peak-like structure very close to $\cos\alpha = 1$, as shown by the insert plot in the lower right graph in Fig. [4.7], can be attributed to the small q^2 (or alternatively, large $1/q^4$) behavior for angle α close to zero (also, see Fig. 11 in Ref. [10]). As expected from a classical bremsstrahlung angular spectrum (see, e.g., Ref. [10]), for relativistic electrons the emitted photons get collimated close to the incoming and outgoing directions of the electron momentum. Several further observations regarding the electron plots are in order:

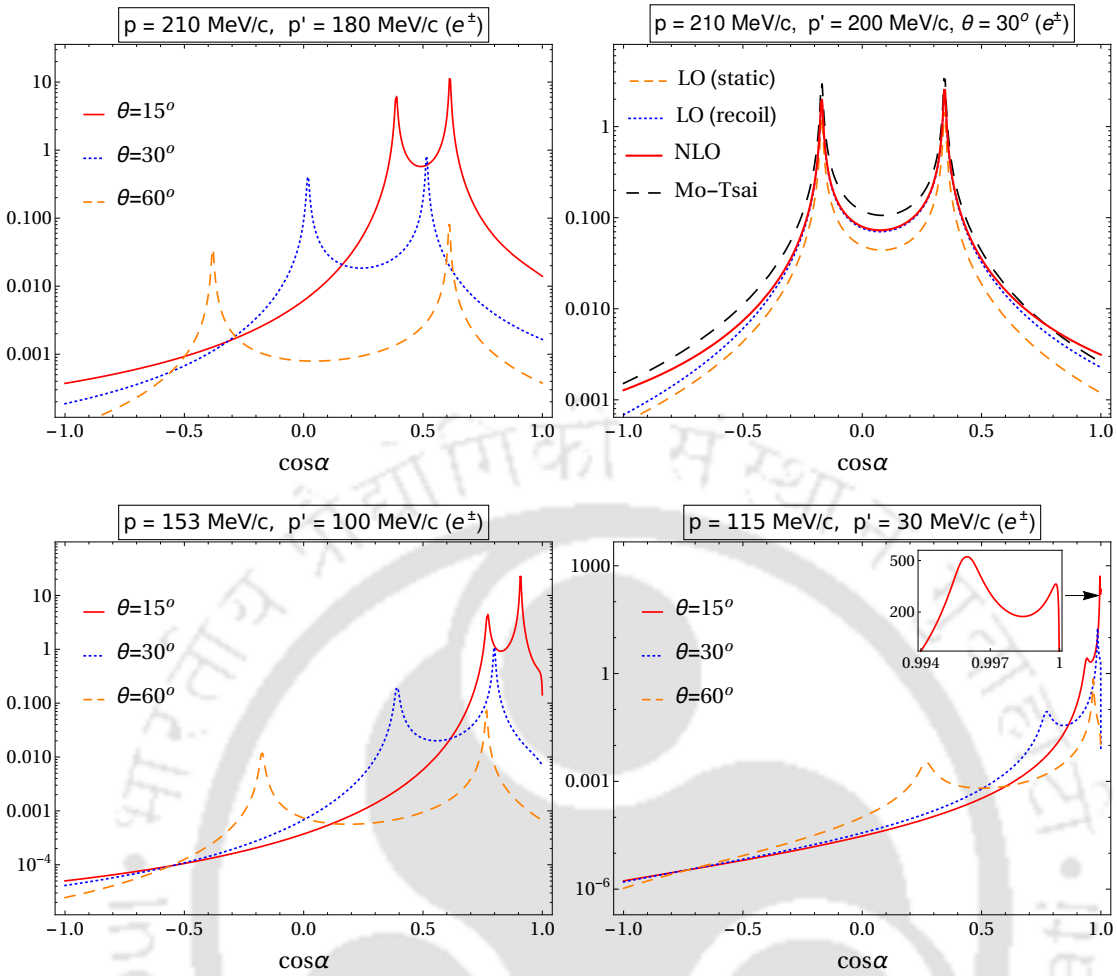

FIGURE 4.7: The bremsstrahlung differential cross section up to and including NLO in χPT, $\mathrm{d}^3\sigma_{br}/(\mathrm{d}|\vec{p}\,'|\,\mathrm{d}\Omega'_l\,\mathrm{d}\cos\alpha)$ (in mb/GeV/sr), versus $\cos\alpha$ for electron scattering for the three incident MUSE specified momenta $p = |\vec{p}\,|$, as displayed. For each p just one value for the outgoing electron momentum $p' = |\vec{p}\,'|$ is plotted. In the two l.h.s. and bottom right plots, the solid (red) curves correspond to $\theta = 15^o$, the dotted (blue) curves to $\theta = 30^o$, and the dashed (orange) curves to $\theta = 60^o$. The insert in the lower right graph shows the dominant ζ-peak and the additional third peak very close to $\cos\alpha = 1$. The top right graph compares the NLO result, Eq. (4.17), with our LO evaluations, without [i.e., *static*, Eq. (4.14), and with the proton recoil terms of $\mathcal{O}(M^{-1})$ in the phase space [i.e., *recoil*, Eq. (4.15). In the same graph, the dashed curve shows the corresponding result obtained using the corrected expression for Eq. (B.5) in Ref. [10] (see text).

- The separation between the peaks increase with increasing scattering angle $\theta = \gamma - \zeta$. For $\theta \to 0$, the two peaks merge together into a single sharp peak, denoting collinear alignment of all momentum vectors.

- For a finite electron mass m_e, incident momentum $|\vec{p}\,|$, and fixed angles (θ, α), the differential cross section becomes maximum when the outgoing three-momentum p'

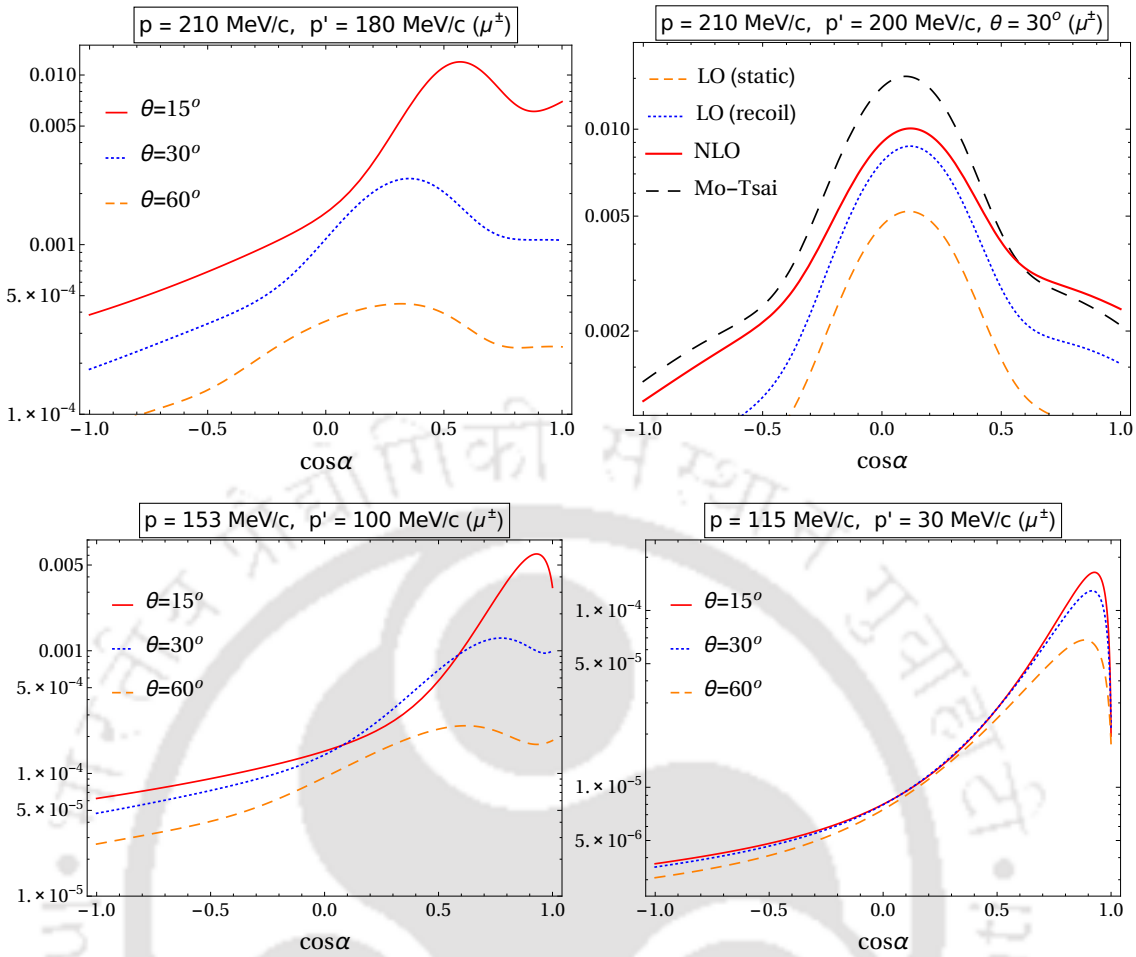

FIGURE 4.8: The bremsstrahlung differential cross section up to and including NLO in χPT, $\mathrm{d}^3\sigma_{br}/(\mathrm{d}|\vec{p}'|\,\mathrm{d}\Omega'_l\,\mathrm{dcos}\alpha)$ (in mb/GeV/sr) versus $\cos\alpha$ for muon scattering for the three incident MUSE specified momenta $p = |\vec{p}|$, as displayed. For each p just one value for the outgoing muon momentum $p' = |\vec{p}'|$ is plotted. See text and caption of Fig. [4.7] for details.

value corresponding to the minimum of $-q^2$ (maximum of $1/q^4$).

- For fixed scattering angle θ and three-momentum transfer $|\vec{Q}| = |\vec{p} - \vec{p}'|$, the differential cross section decreases with increasing incident momentum $|\vec{p}|$.

- For fixed three-momenta p and p', the differential cross section decreases with increasing scattering angle θ.

In contrast to our electron scattering results, the $\cos\alpha$ dependence with the same kinematics for incoming muons is very different, as seen in Fig. [4.8]. The initial muon momenta are not much larger than the muon mass, and the bremsstrahlung differential cross section versus $\cos\alpha$ has a broad angular spectrum. The plots in Figs. [4.7] and [4.8]

clearly demonstrate that the so-called *peaking approximations* [10], a widely used practical recipe for data analysis incorporating radiative corrections, while viable for electron scattering at the low-momentum MUSE kinematics, is not applicable for muon scattering at MUSE energies. As seen from Fig. [4.7] (top right plot), the expressions for the NLO "interference" corrections, namely, Eqs. (4.16)-(4.18), appear to yield contributions much smaller compared to the dominant LO result for the electron scattering. In contrast, for the muon scattering the NLO corrections are appreciably larger, as evidenced from the comparison plot in Fig. [4.8]. Regarding our LO results, we have checked that the interference contribution in the LO differential bremsstrahlung cross section, Eq. (4.15), is much larger and dominates over the "direct" contribution for both the electron and muon scattering (provided that the value for p' is not too small for the electron scattering case). As expected, the muon bremsstrahlung differential cross section is reduced by roughly two orders of magnitude compared to the corresponding electron cross sections for the same kinematic specification.

Zooming in on each peak in the electron angular $\cos\alpha$ dependence reveals the existence of a (3D) cone-like sub-structure, as displayed in Fig. [4.9], i.e., the photon emission is (almost) collinear with the incoming and outgoing electron momenta. It may be recalled that for a charged relativistic particle with an acceleration parallel to its velocity $\vec{\beta}$, the angular intensity distribution of the classical radiation corresponds to a cone with maximal opening angle $\sim \mathcal{O}(\sqrt{1-\beta^2})$ with respect to the direction of motion $\vec{\beta}$. The dashed vertical lines in Fig. [4.9] correspond in our reference system, Fig. [4.4], to the expected directions of the incoming and outgoing leptons. The effect of bremsstrahlung radiation results in the lepton recoiling away in a slightly different direction, leading to the characteristic cone-like feature for each peak with the vertex along the expected axis of the radiation cone. Unlike the $\cos\alpha$ dependence of the electron bremsstrahlung cross section, in case of the muon we observe significant interference effects between the two dominant broad angular peak structures arising entirely from the "direct" terms, labelled $[\ldots]_{\mathrm{dir}(\gamma)}$ and $[\ldots]_{\mathrm{dir}(\zeta)}$, and the "interference" contribution, labelled $[\ldots]_{\mathrm{int}}$, in the LO expression Eq. (4.15). We find in addition a nominal NLO correction Eq. (4.18) to the $\cos\alpha$ behavior. These lead to the deviations of each minimum from the expected directions, as indicated by the vertically (red) dashed lines in the figure. Our graphic demonstrations support part

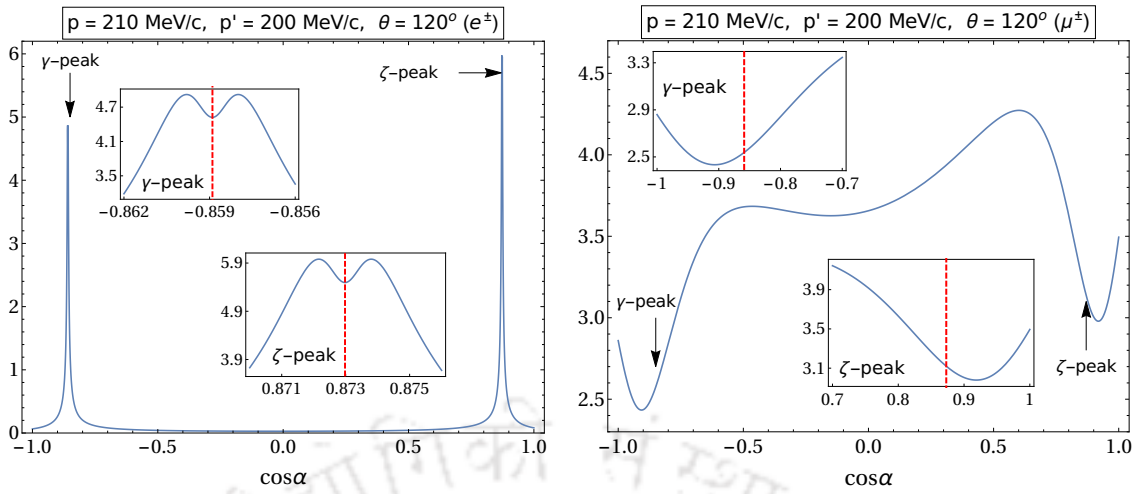

FIGURE 4.9: The bremsstrahlung differential cross sections up to and including NLO in χPT, $\mathrm{d}^3\sigma_{br}/(\mathrm{d}|\vec{p}'|\,\mathrm{d}\Omega'_l\,\mathrm{dcos}\alpha)$ (in mb/GeV/sr), versus $\cos\alpha$, indicating photon emissions from the leptons distributed within a shallow cone about their incident or scattered directions. The left plot is for electrons whereas the right plot is for muons. Both plots correspond to $p = 210$ MeV/c and $p' = 200$ MeV/c, and for the lepton scattering angle $\theta = 120°$. The red dashed lines indicate the directions of the incident and scattered leptons, i.e., $\cos\zeta$ and $\cos\gamma$, respectively.

of the analysis presented in Ref. [153] (e.g., see, Fig. [4] in this reference), where radiative corrections to $(e, e'p)$ coincident experiments were discussed. It is to be, however, noted that if we were to reduce the value of the muon mass from its physical value, there should be a steady reduction of this observed mismatch between the vertical (red) dashed lines and the cone minima.

The NLO results for the electron and muon bremsstrahlung "radiative tail" cross section given in Eq. (4.17) for the MUSE specified values of the incoming lepton momenta, i.e., $p = |\vec{p}| = 210, 153$ and 115 MeV/c, are displayed in Figs. [4.10]. We only display the plots for the forward scattering angles, $\theta = 15^o, 30^o$, and 60^o, also specified for MUSE measurements. The bremsstrahlung cross section versus p' is plotted from 0.1 MeV/c up to $p'_{max} = p'_{elastic} - \Delta p'$, where we have chosen $\Delta p' = 0.1$ MeV/c in order to avoid the IR singular region. There is clearly a large IR enhancement of all the plots toward the large p' endpoint region. Without a proper treatment of the radiative IR divergences, our large p' results are beset with large uncertainties, though in the low-momentum region $p' \lesssim 100$ MeV/c (suitable for MUSE) our results are reasonably accurate. We note that as p' tends toward zero, the differential cross section also goes to zero for the both muon

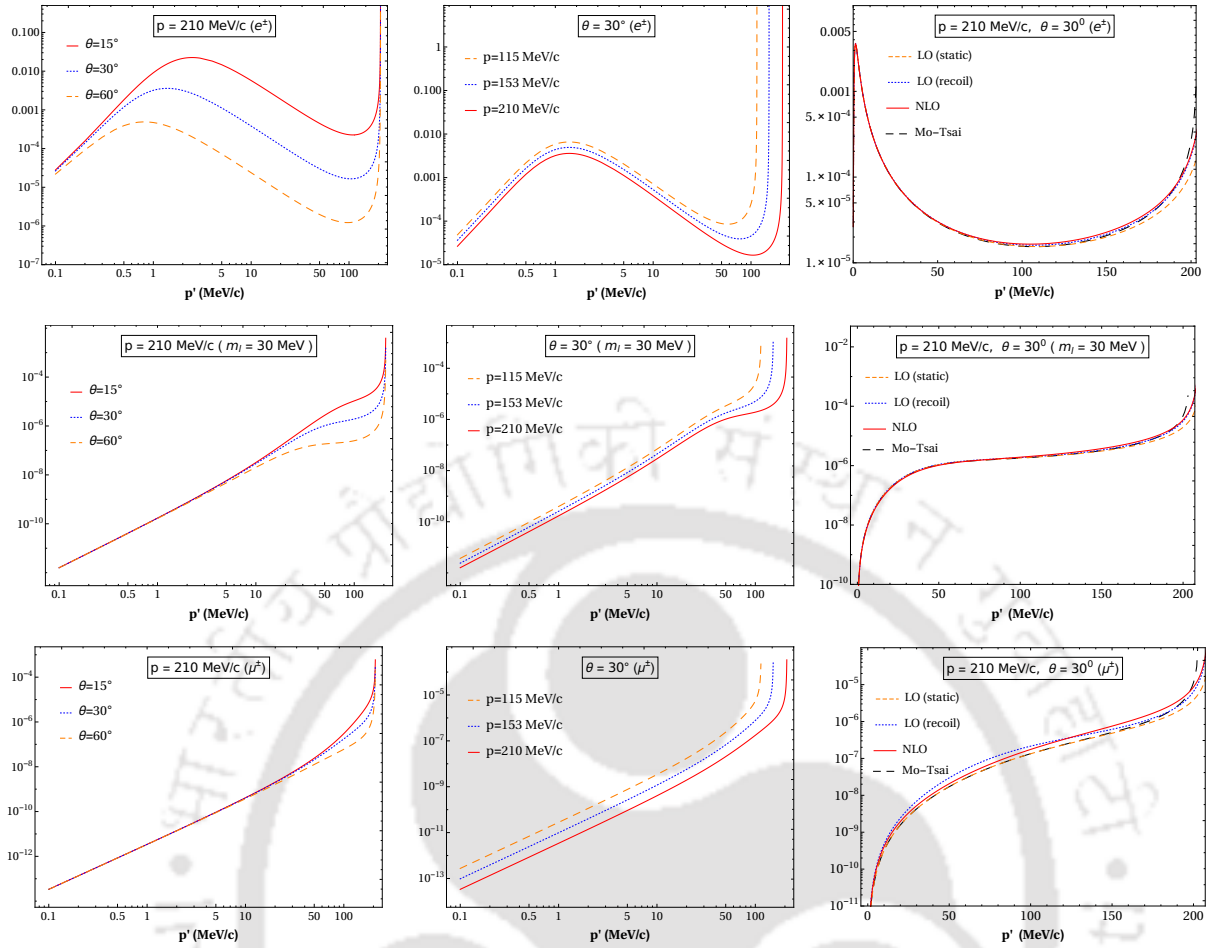

FIGURE 4.10: The "radiative tail spectrum" cross section up to and including NLO in χPT, $\mathrm{d}^2\sigma_{br}/(\mathrm{d}|\vec{p}'|\,\mathrm{d}\Omega'_l)$ (in mb/GeV/sr) is plotted as a function of the scattered lepton momentum $|\vec{p}'|$, for incoming lepton momenta $|\vec{p}|$ and scattering angles θ specified by MUSE. The plots in the upper (lower) row correspond to electron (muon) scattering, while the plots in the middle row correspond to the results for an intermediate lepton mass, $m_l \sim 30$ MeV. In the left column plots, where $|\vec{p}| = 210$ MeV/c, we display the cross sections for $\theta = 15^o$ solid (red) curve, 30^o dotted (blue) curve, and 60^o dashed (orange) curve. For the middle column plots, we show the cross sections with $\theta = 30^o$ for the three incoming MUSE specified momenta, $p = 210$ (solid), 153 (dotted) and 115 (dashed) MeV/c in the static approximation $M \to \infty$. The right column plots (with non-log scale abscissa) compare our NLO results with the *static* and *recoil* LO evaluations, Eqs. (4.14) and (4.15), respectively, as well as with the results obtained using the corrected expression for Eq. (B.5) in Ref. [10], but ignoring the proton form factors.

and electron cases. However, for the electron tail spectrum the cross section reaches a local maximum before going to zero as $p' \to 0$.

This local maximum at small p' values is primarily due to the dominant behavior of our static LO radiative tail cross section. When the outgoing electron momentum $\vec{p}' \to 0$, the photon emission from the electron becomes (almost) collinear with the direction of the

incident electron momentum $\vec{p}$ (reflected in the peaking approximation in Figs. [4.7] and [4.9] and the momentum transfer, $\vec{q} = \vec{p} - \vec{p}' - \vec{k}$. If we artificially let the electron mass go towards zero, we will encounter a *mass singularity* when $p' = 0$. The small electron mass effectively regularizes this singularity, and a remnant of this divergence manifests itself as a local maximum in the cross section. In that case the cross section goes to zero as $p' \to 0$.

Another way to examine the gradual development of the local maximum in the electron cross section is to consider our muon results presented in Fig. [4.10] (lower row plots) and artificially lower the value of the muon mass from the physical value, i.e., $m_\mu = 105.7$ MeV. We find that for a lepton mass, $m_l \sim 30-40$ MeV, the cross section starts developing a "shoulder", which for still smaller lepton mass values develops into a local maximum for small p' values. It then starts to resemble the cross section for electron scattering (upper row plots in Fig. [4.10]. Thus, for sufficiently small values of the lepton mass, the cross section has a distinct local maximum in the cross section in the small p' region.

As evident from Fig. [4.10], our results up to and including the NLO appear to be dominated by the LO results. In other words, the qualitative difference made by the NLO corrections to the electron and the muon cross sections are not at all apparent from the figure. Thus, for a better qualitative estimate of the NLO part of tail spectrum, we present a relative comparison between the LO and NLO contributions in terms of a quantity, $\delta_{\rm NLO}$, which measures the ratio of the NLO correction with respect to the LO contribution, namely

$$\delta_{\rm NLO} = \left[\left(\frac{{\rm d}^2\sigma_{br}^{\rm (NLO)}}{{\rm d}p'{\rm d}\Omega_l} \right) - \left(\frac{{\rm d}^2\sigma_{br}^{\rm (LO)}}{{\rm d}p'{\rm d}\Omega_l} \right) \right] \left(\frac{{\rm d}^2\sigma_{br}^{\rm (LO)}}{{\rm d}p'{\rm d}\Omega_l} \right) . \tag{4.19}$$

This quantity is plotted in Fig. [4.11] against the outgoing lepton momentum p', corresponding to the same kinematics specification as in the right column plots in Fig. [4.10]. Clearly, the $\delta_{\rm NLO}$ for the muon spectrum is an order of magnitude larger than same for the electron spectrum. Moreover, in the electron case, the NLO corrections in the low p' region below 50 MeV/c become negative, in contrast to the NLO corrections for the muon that remain positive definite for the entire range of p' values.

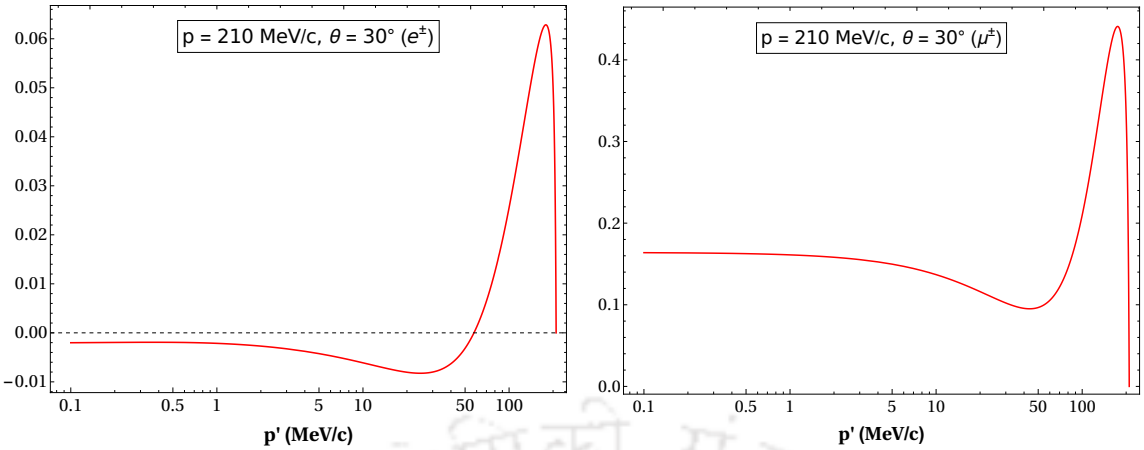

FIGURE 4.11: The quantity $\delta_{\rm NLO}$ of Eq. (4.19), which stands for the NLO corrections relative to LO radiative tail cross section, is plotted as a function of the outgoing lepton momentum $p' < p'_{elastic}$, where $p'_{elastic} \approx 203.8$ MeV/c for electron and about 203.1 MeV/c for muon, for scattering angle $\theta = 30^o$. The left plot is for the electron case and the right plot gives the corresponding muon results.

Finally, in comparing our results with the expression Eq. (B.5) in Ref. [10], we find that the expression has to be corrected as follows. The very first energy factor, E_p/E_s, multiplying the integral in that expression should have been $\vec{p}^{\,2}/(E_pE_s)$. This reduces to the energy factor in Eq. (B.5) provided we neglect the lepton mass. Incorporating this correction and by ignoring the proton form factors (anomalous magnetic moment contribution also excluded) in Eq. (B.5) of Ref. [10], we find only a nominal difference with our LO result obtained from Eq. (4.15). However, once we include the full NLO result obtained by evaluating Eqs. (4.17) and (4.18), which includes the M^{-1} recoil corrections from the phase space, the δ-function, and the matrix elements, the differences with Ref. [10] indeed becomes negligible, as evident from the right column plots in Figs. [4.10]. Note that Ref. [10] treated both the leptons and the proton in a common relativistic framework, whereas in our χPT approach the proton, being a heavy particle, is treated non-relativistically in both the phase-space expressions and the matrix elements.

As mentioned in the introduction and in Sec. II, the pion loops, as well as M^{-2} terms from $\widehat{\mathcal{L}}^{(3)}_{\pi N}$ contribute at NNLO in χPT and generate the low-momentum proton form factors. These contributions are supposed to be small according to standard χPT counting. However, as presented in Sec. 4.2 the χPT counting scheme might not capture the fact that the probability of an electron radiating is much enhanced compared to the radiation from the heavy proton. Hence, we next examine the importance of the proton form

factors generated by NNLO terms. The low-momentum NNLO expressions for the Sachs form factors $G^p_{E,M}$, have already been evaluated in earlier χPT works, e.g., Ref. [216], and they are effectively incorporated in our evaluation. We consider only those LO Feynman graphs where the real photon radiation originates from one of the lepton lines, i.e., diagrams (A) and (B) in Fig. [4.1]. We only include the dominant Sachs electric form factor G^p_E of the proton, in particular the Taylor expanded form given by Eq. (4.2), at the exchanged photon-proton vertices associated with the LO diagrams. In order to have a rough assessment of the relative importance of the proton's structure effects, we show our results as a ratio $\mathscr{R}$, which may be taken as a qualitative measure of the expected NNLO corrections $\delta_{\rm NNLO}$:

$$\mathscr{R} = \frac{\left(\frac{\mathrm{d}^2\sigma_{br}}{\mathrm{d}p'\mathrm{d}\Omega'_l}\right)_{\rm form} - \left(\frac{\mathrm{d}^2\sigma_{br}}{\mathrm{d}p'\mathrm{d}\Omega'_l}\right)_{\rm point}}{\left(\frac{\mathrm{d}^2\sigma_{br}}{\mathrm{d}p'\mathrm{d}\Omega'_l}\right)_{\rm point}} \,. \tag{4.20}$$

Here, the subscripts "form" and "point", respectively, denotes the radiative tail differential cross section evaluated with and without the proton's rms charge radius r^p_E included. Thus, in our analysis we approximate the NNLO χPT contributions as

$$\begin{aligned} \left(\frac{\mathrm{d}^2\sigma_{br}}{\mathrm{d}p'\,\mathrm{d}\Omega'_l}\right)_{\rm form} &\to \int_{-1}^{1} \mathrm{d}(\cos\alpha) \left(\frac{\mathrm{d}^3\sigma^{\rm (LO)}_{br}}{\mathrm{d}p'\,\mathrm{d}\Omega'_l\,\mathrm{d}\cos\alpha}\right) G^p_E(q^2)\,, \\ \left(\frac{\mathrm{d}^2\sigma_{br}}{\mathrm{d}p'\,\mathrm{d}\Omega'_l}\right)_{\rm point} &\to \frac{\mathrm{d}^2\sigma^{\rm (LO)}_{br}}{\mathrm{d}p'\,\mathrm{d}\Omega'_l}\,, \end{aligned} \tag{4.21}$$

with q^2 given by Eq. (4.8), and the charge radius r^p_E of the proton to be used as the input. In phenomenological analyses, the *dipole* parametrization [219] is a commonly employed parametrization for the Sachs form factors, as was used in Ref. [10] that correspond to $r^p_E = 0.81$ fm. Furthermore, the recent high-precision measurements from the study of muonic hydrogen spectroscopy by the CREMA experimental collaboration [21, 23] led to the controversial value of $r^p_E = 0.84$ fm, a result that is $\sim 7\sigma$ smaller than the previously accepted CODATA result, $r^p_E = 0.87$ fm [101]. These three values of r^p_E are used as the "measured" rms radius input to G^p_E in the above relation. The results are displayed in Fig. [4.12] where they are labelled as "χPT (dople)", "χPT (CREMA)" and "χPT (CODATA)", respectively. Finally, these NNLO predictions are compared with the

corresponding result obtained by using Eq. (B.5) of Ref. [10] (with our corrected version), with and without their phenomenological electric form factor G_E^p for obtaining the "form" and "point" contributions, respectively, while ignoring their magnetic dipole form factor G_M^p. This result is labeled as "Mo-Tsai" in the figure.

By comparing the plots in Figs. [4.11] and [4.12], we observe that the NLO and NNLO corrections relative to the LO results can be significant. As evident from the plots, for an incoming electron of momentum $p = 210$ MeV/c, outgoing momentum $p' = 100$ MeV/c, and scattering angle $\theta = 30^o$, we find that the NLO and NNLO corrections modify the LO radiative tail cross section by about 2% and 1%, respectively, with the "χPT" form factors [i.e., Eq. (4.2) with the above phenomenological rms radii.] Using the same kinematics for the muon, the corresponding LO results get modified about 20% and 2%, respectively. In addition, our NNLO results suggest that effectively the pion loops strongly suppress the local maximum at small p' values in the electron radiative tail cross section. In case of the electron the crucial observation is that the NNLO form factor effects are of the same order as our NLO contributions. However, for the muon we find that the NNLO "χPT" contributions are about a factor of two smaller than the NLO contributions and more consistent with the standard χPT counting rules. But again in contrast, Fig. [4.12] shows that for the muon "Mo-Tsai" result the proton's structure contributions are a factors of two larger than those of the NNLO "χPT" results, and therefore, of similar magnitude as that of the muon NLO result shown in Fig. [4.11].

In Fig. [4.10], the bremsstrahlung cross sections diverge as the maximal value p'_{max} approaches the elastic lepton-proton scattering value $p'_{elastic}$. As mentioned this is due to the infrared divergence (IR) of the bremsstrahlung process when the bremsstrahlung photon energy tends to zero. As demonstrated in, e.g., Refs. [10, 50], the cross section is free of IR singularities, provided the *virtual* radiative corrections are included in the calculation. In χPT, one can systematically evaluate the effect of virtual photon-loops, as well as the bremsstrahlung contribution from the leptons and protons in order to remove the IR singularities from observables. For the elastic lepton-proton scattering, the virtual photon loops along with the so-called *two-photon exchange* (TPE) contributions will additionally introduce ultraviolet (UV) divergences. In the next chapter of this thesis,

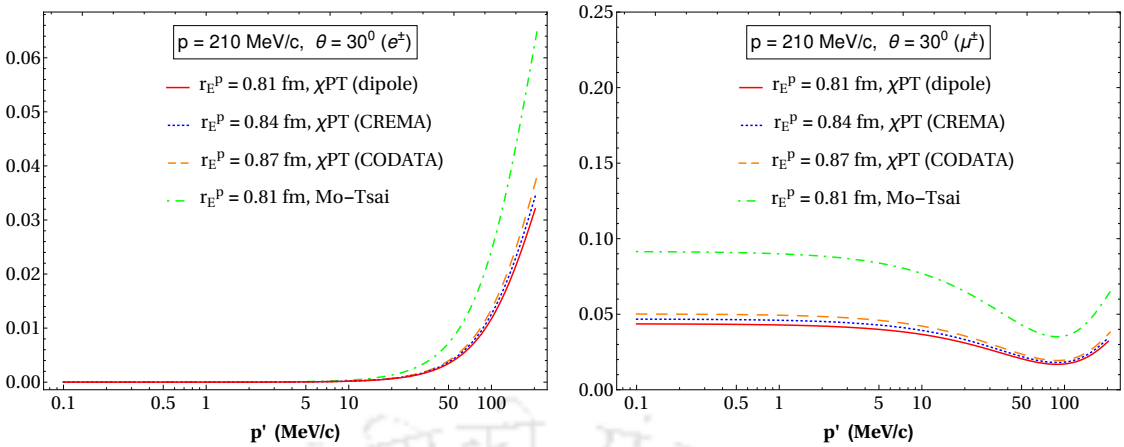

FIGURE 4.12: The quantity, $|\delta_{\rm NNLO}|$ is a qualitative measure of the expected NNLO proton's rms radius contribution to the radiative tail cross section when the lepton is radiating. This quantity is plotted as a function of the outgoing lepton momentum $p' < p'_{elastic}$, where $p'_{elastic} \approx 203.8$ MeV/c for electron and about 203.1 MeV/c for muon, for scattering angle $\theta = 30^o$. Here different rms radii are used as phenomenological input to parametrize the "χPT" electric form factor G_E^p (see text). For comparison, we also display the corresponding result obtained by using Eq. (B.5) of Ref. [10], while ignoring the magnetic form factor contribution. The left (right) plot corresponds to the electron (muon) results.

these divergences are treated systematically in χPT at NLO accuracy using the procedure of dimensional regularization which ensure gauge invariance at every perturbative order. This would naturally involve the introduction of low-energy constants (LECs) in the χPT Lagrangian required for the purpose of renormalization. Fortunately, at NLO in the radiative and recoil corrections (cf. Chapters 5 and 6) no such LECs are needed. Nevertheless, some LECs do appear at NNLO needed to renormalize UV divergences arising from pion-loops and can be taken directly from earlier χPT works, e.g., Ref. [220]. Such a systematic NNLO evaluation is rather involved and beyond the scope of the work presented in this thesis.

4.5 Conclusion

In retrospect, the purpose of the work in this chapter was to present a qualitative but yet pedagogical evaluations of the LO and NLO contributions to the lepton-proton bremsstrahlung cross section in the context of a low-energy EFT framework. Here we highlight some of the key aspects of this work:

- One important issue was to discuss a scenario where a large change in the angular spectrum of the bremsstrahlung process can be expected at typical momenta not much larger than the muon mass. The importance of such a study is very relevant to the MUSE experimental program where high precision lepton-proton scatterings at very low-momentum transfers will be pursued in order to investigate the reason behind the unexpectedly large discrepancy of the proton charge radius extracted from scattering experiments and the radius obtained from muonic hydrogen measurements. Our analysis demonstrates that a non-standard treatment of the bremsstrahlung corrections for muon scattering must be carefully thought through by the MUSE collaboration.

- In χPT employing Coulomb gauge, the two LO diagrams (C) and (D) in Fig. [4.1], and the two NLO diagrams, (I) and (J) in Fig. [4.2], do not contribute. In other words, bremsstrahlung radiation from a LO proton-photon vertex does not contribute in our χPT analysis. However, there is non-trivial proton bremsstrahlung contributions [diagrams (G) and (H) in Fig. [4.2] at NLO associated with chiral order $\nu = 1$ proton-photon vertex in χPT.

- While taking the trace over the amplitude squared in order to determine the unpolarized bremsstrahlung cross section, the spin dependent interactions in the NLO Lagrangian give vanishing contribution. Consequently, the anomalous magnetic moment of the proton does not contribute to the cross section for this process at NLO in χPT, contrary to usual expectations. Thus, the proton's magnetic moment starts contributing to the bremsstrahlung process only at NNLO, as implicitly parametrized in our case in terms of the proton's rms radius.

- Our results displayed in Figs. [4.7] and [4.8], clearly indicate that the widely used peaking approximation in radiative analysis of high energy electron scattering data can not be used in the radiative analyses of the future low-energy muon data from MUSE.

- As evidenced from Fig. [4.10], the radiative tail cross section for the electron scattering process for small outgoing momenta, $|\vec{p}'| \lesssim 5$ MeV/c exhibits a local maximum that can be attributed due to the small but non-zero electron mass. However, in

the same figure we show that such a behavior disappears for the much larger lepton muon mass. Since MUSE is designed only to detect the lepton scattering angle θ and can not determine the value of the outgoing lepton momentum $|\vec{p}\,'\,|$, care must be taken in the analysis of the MUSE data when one corrects for the radiative tail from the bremsstrahlung spectra.

- At NNLO the proton's rms radius enters the evaluation via the LECs in $\widehat{\mathcal{L}}^{(3)}_{\pi N}$, meaning that the low-momentum aspects of the proton's structure (rms radius) naturally contribute at this sub-leading order. In particular, we find that NNLO corrections for electron scattering bremsstrahlung diagrams illustrated in Fig. [4.3], are as large as the NLO corrections, contrary to what is expected in standard chiral power counting.

- Finally, our evaluations revealed an error in the overall expression for the energy factor in the well-known review article [10].

In the following chapter, we focus on the radiative correction to the basic lepton-proton elastic scattering process, where we present an evaluation of the two-photon exchange process in our EFT framework.

Chapter 5

Two-Photon Exchange

5.1 Introduction

In this chapter, we present an evaluation of two-photon exchange (TPE) contributions with an elastic intermediate proton state in HBχPT formalism based on our publication [221]. One of the earliest works on the TPE effects may be the so-called *Feshbach corrections* [222], which considered relativistic electrons scattering off a static Coulomb potential. The later works of Refs. [10, 47, 50] did consider the virtual TPE diagrams in order to cancel the IR divergences arising from the bremsstrahlung diagrams. These calculations suggested that the TPE effects were small. In other words, the dominant contributions arose from the *one-photon exchange* contribution (i.e., the first Born approximation) leading to the celebrated Rosenbluth formula (see Eq. (2.29) of Chapter 2) for elastic lepton-proton scattering cross section. Modern experimental arrangements like the MUSE facilitate simultaneous measurement of the unpolarized elastic $e^{\pm}$p and $\mu^{\pm}$p scattering cross sections, thereby enabling extraction of possible enhanced TPE contributions. In other words, MUSE will measure the difference of the lepton and anti-lepton charge cross sections to which the interference between the Born and the TPE diagrams at $\mathcal{O}(\alpha^3)$ contributes.[1]

[1]This *charge-asymmetry* measurements can not be used to extract the TPE contribution directly. The MUSE experiment can instead observe the *charge odd* combinations of TPE along with parts of

Recent theoretical studies have suggested that the TPE effects can play crucial role in explaining possible discrepancies in various measured observables. It appears to be the general consensus that the TPE contributions have the correct sign and magnitude in order to resolve the bulk of the discrepancies in the extraction of form factors [18, 22, 23, 53, 54, 59, 62, 63, 66, 223, 224]. In this work, where we have evaluated the TPE contribution, we focus only on the elastic intermediate state as it is expected to give the dominant contribution at very low momentum transfers [68, 147, 225–230]. Furthermore, here we only need to deal with the real parts of these amplitudes which contribute to the unpolarized elastic lepton-proton cross section.

This chapter is organized as follows. In Sec. 5.2, we list all possible TPE diagrams within HBχPT, *up-to-and-including* NLO in the chiral power counting. We also discuss some of the details of the kinematics involved in the calculations, which are commensurate with the proposed MUSE kinematic domain. In Sec. 5.3, we outline the crucial steps involved in the systematic removal of the IR divergences from the TPE diagrams at $\mathcal{O}(\alpha^3)$. Especially, we discuss the subtle nature of many cancellations among the NLO TPE amplitudes in the soft photon limit and their relation to the corresponding soft photon bremsstrahlung processes. Next in Sec. 5.4, we present our numerical estimates of the TPE contribution to the unpolarized elastic cross section. Finally, in Sec. 5.5, we present a summary of this chapter and draw some conclusions.

5.2 HBχPT Treatment of TPE

All possible TPE amplitudes at $\mathcal{O}(e^4)$ in HBχPT are diagrammatically illustrated in Figure 5.1. The Feynman graphs, namely, (a)-(h) are the so-called "box" diagrams consisting of the "direct" and "crossed-box" terms, and the graph (i) is the so-called "seagull" term. In the diagrams labeled (a) and (b), the proton-photon vertices arise from the LO chiral Lagrangian $\widehat{\mathcal{L}}^{(1)}_{\pi N}$ (cf. Appendix A) in the , while diagrams (c)-(f) contain one proton-photon vertex insertion from the NLO Lagrangian (c.f. Appendix A).

the bremsstrahlung contributions. In order to isolate the TPE contribution, model-dependent corrections must be applied to the charge-asymmetry data, i.e., one has to extract the charge-dependent bremsstrahlung contributions, e.g., Ref. [22].

Each of the diagrams (g) and (h) contains an NLO propagator insertion, and finally the seagull diagram contains no intermediate proton, instead this diagram has an effective $\gamma\gamma$-interaction vertex associated with the proton originating from the NLO Lagrangian.

As mentioned in the presented chapter, for all theoretical treatments, it is convenient to choose the laboratory (*lab*) or the rest frame of the proton target which allows a straightforward relation to the proposed MUSE kinematics. Furthermore, we may recall that in the HBχPT formalism one introduces a small so-called *residual* incoming proton

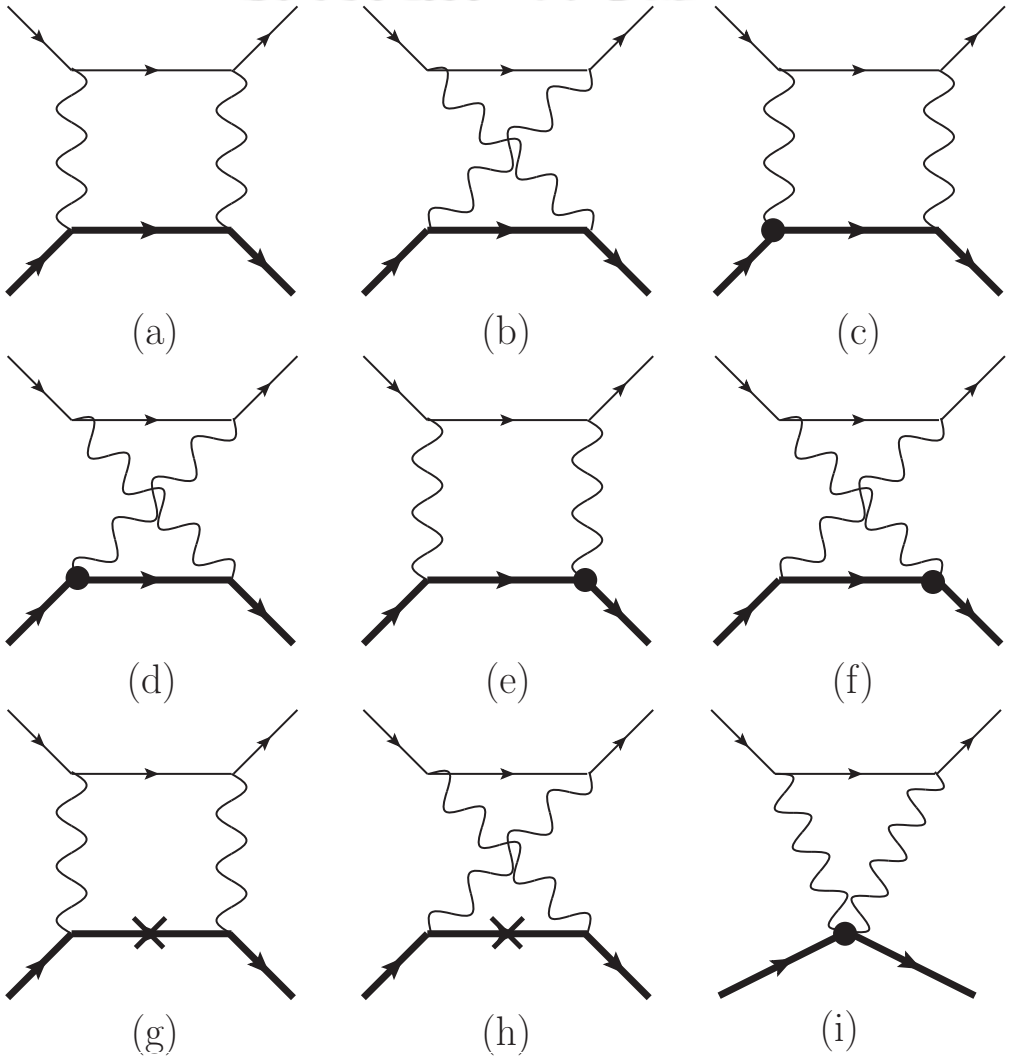

FIGURE 5.1: The TPE Feynman diagrams of $\mathcal{O}(e^4)$ which contribute to the $\mathcal{O}(\alpha^3)$ interference term in the elastic lepton-proton cross section. Thin lines represent lepton propagators, thick lines represent proton propagators, and wiggly lines represent photons propagators. The solid dark circles and the lines with a cross represent vertex and proton propagators insertions, respectively, from the NLO Lagrangian $\widehat{\mathcal{L}}^{(2)}_{\pi N}$ (c.f. Appendix A). Diagrams (a)-(h) are the "box" ("direct" and "crossed-box") terms, and diagram (i) is the "seagull" term.

momentum p_p, as defined through the relation, $P^\mu = Mv^\mu + p_p^\mu$ with $p_p^2 \ll M^2$, which in the *lab*-frame implies $v \cdot p_p = 0$. Similarly, the small residual outgoing proton momentum p'_p, defined via $P'^\mu = Mv^\mu + p'^\mu_p$, where $(p'_p)^2 \ll M^2$, implies

$$v \cdot p'_p = \frac{\vec{p}'^2_p}{2M} + \mathcal{O}(M^{-2})\,. \tag{5.1}$$

Finally, the four-momentum transfer in the elastic process is $Q_\mu = p_\mu - p'_\mu = P'_\mu - P_\mu = (p'_p)_\mu - (p_p)_\mu$, and the lepton scattering angle is θ.

As stated earlier the MUSE collaboration has chosen the incident lepton momenta to have the following values: 115 MeV/c, 153 MeV/c and 210 MeV/c. This means that for elastic scattering the four-momentum transfer Q^2 depends only the scattering angle θ. The corresponding range of Q^2 value in the laboratory frame can be obtained using the relations

$$Q^2 = 2m_l^2 - 2EE'(1 - \beta\beta' \cos\,\theta) = -2M(E - E')\,, \tag{5.2}$$

where $\beta = |\vec{p}|/E$ and $\beta' = |\vec{p'}|/E'$ are the incoming and outgoing lepton velocities, respectively. It may be shown that $0 < |Q^2| < |Q^2_{\rm max}| = 4M^2(E^2 - m_l^2)/(m_l^2 + M^2 + 2ME)$ represents the kinematically allowed (physical) range of momentum transfers [225]. However, the (laboratory frame) scattering angle is proposed by MUSE to be in the range $\theta \in [20^\circ, 100^\circ]$ [41], for which the possible Q^2 range of values obtained from Eq. (5.2) are tabulated in Table 5.1. By examining the Q^2 values in the table we observe that $Q/\Lambda_\chi \ll 1$, i.e., the HBχPT power counting scheme can be applied reasonably well in the domain of the MUSE kinematics.[2] In the next section we evaluate the TPE diagrams in Fig. [5.1] and isolate the IR divergences of the TPE box diagrams.

5.3 Soft Photon Approximation Analysis of TPE

In this section we evaluate all the TPE diagrams in Fig. [5.1] using HBχPT and derive the Q^2 or θ dependence on the IR subtracted TPE diagrams in a gauge-invariant manner.

[2]We note that for the TPE diagrams with either NLO vertex or propagator insertions being already of $\mathcal{O}(M^{-1})$, it is reasonable to write $E' = E + \frac{Q^2}{2M} \approx E$ at NLO.

Momentum (p) in GeV/c	0.115	0.153	0.210
$\lvert Q^2\rvert$ in $(\mathrm{GeV/c})^2$ for Electron			
Angle $\theta = 20^\circ$	0.0016	0.0028	0.0052
Angle $\theta = 100^\circ$	0.027	0.046	0.082
$\lvert Q^2\rvert$ in $(\mathrm{GeV/c})^2$ for Muon			
Angle $\theta = 20^\circ$	0.0016	0.0028	0.0052
Angle $\theta = 100^\circ$	0.026	0.045	0.080

TABLE 5.1: The MUSE range of $|Q^2|$ values for ep and μp scattering at the two limits of the laboratory frame scattering angle, namely, $\theta = 20^\circ$ and 100°, obtained from Eq. (5.2).

The finite (IR subtracted) part of the TPE fractional corrections $\bar{\delta}_{\gamma\gamma}$ up to and including next-to-leading order accuracy, i.e., $\mathcal{O}(\alpha, M^{-1})$, to the elastic scattering cross section is defined by:

$$\left[\frac{\mathrm{d}\sigma_{el}(Q^2)}{\mathrm{d}\Omega_l'}\right]_{\gamma\gamma} = \left[\frac{\mathrm{d}\sigma_{el}(Q^2)}{\mathrm{d}\Omega_l'}\right]_{\gamma} \bar{\delta}_{\gamma\gamma}(Q^2)\,, \tag{5.3}$$

where,

$$\bar{\delta}_{\gamma\gamma}(Q^2) = \frac{2\,\mathcal{R}e\sum_{spins}\left(\mathcal{M}_\gamma^\dagger\,\mathcal{M}_{\gamma\gamma;\mathrm{TPE}}\right)}{\sum_{spins}|\mathcal{M}_\gamma|^2} - \mathbf{IR}_{\gamma\gamma;\mathrm{TPE}}\,. \tag{5.4}$$

In this expression $\mathcal{M}_\gamma$ is the one-photon exchange (Born) amplitude,

$$\mathcal{M}_\gamma = -\frac{e^2}{Q^2}\left[\bar{u}_l(p')\gamma^\mu u_l(p)\right]\,\left[\chi^\dagger(p_p')v_\mu\chi(p_p)\right]\,, \tag{5.5}$$

and $\mathcal{M}_{\gamma\gamma;\mathrm{TPE}} = \mathcal{M}_{\gamma\gamma}^{(\mathrm{box})} + \mathcal{M}_{\mathrm{seagull}}^{(i)}$ is the total TPE amplitude obtained by summing the TPE box amplitudes, $\mathcal{M}_{\gamma\gamma}^{(\mathrm{box})}$, and the seagull amplitude, $\mathcal{M}_{\mathrm{seagull}}^{(i)}$, viz, Feynman diagrams (a) - (i) in Fig. [5.1]. The corresponding Born cross section is $(\mathrm{d}\sigma_{el}/\mathrm{d}\Omega_l')_\gamma$, which to LO in the chiral expansion (including phase space $1/M$ proton recoil contributions) is given by[3]

$$\begin{aligned}
\left[\frac{\mathrm{d}\sigma_{el}(Q^2)}{\mathrm{d}\Omega_l'}\right]_\gamma &= \frac{1}{64\pi^2M^2}\left(\frac{\beta'E'}{E}\right)\left[1+\frac{E}{M}(1-\cos\theta)\right]^{-1}\left(\frac{1}{4}\sum_{spins}|\mathcal{M}_\gamma|^2\right)\,; \\
\frac{1}{4}\sum_{spins}|\mathcal{M}_\gamma|^2 &= \frac{64\pi^2\alpha^2}{Q^4}MEE'(M+E_p')\left[1+\beta\beta'\cos\theta+\frac{m_l^2}{EE'}+\mathcal{O}\left(\frac{1}{M^2}\right)\right]\,,
\end{aligned} \tag{5.6}$$

[3]A more elaborate discussion on Born cross section can be found in the next chapter

where the kinematics at $1/M$ order accuracy yield the following relations:

$$\begin{aligned} E' &= E\left[1-\frac{\beta^2 E}{M}(1-\cos\theta)+\mathcal{O}\left(M^{-2}\right)\right], \\ \beta' &= \beta\left[1-\frac{(1-\beta^2)E}{M}(1-\cos\theta)+\mathcal{O}\left(M^{-2}\right)\right], \\ Q^2 &= -2\beta^2E^2(1-\cos\theta)\left[1-\frac{E}{M}(1-\cos\theta)+\mathcal{O}\left(M^{-2}\right)\right]. \end{aligned} \tag{5.7}$$

In Eq. (5.4), the term $\mathbf{IR}_{\gamma\gamma;\mathrm{TPE}}$ denotes the IR singular part of the TPE box diagrams' contribution to the elastic cross section. Utilizing dimensional regularization (DR) we project out these singularities before deriving the expression for $\mathbf{IR}_{\gamma\gamma;\mathrm{TPE}}$. As demonstrated in the next chapter, the soft bremsstrahlung contribution to the elastic cross section at NLO entails an IR singular term, $\mathbf{IR}_{\gamma\gamma^*}$, which cancels the IR singularity in Eq. (5.4), namely, $\mathbf{IR}_{\gamma\gamma^*} = -\mathbf{IR}_{\gamma\gamma;\mathrm{TPE}}$ at $\mathcal{O}(\alpha^3, M^{-1})$. Our calculations of the finite part of the fractional TPE contributions $\bar{\delta}_{\gamma\gamma}$ in Eq. (5.4) inherently rely on the widely used *soft photon approximation* (SPA). While the HBχPT evaluation details and discussion of the full QED radiative corrections to the ℓp elastic scattering at NLO will be presented in the next chapter, here we simply quote our analytical expression for $\mathbf{IR}_{\gamma\gamma^*}$:

$$\begin{aligned} \mathbf{IR}_{\gamma\gamma^*}(Q^2) &= -\frac{\alpha Q^2}{2\pi ME}\left\{\frac{1}{|\epsilon_{\mathrm{IR}}|}+\gamma_E-\ln\left(\frac{4\pi\mu^2}{-Q^2}\right)\right\}\left\{\frac{1}{\beta}\ln\sqrt{\frac{1+\beta}{1-\beta}}+\frac{E'}{E'\beta'}\ln\sqrt{\frac{1+\beta'}{1-\beta'}}\right\} \\ &= -\frac{\alpha Q^2}{\pi ME\beta}\left\{\frac{1}{|\epsilon_{\mathrm{IR}}|}+\gamma_E-\ln\left(\frac{4\pi\mu^2}{-Q^2}\right)\right\}\ln\sqrt{\frac{1+\beta}{1-\beta}}+\mathcal{O}\left(\frac{1}{M^2}\right). \end{aligned} \tag{5.8}$$

The TPE diagrams in Fig. [5.1] naturally include the contributions to the Coulomb wave functions describing the incoming and outgoing charged leptons. For example, the so-called "Coulomb focusing" or distortion of the scattered lepton spectrum at low-$|Q^2|$ is explained by considering one of the exchanged photons in the box diagrams as a soft photon.[4] The SPA has widely been used in the literature as a practical tool to isolate the IR singularities of the TPE box diagrams. However, the exact implementation of

[4]The Coulomb distortion of the outgoing electrons waves in the second Born approximation was investigated in Refs. [231, 232] (see also Figs. 13 and 17 of Ref. [22]) where it was found to significantly enhance the cross section at backward scattering angles. However, in this case the contribution to the proton's rms charge radius is unlikely to be affected from the extrapolation of the form factor data to extreme forward angles where Coulomb wave function effects are found to be small. Hence, the authors of Refs. [231, 232] concluded that the radius discrepancy could not have been been attributed to an erroneous experimental measurement due to the influence of this kind of SPA in the TPE contributions.

the SPA is somewhat *ad hoc* and differs in different theoretical works. For example, following the work of Maximon and Tjon [50], the SPA is used only in the denominator (propagators) of the integrand in order to single out the IR-divergent TPE amplitude, i.e., the momentum of the soft exchange photon is set to zero. Maximon and Tjon do not set the photon momentum to zero in the numerator of the integrand. On the other hand, following the work of Mo and Tsai [10], the SPA is used simultaneously in the numerator and denominator. As was noted in Ref. [50], the convenience of using the former "less drastic" type of approximation is that the resulting expressions become somewhat simpler. However, some authors, e.g., Ref. [230], have argued in favor of the latter "more drastic" approximation being more self-consistent. The essential point is to let the momenta associated with the soft photon go to zero, irrespective of whether they appear in the numerator or the denominator. Since these soft momentum factors, which appear in the numerator of the amplitudes, originate from those in the denominator, it seems somewhat unreasonable to let them go to zero *only* in the denominator. Concurring with the argument presented in Ref. [230], in the following we shall use the SPA definition of Mo and Tsai [10].

As shown in the Fig. [5.1](a)-(i), the loop integrals up to NLO in HBχPT contributing to the TPE amplitude $\mathcal{M}_{\gamma\gamma;\mathrm{TPE}}$ are, respectively, given by

$$i\mathcal{M}^{(a)}_{\mathrm{box}} = e^4 \int \frac{d^4k}{(2\pi)^4} \frac{\left[\bar{u}_l(p')\gamma^\mu(\not{p}' - \not{k} + m_l)\gamma^\nu u_l(p)\right]\left[\chi^\dagger(p'_p)v_\mu v_\nu \chi(p_p)\right]}{(k^2+i0)\left[(Q-k)^2+i0\right](k^2 - 2k\cdot p + i0)(v\cdot k + i0)} \tag{5.9}$$

$$i\mathcal{M}^{(b)}_{\mathrm{xbox}} = e^4 \int \frac{d^4k}{(2\pi)^4} \frac{\left[\bar{u}_l(p')\gamma^\mu(\not{p}' - \not{k} + m_l)\gamma^\nu u_l(p)\right]\left[\chi^\dagger(p'_p)v_\mu v_\nu \chi(p_p)\right]}{(k^2+i0)\left[(Q-k)^2+i0\right](k^2 - 2k\cdot p + i0)(-v\cdot k + i0)}\,, \tag{5.10}$$

$$i\mathcal{M}^{(c)}_{\mathrm{box}} = \frac{e^4}{2M} \int \frac{d^4k}{(2\pi)^4} \left[\bar{u}_l(p')\gamma^\mu(\not{p}' - \not{k} + m_l)\gamma^\nu u_l(p)\right] \times \frac{\left[\chi^\dagger(p'_p)\{v_\mu(2p_p + k)_\nu - v_\mu v_\nu (v\cdot k)\}\chi(p_p)\right]}{(k^2+i0)\left[(Q-k)^2+i0\right](k^2 - 2k\cdot p + i0)(v\cdot k + i0)}\,, \tag{5.11}$$

$$i\mathcal{M}^{(d)}_{\mathrm{xbox}} = \frac{e^4}{2M} \int \frac{d^4k}{(2\pi)^4} \left[\bar{u}_l(p')\gamma^\mu(\not{p}' - \not{k} + m_l)\gamma^\nu u_l(p)\right] \times \frac{\left[\chi^\dagger(p'_p)\{v_\nu(p_p + p'_p - k)_\mu - v_\mu v_\nu(-v\cdot k))\}\chi(p_p)\right]}{(k^2+i0)\left[(Q-k)^2+i0\right](k^2 - 2k\cdot p + i0)(-v\cdot k + i0)}\,, \tag{5.12}$$

$$i\mathcal{M}^{(e)}_{\rm box} = \frac{e^4}{2M}\int\frac{d^4k}{(2\pi)^4}\left[\bar{u}_l(p')\gamma^\mu(\not{p}-\not{k}+m_l)\gamma^\nu u_l(p)\right] \times\frac{\left[\chi^\dagger(p'_p)\{v_\nu(p_p+p'_p+k)_\mu - v_\mu v_\nu(v\cdot k)\}\chi(p_p)\right]}{(k^2+i0)\left[(Q-k)^2+i0\right](k^2-2k\cdot p+i0)\,(v\cdot k+i0)}\,, \tag{5.13}$$

$$i\mathcal{M}^{(f)}_{\rm xbox} = \frac{e^4}{2M}\int\frac{d^4k}{(2\pi)^4}\left[\bar{u}_l(p')\gamma^\mu(\not{p}-\not{k}+m_l)\gamma^\nu u_l(p)\right] \times\frac{\left[\chi^\dagger(p'_p)\{v_\mu(2p'_p-k)_\nu - v_\mu v_\nu(-v\cdot k))\}\chi(p_p)\right]}{(k^2+i0)\left[(Q-k)^2+i0\right](k^2-2k\cdot p+i0)\,(-v\cdot k+i0)}\,, \tag{5.14}$$

$$i\mathcal{M}^{(g)}_{\rm box} = \frac{e^4}{2M}\int\frac{d^4k}{(2\pi)^4}\frac{\left[\bar{u}_l(p')\gamma^\mu(\not{p}-\not{k}+m_l)\gamma^\nu u_l(p)\right]\,\left[\chi^\dagger(p'_p)v_\mu v_\nu\chi(p_p)\right]}{(k^2+i0)\left[(Q-k)^2+i0\right](k^2-2k\cdot p+i0)} \times\left(1+\frac{p_p^2}{(v\cdot k)^2}-\frac{(p_p+k)^2}{(v\cdot k)^2}\right), \tag{5.15}$$

$$i\mathcal{M}^{(h)}_{\rm xbox} = \frac{e^4}{2M}\int\frac{d^4k}{(2\pi)^4}\frac{\left[\bar{u}_l(p')\gamma^\mu(\not{p}-\not{k}+m_l)\gamma^\nu u_l(p)\right]\,\left[\chi^\dagger(p'_p)v_\mu v_\nu\chi(p_p)\right]}{(k^2+i0)\left[(Q-k)^2+i0\right](k^2-2k\cdot p+i0)} \times\left(1+\frac{p_p'^2}{(v\cdot k)^2}-\frac{(p'_p-k)^2}{(v\cdot k)^2}\right), \tag{5.16}$$

$$i\mathcal{M}^{(i)}_{\rm seagull} = \frac{2e^4}{2M}\int\frac{d^4k}{(2\pi)^4}\frac{\left[\bar{u}_l(p')\gamma^\mu(\not{p}-\not{k}+m_l)\gamma^\nu u_l(p)\right]\,\left[\chi^\dagger(p'_p)(v_\mu v_\nu-g_{\mu\nu})\chi(p_p)\right]}{(k^2+i0)\left[(Q-k)^2+i0\right](k^2-2k\cdot p+i0)}\,, \tag{5.17}$$

where $u_l(p)$ and $\bar{u}_l(p')$ are the incoming and outgoing lepton Dirac spinors, and, $\chi(p)$ and $\chi^\dagger(p'_p)$ are the proton's non-relativistic two-component Pauli spinors. Here we remark that the two LO TPE integrals, Eqs. (5.9) and (5.11), should contain the kinetic energy terms of $\mathcal{O}(M^{-1})$ in the proton propagators [cf. Eq. (5.1)]. However, for the purpose of distinguishing the "true" LO from the NLO parts of the integrals, these $\mathcal{O}(M^{-1})$ terms from the two LO amplitudes have been included in the NLO propagator insertion integrals, Eqs. (5.15) and (5.16), respectively. In that case the first two amplitudes, namely, $\mathcal{M}^{(a)}_{\rm box}$ and $\mathcal{M}^{(b)}_{\rm xbox}$, correspond to the "true" LO contribution of the TPE. All the rest contributing at NLO either correspond to terms that directly arise in the NLO chiral power counting or are attributed to the dynamical recoil $\mathcal{O}(M^{-1})$ terms moved from the LO chiral counting amplitudes. We isolate the IR divergences by taking the soft photon limit, which means: when one of the two photons' four-momenta is considered *soft* (either setting $k=0$ or $k=Q$) the other photon is *hard* (either with $(Q-k)^2\neq 0$ or $k^2\neq 0$). To project out the IR singular terms, we must evaluate the loop integrals at both poles and then consider their sum.

To demonstrate our SPA approach, let us apply it to the LO box, Eq. (5.9), and cross box, Eq. (5.11), amplitudes [cf. Figs. [5.1(a) & (b)]. Treating each of the two photons to be separately soft, leads to the following sum the amplitudes:

$$
\begin{aligned}
i\mathcal{M}^{(a)}_{\rm box} \overset{\gamma_{\rm soft}}{\rightsquigarrow} & -2e^2\,(v\cdot p)\,\mathcal{M}_\gamma \int \frac{d^4k}{(2\pi)^4}\frac{1}{k^2\,(k^2-2k\cdot p)\,(v\cdot k+i0)} \\
& -2e^2\,(v\cdot p')\,\mathcal{M}_\gamma \int \frac{d^4k}{(2\pi)^4}\frac{1}{k^2\,(k^2-2k\cdot p')\,(v\cdot k+i0)}\,,
\end{aligned}
\tag{5.18}
$$

and,

$$
\begin{aligned}
i\mathcal{M}^{(b)}_{\rm xbox} \overset{\gamma_{\rm soft}}{\rightsquigarrow} & \;2e^2\,(v\cdot p)\,\mathcal{M}_\gamma \int \frac{d^4k}{(2\pi)^4}\frac{1}{k^2\,(k^2-2k\cdot p)\,(v\cdot k-i0)} \\
& +2e^2\,(v\cdot p')\,\mathcal{M}_\gamma \int \frac{d^4k}{(2\pi)^4}\frac{1}{k^2\,(k^2-2k\cdot p')\,(v\cdot k-i0)}.
\end{aligned}
\tag{5.19}
$$

It is immediately clear that $\mathcal{M}^{(a)}_{\rm box}$ is effectively cancelled by $\mathcal{M}^{(b)}_{\rm xbox}$, although this cancellation still follow even without SPA for LO TPE amplitudes Eq. (5.9), and Eq. (5.11).[5] Thus, we conclude that there is no TPE contribution at LO in HBχPT. This LO cancellation is anticipated since the proton does not generate any LO bremsstrahlung in HBχPT, *vis-a-vis* no LO IR divergence contributions in $\delta^{(\rm soft)}_{\rm IR}$.

The first non-vanishing TPE contributions in SPA arise from the NLO proton recoil contributions, which is commensurate with the corresponding non-zero HBχPT bremsstrahlung amplitudes with the soft photons radiated from NLO proton-photon vertices. We now analyze the NLO TPE integrals, Eqs. (5.12)-(5.17), and the following observations are in order :

- First, when we sum these amplitudes, the terms containing the $v_\mu v_\nu$ in the amplitudes $\mathcal{M}^{(c)}_{\rm box}$ through $\mathcal{M}^{(f)}_{\rm box}$ cancel with the first terms of amplitudes $\mathcal{M}^{(g)}_{\rm box}$ and $\mathcal{M}^{(h)}_{\rm xbox}$ plus the $v_\mu v_\nu$ part of the seagull term $\mathcal{M}^{(i)}_{\rm seagull}$.

- Second, applying SPA to the remaining parts of the two amplitudes, $\mathcal{M}^{(g)}_{\rm box}$ and $\mathcal{M}^{(h)}_{\rm xbox}$, we observe that they also cancel in the soft photon limits. This is easily

[5] Note the difference in the signs of the $\pm i\eta \to \pm i0$ terms in the heavy proton propagators of the two amplitudes contributes to a residual imaginary part, which is, however, irrelevant in the present context of evaluation of the unpolarized cross section.

seen by analyzing the remaining parts of the NLO proton propagator in each of these integrals in following way:

$$
\begin{aligned}
i\left[\mathcal{M}^{(g)}_{\rm box}+\mathcal{M}^{(h)}_{\rm xbox}\right]_{\rm residual} &= \frac{e^4}{2M}\int\frac{d^4k}{(2\pi)^4}\cdots\left(\frac{p_p^2}{(v\cdot k)^2}-\frac{(p_p+k)^2}{(v\cdot k)^2}+\frac{p_p'^2}{(v\cdot k)^2}-\frac{(p_p'-k)^2}{(v\cdot k)^2}\right)\\
&\overset{\gamma_{\rm soft}}{\rightsquigarrow}\ \frac{e^4}{2M}\int\frac{d^4k}{(2\pi)^4}\cdots\left(\frac{\cancel{p_p^2}}{(v\cdot k)^2}-\frac{\cancel{p_p^2}}{(v\cdot k)^2}+\frac{\cancel{p_p'^2}}{(v\cdot k)^2}-\frac{\cancel{p_p'^2}}{(v\cdot k)^2}\right)_{k\to 0}\\
&\quad+\frac{e^4}{2M}\int\frac{d^4k}{(2\pi)^4}\cdots\left(\frac{\cancel{p_p^2}}{(v\cdot k)^2}-\frac{\cancel{p_p'^2}}{(v\cdot k)^2}+\frac{\cancel{p_p'^2}}{(v\cdot k)^2}-\frac{\cancel{p_p^2}}{(v\cdot k)^2}\right)_{k\to Q}\\
&= 0\,. \qquad (5.20)
\end{aligned}
$$

Consequently, applying SPA, the two amplitudes, $\mathcal{M}^{(g)}_{\rm box}$ and $\mathcal{M}^{(h)}_{\rm xbox}$, which are the amplitudes with intermediate NLO proton propagator insertions, effectively do not contribute to the sum of the NLO TPE box amplitudes. Furthermore, we observe that in the seagull amplitude, Eq. (5.17), only the terms proportional to $g_{\mu\nu}$ contribute to the total TPE amplitude. The residual parts of the TPE integrals at NLO, after applying SPA to the box diagrams, yield the following simplified soft photon amplitudes.[6]

$$
\begin{aligned}
i\widetilde{\mathcal{M}}^{(c)}_{\rm box} &= \frac{e^4}{M}(v\cdot p')\int\frac{d^4k}{(2\pi)^4}\frac{[\bar u_l(p')\gamma^\nu u_l(p)]\ [\chi^\dagger(p_p')(p_p+p_p')_\nu\chi(p_p)]}{k^2\,Q^2\,(k^2-2k\cdot p')\,(v\cdot k+i0)}\\
&\quad-\frac{2e^2}{M}(p\cdot p_p)\,\mathcal{M}_\gamma\int\frac{d^4k}{(2\pi)^4}\frac{1}{k^2\,(k^2-2k\cdot p+i0)\,(v\cdot k+i0)}\,, \qquad (5.21)\\
i\widetilde{\mathcal{M}}^{(d)}_{\rm xbox} &= -\frac{e^4}{M}(v\cdot p)\int\frac{d^4k}{(2\pi)^4}\frac{[\bar u_l(p')\gamma^\mu u_l(p)]\ [\chi^\dagger(p_p')(p_p+p_p')_\mu\chi(p_p)]}{k^2\,Q^2\,(k^2-2k\cdot p)\,(v\cdot k-i0)}\\
&\quad+\frac{2e^2}{M}(p'\cdot p_p)\,\mathcal{M}_\gamma\int\frac{d^4k}{(2\pi)^4}\frac{1}{k^2\,(k^2-2k\cdot p')\,(v\cdot k-i0)}\,, \qquad (5.22)\\
i\widetilde{\mathcal{M}}^{(e)}_{\rm box} &= \frac{e^4}{M}(v\cdot p)\int\frac{d^4k}{(2\pi)^4}\frac{[\bar u_l(p')\gamma^\mu u_l(p)]\ [\chi^\dagger(p_p')(p_p+p_p')_\mu\chi(p_p)]}{k^2\,Q^2\,(k^2-2k\cdot p)\,(v\cdot k+i0)}\\
&\quad-\frac{2e^2}{M}(p'\cdot p_p')\,\mathcal{M}_\gamma\int\frac{d^4k}{(2\pi)^4}\frac{1}{k^2\,(k^2-2k\cdot p')\,(v\cdot k+i0)}\,, \qquad (5.23)
\end{aligned}
$$

[6] We do not apply SPA in the evaluation of the IR-finite seagull diagram. A *naive* application of SPA to this diagram leads to lepton self-energy-like contributions with spurious IR-divergent terms. However, an exact evaluation (see Appendix B) shows no such singularities.

$$
\begin{aligned}
i\widetilde{\mathcal{M}}^{(f)}_{\rm xbox} &= -\frac{e^4}{M}(v\cdot p')\int\frac{d^4k}{(2\pi)^4}\frac{\left[\bar u_l(p')\gamma^\nu u_l(p)\right]\,\left[\chi^\dagger(p'_p)(p_p+p'_p)_\nu\chi(p_p)\right]}{k^2\,Q^2\,(k^2-2k\cdot p')\,(v\cdot k-i0)}\\
&\quad+\frac{2e^2}{M}(p\cdot p'_p)\,\mathcal{M}_\gamma\int\frac{d^4k}{(2\pi)^4}\frac{1}{k^2\,(k^2-2k\cdot p)\,(v\cdot k-i0)}\,, \qquad (5.24)\\
i\widetilde{\mathcal{M}}^{(i)}_{\rm seagull} &= -\frac{e^4}{M}\int\frac{d^4k}{(2\pi)^4}\frac{\left[\bar u_l(p')\gamma^\mu(\not p-\not k+m_l)\gamma_\mu u_l(p)\right]\,\left[\chi^\dagger(p'_p)\chi(p_p)\right]}{k^2\,(Q-k)^2\,(k^2-2k\cdot p+i0)}\,, \qquad (5.25)
\end{aligned}
$$

where the *tilde* symbols denote the residual NLO TPE amplitudes of Eqs. (5.12)-(5.17). Here we note again that there is a cancellation between $\widetilde{\mathcal{M}}^{(c)}_{\rm box}$ and $\widetilde{\mathcal{M}}^{(f)}_{\rm xbox}$ for the coefficient of $v\cdot p'$, and between $\widetilde{\mathcal{M}}^{(d)}_{\rm xbox}$ and $\widetilde{\mathcal{M}}^{(e)}_{\rm box}$ for the coefficient of $v\cdot p$ (up to an irrelevant imaginary part.) Then the resulting sum of the NLO TPE box amplitudes in the soft photon limit gets "factorized" into a Q^2 dependent function $f(Q^2)$ times the Born amplitude $\mathcal{M}_\gamma$ [68], namely,

$$
\mathcal{M}^{\rm (box)}_{\gamma\gamma}\ \overset{\gamma_{\rm soft}}{\rightsquigarrow}\ \widetilde{\mathcal{M}}^{\rm (box)}_{\gamma\gamma}\equiv f(Q^2)\mathcal{M}_\gamma=\widetilde{\mathcal{M}}^{(c)}_{\rm box}+\widetilde{\mathcal{M}}^{(d)}_{\rm xbox}+\widetilde{\mathcal{M}}^{(e)}_{\rm box}+\widetilde{\mathcal{M}}^{(f)}_{\rm xbox}\,, \qquad (5.26)
$$

where,

$$
f(Q^2)=-\frac{2e^2}{M}\Big[(p\cdot p_p)\mathcal{K}^{(+)}_v(p)-(p'\cdot p_p)\mathcal{K}^{(-)}_v(p')+(p'\cdot p'_p)\mathcal{K}^{(+)}_v(p')-(p\cdot p'_p)\mathcal{K}^{(-)}_v(p)\Big] \qquad (5.27)
$$

The integrals $\mathcal{K}^{(+)}_v$ and $\mathcal{K}^{(-)}_v$ are solved in d dimensions, i.e., $d>4$ is the analytically continued space-time dimension. In the expressions below, $|\epsilon_{\rm IR}|=-(4-d)/2$, μ corresponds to the subtraction scale, $\gamma_E=0.577216...$ is the Euler-Mascheroni constant, and the integrals $\mathcal{K}^{(\pm)}_v(p)$ in the above expression are given by

$$
\begin{aligned}
\mathcal{K}^{(+)}_v(p) &= \frac{1}{i}\int\frac{d^4k}{(2\pi)^4}\frac{1}{k^2(k^2-2k\cdot p)(v\cdot k+i0)}\\
&= \frac{1}{(4\pi)^2E\beta}\left[\left\{\frac{1}{|\epsilon_{\rm IR}|}+\gamma_E-\ln\left(\frac{4\pi\mu^2}{-Q^2}\right)\right\}\ln\sqrt{\frac{1+\beta}{1-\beta}}+\ln^2\sqrt{\frac{1+\beta}{1-\beta}}\right.\\
&\qquad\left.+{\rm Sp}\left(\frac{2\beta}{1+\beta}\right)-\frac{\pi^2}{2}-i\pi\left\{\frac{1}{|\epsilon_{\rm IR}|}+\gamma_E-\ln\left(\frac{\pi\mu^2}{E^2\beta^2}\right)\right\}\right]\,,\\
\mathcal{K}^{(-)}_v(p) &= \frac{1}{i}\int\frac{d^4k}{(2\pi)^4}\frac{1}{k^2(k^2-2k\cdot p)(v\cdot k-i0)}\\
&= \frac{1}{(4\pi)^2E\beta}\left[\left\{\frac{1}{|\epsilon_{\rm IR}|}+\gamma_E-\ln\left(\frac{4\pi\mu^2}{-Q^2}\right)\right\}\ln\sqrt{\frac{1+\beta}{1-\beta}}+\ln^2\sqrt{\frac{1+\beta}{1-\beta}}+{\rm Sp}\left(\frac{2\beta}{1+\beta}\right)\right]\,,
\end{aligned}
\qquad (5.28)
$$

where the term 'Sp' stands for the standard *Spence function* defined in Eq.(2.13). Likewise, we find the expression for the integrals $\mathcal{K}_v^{(\pm)}(p')$ in Eq. (5.27) by replacing $E \leftrightarrow E'$ and $\beta \leftrightarrow \beta'$. The IR divergences correspond to the poles in the dimensionally regularized integrals in the limit $\epsilon = -|\epsilon_{\rm IR}| = (4-D)/2 \to 0^-$. The appearance of an imaginary part in these integrals depends on the sign of the $\pm i\eta$ term as $\eta \to 0$ in the proton propagator. As mentioned, the imaginary parts are irrelevant in our present context of the unpolarized cross section analysis. Nevertheless, it might be interesting to note that an additional IR divergence arises in the imaginary part of $\mathcal{K}_v^{(+)}(p)$ which is of importance in a polarized cross section analysis.

Finally, we sum the TPE amplitudes and compute their interference with the Born amplitude in order to determine their contribution to the elastic cross section, with the appropriate IR singular term subtracted as shown in Eq. (5.4). To this end, the sum of the factorisable IR-divergent TPE box amplitudes with the non-factorisable IR-free seagull amplitude (evaluated in the Appendix B) is given as

$$\mathcal{M}_{\gamma\gamma;\rm TPE} = \widetilde{\mathcal{M}}^{(\rm box)}_{\gamma\gamma} + \widetilde{\mathcal{M}}^{(i)}_{\rm seagull} = f(Q^2)\mathcal{M}_\gamma + \widetilde{\mathcal{M}}^{(i)}_{\rm seagull}\,. \tag{5.29}$$

Denoting the corresponding fractional TPE contributions to the elastic cross section as

$$\delta_{\gamma\gamma}(Q^2) = \delta^{(\rm box)}_{\gamma\gamma}(Q^2) + \delta^{(\rm seagull)}_{\gamma\gamma}(Q^2)\,, \tag{5.30}$$

we obtain the following NLO expressions,[7] noting that $E' = E + \mathcal{O}(M^{-1})$ and $\beta' = \beta + \mathcal{O}(M^{-1})$:

$$\begin{aligned}
\delta^{(\rm box)}_{\gamma\gamma}(Q^2) &= \frac{2\mathcal{R}e\sum_{spins}\left(\mathcal{M}^\dagger_\gamma\,\widetilde{\mathcal{M}}^{(\rm box)}_{\gamma\gamma}\right)}{\sum_{spins}|\mathcal{M}_\gamma|^2} = 2\mathcal{R}e[f(Q^2)] \\
&= \frac{\alpha Q^2}{2\pi ME}\left[\left\{\frac{1}{|\epsilon_{\rm IR}|} + \gamma_E - \ln\left(\frac{4\pi\mu^2}{-Q^2}\right)\right\}\left\{\frac{1}{\beta}\ln\sqrt{\frac{1+\beta}{1-\beta}} + \frac{E}{E'\beta'}\ln\sqrt{\frac{1+\beta'}{1-\beta'}}\right\}\right. \\
&\quad -\frac{1}{\beta}\left\{\frac{\pi^2}{2} - \ln^2\sqrt{\frac{1+\beta}{1-\beta}} - {\rm Sp}\left(\frac{2\beta}{1+\beta}\right)\right\} - \frac{E}{E'\beta'}\left\{\frac{\pi^2}{2} - \ln^2\sqrt{\frac{1+\beta'}{1-\beta'}}\right. \\
&\quad \left.\left.-{\rm Sp}\left(\frac{2\beta'}{1+\beta'}\right)\right\}\right]
\end{aligned}$$

[7] Since the corrections in Eqs. (5.31) and (5.32) originate at NLO, we use the LO expression for the four-momentum transferred, i.e., $Q^2 \to Q_0^2 = -2\beta^2E^2(1-\cos\theta)$.

$$= \mathbf{IR}_{\gamma\gamma;\mathrm{TPE}} - \frac{\alpha Q^2}{\pi M E \beta}\left[\frac{\pi^2}{2} + \ln\left(\frac{-Q^2}{m_l^2}\right)\ln\sqrt{\frac{1+\beta}{1-\beta}} - \ln^2\sqrt{\frac{1+\beta}{1-\beta}} - \mathrm{Sp}\left(\frac{2\beta}{1+\beta}\right)\right] + \mathcal{O}\left(\frac{1}{M^2}\right), \tag{5.31}$$

for the TPE box contribution, with $\mathbf{IR}_{\gamma\gamma;\mathrm{TPE}} = -\mathbf{IR}_{\gamma\gamma^*}$ as given in Eq. (5.8), and the finite seagull contribution

$$\begin{aligned}\delta_{\gamma\gamma}^{(\mathrm{seagull})}(Q^2) &= \frac{2\mathcal{R}e\sum_{spin}\left(\mathcal{M}_\gamma^\dagger\,\widetilde{\mathcal{M}}_{\mathrm{seagull}}^{(i)}\right)}{\sum_{spin}|\mathcal{M}_\gamma|^2} \\ &= -\frac{2\alpha Q^2}{\pi M E}\left[\frac{E^2+EE'}{Q^2+4EE'}\right]\left(\mathcal{I}_1(Q^2)+\mathcal{I}_2(Q^2)+\frac{Q^2}{m_l^2}\left[\mathcal{I}_3(Q^2)-\mathcal{I}_4(Q^2)\right]\right) \\ &= -\frac{4\alpha Q^2}{\pi M E}\left[\frac{E^2}{Q^2+4E^2}\right]\left(\mathcal{I}_1(Q^2)+\mathcal{I}_2(Q^2)+\frac{Q^2}{m_l^2}\left[\mathcal{I}_3(Q^2)-\mathcal{I}_4(Q^2)\right]\right)+\mathcal{O}\left(\frac{1}{M^2}\right).\end{aligned} \tag{5.32}$$

The integrals $\mathcal{I}_i$ $(i = 1-4)$ are presented in Appendix B where we evaluate the seagull term. We subsequently use Eq. (5.4) to obtain the finite fractional TPE contribution in SPA, namely, $\bar{\delta}_{\gamma\gamma} = \delta_{\gamma\gamma}^{(\mathrm{box})} - \mathbf{IR}_{\gamma\gamma;\mathrm{TPE}} + \delta_{\gamma\gamma}^{(\mathrm{seagull})}$.

5.4 Calculations and Results

Next we present numerical estimates of the analytically derived expressions for the box and seagull TPE contributions obtained in the previous section. Fig. [5.2] displays our results showing the dependence of the finite fractional TPE corrections, $\bar{\delta}_{\gamma\gamma}$, of the ep and μp elastic scattering versus the squared four-momentum transfer at $\mathcal{O}(\alpha, M^{-1})$. The results displayed in figure indicate that the TPE corrections for electron-proton scattering goes up to about 4.5% and that for the muon-proton scattering up to around 0.5 % for the largest MUSE incoming momentum. As anticipated from recent TPE works, e.g., Refs. [22, 225, 230], our TPE contributions are vanishing when Q^2 becomes zero.[8] As

[8]It may be noted that in Ref. [230] a direct evaluation of the TPE (c.f. Eq. (20) of this reference) leads to a non-zero contribution at $Q^2 = 0$, and hence, needed to be shifted by a constant factor to provide physical justification of vanishing asymmetry at $Q^2 = 0$. However, we checked that an expansion of their Eq. (20) to $\mathcal{O}(1/M)$ indeed vanishes at $Q^2 = 0$.

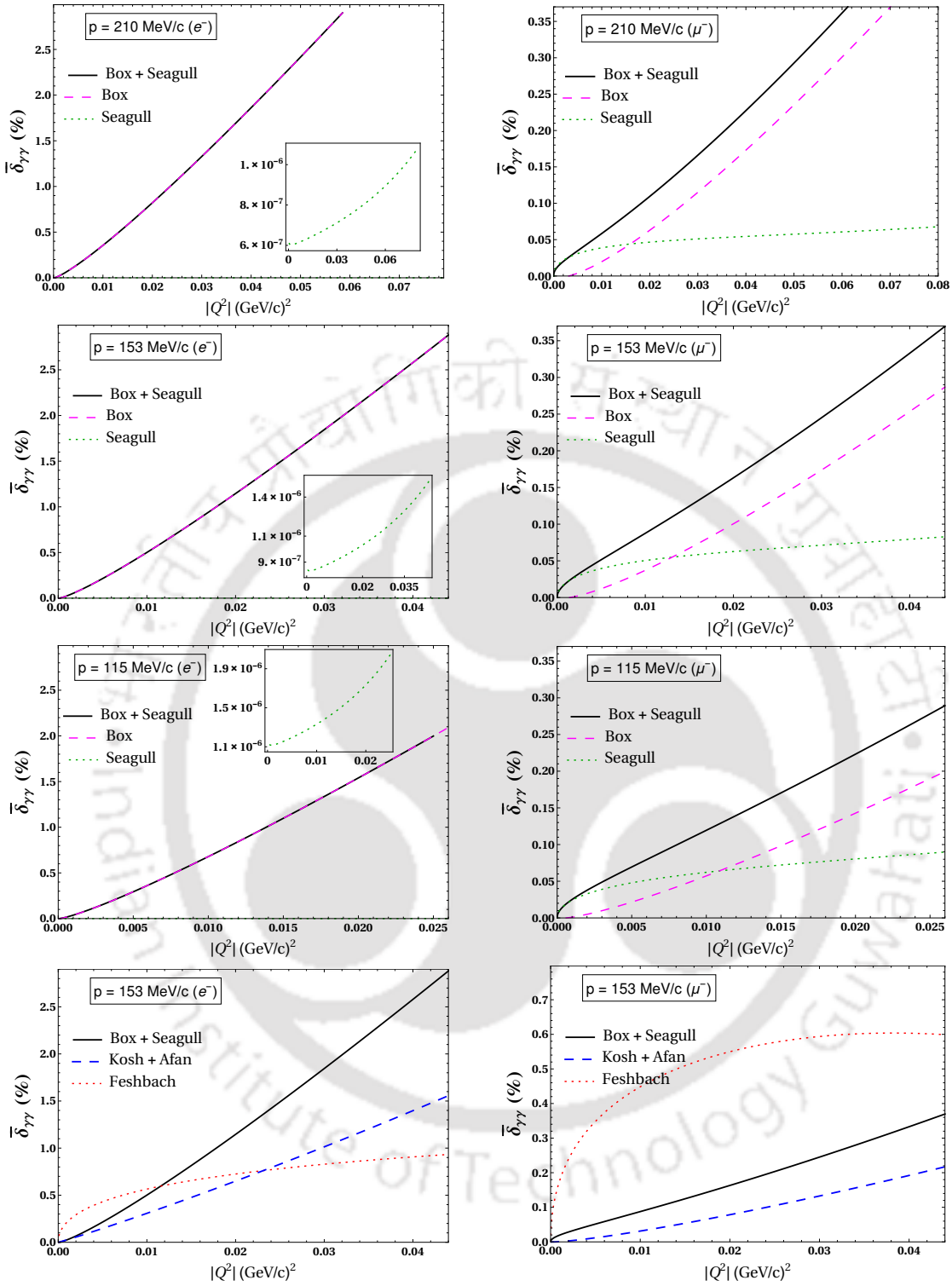

FIGURE 5.2: Comparison of the finite TPE contributions for the box and seagull diagrams to the ep (left panel) and μp (right panel) elastic scattering cross sections as a function of the squared four-momentum transfer $|Q^2|$ given at the three proposed MUSE incoming lepton momenta, namely, 210 MeV/c, 153 MeV/c and 115 MeV/c. The seagull contributions for the ep scattering, being numerically much smaller, are shown within the inset plots. The plots in the bottom panel (4^{th} row) show the comparison of our results (for incoming lepton momentum, $p = 153$ MeV/c) with the qualitatively similar TPE results from the recent relativistic hadronic model calculation of Ref. [230] (labelled as "Kosh + Afan"). The contribution of the Feshbach term of Ref. [222] (labelled as "Feshbach") is also displayed.

observed in the figure, the TPE contributions for electron-proton scattering are about an order of magnitude larger than for muon-proton scattering. At a given $|Q^2|$ and for increasing incident MUSE lepton momenta, $\bar{\delta}_{\gamma\gamma}$ becomes smaller but the relative electron-proton to muon-proton ratio for $\bar{\delta}_{\gamma\gamma}$ stay almost the same. In Fig. [5.2] we also compare our evaluations of the TPE box, $\bar{\delta}_{\gamma\gamma}^{(\mathrm{box})}$, and the seagull, $\delta_{\gamma\gamma}^{(\mathrm{seagull})}$, contributions. Here we note that in relativistic QED the TPE box diagrams give the TPE amplitude, whereas in HBχPT the baryons being treated non-relativistically, the seagull diagram naturally appears. In this case, the magnitude of the finite seagull contribution is found to be quite insensitive to the Q^2 dependence except when $Q^2 \to 0$. For electron-proton scattering, the seagull contribution is more or less inconsequential yielding a minuscule contribution, i.e., $\sim 10^{-6}$ % for the range of MUSE kinematics, while for the muon-proton scattering its contribution is much larger going up to about 0.06 %. The TPE box diagrams, however, mostly dominate the entire MUSE range of momentum transfers. An exception only occurs for muon-proton scattering in the region, $Q^2 \lesssim 0.01$ (GeV/c)^2, where our result indicates that the seagull terms become numerically larger than the box contributions.

The TPE results of Ref. [230], which we label as "Kosh + Afan", are compared with our evaluations in the bottom panels of Fig. [5.2], when we adjust their expressions to reflect our IR treatment of the TPE amplitude. To be specific, in the method used for comparing the TPE results, we consider only the relevant finite part of their TPE result (c.f. Eq. (20) in Ref. [230]), leaving out the IR singular terms which must cancel against those from soft bremsstrahlung. In our notation Eq. (20) of Ref. [230] for the TPE (adjusted by a constant factor such that it vanishes at $Q^2 = 0$) in the SPA is written as follows:

$$\begin{aligned}\bar{\delta}_{\gamma\gamma}(Q^2)\Big|_{\text{Ref. [57]}} = -\frac{\alpha}{\pi}\Bigg[-\frac{b_{11}}{\gamma_{11}}\Bigg\{\ln\left(\frac{-Q^2}{m_l M}\right) + \frac{1}{2}\ln\alpha_{12}\cdot\ln\left(\frac{4\gamma_{11}^2}{m_l^4\alpha_{11}(1-\alpha_{11})^2}\right) \\ + \mathrm{Sp}\left(\frac{\alpha_{11}(m_l^2 - b_{11} + M^2)}{2\gamma_{11}(1-\alpha_{11})}\right) - \mathrm{Sp}\left(\frac{m_l^2 - b_{11} + M^2}{2\gamma_{11}(1-\alpha_{11})}\right)\Bigg\} \\ + \frac{b_{12}}{\gamma_{12}}\Bigg\{\ln\left(\frac{-Q^2}{m_l M}\right) + \frac{1}{2}\ln\alpha_{12}\cdot\ln\left(\frac{4\gamma_{12}^2}{m_l^4\alpha_{12}(1-\alpha_{12})^2}\right) \\ + \mathrm{Sp}\left(\frac{\alpha_{12}(m_l^2 - b_{12} + M^2)}{2\gamma_{12}(1-\alpha_{12})}\right) - \mathrm{Sp}\left(\frac{m_l^2 - b_{12} + M^2}{2\gamma_{12}(1-\alpha_{12})}\right)\Bigg\}\Bigg]\,,\end{aligned} \tag{5.33}$$

where

$$\begin{aligned} b_{11} &= 2EM \quad , \quad b_{12} = Q^2 + b_{11}\,, \\ \alpha_{11} &= \frac{b_{11}+2\gamma_{11}}{2m_l^2} \quad , \quad \gamma_{11} = \frac{1}{2}\sqrt{b_{11}^2 - 4m_l^2M^2}\,, \\ \alpha_{12} &= \frac{b_{12}+2\gamma_{12}}{2m_l^2} \quad , \quad \gamma_{12} = \frac{1}{2}\sqrt{b_{12}^2 - 4m_l^2M^2}\,. \end{aligned} \tag{5.34}$$

In order to facilitate the comparison with our dimensionally regularized TPE expression $\bar{\delta}_{\gamma\gamma}(Q^2)$ [cf. Eqs. (5.4), (5.31) and (5.32)] we modify their analytically regularized IR singular terms proportional to $\ln\lambda^2$, where λ is a fictitious photon mass, in the following way:

$$\ln\left(\frac{\lambda^2}{m_l M}\right) \mapsto \ln\left(\frac{-Q^2}{m_l M}\right) + \ln\left(\frac{\lambda^2}{-Q^2}\right)\,. \tag{5.35}$$

Note that the IR-divergent terms proportional to $\ln\lambda^2$ for the TPE correction gets canceled by similar IR terms from soft photon bremsstrahlung process leading to their finite expression, Eq. (38) in Ref. [230]. We observe in Fig. [5.2] that the overall low-$|Q^2|$ behavior of our TPE contributions is roughly consistent with Ref. [230] SPA results which are based on the use of relativistic point-like (Dirac) protons. Nevertheless, despite the apparent qualitative similarity, our total TPE contribution differs in magnitude roughly by about a factor of two from that in Ref. [230]. Moreover, we note that our results substantially differ from the results of another recent TPE work, Ref. [225], which evaluated the box diagrams for muon-proton scattering using a relativistic hadronic model. However, unlike Ref. [230] and our work, the authors of Ref. [225] did not employ SPA in their calculations, and instead numerically evaluated the TPE amplitudes involving the so-called *four-point integrals* [233, 234] and their derivatives. In addition, they isolated the IR singular terms analytically from their TPE amplitude according to the Maximon and Tjon prescription [50]. The significant difference of our TPE correction as well as the results of Ref. [230] from those in Ref. [225] may imply that a part of the TPE box diagram loop integration involves contributions from two "hard" photon exchanges in muon-proton scattering. This is precisely the integration region of these TPE loops excluded in SPA.

Furthermore, in Fig. [5.2] we compare our TPE results with the Coulomb potential scattering result in the second Born approximation by McKinley and Feshbach [222], labelled "Feshbach" in the figure. As shown in Refs. [225, 229], the relativistic evaluation of the TPE diagrams for a point-like Dirac proton without SPA are qualitatively very similar to the Feshbach contribution for muon-proton scattering. Nevertheless, it may be worth noting that the original Feshbach derivation is applicable only for ultra-relativistic electrons. As seen in Fig. [5.2] for the electron-proton scattering, our results as well as those in Ref. [230] are comparable to the Feshbach term for low-$|Q^2|$ values, thereby indicating that the "hard" photon TPE loop contributions might not be too important for electron-proton scattering.

It is also instructive to study the TPE dependence on the virtual photon "polarization" flux factor ε which may be expressed in terms of the four-momentum transfer Q^2 by the relation [225]

$$\varepsilon(Q^2) = \frac{16\,\widetilde{\nu}^{\,2} + Q^2(4M^2 - Q^2)}{16\,\widetilde{\nu}^{\,2} - (4M^2 - Q^2)(4m_l^2 + Q^2)}\,, \tag{5.36}$$

where $\widetilde{\nu} = (s-u)/4 = (4EM+Q^2)/4$ is the crossing symmetric variable in the target rest frame. For fixed incident lepton beam momenta, the full kinematically allowed elastic scattering range, namely, $0 < \theta < \pi$ and $0 < |Q^2| < |Q^2_{\rm max}|$ [cf. below Eq. (5.2)], yields the physical bound on the flux factor, namely, $\varepsilon_{\rm max} > \varepsilon > \varepsilon_{\rm min}$, where

$$\begin{aligned} \varepsilon_{\rm max} &\equiv \varepsilon(0) = \frac{1}{\beta^2}\,, \\ \varepsilon_{\rm min} &\equiv \varepsilon(Q^2_{\rm max}) = \frac{m_l^2(m_l^2 + M^2 + 2EM)}{2\beta^2 E^2 M^2}\,. \end{aligned} \tag{5.37}$$

While for fixed four-momentum transfers, if $|Q^2| > 2m_l^2$, then $2m_l^2/|Q^2| < \varepsilon < 1$, and if $|Q^2| < 2m_l^2$, then $1 < \varepsilon < 2m_l^2/|Q^2|$. The critical case, $|Q^2| = |Q^2_{\rm crit}| = 2m_l^2$ correspond to $\varepsilon = 1$ for all possible incoming lepton momenta. It is worth noting that for the massless lepton case, ε may be interpreted as the longitudinal polarization of the photon in case of one-photon exchange [225]. Fig. [5.3] displays the $|Q^2|$ dependence of ε for ep and μp elastic scatterings. The figure identifies both the kinematically allowed and the relevant MUSE range of ε values. Correspondingly, Fig. [5.4] displays the ε dependence of our TPE corrections for three specific choices of $|Q^2|$, namely, 0.005 $(\text{GeV/c})^2$, 0.01

$(\mathrm{GeV/c})^2$ and 0.02 $(\mathrm{GeV/c})^2$. In each case of fixed $|Q^2|$ the TPE effects vanish as $\varepsilon \to 1$, i.e., the forward scattering limit, and tend towards maximum as $\varepsilon \to 2m_l^2/|Q^2|$ for backward scatterings [22], as reflected in Fig. [5.4]. This feature of our TPE result is again qualitatively similar to the result obtained in Ref. [230][9], but contrasts sharply with the Feshbach result [222] as well as that of Ref. [225].

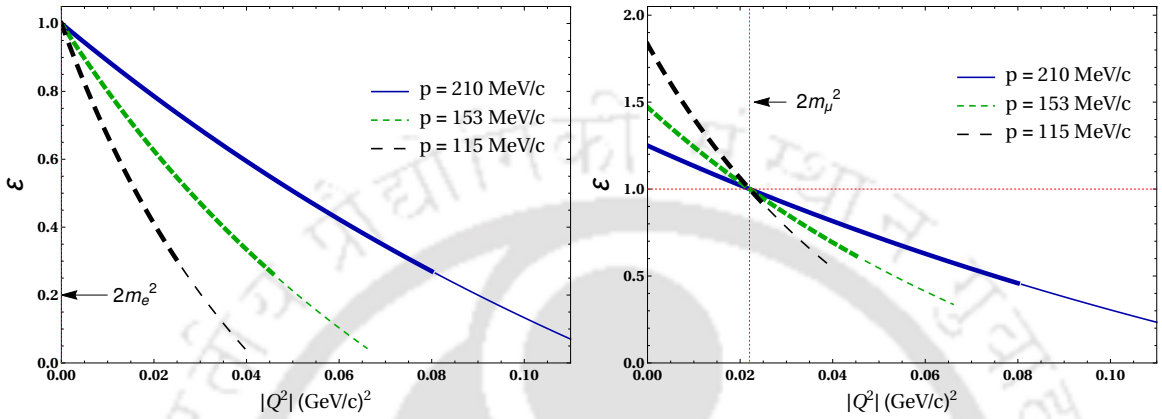

FIGURE 5.3: The dependence of the virtual photon "polarization" factor ε on the squared four-momentum transfer $|Q^2|$ for the proposed MUSE beam momenta for ep scattering (upper panel) and μp scattering (lower panel.) Each plot corresponds to the full kinematically allowed scattering range $0 < |Q^2| < |Q^2_{\mathrm{max}}|$ when $\theta \in [0, \pi]$ (thin lines). The thick lines are associated with the MUSE kinematic range where $\theta \in [20^\circ, 100^\circ]$. The curves intersect at $\varepsilon = 1$, which correspond to the critical values, $|Q^2_{\mathrm{crit}}| = 2m_e^2 = 5 \times 10^{-7}$ $(\mathrm{GeV/c})^2$ and $|Q^2_{\mathrm{crit}}| = 2m_\mu^2 = 0.02205$ $(\mathrm{GeV/c})^2$.

5.5 Conclusion

In this chapter we presented a low-energy model-independent calculation of the two-photon exchange contributions to the lepton-proton elastic unpolarized cross section at next-to-leading order in HBχPT. The lepton mass is included in all our expressions. Our approach contrasts many previous TPE evaluations using relativistic hadronic models which often use phenomenological form factors to parametrize the proton-photon vertices. In HBχPT the heavy proton is treated in a manifestly non-relativistic framework which makes it ideal for investigating the structure of the proton at very low momentum transfers. Our evaluation is based on the assumption that the most dominant contributions to the TPE loop diagrams arise from the elastic proton intermediate state while

[9]Here the disagreement with our result is understandable as they have used a fully relativistic model calculation utilizing proton's Dirac and Pauli form factors $F^p_{1,2}(Q^2)$ in their calculations. In our NLO χPT calculations, the proton's structure effects does not enter since pion-loop contributions count as $\mathcal{O}(1/M^2)$. The resulting difference perhaps hints the need to include the NNLO contributions to our existing results presented in this chapter.

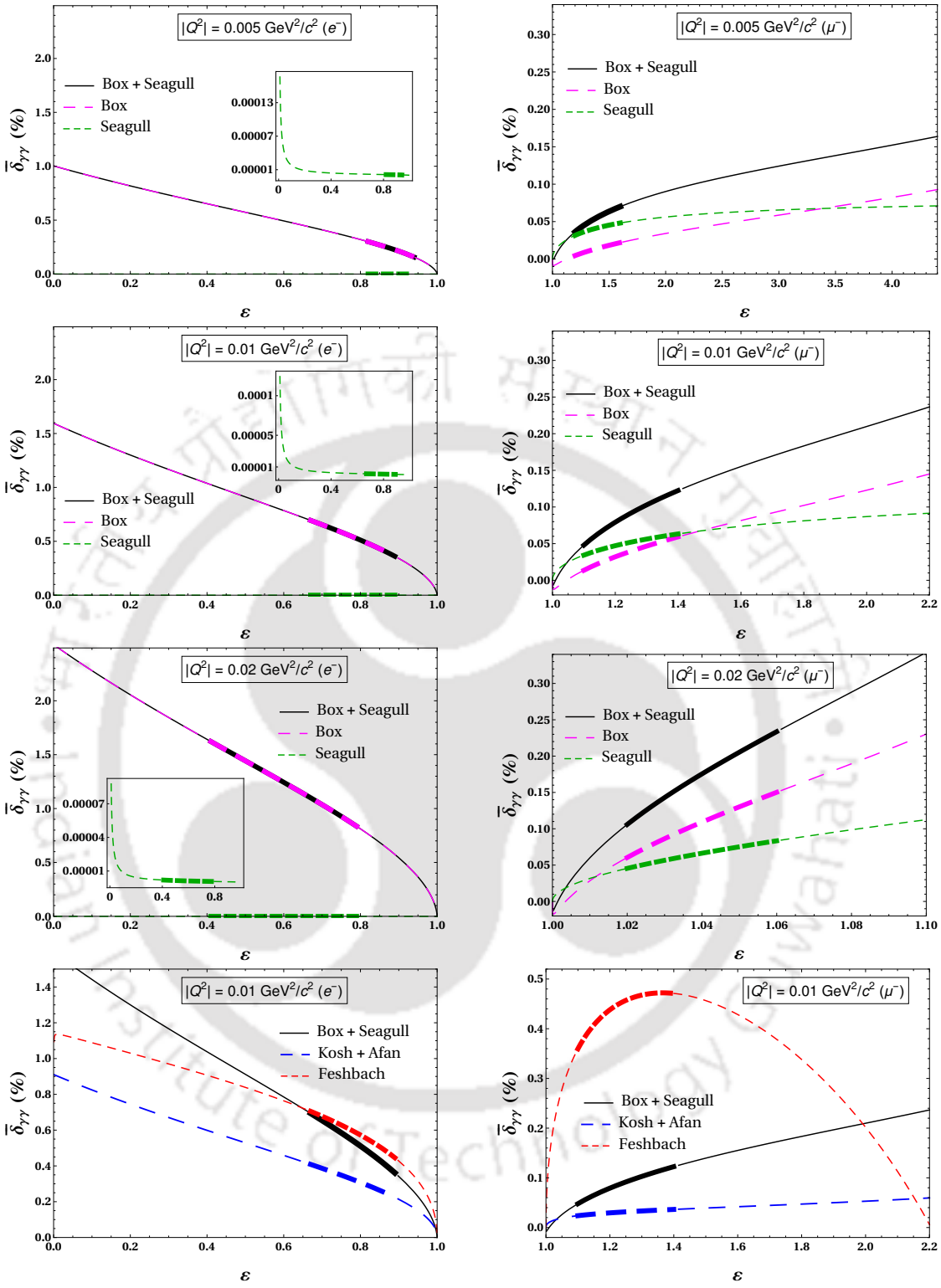

FIGURE 5.4: The ε dependence of the finite TPE contributions for ep (left panel) and μp (right panel) elastic cross sections for three specific $|Q^2|$ values in the proposed MUSE kinematic range. The seagull contributions for the ep scattering being numerically much smaller are shown within the inset plots. The plots in the bottom panel (4^{th} row) shows the comparison of our results for $|Q^2| = 0.01$ (GeV/c)^2 with the qualitatively similar results from Ref. [230] (labelled as "Kosh + Afan".) The contribution of the Feshbach term [222] (labelled as "Feshbach") is also displayed. Each plot corresponds to the kinematically allowed range of ε when $\theta \in [0, \pi]$ (thin lines), and the 'segment' relevant to the MUSE kinematic range with $\theta \in [20°, 100°]$ (thick lines).

inelastic contributions are considered small for low-$|Q^2|$ values. This is especially relevant in the proposed low-energy MUSE kinematic domain where incoming lepton beam momenta are between $p = |\vec{p}| = 115 - 210$ MeV/c. We note that while most other works use analytic regularization schemes with a non-zero photon mass, we used the gauge invariant prescription of dimensional regularization scheme to isolate the infrared singularities of the TPE loops diagrams. In this approach, however, the exact evaluation of the IR-divergent four-point one-loop Green's function [233, 234] demands analytical evaluations of D-dimensional integrals which to the best of our knowledge has not been pursued for exchanges of massless photons. Further, we demonstrated in Sec. 5.3 that the soft photon limit was taken only after the cancellations among the NLO amplitudes were taken into account. Moreover, one should bear in mind that we restricted the soft photon approximation only to the IR-divergent diagrams. Thus, we evaluated the IR-free seagull diagram without invoking the soft photon approximation.

The evaluation of the TPE box diagrams (with exchange bosons with non-zero masses) involves scalar and tensor four-point loop integrals, a topic that has been discussed extensively in many previous works, e.g., Refs. [233–237]. In the pioneering works of Refs. [233, 234], such tensor integrals were reduced to scalar one-loop *master* integrals involving one-, two-, three- and four-point functions which were evaluated analytically using the dimensional regularization scheme. The work of Ref. [237] extended the above formalism to include heavy-fermion propagators. However, these approaches are unsuitable for dealing with IR divergences using dimensional regularization with massless photon exchanges. In fact, for massless photon exchanges the exact analytical evaluation of the IR-divergent four-point functions in dimensional regularization remains an open issue. Nevertheless, using dimensional regularization with the soft photon approximation provides a viable alternative for the reduction of the four-point scalar integrals into well-known standard ones. This approximation allows us to easily project out the IR-divergent parts of the TPE box diagrams in order to obtain a finite contribution to the elastic cross section. In the soft photon limit the four-point loop integral reduces to a three-point integrals which can be evaluated analytically, wherein each of the TPE loop momentum, $0 \leq (k_0, |\mathbf{k}|) \leq \infty$, can be decomposed as a sum of two integrals each with a

hard and a soft photon. The contributions from two simultaneous hard photon exchanges are ignored in the soft photon limit.

The results for the electron-proton scattering seem to indicate that the dominant contribution from the TPE loop momenta are expected to arise from the integration domain where the contribution of the two hard photon exchanges may give small contributions. In contrast, it appears that for muon-proton scattering the hard two-photon exchange part of the TPE loops could give significant contributions. This conclusion is based on a comparison with the muon-proton scattering analysis presented in Ref. [229] (c.f. Fig. 2 of this reference), where the TPE amplitude was evaluated relativistically with point-like protons. This may indicate the importance of including two hard photon exchanges even in very low-energy muon-proton scattering for a more robust estimation of the TPE contribution.

In conclusion, we demonstrated in this chapter many cancellations among the NLO box and seagull diagrams, which are likely to remain approximately valid beyond SPA. Furthermore, we showed that while the LO TPE contributions vanish (up to an irrelevant imaginary part), the dominant TPE effects arise from the box diagrams with NLO proton-photon vertices except at very low-$|Q^2|$ values where the finite seagull terms become significantly large for muon-proton scattering. However, the seagull diagram gives only a tiny contribution for electron-proton scattering at MUSE energies. We find that the low-$|Q^2|$ behavior of our TPE contributions are in rough agreement with the results in Ref. [230], although they differ substantially from those in Ref. [225]. In the next chapter we will include all the virtual one loop diagrams along with TPE and also the soft bremsstrahlung up to NLO in HBχPT in our radiative analysis program.

Chapter 6

Total Radiative Corrections

6.1 Introduction

In this chapter, we present a complete one-loop radiative correction analysis to unpolarized ℓ-p scattering cross section, including all the one-loop virtual as well as soft bremsstrahlung contributions up to NLO in HBχPT. In the fourth and the fifth chapters, we have seen that the bremsstrahlung and the TPE amplitudes diverge in the vanishing limit of the photon momenta, *vis-a-vis*, IR divergences. Here we demonstrate how these IR-divergent terms systematically cancel between the one-loop virtual photon diagrams, namely, the self-energy, vertex and TPE corrections, and the corresponding soft photon bremsstrahlung diagrams. The general methodology described in this chapter was originally developed in the seminal work of Ref. [151] in the context of pure QED processes with relativistic point-like Dirac particles. Radiative corrections to the basic cross section at the one-loop level in QED are $\mathcal{O}(\alpha)$ suppressed compared to the tree-level terms consisting of an additional real or virtual photon emission or absorption by both the proton and lepton. In our context of HBχPT we also need to deal with the low-energy non-relativistic strong dynamics of the proton incorporating chiral symmetry. This is reflected in the power counting scheme which incorporates a simultaneous expansion in the QED coupling α, along with a *chiral expansion* in powers of the generic small external three-momentum $|\vec{P}|$ of the proton over the hard scale, $\Lambda_\chi \simeq 1$ GeV, and an additional

recoil expansion organized in powers of $|\vec{P}|$ over the "heavy" proton's mass M, namely,

$$\frac{|\vec{P}|}{\Lambda_\chi} \sim \frac{|\vec{P}|}{M}.$$

Thus, tree amplitudes of $\mathcal{O}(e^2)$ are counted as LO terms in HBχPT and distinguished from the corresponding $\mathcal{O}\left(e^2, \frac{1}{M}\right)$ "recoil amplitudes" counted as NLO in the chiral expansion. Likewise, the radiative one-loop amplitudes of $\mathcal{O}(e^4)$ are considered LO in HBχPT and the corresponding $\mathcal{O}\left(e^4, \frac{1}{M}\right)$ recoil amplitudes are counted as NLO. Moreover, to render the radiative corrections IR-finite, we also need to deal with LO and NLO soft photon bremsstrahlung diagrams of $\mathcal{O}(e^3)$ and $\mathcal{O}\left(e^3, \frac{1}{M}\right)$, respectively, in equal footings with respect to the virtual diagrams. In the ensuing analysis below, the leading radiative corrections at the leading chiral order shall be denoted by the superscript index "(0)", while those at the subleading chiral order shall be denoted by the superscript "(1)". Thus, the complete leading radiative correction [i.e., $\mathcal{O}(\alpha)$] to the *one-photon exchange* (OPE) or the Born elastic cross section due to the one-loop virtual contributions are represented as $\delta^{(0)}_{\gamma\gamma}$ and $\delta^{(1)}_{\gamma\gamma}$, and those due to the real soft photon emissions are represented as $\delta^{(0)}_{\gamma\gamma^*}$ and $\delta^{(1)}_{\gamma\gamma^*}$. In other words, the total fractional radiative corrections are given by,

$$\begin{aligned} \delta^{(0)}_{2\gamma} &= \delta^{(0)}_{\gamma\gamma} + \delta^{(0)}_{\gamma\gamma^*} \quad \text{(LO in HB}\chi\text{PT)}\,, \\ \delta^{(1)}_{2\gamma} &= \delta^{(1)}_{\gamma\gamma} + \delta^{(1)}_{\gamma\gamma^*} \quad \text{(NLO in HB}\chi\text{PT)}\,, \end{aligned} \tag{6.1}$$

respectively. Then, the complete fractional $\mathcal{O}(\alpha)$ radiative and recoil correction to the ℓ-p elastic cross section *up-to-and-including* NLO in HBχPT can be expressed as

$$\delta_{2\gamma} = \delta^{(0)}_{2\gamma} + \delta^{(1)}_{2\gamma}\ ; \quad \delta^{(0)}_{2\gamma} \sim \mathcal{O}(\alpha)\,, \quad \delta^{(1)}_{2\gamma} \sim \mathcal{O}\left(\alpha, \frac{1}{M}\right)\,. \tag{6.2}$$

As discussed in Chapter 2, the real photon radiation can be identified as either being soft or hard compared to some frame dependent arbitrarily small value of a reference energy scale of the outgoing lepton ΔE, that can be practically associated with the upper limit of integration of the undetected *soft* photon energy[1] in determining the bremsstrahlung

[1]For the present purpose of radiative correction analysis for the ℓ-p elastic scattering process, we shall address only the *soft* photons whose energies lie below some frame dependent threshold value Δ_S, while the *hard* photons with energies above this threshold will not be considered. Since all these soft photons

cross section. In particular, by adopting to the dynamics of the so-called S-frame, where the integration over the photon emission angle becomes almost trivial, and as shown in the Appendix D, the integration limit, $\Delta E = \Delta_S$, could finally be related to the *lab*-frame frame detector acceptance Δ^*_γ, namely, $\Delta_S \simeq \eta\Delta^*_\gamma$ [10, 50, 139], where $\eta = E/E'^{el}$ is the *lab*-frame proton recoil factor and given as the ratio of the incoming and the elastically scattered outgoing lepton energies, E and E'^{el}, respectively, in the *lab*-frame. Thus, our final result will necessarily depend on the upper limit of integration which of course depends on the design of the experimental arrangement. In the present analysis we may choose the value of the detector resolution to be about $\sim 1\,\%$ of the incoming lepton energies, consistent with the proposed MUSE experimental design.

The diagrammatic evaluation of all the virtual or real processes results in both UV and IR divergences which are tackled using dimensional regularization (DR). In case of UV divergences we are required to evaluate the analytically continued integrals in $d = 4-2\epsilon_{\rm UV}$ space-time dimension with $\epsilon_{\rm UV} > 0$, while for the IR cases integrals are evaluated in $d = 4-2\epsilon_{\rm IR}$ space-time dimension with $\epsilon_{\rm IR} < 0$. The resulting UV and IR divergences in such cases typically appear as poles in $\epsilon_{\rm IR,\,UV}$, e.g.,

$$\frac{1}{\epsilon_{\rm UV}} - \gamma_E + \ln\left(\frac{4\pi\mu^2}{m_l^2}\right) \quad \text{and} \quad \frac{1}{|\epsilon_{\rm IR}|} + \gamma_E - \ln\left(\frac{4\pi\mu^2}{-Q^2}\right) , \tag{6.3}$$

respectively, where m_l is the lepton mass, Q^2 is the squared four-momentum transfer, μ is the subtraction scale (typically chosen as the momentum scale associated with the scattering process), and $\gamma_E = 0.577216...$ is the Euler-Mascheroni constant. It is noteworthy that apart from the relatively few recent analyses of radiative corrections using DR presented, e.g., in Ref. [139, 160, 238, 239], most works in the past have used the photon mass or λ-regularization in dealing with IR divergences (e.g., see Refs. [10, 50]). A naive comparison with those analyses roughly leads to the correspondence:

$$\frac{1}{|\epsilon_{\rm IR}|} + \gamma_E - \ln\left(\frac{4\pi\mu^2}{-Q^2}\right) \leftrightarrow -\ln\left(\frac{\lambda^2}{-Q^2}\right) . \tag{6.4}$$

go undetected in a typical experimental set-up, it is necessary to integrate the part of the radiative tail spectrum for photon energies between 0 to Δ_S in order to obtain the differential cross section.

Finally, all UV divergences are removed using counterterms, while the IR-divergent terms exactly cancel out in the sum of the real and virtual correction to the elastic cross section.

Before going down to the one-loop level, we start our discussion with tree level ℓ-p scattering cross section in HBχPT formalism. The relevant Born diagrams, $\mathrm{B}^{(0)}$ at LO and $\mathrm{B}^{(1)}$ at NLO in HBχPT, are displayed in Fig. [6.1]. The amplitude for these diagrams are written as

$$
\begin{aligned}
i\mathcal{M}_{\gamma}^{(0)} &= [\bar{u}_l(p')(-ie\gamma^{\mu})u_l(p)]\ \frac{-i}{Q^2}\ \left[\mathcal{N}_v^{\dagger}(p'_p)\frac{ie}{2}(1+\tau^3)v_{\mu}\mathcal{N}_v(p_p)\right] \\
&= \ -\frac{ie^2}{Q^2}[\bar{u}_l(p')\gamma^{\mu}\,u_l(p)]\ \left[\chi^{\dagger}(p'_p)v_{\mu}\chi(p_p)\right]\ , \\
i\mathcal{M}_{\gamma}^{(1)} &= [\bar{u}_l(p')(-ie\gamma^{\mu})u_l(p)]\ \frac{-i}{Q^2} \\
&\quad \times\ \left[\mathcal{N}_v^{\dagger}(p'_p)\frac{ie}{4M}(1+\tau^3)\Big\{(p_p+p'_p)_{\mu}-[v\cdot(p_p+p'_p)]v_{\mu}\Big\}\mathcal{N}_v(p_p)\right] \\
&= \ -\frac{ie^2}{2MQ^2}[\bar{u}_l(p')\gamma^{\mu}\,u_l(p)]\ \left[\chi^{\dagger}(p'_p)\left\{(p_p+p'_p)_{\mu}-[v\cdot(p_p+p'_p)]v_{\mu}\right\}\chi(p_p)\right]\ , \\
&= \ -\frac{ie^2}{2MQ^2}[\bar{u}_l(p')\gamma^{\mu}\,u_l(p)]\ \left[\chi^{\dagger}(p'_p)(p_p+p'_p)_{\mu}\chi(p_p)\right]+\mathcal{O}\left(\frac{1}{M^2}\right)\ ,
\end{aligned}
\tag{6.5}
$$

where $Q_{\mu}=p_{\mu}-p'_{\mu}=P'_{\mu}-P_{\mu}=(p'_p)_{\mu}-(p_p)_{\mu}$ is the four-momentum transfer in the elastic scattering process, $\ell(p)+\mathrm{p}(p_p)\to\ell(p')+\mathrm{p}(p'_p)$, noting that in the heavy baryon formalism the initial and final state proton four-momenta can be written as $P^{\mu}=Mv^{\mu}+p_p^{\mu}$ and $P'^{\mu}=Mv^{\mu}+p_p'^{\mu}$, respectively, with $v\cdot p_p=0$ and $v\cdot p'_p=-\frac{(p'_p)^2}{2M}+\mathcal{O}(M^{-2})$. Also, note that in the above expressions $\mathcal{N}_v^{\dagger}$, $\mathcal{N}_v$ are the non-relativistic nucleon isospinors which are related to the corresponding *large* components of the standard relativistic Dirac isospinors

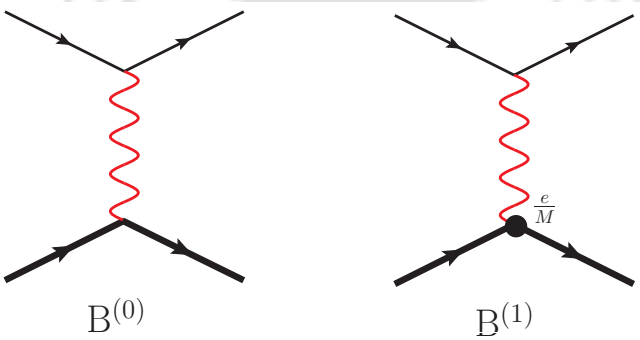

FIGURE 6.1: Born diagrams for ℓ-p elastic scattering at LO [i.e., $\mathcal{O}(e^2)$] and NLO [i.e., $\mathcal{O}\left(e^2,\frac{1}{M}\right)$] in HB$\chi$PT. The dark blob represents the proton-photon NLO vertex.

$\bar{\mathcal{U}}_N, \mathcal{U}_N$ via

$$\begin{pmatrix} \mathcal{N}_v(p_p) \\ \mathbf{0}_{2\times 1} \end{pmatrix} = \sqrt{2M_N} \left(\frac{1+\not{v}}{2} \right) \mathcal{U}_N(P) \,, \tag{6.6}$$

while $\chi^\dagger, \chi$ are the two-component Pauli spinors for the non-relativistically treated proton and $\bar{u}_l, u_l$ are the standard Dirac spinors for the relativistically treated lepton. Now expanding the square of the tree-level elastic amplitude up to $\mathcal{O}\left(M^{-1}\right)$, namely, $\mathcal{M}_\gamma = \mathcal{M}_\gamma^{(0)} + \mathcal{M}_\gamma^{(1)}$, and summing over the initial and final particle spins, we have

$$\sum_{spins} |\mathcal{M}_\gamma|^2 \;=\; \sum_{spins} \left\{ |\mathcal{M}_\gamma^{(0)}|^2 + 2\,\mathcal{R}\mathrm{e}\left(\mathcal{M}_\gamma^{(0)\dagger} \mathcal{M}_\gamma^{(1)}\right) \right\} + \mathcal{O}\left(\frac{1}{M^2}\right) , \tag{6.7}$$

where,

$$\sum_{spins} |\mathcal{M}_\gamma^{(0)}|^2 \;=\; \frac{\alpha^2}{Q^4} 256\pi^2 MEE'(M+E'_p) \left[1 + \beta\beta' \cos\theta + \frac{m_l^2}{EE'} \right] , \tag{6.8}$$

in the *lab*-frame (i.e., in the rest frame of the target) with lepton scattering angle θ, and the interference term can be shown to be of $\mathcal{O}(M^{-2})$, such that the fractional contribution

$$\mathscr{R}_Q = \frac{2\sum_{spins} \mathcal{R}\mathrm{e}\left(\mathcal{M}_\gamma^{(0)\dagger} \mathcal{M}_\gamma^{(1)}\right)}{\sum_{spins} |\mathcal{M}_\gamma^{(0)}|^2} = \frac{Q^2}{2M^2} \sim \mathcal{O}\left(\frac{1}{M^2}\right) . \tag{6.9}$$

So up to the "recoil" order, i.e., $\mathcal{O}\left(M^{-1}\right)$, of our working accuracy that we consider in this analysis, the NLO Born diagram does not contribute. Now, the *lab*-frame cross section at tree-level including the $\mathcal{O}(M^{-1})$ recoil correction amounts to evaluating the phase-space integral of the form

$$\left[\mathrm{d}\sigma_{el}\right]_\gamma = \frac{(2\pi)^4 \delta^4\left(p + P - p' - P'\right)}{4ME} \frac{\mathrm{d}^3\vec{p}'}{(2\pi)^3 2E'} \frac{\mathrm{d}^3\vec{P}'}{(2\pi)^3 2E'_p} \frac{1}{4} \sum_{spins} |\mathcal{M}_\gamma|^2 \,.$$

Here we note that in the context of an experiment like that of the MUSE that is designed to measure a single arm lepton spectrum (where the outgoing lepton is only detected while the recoil proton remains undetected), we first need to eliminate the final state proton's three-momenta $\vec{P}'$ from the differential cross section. Thus, after integrating out $\vec{P}'$ using

the three-momentum conserving δ-function, the differential cross section reads

$$\left[\frac{\mathrm{d}\sigma_{el}(Q^2)}{\mathrm{d}\Omega_l'}\right]_\gamma = \int \frac{|\vec{p}'\,|\,\mathrm{d}E'}{(2\pi)^2 16M^2E}\,\delta\left(E - E' - \frac{(\vec{p}-\vec{p}')^2}{2M} + \mathcal{O}\left(\frac{1}{M^2}\right)\right) \times \frac{1}{4}\sum_{spins}\left\{|\mathcal{M}_\gamma^{(0)}|^2 + \mathcal{O}\left(\frac{1}{M^2}\right)\right\} = \frac{\alpha^2\beta' E'^2(M+E_p')}{MQ^4}\left[1+\frac{E}{M}(1-\cos\theta)\right]^{-1}\left[1+\beta\beta'\cos\theta+\frac{m_l^2}{EE'}\right], \tag{6.10}$$

where $\beta = |\vec{p}|/E$ and $\beta' = |\vec{p}'|/E'$ are the incoming and outgoing lepton velocity factors. Note that the $\mathcal{O}(M^{-1})$ terms within the first parenthesis in the above expression solely arise from the phase-space contribution, and as far as the radiative corrections are concerned exactly the same phase-space factors arise as above which ultimately cancel in taking the ratio of the radiative corrections to the leading Born contribution. Thus, all $1/M$ terms that appear in the fractional radiative corrections $\delta_{2\gamma}$, originate in the part of the squared matrix elements, $\delta_{2\gamma}^{(1)} = \delta_{\gamma\gamma}^{(1)} + \delta_{\gamma\gamma^*}^{(1)}$, either due to NLO interactions vertices from the HBχPT Lagrangian or from NLO propagator insertions. These constitute the so-called *radiative and recoil* corrections.

6.2 Radiative Correction at LO in HBχPT

The topic of higher order radiative effects in QED has a long-standing venerated history producing a plethora of Nobel Laureates in the past. A comprehensive history and foundation on this topic can be found in the monograph *Quantum Electrodynamics* by A. I. Akhiezer and V. B. Berestetskii [162]. Such QED type of radiative corrections were first considered by Schwinger for potential scattering [13] in a canonical perturbation formalism, which was later extended by Tsai [47] for a diagrammatic evaluation of the electron-proton scattering process considering both elastic as well as inelastic bremsstrahlung contributions, adopting the framework of Ref. [151]. The review papers [10, 50] present a nice exposition on the methodology of systematically incorporating radiative correction to the *raw* experimental data to yield meaningful results subsequently to be used in extracting quantities like electromagnetic form factors or rms radii. However in majority of the past approaches hadronic structure effects arising from the proton-photon interacting

vertices were parametrized using phenomenological form factors. However, as described in the previous chapters, in HBχPT the proton-photon vertices are treated as being "elementary" (cf. Feynman rules in the Appendix A) with hadronic effects systematically incorporated via a perturbative power counting scheme.

The radiative corrections to the ℓ-p elastic scattering process constitute diagrams either of $\mathcal{O}(e^4)$, which arise from one-loop virtual corrections, or of $\mathcal{O}(e^3)$, associated with the emission of a single undetectable real soft photon with energy below Δ_γ^*. In our analysis below we shall consider all the UV and IR divergences arising in the evaluation of the fractional radiative corrections to the elastic cross section, $\delta_{2\gamma}^{(0)} \sim \mathcal{O}(\alpha)$, and LO in HB$\chi$PT, which are treated using the gauge invariant method of DR and subsequently renormalized using counterterms to render UV finite results. As in the previous chapter, we analytically evaluate the one-loop virtual diagrams in order to project out the complete IR singularity structure of the one-loop ensuring exact cancellation with the soft bremsstrahlung counterpart. Note, however, that in contrast to the *soft photon approximation* (SPA) that was used to analytically evaluate the *two-photon exchange* (TPE) box diagrams in the previous chapter, we do not use SPA in the evaluations of the virtual loops presented in this chapter. Nevertheless, for obtaining the sum of all one-loop diagrams contributing to the elastic cross section, we do use same SPA evaluated TPE expressions from the previous chapter. Moreover, for the purpose of extracting the IR-singularities from the soft photon bremsstrahlung diagrams we also use SPA. So let us now consider each of the two aforementioned kinds of contributions, namely, the *virtual* and *real* contribution separately as below.

6.2.1 One-loop Virtual Corrections

As described in the second chapter, the one-loop diagrams which contribute to the radiative corrections include the lepton and proton self-energy (SE), vertex correction (VC), vacuum polarization (VP), and the two-photon exchange (TPE) diagrams, as displayed in Fig. [6.2]. The SE diagrams renormalize the masses and the wave functions of the lepton and proton. For external particles in the on-shell limit the SE contributions exactly vanish after renormalization, so that these corrections are only needed for internal lines and

need not be considered explicitly when summing over amplitudes. Nonetheless, their expressions are needed to determine the respective wave-function renormalization constants $Z_2^{l,p}$, which by virtue of Ward-Takahashi identity in QED is equal to the corresponding vertex renormalization constants $Z_1^{l,p}$. Furthermore, as discussed in the previous chapter, the sum of the TPE "direct" and "crossed" box diagrams at LO in HBχPT (diagrams in the last row of Fig. [6.2]) effectively have vanishing contribution to the elastic cross section, with as well as without SPA.[2] The remaining one-loop contributions listed in Fig. [6.2] are evaluated without SPA, and will be briefly discussed below.

6.2.1.1 Lepton Vertex Correction

The one-loop lepton VC diagram $\mathrm{VC}^{l(0)}$ of Fig. [6.2] have been extensively calculated in the past using different regularization schemes, and its evaluation is considered as a standard text book exercise. Parametrizing the higher order radiative corrections to lepton-photon vertex in terms of the relativistic Dirac $F_1^l = 1 + \delta F_1^l$ and Pauli F_2^l form factors, namely,

$$\delta\Gamma_l^\mu(p,p') = \gamma^\mu \delta F_1^l(Q^2) + \frac{i\sigma^{\mu\nu}Q_\nu}{2m_l} F_2^l(Q^2)\,, \quad Q_\mu = p_\mu - p'_\mu\,, \tag{6.11}$$

such that the lepton VC amplitude $\mathrm{VC}^{l(0)}$ can be expressed in the general form

$$\begin{aligned} i\mathcal{M}^{l(0)}_{\gamma\gamma;\,\mathrm{vertex}} &= \left[\bar{u}_l(p')\left\{-ie\,\delta\Gamma_l^\mu(p,p')\right\}u_l(p)\right]\,\frac{-i}{Q^2}\,\left[\mathcal{N}_v^\dagger(p'_p)\frac{ie}{2}(1+\tau^3)v_\mu\mathcal{N}_v(p_p)\right] \\ &= -\frac{ie^2}{Q^2}\left[\bar{u}_l(p')\delta\Gamma_l^\mu(p,p')u_l(p)\right]\,\left[\chi^\dagger(p'_p)v_\mu\chi(p_p)\right]\,, \end{aligned} \tag{6.12}$$

Note here that at our working accuracy isospin breaking effects are not considered, so that the nucleon mass M_N can be associated with the physical mass of the proton, i.e., $M_N \equiv M$. The evaluation of diagram $\mathrm{VC}^{l(0)}$ leads to both UV and IR divergence for F_1^l, while F_2^l at one-loop level is completely finite. It is noteworthy that the "Dirac" part of amplitude proportional to the form factor F_1^l factorizes into the Born amplitude, while the "Pauli" part of the amplitude proportional to F_2^l does not manifest in the same way,

[2]The imaginary part of the sum of the LO TPE box amplitudes, is however, non vanishing even using SPA, but irrelevant in the present context of determination of the unpolarized cross section.

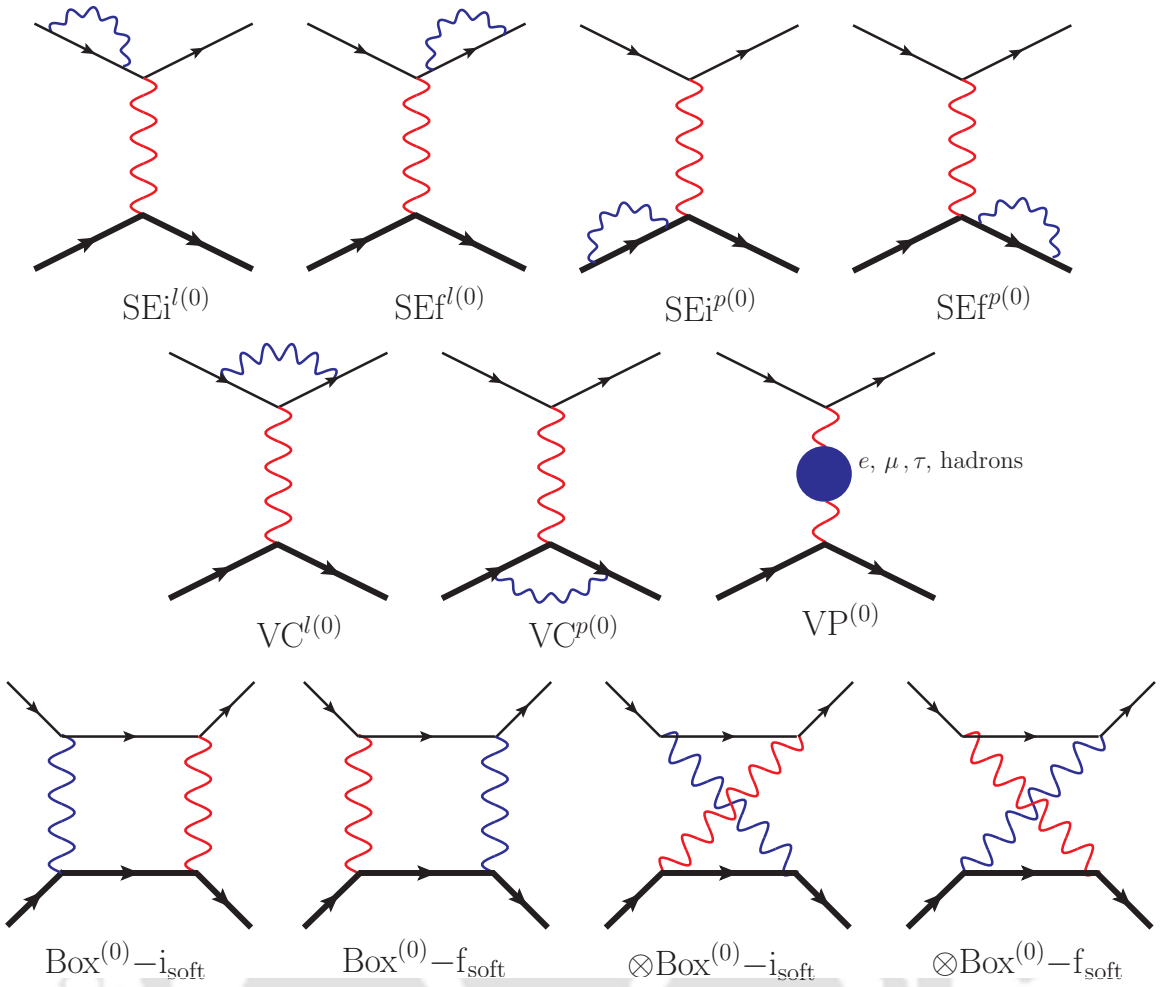

FIGURE 6.2: The one-loop diagrams at LO in HBχPT [i.e., $\mathcal{O}(e^4)$], contributing to the virtual radiative corrections to the elastic ℓ-p scattering cross section, $\overline{\delta}^{(0)}_{\gamma\gamma} \sim \mathcal{O}(\alpha)$ [see Eq. (6.37)]. The blob in the diagram VP$^{(0)}$ only consists of one-loop leptonic and hadronic contributions. For the sake of illustration, each LO TPE ("direct" and "crossed") box diagram is shown as the sum of two diagrams each having one hard photon and one soft photon exchange. However, the sum of these TPE diagrams effectively have vanishing contribution to the elastic cross section with or without using soft photon approximation.

namely,

$$\mathcal{M}^{l(0)}_{\gamma\gamma;\,\rm vertex} = \mathcal{M}^{(0)}_{\gamma}\delta F^{l}_{1}(Q^2) + \overline{\mathcal{M}}^{(0)}_{\gamma} F^{l}_{2}(Q^2)\,;$$

$$\overline{\mathcal{M}}^{(0)}_{\gamma} = -\frac{e^2}{2m_l Q^2}\left[\bar{u}_l(p')i\sigma^{\mu\nu}Q_\nu u_l(p)\right]\left[\chi^\dagger(p'_p)v_\mu\chi(p_p)\right]\,. \tag{6.13}$$

The one-loop expressions for the Dirac and Pauli form factor evaluated using dimensional regularization are, respectively, given as [139, 160]

$$\delta F_1^l(Q^2) = \frac{\alpha}{4\pi}\Bigg[\left[\frac{1}{\epsilon_{\rm UV}} - \gamma_E + \ln\left(\frac{4\pi\mu^2}{m_l^2}\right)\right] - \left[\frac{1}{|\epsilon_{\rm IR}|} + \gamma_E - \ln\left(\frac{4\pi\mu^2}{m_l^2}\right)\right]\frac{\nu^2+1}{\nu} \times \ln\left[\frac{\nu+1}{\nu-1}\right] + \frac{\nu^2+1}{2\nu}\ln\left[\frac{\nu+1}{\nu-1}\right]\ln\left[\frac{\nu^2-1}{4\nu^2}\right] + \frac{2\nu^2+1}{\nu} \times \ln\left[\frac{\nu+1}{\nu-1}\right] - \frac{\nu^2+1}{\nu}\left\{{\rm Sp}\left(\frac{\nu+1}{2\nu}\right) - {\rm Sp}\left(\frac{\nu-1}{2\nu}\right)\right\}\Bigg], \quad (6.14)$$

$$F_2^l(Q^2) = -\frac{\alpha}{4\pi}\frac{\nu^2-1}{\nu}\ln\left[\frac{\nu+1}{\nu-1}\right]; \quad \nu = \sqrt{1-\frac{4m_l^2}{Q^2}}, \quad (6.15)$$

where Sp(x) is the Spence function as defined in Eq. (2.13).

The UV divergence is renormalized by adding the counterterm vertex $(Z_1^l - 1)\gamma^\mu$ to the vertex function Γ_l^μ, requiring that the total vertex $\tilde{\Gamma}_l^\mu = \Gamma_l^\mu + (Z_1^l - 1)\gamma^\mu$ defines the physical charge at $Q^2 = 0$ according to the renormalization condition, $\tilde{\Gamma}^\mu(Q^2 = 0) = \gamma^\mu$. To one-loop the wave function renormalization constant Z_2^l is defined in terms of the derivative of the lepton SE function $\Sigma_l(p)$ as

$$Z_2^l = 1 + \left.\frac{\partial\Sigma^l(p)}{\partial(\gamma\cdot p)}\right|_{\gamma\cdot p = m_l} + \mathcal{O}(\alpha^2) \equiv Z_1^l = 1 - \delta F_1^l(Q^2 = 0)\,. \quad (6.16)$$

Noting the result that in the limit $Q^2 \to 0$, i.e., $\nu \to \infty$,

$$\lim_{\nu\to\infty}\frac{\nu^2 \pm 1}{\nu}\ln\left[\frac{\nu+1}{\nu-1}\right] = 2\,, \quad (6.17)$$

we get

$$\left.\frac{\partial\Sigma^l(p)}{\partial(\gamma\cdot p)}\right|_{\gamma\cdot p = m_l} = -\frac{\alpha}{4\pi}\left[\frac{1}{\epsilon_{\rm UV}} - \gamma_E + \ln\left(\frac{4\pi\mu^2}{m_l^2}\right)\right] + \frac{\alpha}{2\pi}\left[\frac{1}{|\epsilon_{\rm IR}|} + \gamma_E - \ln\left(\frac{4\pi\mu^2}{m_l^2}\right) - 2\right]. \quad (6.18)$$

Thus, the renormalized amplitude is given by

$$\left[\mathcal{M}^{l(0)}_{\gamma\gamma;\,\rm vertex}\right]_{\rm ren} = \mathcal{M}^{(0)}_\gamma[\delta F_1^l(Q^2) - \delta F_1^l(0)] + \overline{\mathcal{M}}^{(0)}_\gamma F_2^l(Q^2)\,, \quad (6.19)$$

where $\overline{\mathcal{M}}_{\gamma}^{(0)}$ is given in Eq. (6.13), and the renormalized one-loop expression for the lepton's Dirac form factor is given as [139, 160]

$$\begin{aligned} F_1^{l;\,\mathrm{ren}}(Q^2) &= 1 + \delta F_1^l(Q^2) - \delta F_1^l(0) \\ &= 1 + \frac{\alpha}{2\pi}\Bigg[- \left[\frac{1}{|\epsilon_{\mathrm{IR}}|} + \gamma_E - \ln\left(\frac{4\pi\mu^2}{m_l^2}\right)\right]\left[\frac{\nu^2+1}{2\nu}\ln\left[\frac{\nu+1}{\nu-1}\right] - 1\right] \\ &\quad + \frac{\nu^2+1}{4\nu}\ln\left[\frac{\nu+1}{\nu-1}\right]\ln\left[\frac{\nu^2-1}{4\nu^2}\right] + \frac{2\nu^2+1}{2\nu}\ln\left[\frac{\nu+1}{\nu-1}\right] \\ &\quad - 2 - \frac{\nu^2+1}{2\nu}\left\{\mathrm{Sp}\left(\frac{\nu+1}{2\nu}\right) - \mathrm{Sp}\left(\frac{\nu-1}{2\nu}\right)\right\}\Bigg]. \end{aligned} \tag{6.20}$$

The finite Pauli form factor F_2^l contributes to the lepton's spin magnetic moment as [139]

$$\vec{\mu}_S^l = -\frac{e\vec{S}}{2m_l}[1 + F_2^l(Q^2=0)] = \frac{e\vec{S}}{2m_l}\left(1 + \frac{\alpha}{2\pi}\right). \tag{6.21}$$

Also it is important to note that for $|Q^2| \gg m_l^2$, $\nu \to 1$, which implies $F_2^l \to 0$, and hence, its contribution can be safely ignored relative to F_1^l for the case of electron scatterings, as done in most high-energy analyses in the past. However, for low-energy muon scattering, especially associated with the proposed MUSE kinematics, the Pauli form factor could have significant contribution, so that we have included it in our calculations.

6.2.1.2 Proton Vertex Correction

In literature the one-loop proton VC diagram $\mathrm{VC}^{p(0)}$ of Fig. [6.2] has been calculated using phenomenological form factors [10, 50], but HBχPT allows a calculation using gauge invariant proton-photon couplings. Parametrizing the higher order radiative corrections to proton-photon vertex in terms of the nonrelativistic Sachs electric G_E^p and magnetic G_M^p proton form factors, the matrix element of the electromagnetic quark current between proton states is given by

$$\left\langle \mathcal{N}(P')\middle|\bar{q}\gamma^{\mu}\left(\frac{1+\tau^3}{2}\right)q\middle|\mathcal{N}(P)\right\rangle \sim \chi^{\dagger}(p_p')\Lambda_p^{\mu}(p_p,p_p')\chi(p_p)\,, \tag{6.22}$$

where

$$\Lambda_p^\mu(p_p, p_p') = \left(v^\mu G_E^p(Q^2) + \frac{[S^\mu, S\cdot Q]}{M} G_M^p(Q^2) \right), \quad Q_\mu = (p_p')_\mu - (p_p)_\mu \,. \tag{6.23}$$

To the LO in HBχPT only the first term of Λ_p^μ containing the proton's electric form factor G_E^p contributes.[3] Here we write, $G_E^p = G_E^{p(0)} + \delta G_E^{p(0)}$, where $\delta G_E^{p(0)}$ incorporates the radiative corrections to the electric form factor. Noting the on-shell conditions for the external proton lines, namely, $v\cdot p_p = 0$ and $v\cdot p_p' = -\frac{(p_p')^2}{2M} + \mathcal{O}(M^{-2})$, the amplitude of the one-loop proton vertex diagram is given as

$$\begin{aligned} i\mathcal{M}^{p(0)}_{\gamma\gamma;\,\text{vertex}} &= [\bar u_l(p')(-ie\gamma^\mu)u_l(p)]\,\frac{-i}{Q^2}\int\frac{\mathrm{d}^4k}{(2\pi)^4}\Big[\mathcal{N}_v^\dagger(p_p')\frac{ie}{2}(1+\tau^3)v^\alpha\frac{i}{v\cdot(p_p'-k)+i0} \\ &\quad\times\frac{ie}{2}(1+\tau^3)v_\mu\frac{i}{v\cdot(p_p-k)+i0}\frac{ie}{2}(1+\tau^3)v_\alpha\,\mathcal{N}_v(p_p)\Big]\frac{-i}{k^2+i0} \\ &= -\frac{e^4}{Q^2}\Big[\bar u_l(p')\gamma^\mu(p,p')u_l(p)\Big]\;\big[\chi^\dagger(p_p')v_\mu\chi(p_p)\big] \\ &\quad\times\int\frac{\mathrm{d}^4k}{(2\pi)^4}\frac{1}{(k^2+i0)(-v\cdot k+i0)^2}\left(1-\frac{(p_p')^2}{2M(v\cdot k)}+\cdots\right) \\ &\equiv i\mathcal{M}_\gamma^{(0)}\delta G_E^{p(0)} \xrightarrow{\text{DR}} 0\,, \end{aligned} \tag{6.24}$$

where we used the fact that all scaleless loop integrals of the type

$$\mathcal{I}(m,n) = \int\frac{\mathrm{d}^dk}{(2\pi)^d}\frac{(k^2)^m}{(-v\cdot k+i0)^n} \tag{6.25}$$

vanish in DR (see Appendix C of Ref. [240]; also see Ref. [241]). Consequently, there is no contribution to the proton VC at LO in HBχPT. In fact, this result is naturally anticipated from the fact that in HBχPT there is no proton bremsstrahlung at the LO. Otherwise, supposing that the proton vertex correction diagram were to survive at this order, then the IR divergences from the photon loops would not cancel in the absence of the soft bremsstrahlung IR-divergent counterparts, and rendering the elastic cross section unphysical. In other words, at LO the proton is essentially static and unaffected by radiative correction.

[3] The term containing the magnetic form factor G_M^p only starts contributing at NNLO in HBχPT.

6.2.1.3 Vacuum Polarization

The one-loop VP contribution (diagram $\mathrm{VP}^{(0)}$) at LO in HBχPT, as shown in Fig. [6.3], is IR-finite but contains a logarithmic UV divergence. Its unrenormalized amplitude in terms of the bare charge e_0 is given by

$$i\mathcal{M}^{(0)}_{\gamma\gamma;\,\mathrm{v.p.}} = \left[\bar{u}_l(p')\,(-ie_0\gamma_\mu)\,u_l(p)\right]\, iD^{\mu\nu}(Q)\, \left[\chi^\dagger(p'_p) ie_0 v_\nu \chi(p_p)\right] . \tag{6.26}$$

The full photon propagator expressed in terms of the polarization tensor, $\Pi^{\mu\nu} = (Q^2 g^{\mu\nu} - Q^\mu Q^\nu)\Pi(Q^2)$, is

$$\begin{aligned} iD^{\mu\nu}(Q) &= \frac{-ig^{\mu\nu}}{Q^2} + iD^{\mu\rho}(Q)\, i\Pi_{\rho\sigma}(Q) \left(\frac{-ig^{\sigma\nu}}{Q^2}\right) \\ &= \frac{-ig^{\mu\nu}}{Q^2[1-\Pi(Q^2)]} + \text{terms with } Q^\mu Q^\nu \\ &\simeq \frac{-ig^{\mu\nu}}{Q^2\,[1-\Pi(0)]\,[1-(\Pi(Q^2)-\Pi(0))]} + \text{terms with } Q^\mu Q^\nu\,. \end{aligned} \tag{6.27}$$

The UV divergence is renormalized by adding the counterterm $-(Q^2 g^{\mu\nu} - Q^\mu Q^\nu)(Z_3 - 1)$ to $\Pi^{\mu\nu}$ which renormalizes the photon propagator, namely,

$$i\tilde{D}^{\mu\nu}(Q) = \frac{-ig^{\mu\nu}}{Q^2[1-\Pi(Q^2)+(Z_3-1)]} + \text{terms with } Q^\mu Q^\nu\,. \tag{6.28}$$

Next requiring that the renormalized propagator $\tilde{D}^{\mu\nu}$ has a pole at $Q^2 = 0$ with residue 1, yields the constant, $Z_3 = 1 + \Pi(Q^2 = 0)$, which renormalizes the bare QED coupling,

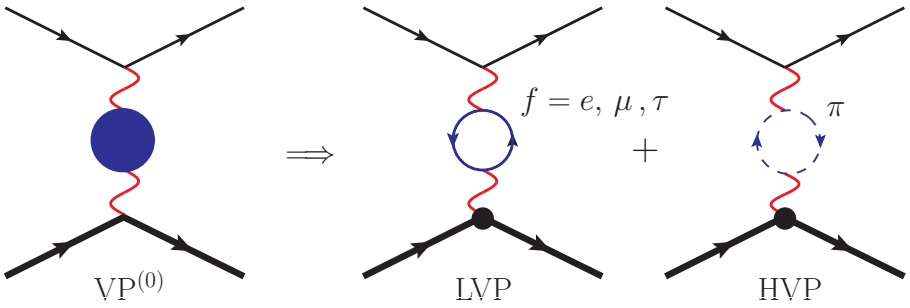

FIGURE 6.3: The one-loop vacuum polarization diagram receives contributions from both leptonic (LVP) and hadronic (HVP) particle-antiparticle pairs in loops, where we only consider the dominant hadronic part arising due to structureless $\pi^+\pi^-$ evaluated perturbatively in Scalar QED.

$\alpha_0 = \alpha/Z_3$. Finally, the renormalized amplitude is given as [139]

$$\left[\mathcal{M}^{(0)}_{\gamma\gamma;\,\text{v.p.}}\right]_{\text{ren}} = \mathcal{M}^{(0)}_{\gamma}\Delta\Pi(Q^2)\,, \tag{6.29}$$

where the renormalized polarization function expressed in terms of the physical QED coupling $\alpha = \frac{e^2}{4\pi}$ is defined as

$$\Delta\Pi(Q^2) = \Pi(Q^2) - \Pi(0) = \Delta\Pi_{\text{lepton}}(Q^2) + \Delta\Pi_{\text{hadron}}(Q^2)\,. \tag{6.30}$$

A one-loop evaluation of the fermionic loop (in Feynman gauge) using dimensional regularization yields the standard expression

$$\begin{aligned}\Pi_{\text{lepton}}(Q^2) = -\frac{\alpha_0}{2\pi}\sum_{f=e,\mu,\tau}\Bigg\{&\frac{2}{3}\left[\frac{1}{\epsilon_{\text{UV}}} - \gamma_E + \ln\left(\frac{4\pi\mu^2}{m_f^2}\right)\right] - \frac{2}{3}\left(\nu_f^2 - \frac{8}{3}\right)\\ &- \nu_f\left(\frac{3-\nu_f^2}{3}\right)\ln\left[\frac{\nu_f+1}{\nu_f-1}\right]\Bigg\}; \quad \nu_f = \sqrt{1-\frac{4m_f^2}{Q^2}}\,,\end{aligned} \tag{6.31}$$

where the index $f = e, \mu, \tau$ is used to distinguish between the particular type of lepton flavor/generation contributing to the fermion loop, and $\alpha_0 = \frac{e_0^2}{4\pi}$ is the bare QED coupling. The corresponding renormalized contribution is

$$\Delta\Pi_{\text{lepton}}(Q^2) = \frac{\alpha}{2\pi}\sum_{f=e,\mu,\tau}\left\{\frac{2}{3}\left(\nu_f^2 - \frac{8}{3}\right) + \nu_f\left(\frac{3-\nu_f^2}{3}\right)\ln\left[\frac{\nu_f+1}{\nu_f-1}\right]\right\}\,, \tag{6.32}$$

For the hadronic vacuum polarization (HVP) there is no unique method of determining all the perturbative and non-perturbative contributions. It receives contributions not only from particle-antiparticle pairs (dispersive part) but even three or more intermediate particles accounting for all absorptive contributions as well. Such non-perturbative contributions are generally evaluated numerically using Dispersion techniques, whose estimation become vital in assessing its role in several physical quantities that have elicited much recent interest, especially in regard to the resolution of muon-$(g-2)$ puzzle. However, in this work without delving much into such rigorous evaluations of the HVP with contributions amounting to $\lesssim 1\,\%$ of the total VP contribution in the present case, we consider a simplistic one-loop perturbative estimate that arise due to structure-less $\pi^+\pi^-$

pair, evaluated using Scalar QED.[4] Here we directly quote the renormalized expression obtained by Tsai [142]:

$$\Delta\Pi_{\rm hadron}(Q^2) \to \Delta\Pi_{\pi^+\pi^-}(Q^2) = \frac{\alpha}{2\pi}\left\{-\frac{2}{3}\left(\nu_\pi^2+\frac{1}{3}\right)+\frac{\nu_\pi^3}{3}\ln\left[\frac{\nu_\pi+1}{\nu_\pi-1}\right]\right\}, \qquad (6.33)$$

where

$$\nu_\pi = \sqrt{1-4m_\pi^2/Q^2}.$$

Fig. [6.4] displays the $\mathcal{O}(\alpha)$ fractional leptonic and pionic one-loop VP contributions at LO in HBχPT, namely, $\delta^{(0)}_{{\rm vac};\,f,\pi}(Q^2) = 2\Delta\Pi_{f,\pi}(Q^2)$, to the lepton-proton elastic cross section, especially covering the proposed MUSE kinematic range of Q^2 values corresponding to one of the specified representative incident lepton momentum, say, $p = |\vec{p}| = 210$ MeV/c. Note that since these corrections are independent of the incident energy of the leptons, the results do not change with other values of the beam momenta apart from effecting their $|Q^2|$ range of validity (cf. Table 5.1 of Chapter 5). Furthermore, these contributions are independent of the type of external ℓ-p scattering process. Clearly the largest contribution arises from the e^+e^- pair propagating in the loop which is an order larger than the rest of the VP corrections combined, amounting up to 1.7 % in MUSE kinematic range. While $\mu^+\mu^-$, $\tau^+\tau^-$ and $\pi^+\pi^-$ pairs contribute up to about 0.15 %, 0.002 %, and 0.03 %, respectively, in the same kinematic range. Thus, the total VP contribution (i.e., LVP+HVP) at LO in HBχPT given by $\delta^{(0)}_{\rm vac} = \sum_{f=e,\mu,\tau}\delta^{(0)}_{{\rm vac};f} + \delta^{(0)}_{{\rm vac};\,\pi}$, amounts to $\lesssim 2\,\%$ of the overall correction to the LO Born cross section.

6.2.1.4 Total one-loop Virtual Contribution at LO

By summing all the non-vanishing renormalized virtual contributions from the one-loop diagrams of Fig. [6.2] along with the Born amplitude $\mathcal{M}^{(0)}_\gamma$, one obtains the total UV-finite

[4] Here we did not involve a χPT evaluation to include the non-perturbative effects due to the pion VP loop. The rationale was that such a calculation is likely to fail since at $\mathcal{O}(\alpha)$ such a pion loop is only associated with hard photon exchange in the Born diagram. A more robust non-pertubative calculation requires a Dispersive Relation analysis which is beyond the scope of the present work. Moreover, in our case, we find that the perturbative pion loop contribution at such low-$|Q^2|$ is rather small, so that we do not anticipate any significant non-perturbative effects at this scale.

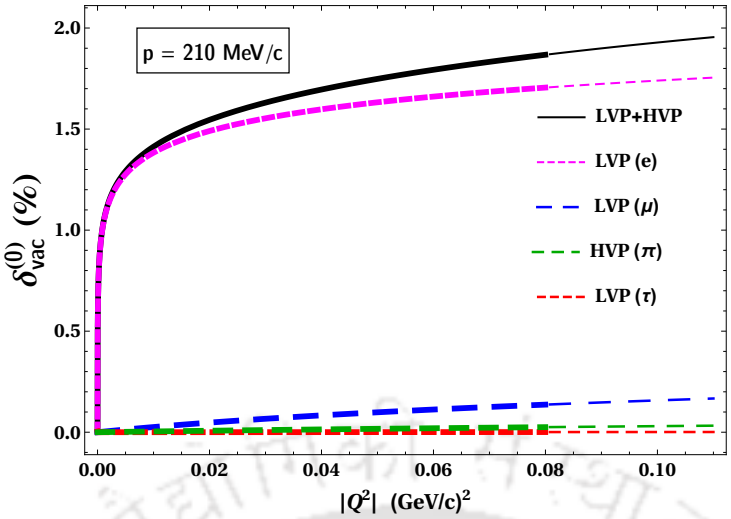

FIGURE 6.4: The individual fractional one-loop leptonic and hadronic vacuum polarization corrections $\delta^{(0)}_{\text{vac};\,e,\mu,\tau,\pi}$ and their sum total $\delta^{(0)}_{\text{vac}}$ contributing to the ℓ-p elastic cross section (in percentage) at LO as a function of the squared four-momentum transfer $|Q^2|$. The plot covers the full kinematically allowed scattering range, $0 < |Q^2| < |Q^2_{\text{max}}|$, when $\theta \in [0, \pi]$ with incoming lepton momentum $p = 210$ MeV/c (cf. Table I of Chapter 5). The thickened section of each curve corresponds to the MUSE kinematic cut, where $\theta \in [20°, 100°]$.

amplitude for elastic lepton-proton scattering at LO in HBχPT, i.e.,

$$\begin{aligned}\mathcal{M}^{(0)}_{\gamma\gamma} &= \mathcal{M}^{(0)}_{\gamma} + \left[\mathcal{M}^{l(0)}_{\gamma\gamma;\,\text{vertex}}\right]_{\text{ren}} + \left[\mathcal{M}^{(0)}_{\gamma\gamma;\,\text{v.p.}}\right]_{\text{ren}} \\ &= \mathcal{M}^{(0)}_{\gamma}\left[F_1^{l;\,\text{ren}}(Q^2) + \Delta\Pi(Q^2)\right] + \overline{\mathcal{M}}^{(0)}_{\gamma} F_2^{l}(Q^2)\,, \end{aligned} \tag{6.34}$$

where $\overline{\mathcal{M}}^{(0)}_{\gamma}$ is given in Eq. (6.13) and $F_1^{l;\,\text{ren}}$ is the renormalized one-loop lepton's Dirac form factor given in Eq. (6.20). The remnant IR divergences arising from the photon loops are still present in the factor multiplying the Born amplitude. Using the full one-loop virtual amplitude, we are now in a position to determine the radiative correction to the elastic differential cross section at LO in HBχPT given by

$$\left[\frac{\mathrm{d}\sigma^{(\text{LO})}_{el}(Q^2)}{\mathrm{d}\Omega'_l}\right]_{\gamma\gamma} = \left[\frac{\mathrm{d}\sigma_{el}(Q^2)}{\mathrm{d}\Omega'_l}\right]_{\gamma} \delta^{(0)}_{\gamma\gamma}(Q^2)\,, \tag{6.35}$$

where the $\mathcal{O}(\alpha)$ fractional contribution from the virtual part at LO can be expressed as

$$\delta^{(0)}_{\gamma\gamma}(Q^2) = \frac{2\sum_{spins}\mathcal{R}\text{e}\left(\mathcal{M}^{(0)\dagger}_{\gamma}\mathcal{M}^{(0)}_{\gamma\gamma}\right)}{\sum_{spins}|\mathcal{M}^{(0)}_{\gamma}|^2} - 2 = \mathbf{IR}^{(0)}_{\gamma\gamma} + \overline{\delta}^{(0)}_{\gamma\gamma}(Q^2)\,. \tag{6.36}$$

The finite part of $\delta^{(0)}_{\gamma\gamma}$ reads

$$\begin{aligned}\overline{\delta}^{(0)}_{\gamma\gamma}(Q^2) &= \overline{\delta}^{(0)}_{\gamma\gamma;1}(Q^2) + \delta^{(0)}_{\gamma\gamma;2}(Q^2) + \sum_{f=e,\mu,\tau}\delta^{(0)}_{\text{vac};f}(Q^2) + \delta^{(0)}_{\text{vac};\pi}(Q^2)\\ &= \frac{\alpha}{\pi}\left[\frac{\nu^2+1}{4\nu}\ln\left[\frac{\nu+1}{\nu-1}\right]\ln\left[\frac{\nu^2-1}{4\nu^2}\right] + \ln\left(\frac{-Q^2}{m_l^2}\right)\left[\frac{\nu^2+1}{2\nu}\ln\left[\frac{\nu+1}{\nu-1}\right]-1\right]\right.\\ &\quad + \frac{2\nu^2+1}{2\nu}\ln\left[\frac{\nu+1}{\nu-1}\right] - 2 - \frac{\nu^2+1}{2\nu}\left\{\text{Sp}\left(\frac{\nu+1}{2\nu}\right) - \text{Sp}\left(\frac{\nu-1}{2\nu}\right)\right\}\\ &\quad + \sum_{f=e,\mu,\tau}\left\{\frac{2}{3}\left(\nu_f^2 - \frac{8}{3}\right) + \nu_f\left(\frac{3-\nu_f^2}{3}\right)\ln\left[\frac{\nu_f+1}{\nu_f-1}\right]\right\}\\ &\quad \left. - \frac{2}{3}\left(\nu_\pi^2 + \frac{1}{3}\right) + \frac{\nu_\pi^3}{3}\ln\left[\frac{\nu_\pi+1}{\nu_\pi-1}\right]\right] + \delta^{(0)}_{\gamma\gamma;2}(Q^2)\,, \end{aligned} \tag{6.37}$$

where $\overline{\delta}^{(0)}_{\gamma\gamma;1} = 2(F_1^{l;\,\text{ren}} - 1)$ and $\delta^{(0)}_{\gamma\gamma;2}$ [cf. Eq. (6.39) below] are the LO contributions from the finite part of the lepton-photon VC terms containing the form factors, F_1^l and F_2^l, respectively, and the other two terms correspond to the finite part of the LO VP corrections. While,

$$\mathbf{IR}^{(0)}_{\gamma\gamma} \equiv \mathbf{IR}^{l(0)}_{\gamma\gamma;\,\text{vertex}} = -\frac{\alpha}{\pi}\left[\frac{1}{|\epsilon_{\text{IR}}|} + \gamma_E - \ln\left(\frac{4\pi\mu^2}{-Q^2}\right)\right]\left[\frac{\nu^2+1}{2\nu}\ln\left[\frac{\nu+1}{\nu-1}\right]-1\right] \tag{6.38}$$

is the sole IR-divergent one-loop correction term at LO arising from the lepton VC. This divergence should be cancelled by a counterpart IR-divergent term from the soft-bremsstrahlung process. It may be noted in the above expressions, that the factor, $\nu = \sqrt{1-4m_l^2/Q^2}$, depends on the external (on-shell) lepton ($\ell = e, \mu$) taking part in the elastic scattering process, while the factor, $\nu_{f,\pi} = \sqrt{1-4m_{f,\pi}^2/Q^2}$, arises due to a given generation of fermion ($f = e, \mu, \tau$) or pion loop contributing to the diagram VP$^{(0)}$ of Fig. [6.2]. Finally, the term

$$\begin{aligned}\delta^{(0)}_{\gamma\gamma;2}(Q^2) &= \frac{2\sum_{spins}\mathcal{R}\text{e}\left(\mathcal{M}^{(0)\dagger}_\gamma\,\overline{\mathcal{M}}^{(0)}_\gamma\right)}{\sum_{spins}|\mathcal{M}^{(0)}_\gamma|^2}F_2^l(Q^2) = \left(\frac{2m_l^2 + 2\vec{p}\cdot\vec{p}\,' - E^2 - E'^2}{EE' + m_l^2 + \vec{p}\cdot\vec{p}\,'}\right)F_2^l(Q^2)\\ &= 2\left(\frac{Q^2}{Q^2+4EE'}\right)\left(1 - \frac{Q^2}{4M^2}\right)F_2^l(Q^2)\\ &= \frac{\alpha}{\pi\nu}\left(\frac{2m_l^2}{Q^2+4EE'}\right)\ln\left[\frac{\nu+1}{\nu-1}\right] + \mathcal{O}\left(\frac{1}{M^2}\right)\,, \end{aligned} \tag{6.39}$$

represents the one-loop contribution arising from magnetic form factor F_2^l which is finite at this order. Fig. [6.5] displays the LO finite contributions from the lepton-photon VC terms, $\overline{\delta}^{(0)}_{\gamma\gamma;1}$ and $\delta^{(0)}_{\gamma\gamma;2}$, arising due to the form factors F_1^l and F_2^l, respectively, for the full kinematically allowed elastic scattering range $0 < |Q^2| < |Q^2_{\rm max}|$ for $0 < \theta < \pi$, especially for the proposed MUSE specified incoming lepton momenta $p = |\vec{p}\,|$, namely, 115 MeV/c, 153 MeV/c, and 210 MeV/c (cf. Table I of Chapter 5). Few observations are in order concerning the LO virtual corrections:

- All the corrections vanish in the limit $Q^2 \to 0$.
- As mentioned earlier, there is no LO contribution from the TPE box diagrams, even without SPA.

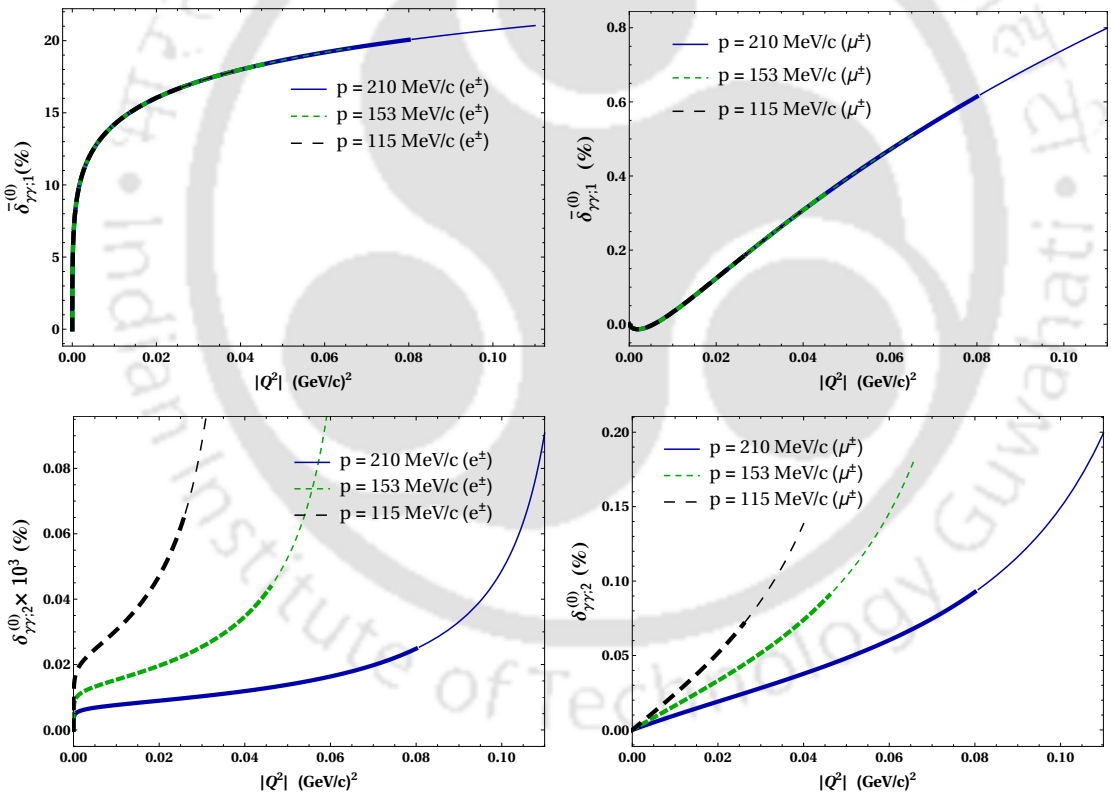

FIGURE 6.5: Fractional one-loop LO contributions $\overline{\delta}^{(0)}_{\gamma\gamma;1}$ (upper panel) and $\delta^{(0)}_{\gamma\gamma;2}$ (lower panel) to the ep (left panel) and μp (right panel) elastic cross sections (in percentage) from the finite lepton-photon vertex terms containing the form factors $F^l_{1,2}$ as a function of the squared four-momentum transfer $|Q^2|$ for the proposed MUSE beam momenta. Each plot covers the full kinematically allowed scattering range, $0 < |Q^2| < |Q^2_{\rm max}|$, when $\theta \in [0, \pi]$ and the incoming lepton momenta, namely, $p = 115$, 153, 210 MeV/c (cf. Table I of Chapter 5). The thickened section of each curve corresponds to the MUSE kinematic cut, where $\theta \in [20^\circ, 100^\circ]$.

- The electronic and muonic Dirac form factor contributions in the region of low momentum transfers, $|Q^2| < 0.1$ (GeV/c)^2, differs by almost two orders of magnitudes. The reason for this stark contrast being that the electronic Dirac term $\bar{\delta}^{l(0)}_{\gamma\gamma;1}$ is enhanced in the soft and collinear region of the loop-momentum integration resulting from the so-called *Sudakov double-logarithms*, namely,

$$\frac{\nu^2+1}{4\nu}\ln\left[\frac{\nu+1}{\nu-1}\right]\ln\left[\frac{\nu^2-1}{4\nu^2}\right]+\frac{\nu^2+1}{2\nu}\ln\left(\frac{-Q^2}{m_l^2}\right)\ln\left[\frac{\nu+1}{\nu-1}\right]\approx\frac{1}{2}\ln^2\left(\frac{-Q^2}{m_l^2}\right),$$

  in the limit of small lepton mass (i.e., $|Q^2| \gg m_l^2$). However, for muon scattering, especially in regard to MUSE kinematics where $m_\mu^2 = 0.01$ GeV$^2 \approx |Q^2|$, there is no such enhancements.

- In contrast, the Pauli form factor contributions which are practically negligible $\sim 10^{-6}\,\%$ for electron scattering in the MUSE range, turn out to be much larger $\sim 10^{-2}\,\%$ in muon scattering. Interestingly, for intermediate or high-energy muon scattering (though not relevant in the context of the MUSE project), the Pauli form factor contributions to the elastic cross section can become significantly large, although F_2^μ itself becomes small for $|Q^2| \gg m_\mu^2$.

- Unlike the Pauli VC term, the Dirac term is independent of the lepton beam energy. Thus, the curves corresponding to the different incident lepton beam momenta overlap, though they differ in their respective maximal values $|Q^2_{\rm max}|$.

Thus, it is quite evident that in the context of high-precision analysis of scattering data at $\lesssim 1\,\%$ accuracy, as currently being planned for the future MUSE data, the muonic Pauli form factor contributions are non-negligible in comparison to the Dirac contributions. Therefore, their contributions must not be ignored unlike traditionally done in the case of high-energy electron scattering.

6.2.2 Soft Bremsstrahlung Corrections

Considering our investigations in the previous chapter, we concluded that at LO in HBχPT proton does not radiate. The only diagrams needed to be considered at this

order involve a single soft photon emitted from either the incoming lepton, diagram $\mathrm{Ri}^{l(0)}$, or the outgoing lepton, diagram $\mathrm{Rf}^{l(0)}$, as displayed in Fig. [6.6]. The respective amplitudes are given as

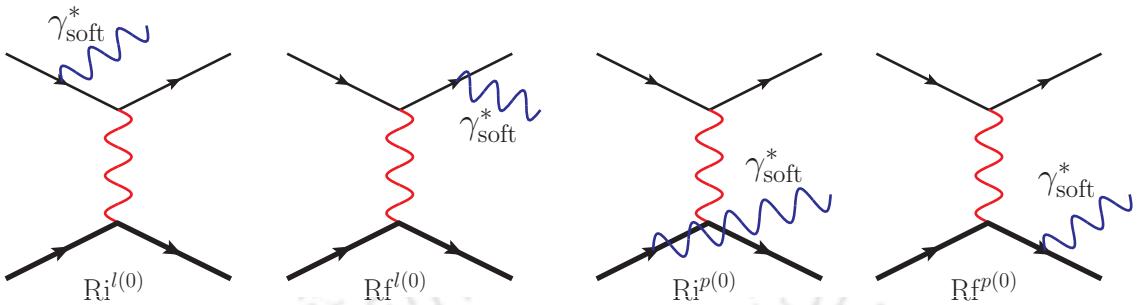

FIGURE 6.6: Soft photon ($\gamma^*_{\rm soft}$) bremsstrahlung diagrams at LO in HBχPT [i.e., $\mathcal{O}\left(e^3\right)$], contributing to the radiative corrections to the ℓ-p scattering cross section, $\bar{\delta}^{(0)}_{\gamma\gamma^*} \sim \mathcal{O}(\alpha)$ [see Eq .(6.49)]. At this order, the last two proton radiating diagrams vanish.

$$
\begin{aligned}
i\mathcal{M}^{l(0);\,\mathrm{i}}_{\gamma\gamma^*} &= \int \frac{\mathrm{d}^4k}{(2\pi)^4}\left[\bar{u}_l(p')(-ie\,\epsilon^*\cdot\gamma)\frac{i(\not{p}-\not{k}+m)}{(p-k)^2-m_l^2}(-ie\gamma^\mu)u_l(p)\right] \\
&\qquad\times\frac{-i}{(Q-k)^2}\left[\chi^\dagger(p'_p)(ie\,v_\mu)\chi(p_p)\right]\,, \\
i\mathcal{M}^{l(0);\,\mathrm{f}}_{\gamma\gamma^*} &= \int \frac{\mathrm{d}^4k}{(2\pi)^4}\left[\bar{u}_l(p')(-ie\gamma^\mu)\frac{i(\not{p}'+\not{k}+m)}{(p'+k)^2-m_l^2}(-ie\,\epsilon^*\cdot\gamma)u_l(p)\right] \\
&\qquad\times\frac{-i}{(Q-k)^2}\left[\chi^\dagger(p'_p)(ie\,v_\mu)\chi(p_p)\right]\,,
\end{aligned}
\tag{6.40}
$$

where the $\gamma^*_{\rm soft}$ symbol in the above amplitudes denote the emission of a real *soft* photon. Since here we are only concerned with such undetectable soft photon emissions, unlike for the loop diagrams, it is fully legitimate to use SPA in evaluating these soft photon amplitudes, where the photon momentum in the propagator numerator is taken zero, i.e., $k \to 0$, with the assumption that the soft emissions does not alter the elastic kinematics, viz. the four-momentum transfer, $Q_\mu = p_\mu - p'_\mu = P'_\mu - P_\mu$ is unaffected. In this case the matrix elements get factorized into LO Born amplitude, namely,

$$
\begin{aligned}
\mathcal{M}^{l(0);\,\mathrm{i}}_{\gamma\gamma^*} &\overset{\gamma^*_{\rm soft}}{\rightsquigarrow} \widetilde{\mathcal{M}^{l(0);\,\mathrm{i}}_{\gamma\gamma^*}} = e\mathcal{M}^{(0)}_\gamma\left(\frac{p\cdot\epsilon^*}{p\cdot k}\right)\,, \\
\mathcal{M}^{l(0);\,\mathrm{f}}_{\gamma\gamma^*} &\overset{\gamma^*_{\rm soft}}{\rightsquigarrow} \widetilde{\mathcal{M}^{l(0);\,\mathrm{f}}_{\gamma\gamma^*}} = -e\mathcal{M}^{(0)}_\gamma\left(\frac{p'\cdot\epsilon^*}{p'\cdot k}\right)\,,
\end{aligned}
\tag{6.41}
$$

leading to a cross section which is in accordance with the so-called *Low's Soft-photon Theorem* [242]: *the first two terms in the series expansion of the unpolarized radiative cross section in terms of the bremsstrahlung soft photon energy depend only on the non-radiative unpolarized cross section and the electromagnetic coupling constant.* Thus, the LO bremsstrahlung squared matrix in the soft photon limit is

$$\sum_{spin} |\mathcal{M}^{(0)}_{\gamma\gamma^*}|^2 \overset{\gamma^*_{\rm soft}}{\rightsquigarrow} -e^2 \sum_{spins} |\mathcal{M}^{(0)}_{\gamma}|^2 \left(\frac{m_l^2}{(p\cdot k)^2} + \frac{m_l^2}{(p'\cdot k)^2} - \frac{2p'\cdot p}{(p\cdot k)(p'\cdot k)} \right) . \tag{6.42}$$

Now, the differential cross section for the LO bremsstrahlung process amounts to evaluating the phase-space integral of the expression

$$\left[\mathrm{d}\sigma^{(\rm LO)}_{br} \right]_{\gamma\gamma^*} = \frac{\mathrm{d}^3\vec{p}'}{(2\pi)^3 2E'} \frac{\mathrm{d}^3\vec{P}'}{(2\pi)^3 2E'_p} \frac{\mathrm{d}^3\vec{k}}{(2\pi)^3 2E_\gamma} \times \frac{(2\pi)^4 \delta^4 \left(p + P - p' - P' - k\right)}{4ME} \frac{1}{4} \sum_{spins} |\mathcal{M}^{(0)}_{\gamma\gamma^*}|^2 .$$

Subsequently, in the *lab*-frame the integrated cross section also factorizes into the Born cross section, as displayed earlier in Eq. (6.11), reading

$$\left[\frac{\mathrm{d}\sigma^{(\rm LO)}_{br}(Q^2)}{\mathrm{d}\Omega'_l} \right]_{\gamma\gamma^*} \overset{\gamma^*_{\rm soft}}{\rightsquigarrow} \frac{\alpha}{2\pi^2} \left[\frac{\mathrm{d}\sigma_{el}(Q^2)}{\mathrm{d}\Omega'_l} \right]_{\gamma} \left(-L_{\rm ii} - L_{\rm ff} + L_{\rm if} \right) , \tag{6.43}$$

where $L_{\rm ii}$, $L_{\rm ff}$ and $L_{\rm if}$ are three-momentum integrals involving the soft photons radiated by the leptons. Such integrals are easily evaluated by boosting to the so-called S-frame (center-of-mass system of the recoil proton and the emitted soft photon), where the photon energy is integrated from $E^S_{\gamma^*} = 0$ up to $E^S_{\gamma^*} = \eta\Delta^*_\gamma$, as defined in Chapter 2.[5] To extract the IR singularities in each of these integrals we use DR where we perform

[5] We recall here the discussing presented in Chapter 2 that the photon four-momentum integration in the *lab*-frame becomes very complicated being defined over a highly eccentric ellipsoidal volume due to the presence of the photon emission angle dependent energy conserving δ-function, namely, $\delta\Big(E + E_P - E' - \sqrt{(\vec{Q}-\vec{k})^2 + M^2} - |\vec{k}|\Big)$, after having integrated $\vec{P}\,'$. However, by boosting to the S-frame, defined by $\vec{p}\,'_p + \vec{k} = \vec{Q}$, this integration reduces trivially over a spherical volume, with the energy conserving δ-function becoming free of the photon angles in the soft photon limit, $|\vec{k}| \to 0$, effectively reducing to the (reversed) elastic kinematical constraint. In this case the transformations of the leptonic part of the results between those evaluated in the S-frame and the *lab*-frame are easily effected by simply interchanging the the kinematical quantities, like $E, \beta \rightleftharpoons E', \beta'$. Furthermore, using SPA one can show that the kinematics corresponding to the initial and final state protons also get reversed.

the integrals in the S-frame by analytically continuing in $d-1$ spatial dimensions, where $d-1 = 3-2\epsilon_{\rm IR}$ with $\epsilon_{\rm IR} < 0$, namely,

$$
\begin{aligned}
L_{\rm ii}^{(S)} &= \frac{m_l^2}{2}\int \frac{{\rm d}^3\vec{k}_S}{k_S}\frac{1}{(p_S\cdot k_S)^2} \overset{\rm DR}{\mapsto} \frac{m_l^2}{2}(2\pi\mu)^{2\epsilon_{\rm IR}}\int_0^{\eta\Delta_\gamma^*} k_S^{d-3}{\rm d}k_S \oiint {\rm d}^{d-2}\,\Omega_k^S \frac{1}{(p_S\cdot k_S)^2} \\
&= \pi\left\{\left[\frac{1}{|\epsilon_{\rm IR}|}+\gamma_E-\ln\left(\frac{4\pi\mu^2}{-Q^2}\right)\right]+2\widetilde{L}_{\rm ii}^{(S)}\right\}, \\
L_{\rm ff}^{(S)} &= \frac{m_l^2}{2}\int \frac{{\rm d}^3\vec{k}_S}{k_S}\frac{1}{(p_S'\cdot k_S)^2} \overset{\rm DR}{\mapsto} \frac{m_l^2}{2}(2\pi\mu)^{2\epsilon_{\rm IR}}\int_0^{\eta\Delta_\gamma^*} k_S^{d-3}{\rm d}k_S \oiint {\rm d}^{d-2}\,\Omega_k^S \frac{1}{(p_S'\cdot k_S)^2} \\
&= \pi\left\{\left[\frac{1}{|\epsilon_{\rm IR}|}+\gamma_E-\ln\left(\frac{4\pi\mu^2}{-Q^2}\right)\right]+2\widetilde{L}_{\rm ff}^{(S)}\right\}, \\
L_{\rm if}^{(S)} &= (p_S'\cdot p_S)\int \frac{{\rm d}^3\vec{k}_S}{k_S}\frac{1}{(p_S\cdot k_S)(p_S'\cdot k_S)} \\
&\overset{\rm DR}{\mapsto} (p_S'\cdot p_S)\,(2\pi\mu)^{2\epsilon_{\rm IR}}\int_0^{\eta\Delta_\gamma^*} k_S^{d-3}{\rm d}k_S \oiint {\rm d}^{d-2}\,\Omega_k^S \frac{1}{(p_S\cdot k_S)(p_S'\cdot k_S)} \\
&= (p_S'\cdot p_S)\,(2\pi\mu)^{2\epsilon_{\rm IR}}\int_0^1 {\rm d}x\int_0^{\eta\Delta_\gamma^*} k_S^{d-3}{\rm d}k_S \oiint {\rm d}^{d-2}\,\Omega_k^S \frac{1}{(p_x^S\cdot k_S)^2} \\
&= \pi\left\{\left[\frac{1}{|\epsilon_{\rm IR}|}+\gamma_E-\ln\left(\frac{4\pi\mu^2}{-Q^2}\right)\right]\frac{\nu^2+1}{\nu}\ln\left[\frac{\nu+1}{\nu-1}\right]+2\widetilde{L}_{\rm if}^{(S)}\right\},
\end{aligned}
\tag{6.44}
$$

respectively, noting that, $\nu_S \equiv \nu$, which is a function of Q^2 which is Lorentz invariant. The mass scale μ is introduced to keep the above integration measures dimensionless. Furthermore, in the integrals $L_{\rm if}^{(S)}$, we used Feynman parametrization in terms of the variable x such that $p_x^S = xp_S' + (1-x)p_S$. On boosting back to the *lab*-frame, the IR-finite parts of these integrals, namely, $\widetilde{L}_{\rm ii}^{(S)}$, $\widetilde{L}_{\rm ff}^{(S)}$ and $\widetilde{L}_{\rm if}^{(S)}$, become

$$
\widetilde{L}_{\rm ii} = \frac{1}{2}\ln\left(\frac{4\eta^2\Delta_\gamma^{*2}}{-Q^2}\right)-\frac{1}{4\beta}\ln\sqrt{\frac{1+\beta}{1-\beta}},
$$

$$
\widetilde{L}_{\rm ff} = \frac{1}{2}\ln\left(\frac{4\eta^2\Delta_\gamma^{*2}}{-Q^2}\right)-\frac{1}{4\beta'}\ln\sqrt{\frac{1+\beta'}{1-\beta'}},
$$

and

$$\widetilde{L}_{\rm if} = \frac{\nu^2+1}{2\nu}\left[\ln\left(\frac{4\eta^2\Delta_\gamma^{*2}}{-Q^2}\right)\ln\left[\frac{\nu+1}{\nu-1}\right] + \ln^2\sqrt{\frac{1+\beta'}{1-\beta'}} - \ln^2\sqrt{\frac{1+\beta}{1-\beta}} - {\rm Sp}\left(1-\frac{\lambda_\nu E'-E}{(1-\beta')E'\xi_\nu}\right) - {\rm Sp}\left(1-\frac{\lambda_\nu E'-E}{(1+\beta')E'\xi_\nu}\right) + {\rm Sp}\left(1-\frac{\lambda_\nu E'-E}{(1-\beta)E\lambda_\nu\xi_\nu}\right) + {\rm Sp}\left(1-\frac{\lambda_\nu E'-E}{(1+\beta)E\lambda_\nu\xi_\nu}\right)\right], \tag{6.45}$$

where $\xi_\nu = \dfrac{2\nu}{(\nu+1)(\nu-1)}$ and $\lambda_\nu = \dfrac{3\nu-1}{\nu-1}$. Note that same result has been reported earlier in Ref. [160], albeit possible typographical errors.

Finally adding up all the contributions yields the LO differential cross section of emission of a real soft photon with all possible energies less then Δ_γ^* in the *lab*-frame:

$$\left[\frac{{\rm d}\sigma_{br}^{\rm (LO)}(Q^2)}{{\rm d}\Omega_l'}\right]_{\gamma\gamma^*}^{(E_{\gamma^*}<\Delta_\gamma^*)} = \left[\frac{{\rm d}\sigma_{el}(Q^2)}{{\rm d}\Omega_l'}\right]_\gamma\left[{\bf IR}_{\gamma\gamma^*}^{l(0)} + \frac{\alpha}{\pi}\left(-\widetilde{L}_{\rm ii} - \widetilde{L}_{\rm ff} + \widetilde{L}_{\rm if}\right)\right], \tag{6.46}$$

where the term

$${\bf IR}_{\gamma\gamma^*}^{(0)} \equiv {\bf IR}_{\gamma\gamma^*}^{l(0)} = \frac{\alpha}{\pi}\left[\frac{1}{|\epsilon_{\rm IR}|} + \gamma_E - \ln\left(\frac{4\pi\mu^2}{-Q^2}\right)\right]\left[\frac{\nu^2+1}{2\nu}\ln\left[\frac{\nu+1}{\nu-1}\right] - 1\right], \tag{6.47}$$

collects all the leading chiral order IR divergences arising from the soft photon emission contribution of the leptons. Correspondingly, the $\mathcal{O}(\alpha)$ fractional contribution from the LO bremsstrahlung cross section can be obtained in the form

$$\delta_{\gamma\gamma^*}^{(0)}(Q^2) = {\bf IR}_{\gamma\gamma^*}^{(0)} + \overline{\delta}_{\gamma\gamma^*}^{(0)}(Q^2), \tag{6.48}$$

where the finite part of $\delta_{\gamma\gamma^*}^{(0)}$ reads [50, 139]

$$\begin{aligned}\overline{\delta}_{\gamma\gamma^*}^{(0)} &= \frac{\alpha}{\pi}\left(-\widetilde{L}_{\rm ii} - \widetilde{L}_{\rm ff} + \widetilde{L}_{\rm if}\right)\\ &= \frac{\alpha}{\pi}\left[\ln\left(\frac{4\eta^2\Delta_\gamma^{*2}}{-Q^2}\right)\left[\frac{\nu^2+1}{2\nu}\ln\left[\frac{\nu+1}{\nu-1}\right]-1\right] + \frac{1}{4\beta}\ln\sqrt{\frac{1+\beta}{1-\beta}}\right.\\ &\quad + \frac{1}{4\beta'}\ln\sqrt{\frac{1+\beta'}{1-\beta'}} - \frac{\nu^2+1}{2\nu}\left\{\ln^2\sqrt{\frac{1+\beta}{1-\beta}} - \ln^2\sqrt{\frac{1+\beta'}{1-\beta'}}\right.\\ &\quad \left.\left. + {\rm Sp}\left(1-\frac{\lambda_\nu E'-E}{(1-\beta')E'\xi_\nu}\right) + {\rm Sp}\left(1-\frac{\lambda_\nu E'-E}{(1+\beta')E'\xi_\nu}\right)\right.\right.\end{aligned}$$

$$- \mathrm{Sp}\left(1 - \frac{\lambda_\nu E' - E}{(1-\beta)E\lambda_\nu\xi_\nu}\right) - \mathrm{Sp}\left(1 - \frac{\lambda_\nu E' - E}{(1+\beta)E\lambda_\nu\xi_\nu}\right)\Bigg\}\Bigg]. \tag{6.49}$$

Thus, we observe that the IR divergence appearing at this order from the bremsstrahlung contributions are exactly equal and opposite to that arising from the one-loop virtual contributions found earlier [cf. Eq. (6.38)].

In this section, we have demonstrated an IR-free result for the total radiative contributions at this order. To that end we now present the one-loop $\mathcal{O}(\alpha)$ (finite) expression for the full fractional radiative corrections to the $\ell\mathrm{p} \to \ell\mathrm{p}$ elastic scattering cross section at LO in HBχPT as given by sum, $\delta^{(0)}_{2\gamma} = \delta^{(0)}_{\gamma\gamma} + \delta^{(0)}_{\gamma\gamma^*} \equiv \overline{\delta}^{(0)}_{\gamma\gamma} + \overline{\delta}^{(0)}_{\gamma\gamma^*}$, i.e.,

$$\begin{aligned}
\delta^{(0)}_{2\gamma} = \frac{\alpha}{\pi}\Bigg[&\frac{\nu^2+1}{4\nu}\ln\left[\frac{\nu+1}{\nu-1}\right]\ln\left[\frac{\nu^2-1}{4\nu^2}\right] + \frac{2\nu^2+1}{2\nu}\ln\left[\frac{\nu+1}{\nu-1}\right] - \frac{\nu^2+1}{2\nu}\Bigg\{\mathrm{Sp}\left(\frac{\nu+1}{2\nu}\right) \\
&- \mathrm{Sp}\left(\frac{\nu-1}{2\nu}\right)\Bigg\} - 2 + \sum_{f=e,\mu,\tau}\Bigg\{\frac{2}{3}\left(\nu_f^2 - \frac{8}{3}\right) + \nu_f\left(\frac{3-\nu_f^2}{3}\right)\ln\left[\frac{\nu_f+1}{\nu_f-1}\right]\Bigg\} \\
&- \frac{2}{3}\left(\nu_\pi^2 + \frac{1}{3}\right) + \frac{\nu_\pi^3}{3}\ln\left[\frac{\nu_\pi+1}{\nu_\pi-1}\right] + \frac{1}{\nu}\left(\frac{2m_l^2}{Q^2+4EE'}\right)\ln\left[\frac{\nu+1}{\nu-1}\right] \\
&+ \ln\left(\frac{4\eta^2\Delta_\gamma^{*2}}{m_l^2}\right)\left[\frac{\nu^2+1}{2\nu}\ln\left[\frac{\nu+1}{\nu-1}\right] - 1\right] + \frac{1}{4\beta}\ln\sqrt{\frac{1+\beta}{1-\beta}} + \frac{1}{4\beta'}\ln\sqrt{\frac{1+\beta'}{1-\beta'}} \\
&- \frac{\nu^2+1}{2\nu}\Bigg\{\ln^2\sqrt{\frac{1+\beta}{1-\beta}} - \ln^2\sqrt{\frac{1+\beta'}{1-\beta'}} + \mathrm{Sp}\left(1 - \frac{\lambda_\nu E' - E}{(1-\beta')E'\xi_\nu}\right) \\
&\quad + \mathrm{Sp}\left(1 - \frac{\lambda_\nu E' - E}{(1+\beta')E'\xi_\nu}\right) - \mathrm{Sp}\left(1 - \frac{\lambda_\nu E' - E}{(1-\beta)E\lambda_\nu\xi_\nu}\right) \\
&\quad - \mathrm{Sp}\left(1 - \frac{\lambda_\nu E' - E}{(1+\beta)E\lambda_\nu\xi_\nu}\right)\Bigg\}\Bigg] + \mathcal{O}\left(\frac{1}{M^2}\right).
\end{aligned} \tag{6.50}$$

In Fig. [6.7] we summarize all the hitherto discussed fractional radiative correction (with respect to the LO Born ℓ-p elastic cross section) at LO in HBχPT, namely, the total VP correction, $\delta^{(0)}_{\mathrm{vac}} = \sum_{f=e,\mu,\tau}\delta^{(0)}_{\mathrm{vac};f} + \delta^{(0)}_{\mathrm{vac};\pi}$, total lepton-photon VC, $\overline{\delta}^{(0)}_{\gamma\gamma;\,\mathrm{vertex}} = \overline{\delta}^{(0)}_{\gamma\gamma;1} + \delta^{(0)}_{\gamma\gamma;2}$, and the bremsstrahlung correction due to soft photon emission $\overline{\delta}^{(0)}_{\gamma\gamma^*}$, in the MUSE kinematic range. A key feature of these LO radiative corrections is that they are *charge-symmetric*, viz. the cross section is identical for both $\ell^-\mathrm{p}$ and $\ell^+\mathrm{p}$ scatterings. We find that the negative bremsstrahlung contributions constitute the most dominant corrections in this low-Q^2 domain. In contrast, the lepton-photon VC and VP correction are both

positive. Clearly, the plots in the figure suggest little sensitivity of the radiative corrections to the variation in incoming lepton beam momenta. While the VP contributions are identical in both electronic and muonic scattering, the following observations depict the contrasting nature in regard to the other two LO radiative corrections for electron and muon scattering in the MUSE domain:

- While both electronic VC and the soft photon bremsstrahlung contributions are very large and of comparable magnitudes (the latter going up to as large as 40 %, and more than twice larger than the former), the muonic VC is roughly two orders of magnitude smaller. The reason for this contrast is evidently the absence of Sudakov enhancement in muonic scattering, as explained earlier.

- The electron and muon bremsstrahlung corrections are both negative, but the latter is more than a magnitude smaller. Here too the Sudakov enhancement of the term $\overline{\delta}^{(0)}_{\gamma\gamma^*}$ plays a vital role which can be seen as follows. In the limit of small lepton mass (i.e., $|Q^2| \gg m_l^2$) we can write[6]

$$\overline{\delta}^{(0)}_{\gamma\gamma^*} \overset{Q^2\gg m_l^2}{\approx} \frac{\alpha}{\pi}\left[\ln\left(\frac{\eta^2\Delta^{*2}_\gamma}{EE'}\right)\left[\ln\left(\frac{-Q^2}{m_l^2}\right)-1\right]-\frac{1}{2}\ln^2\left(\frac{-Q^2}{m_l^2}\right)-\frac{1}{2}\ln^2\left(\frac{E}{E'}\right)\right.$$
$$\left.+\ln\left(\frac{-Q^2}{m_l^2}\right)-\frac{\pi^2}{3}-\mathrm{Sp}\left(\cos^2\frac{\theta}{2}\right)\right]. \tag{6.51}$$

  With regard to the MUSE kinematics this is indeed a good approximation for electron scattering ($m_e^2 = 0.25\times10^{-6}$ GeV^2) but invalid in the case of muon. Noting that Δ^*_γ is numerically very small, the first Sudakov-like term dominates the contribution making the whole expression negative.

- Large cancellations are seen to occur between the positive VC and negative soft bremsstrahlung contributions, leading up to 20 % radiative correction in electron

[6] It should be noted here that this expression differs by a factor $\ln\left(\frac{-Q^2}{m_l^2}\right)\left[\ln\left(\frac{-Q^2}{m_l^2}\right)-1\right]$ compared to the standard expression known in existing literature (see e.g., in Refs. [50, 139]). Such a difference arises due to the regularization scheme that we have adopted to separate the IR-divergent parts from the finite contribution to the radiative corrections. Specifically, in our dimensional regularized expressions we prefer to retain a factor of $\ln\left(\frac{4\pi\mu^2}{-Q^2}\right)$ in the IR singular part $\mathbf{IR}^{(0)}_{\gamma\gamma^*}$, instead of the similar factor $\ln\left(\frac{4\pi\mu^2}{m_l^2}\right)$ which is more standard in the literature. Observe that for the same reason our leptonic VC result [cf. Eq. (6.37)] also differs by the same extra factor.

scattering, while in muon scattering essential cancellation result between the comparable positive VP and negative bremsstrahlung contributions, leading up to 1 % correction for the largest beam momenta expected at MUSE.

6.3 Radiative correction at NLO in HBχPT

At LO in HBχPT the proton is essentially an infinitely heavy static object, such that the diagrams so far considered represent the scattering of leptons off a static Coulomb potential. The contribution from the recoil proton was completely ignored. At NLO in HBχPT, the leading corrections due to the proton recoil effects are represented by $\mathcal{O}(M^{-1})$ suppressed terms. In principle, the origin of these contributions are either (i) *kinematical* in nature, arising from the phase-space part of the integration leading to the cross section, or (ii) *dynamical* in nature, arising from the matrix element associated with the NLO interactions in the HBχPT Lagrangian. As discussed earlier, the former contributions drop out in the evaluation of $\delta_{2\gamma}^{(1)}$ that involve taking the ratio with respect to the Born cross section, Eq. (6.11), which already includes the $\mathcal{O}(M^{-1})$ phase-space recoil corrections. Thus, considering the relevant NLO interactions, the HBχPT power counting scheme discussed in the third chapter allows for diagrams containing either one NLO vertex or one NLO proton propagator. Also investigations in the previous chapter showed that the new contributions that appear at this order are NLO TPE diagrams as well as the non-vanishing bremsstrahlung contribution from NLO proton-photon vertices.

The NLO diagrams involved in the radiative and recoil corrections that we consider next are the $\mathcal{O}(e^4, \frac{1}{M})$ one-loop virtual corrections, along with those of the $\mathcal{O}(e^3, \frac{1}{M})$ real soft photon bremsstrahlung process. We again use DR to segregate the UV and IR divergences arising in the fractional radiative corrections to the cross section $\delta_{2\gamma}^{(1)} \sim \mathcal{O}\left(\alpha, \frac{1}{M}\right)$, i.e., NLO in HB$\chi$PT. To reiterate again, apart from the NLO TPE box diagrams, which were evaluated analytically in Chapter 5 using SPA, all the remaining virtual one-loop diagrams at NLO are evaluated exactly in this section. Let us then consider below each of the two kinds of NLO contributions below.

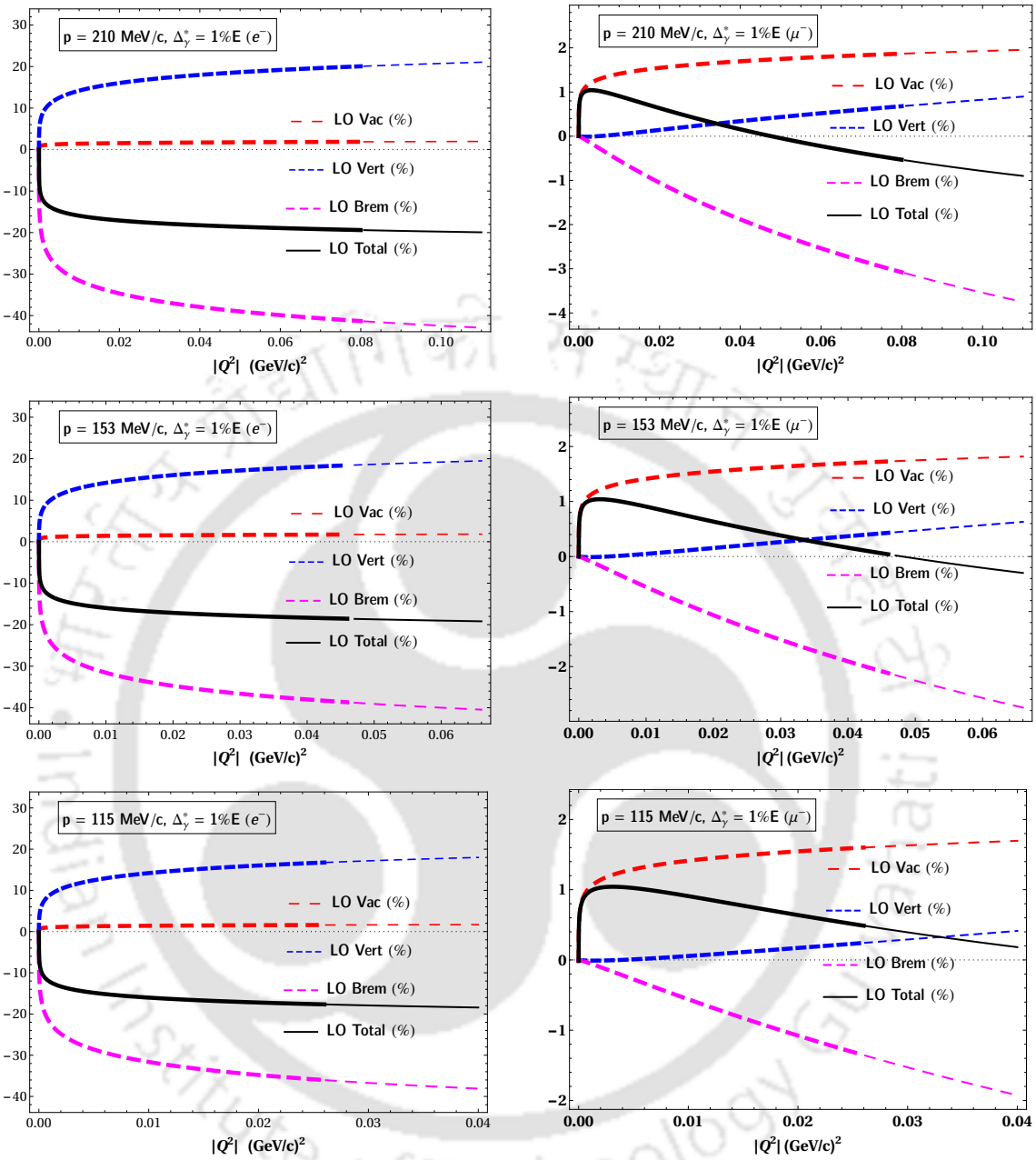

FIGURE 6.7: The individual one-loop LO fractional contributions (in percentage), namely, the vacuum polarization correction $\delta^{(0)}_{\rm vac}$, lepton-photon vertex correction $\overline{\delta}^{(0)}_{\gamma\gamma;\,\rm vertex}$, and the soft photon bremsstrahlung correction $\overline{\delta}^{(0)}_{\gamma\gamma^*}$, to the ep (left panel) and μp (right panel) elastic cross sections as a function of the squared four-momentum transfer $|Q^2|$ for the proposed MUSE beam momenta, namely, $p = 115,\ 153,\ 210$ MeV/c. The total LO contribution $\overline{\delta}^{(0)}_{\gamma\gamma}$ is also displayed. Each plot covers the full kinematically allowed scattering range, $0 < |Q^2| < |Q^2_{\rm max}|$, when $\theta \in [0, \pi]$ (cf. Table I of Chapter 5). The thickened portion of each curve corresponds to the MUSE kinematic cut, where $\theta \in [20^\circ, 100^\circ]$. The *lab*-frame detector resolution Δ^*_γ is taken to be 1 % of the incident lepton energy E.

6.3.1 One-loop NLO Virtual Corrections

Again in this case the contributions of the lepton and proton SEs (diagrams SEi,f$^{l(1)}$ and SEi,f$^{p(1)}_{\mathrm{A},\cdots,\mathrm{F}}$ shown in Fig. [6.8]) disappear in the on-shell limit for the external proton legs. Their derivatives, however, contribute to the respective wave function renormalization constants $Z_1^{l,p(1)}$. Thus, the contributions at this order [i.e., $\mathcal{O}(e^4, \frac{1}{M})$] should arise from other one-loop diagrams that include the lepton VC (diagram VC$^{l(1)}$ in Fig. [6.8]), proton VCs (diagrams VC$^{p(1)}_{\mathrm{A},..,\mathrm{G}}$ in Fig. [6.9]), VP (diagram VP$^{(1)}$ in Fig. [6.8]), and the NLO TPE corrections (cf. diagrams in Fig. [1] of Chapter 5).

6.3.1.1 Lepton Vertex and Vacuum Polarization Corrections at NLO

The NLO contributions from the lepton SE, lepton VC and the VP diagrams are shown in Fig. [6.8]. The result is akin to the LO result, Eq. (6.34), in that the amplitude of each of the above NLO diagram, apart from the lepton vertex term $\propto F_2^l$, factorizes into the NLO Born amplitude $\mathcal{M}_\gamma^{(1)}$, namely,

$$\begin{aligned}
\mathcal{M}_{\gamma\gamma}^{l(1)} &= \mathcal{M}_\gamma^{(1)} \left[F_1^{l;\,\mathrm{ren}}(Q^2) + \Delta\Pi(Q^2) \right] + \overline{\mathcal{M}}_\gamma^{(1)} F_2^l(Q^2)\,, \\
\overline{\mathcal{M}}_\gamma^{(1)} &= -\,\frac{e^2}{4m_l M Q^2} \left[\bar{u}_l(p') i\sigma^{\mu\nu} Q_\nu\, u_l(p) \right] \left[\chi^\dagger(p'_p)(p_p + p'_p)_\mu \chi(p_p) \right]\,,
\end{aligned} \tag{6.52}$$

where $F_1^{l;\,\mathrm{ren}}$ is the renormalized Dirac form factor of the lepton, Eq. (6.20). As demonstrated in the first section, the interference of the LO and NLO Born amplitudes being already of $\mathcal{O}(M^{-2})$ does not contribute to the elastic cross section. The same is also applicable to the interference of the LO Born amplitude $\mathcal{M}_\gamma^{(0)}$ with the above NLO amplitude $\overline{\mathcal{M}}_\gamma^{(1)}$, and the interference between the NLO Born amplitude $\mathcal{M}_\gamma^{(1)}$ and the LO radiative correction amplitude $\overline{\mathcal{M}}_\gamma^{(0)} \propto F_2^l$, resulting in $\mathcal{O}(M^{-2})$ expressions, such that the term

$$\begin{aligned}
\delta^{(1)}_{\gamma\gamma;2}(Q^2) &= \frac{2\sum_{spins} \mathcal{R}\mathrm{e}\left(\mathcal{M}_\gamma^{(0)\dagger}\, \overline{\mathcal{M}}_\gamma^{(1)} + \mathcal{M}_\gamma^{(1)\dagger}\, \overline{\mathcal{M}}_\gamma^{(0)} \right)}{\sum_{spins} |\mathcal{M}_\gamma^{(0)}|^2} F_2^l(Q^2) \\
&= \frac{Q^2}{2M^2} \frac{2\sum_{spins} \mathcal{R}\mathrm{e}\left(\mathcal{M}_\gamma^{(0)\dagger}\, \overline{\mathcal{M}}_\gamma^{(0)} \right)}{\sum_{spins} |\mathcal{M}_\gamma^{(0)}|^2} F_2^l(Q^2) = \mathscr{R}_Q \delta^{(0)}_{\gamma\gamma;2} \sim \mathcal{O}\left(\frac{1}{M^2} \right)\,,
\end{aligned} \tag{6.53}$$

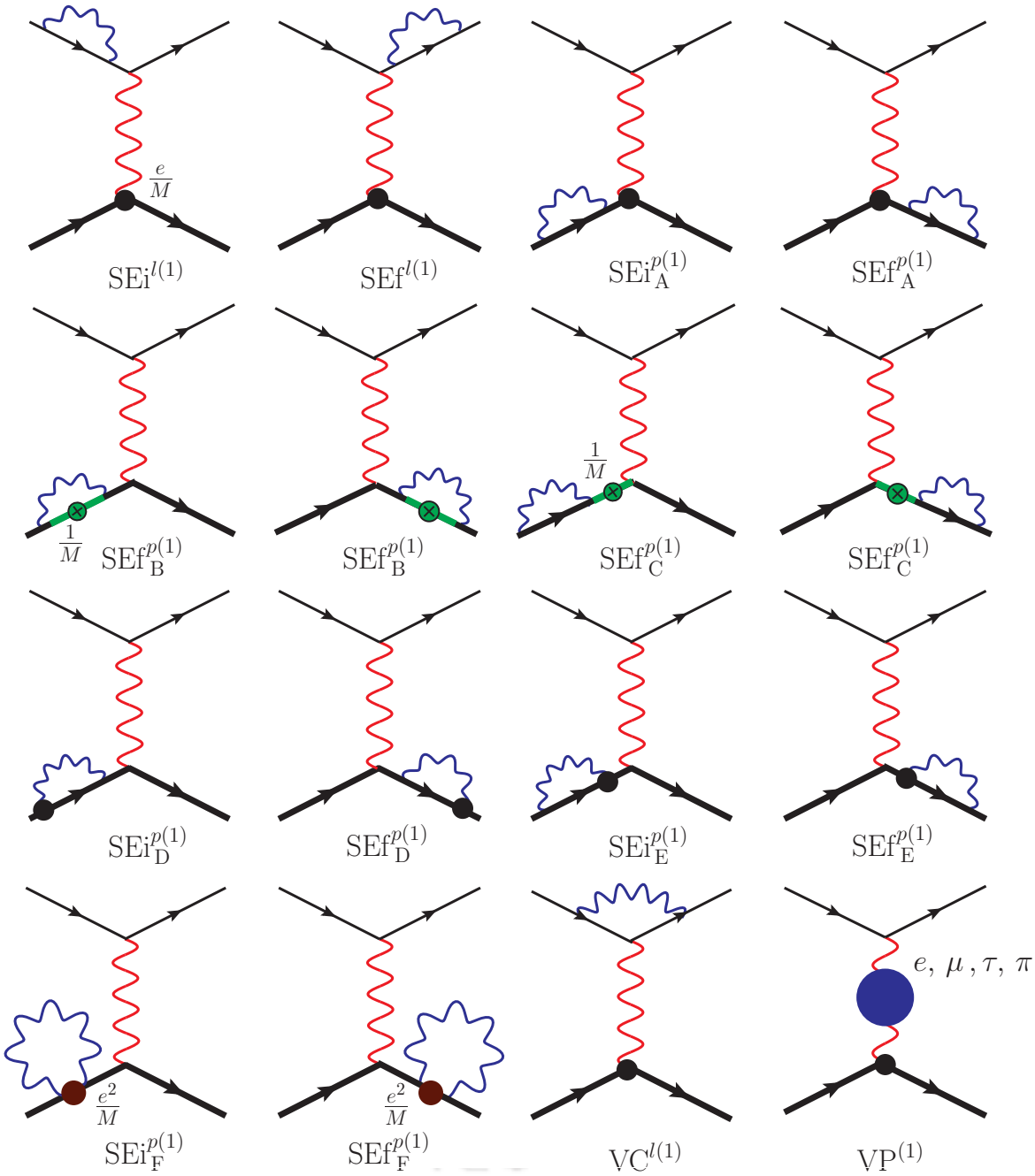

FIGURE 6.8: The one-loop lepton and proton self-energies, lepton vertex corrections and the leptonic and pionic vacuum polarization contributions at NLO in HBχPT [i.e., $\mathcal{O}\left(e^4, \frac{1}{M}\right)$], contributing to the fractional radiative corrections to the elastic ℓ-p scattering cross section, $\delta^{(1)}_{\gamma\gamma} \sim \mathcal{O}\left(\alpha, \frac{1}{M}\right)$. The proton-photon vertices represented by the filled blobs represent $\mathcal{O}(1/M)$ vertices. In particular, the proton self-energy "tadpoles" (diagrams SEi,f$^{p(1)}_{\rm F}$) are of $\mathcal{O}(e^2/M)$ in the proton-photon vertices. The self-energy contributions, however, disappear in on-shell limit of the external proton legs.

where $\mathscr{R}_Q = Q^2/(2M^2)$ [cf. Eq. (6.9) in the first section] and $\delta^{(0)}_{\gamma\gamma;2} \propto F_2^l$ [cf. Eq. (6.39) in the second section] is the LO lepton-photon VC. Therefore, the above term is not needed in our present analysis of $\mathcal{O}(1/M)$ working accuracy.

6.3.1.2 Proton Vertex Correction at NLO

A total of seven diagrams, $\mathrm{VC}_{\mathrm{A}}^{p(1)}$ to $\mathrm{VC}_{\mathrm{G}}^{p(1)}$, contribute to the proton-photon VC at NLO in HBχPT, five of which involve NLO vertex insertions, and the remaining two involve NLO propagator insertions, as displayed in Fig. [6.9]. The amplitudes of these diagrams, $\mathcal{M}^{p;(1);A,\ldots,G}_{\gamma\gamma;\,\mathrm{vertex}}$, can be expressed as follows:

$$
\begin{aligned}
i\mathcal{M}^{p(1);A}_{\gamma\gamma;\,\mathrm{vertex}} &= -\frac{e^4}{2MQ^2}\left[\bar{u}_l(p')\gamma^\mu u_l(p)\right]\int\frac{\mathrm{d}^4k}{(2\pi)^4} \\
&\quad\times\frac{\left[\chi^\dagger(p'_p)\left\{(p_p+p'_p-2k)_\mu-[v\cdot(p_p+p'_p-2k)]v_\mu\right\}\chi(p_p)\right]}{(k^2+i0)\,[v\cdot(p_p-k)+i0][v\cdot(p'_p-k)+i0]}\,,
\end{aligned}
$$

$$
\begin{aligned}
i\mathcal{M}^{p(1);B}_{\gamma\gamma;\,\mathrm{vertex}} &= -\frac{e^4}{2MQ^2}\left[\bar{u}_l(p')\gamma^\mu u_l(p)\right]\int\frac{\mathrm{d}^4k}{(2\pi)^4} \\
&\quad\times\frac{\left[\chi^\dagger(p'_p)\,v_\mu\chi(p_p)\right]}{(k^2+i0)\,[v\cdot(p'_p-k)+i0]}\left(1+\frac{p_p^2}{(v\cdot k)^2}-\frac{(p_p-k)^2}{(v\cdot k)^2}\right),
\end{aligned}
$$

$$
\begin{aligned}
i\mathcal{M}^{p(1);C}_{\gamma\gamma;\,\mathrm{vertex}} &= -\frac{e^4}{2MQ^2}\left[\bar{u}_l(p')\gamma^\mu u_l(p)\right]\int\frac{\mathrm{d}^4k}{(2\pi)^4} \\
&\quad\times\frac{\left[\chi^\dagger(p'_p)\,v_\mu\chi(p_p)\right]}{(k^2+i0)\,[v\cdot(p_p-k)+i0]}\left(1+\frac{(p'_p)^2}{(v\cdot k)^2}-\frac{(p'_p-k)^2}{(v\cdot k)^2}\right),
\end{aligned}
$$

$$
\begin{aligned}
i\mathcal{M}^{p;(1);D}_{\gamma\gamma;\,\mathrm{vertex}} &= -\frac{e^4}{2MQ^2}\left[\bar{u}_l(p')\gamma^\mu u_l(p)\right]\int\frac{\mathrm{d}^4k}{(2\pi)^4} \\
&\quad\times\frac{\left[\chi^\dagger(p'_p)v_\mu\left\{[v\cdot(2p_p-k)]-[v\cdot(2p_p-k)]v^2\right\}\chi(p_p)\right]}{(k^2+i0)\,[v\cdot(p_p-k)+i0][v\cdot(p'_p-k)+i0]}=0\,,
\end{aligned}
$$

$$
\begin{aligned}
i\mathcal{M}^{p(1);E}_{\gamma\gamma;\,\mathrm{vertex}} &= -\frac{e^4}{2MQ^2}\left[\bar{u}_l(p')\gamma^\mu u_l(p)\right]\int\frac{\mathrm{d}^4k}{(2\pi)^4} \\
&\quad\times\frac{\left[\chi^\dagger(p'_p)v_\mu\left\{[v\cdot(2p'_p-k)]-[v\cdot(2p'_p-k)]v^2\right\}\chi(p_p)\right]}{(k^2+i0)\,[v\cdot(p_p-k)+i0][v\cdot(p'_p-k)+i0]}=0\,,
\end{aligned}
$$

$$
i\mathcal{M}^{p(1);F}_{\gamma\gamma;\,\mathrm{vertex}} = -\frac{e^4}{2MQ^2}\int\frac{\mathrm{d}^4k}{(2\pi)^4}\frac{\left[\bar{u}_l(p')\gamma^\mu u_l(p)\right]\,\left[\chi^\dagger(p'_p)v_\mu(1-v^2)\chi(p_p)\right]}{(k^2+i0)\,[v\cdot(p_p-k)+i0]}=0\,,
$$

$$i\mathcal{M}^{p(1);G}_{\gamma\gamma;\,\text{vertex}} = -\frac{e^4}{2MQ^2}\int\frac{\mathrm{d}^4k}{(2\pi)^4}\frac{[\bar{u}_l(p')\gamma^\mu u_l(p)]\,\left[\chi^\dagger(p'_p)v_\mu(1-v^2)\chi(p_p)\right]}{(k^2+i0)\,[v\cdot(p'_p-k)+i0]} = 0\,. \quad (6.54)$$

Since $v^2 = 1$, the last four amplitudes vanish, namely, $\mathcal{M}^{p(1);D,..,G}_{\gamma\gamma;\,\text{vertex}} = 0$. To obtain the remaining three amplitudes, $\mathcal{M}^{p(1);A,B,C}_{\gamma\gamma;\,\text{vertex}}$, we have used the NLO relations, $v\cdot p_p = -\frac{p_p^2}{2M} + \mathcal{O}(M^{-2})$ and $v\cdot p'_p = -\frac{(p'_p)^2}{2M} + \mathcal{O}(M^{-2})$, in the denominators of the proton propagators, followed by a $1/M$ expansion and retaining terms up to $\mathcal{O}(M^{-1})$. Thus, we obtain the total NLO proton VC amplitude as

$$\begin{aligned} i\mathcal{M}^{p(1)}_{\gamma\gamma;\,\text{vertex}} &= i\mathcal{M}^{p(1);A}_{\gamma\gamma;\,\text{vertex}} + i\mathcal{M}^{p(1);B}_{\gamma\gamma;\,\text{vertex}} + i\mathcal{M}^{p(1);C}_{\gamma\gamma;\,\text{vertex}} \\ &= -\frac{e^4}{2MQ^2}\,[\bar{u}_l(p')\gamma^\mu u_l(p)]\int\frac{\mathrm{d}^4k}{(2\pi)^4}\frac{\left[\chi^\dagger(p'_p)(p_p+p'_p-2k)_\mu\chi(p_p)\right]}{(k^2+i0)\,(-v\cdot k+i0)^2} \\ &\qquad\times\left(1-\frac{p_p^2}{2M(v\cdot k)}+\cdots\right)\left(1-\frac{(p'_p)^2}{2M(v\cdot k)}+\cdots\right) \end{aligned}$$

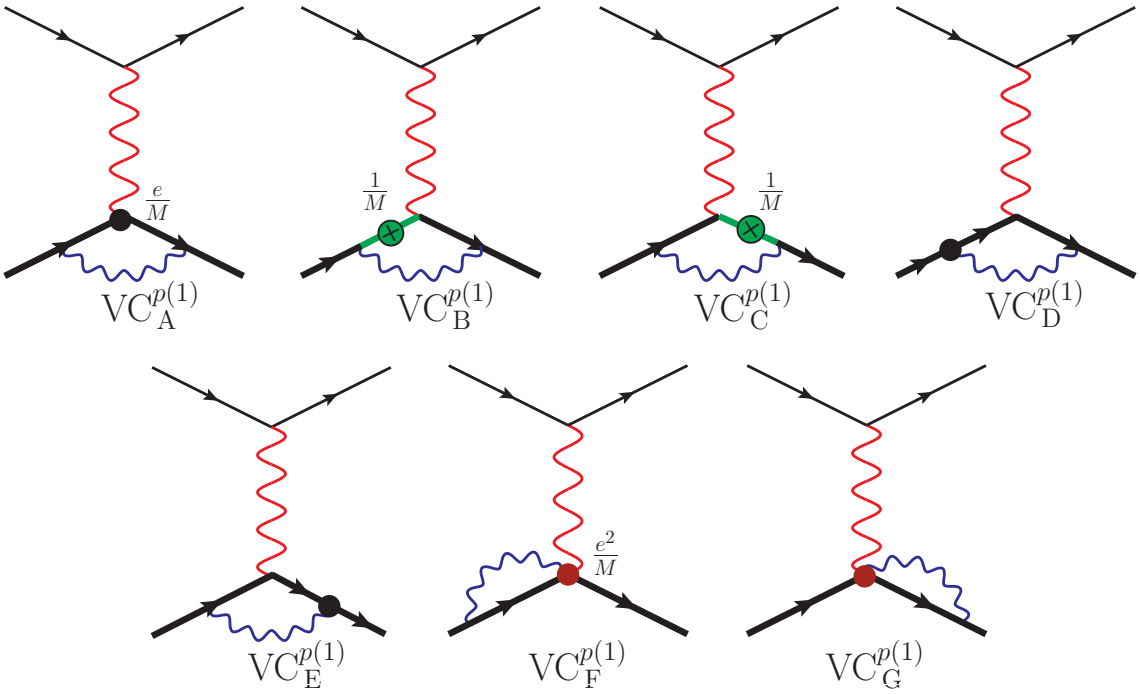

FIGURE 6.9: One-loop proton-photon vertex correction diagrams at NLO in HBχPT [i.e., $\mathcal{O}(e^4, \frac{1}{M})$], contributing to the fractional radiative corrections to the elastic ℓ-p scattering cross section, $\delta^{(1)}_{\gamma\gamma} \sim \mathcal{O}\left(\alpha, \frac{1}{M}\right)$. The proton-photon vertices represented by the filled blobs represent $\mathcal{O}(1/M)$ vertices. In particular, the two-photon proton vertices (diagrams $\text{VC}^{p(1)}_{\text{F,G}}$) are of $\mathcal{O}(e^2/M)$. The proton propagators with the crossed blobs "$\otimes$" represent $\mathcal{O}(1/M)$ propagator insertions (diagrams $\text{VC}^{p(1)}_{\text{B,C}}$). All these diagrams, however, disappear and do contribute to the cross section.

$$
\begin{aligned}
&- \frac{e^4}{2MQ^2}\left[\bar{u}_l(p')\gamma^\mu u_l(p)\right]\,\left[\chi^\dagger(p'_p)v_\mu\chi(p_p)\right]\int\frac{\mathrm{d}^4k}{(2\pi)^4}\frac{1}{k^2(-v\cdot k+i0)}\\
&\qquad\times\left\{\left(1-\frac{p_p^2}{2M(v\cdot k)}+\cdots\right)\left(\frac{(p_p)^2}{(v\cdot k)^2}-\frac{(p_p-k)^2}{(v\cdot k)^2}\right)\right.\\
&\qquad\left.+\left(1-\frac{(p'_p)^2}{2M(v\cdot k)}+\cdots\right)\left(\frac{(p'_p)^2}{(v\cdot k)^2}-\frac{(p'_p-k)^2}{(v\cdot k)^2}\right)\right\},
\end{aligned}
$$

where the ellipses in the above expression represent k^2 (loop momentum) dependent terms of $\mathcal{O}(1/M^2)$. After removing the odd integrals the remaining expression involving scaleless loop integrals vanishes using DR (see Appendix C of Ref. [240]; also see Ref. [241]), as akin to the LO proton VC result obtained earlier, namely,

$$
\begin{aligned}
\mathcal{M}^{p(1)}_{\gamma\gamma;\,\mathrm{vertex}} &= \frac{ie^4}{2MQ^2}\left[\bar{u}_l(p')\gamma^\mu u_l(p)\right]\,\left[\chi^\dagger(p'_p)(p_p+p'_p)_\mu\chi(p_p)\right]\\
&\quad\times\int\frac{\mathrm{d}^4k}{(2\pi)^4}\frac{1}{(k^2+i0)(-v\cdot k+i0)^2}\left(1-\frac{p_p^2}{2M(v\cdot k)}-\frac{(p'_p)^2}{2M(v\cdot k)}+\cdots\right)\\
&\quad-\frac{ie^4}{2MQ^2}\left[\bar{u}_l(p')\gamma^\mu u_l(p)\right]\,\left[\chi^\dagger(p'_p)v_\mu\chi(p_p)\right]\\
&\quad\times\int\frac{\mathrm{d}^4k}{(2\pi)^4}\frac{k^2}{(k^2+i0)(-v\cdot k+i0)^3}\left(2-\frac{p_p^2}{2M(v\cdot k)}-\frac{(p'_p)^2}{2M(v\cdot k)}+\cdots\right)\\
&\xrightarrow{\text{DR}}\ 0\,.
\end{aligned}
\tag{6.55}
$$

Consequently, none of the one-loop diagrams associated with the proton-photon VC shown in Fig. [6.9] contributes to radiative correction at NLO in HBχPT, leaving only the NLO TPE diagrams that account for the radiative and recoil effects at the one-loop level which we now discuss.

6.3.1.3 Two-Photon Exchange (TPE) Corrections at NLO

The NLO TPE diagrams at $\mathcal{O}\left(e^4, M^{-1}\right)$ contributing to the fractional radiative correction, $\delta^{(1)}_{2\gamma} \sim \mathcal{O}\left(\alpha, M^{-1}\right)$, comprising of the direct-box, crossed-box and the seagull amplitudes (cf. Fig. [1] of Chapter 5), have been studied in details in the previous chapter. While the box diagrams were evaluated analytically using SPA, the relevant part of the seagull diagram was evaluated exactly. As we have seen, only the former amplitudes (in

the SPA) get factorized into the LO Born amplitude, namely [221],

$$\begin{aligned}\mathcal{M}^{lp(1)}_{\gamma\gamma;\,\mathrm{TPE}} = &-\frac{\alpha Q^2}{4\pi ME}\mathcal{M}^{(0)}_{\gamma}\Bigg\{-\left[\frac{1}{|\epsilon_{\mathrm{IR}}|}+\gamma_E-\ln\left(\frac{4\pi\mu^2}{-Q^2}\right)\right]\left[\frac{1}{\beta}\ln\sqrt{\frac{1+\beta}{1-\beta}}\right.\\ &\left.+\frac{E}{\beta' E'}\ln\sqrt{\frac{1+\beta'}{1-\beta'}}\right]+\frac{1}{\beta}\left[\frac{\pi^2}{2}+\ln\left(\frac{-Q^2}{m_l^2}\right)\ln\sqrt{\frac{1+\beta}{1-\beta}}\right.\\ &\left.-\ln^2\sqrt{\frac{1+\beta}{1-\beta}}-\mathrm{Sp}\left(\frac{2\beta}{1+\beta}\right)\right]+\frac{E}{\beta' E'}\left[\frac{\pi^2}{2}+\ln\left(\frac{-Q^2}{m_l^2}\right)\right.\\ &\left.\times\ln\sqrt{\frac{1+\beta'}{1-\beta'}}-\ln^2\sqrt{\frac{1+\beta'}{1-\beta'}}-\mathrm{Sp}\left(\frac{2\beta'}{1+\beta'}\right)\right]\Bigg\}+\widetilde{\mathcal{M}}^{(i)}_{\mathrm{seagull}}\\ =&-\frac{\alpha Q^2}{2\pi ME\beta}\mathcal{M}^{(0)}_{\gamma}\Bigg\{-\left[\frac{1}{|\epsilon_{\mathrm{IR}}|}+\gamma_E-\ln\left(\frac{4\pi\mu^2}{-Q^2}\right)\right]\ln\sqrt{\frac{1+\beta}{1-\beta}}+\frac{\pi^2}{2}\\ &+\ln\left(\frac{-Q^2}{m_l^2}\right)\ln\sqrt{\frac{1+\beta}{1-\beta}}-\ln^2\sqrt{\frac{1+\beta}{1-\beta}}\\ &-\mathrm{Sp}\left(\frac{2\beta}{1+\beta}\right)\Bigg\}+\widetilde{\mathcal{M}}^{(i)}_{\mathrm{seagull}}+\mathcal{O}\left(\frac{1}{M^2}\right)\,,\end{aligned}\tag{6.56}$$

where $\widetilde{\mathcal{M}}^{(i)}_{\mathrm{seagull}}$ is the non-factorizable "residual" part of the seagull amplitude contributing to the elastic amplitude that is evaluated in details in Appendix C.

We can now determine the total one-loop virtual radiative and recoil correction amplitude at NLO:

$$\mathcal{M}^{(1)}_{\gamma\gamma}=\mathcal{M}^{l(1)}_{\gamma\gamma}+\mathcal{M}^{lp(1)}_{\gamma\gamma;\,\mathrm{TPE}}\,,\tag{6.57}$$

where $\mathcal{M}^{l(1)}_{\gamma\gamma}$ was determined from the lepton VC and the VP diagrams at NLO [cf. Eq. (6.52)], and $\mathcal{M}^{lp(1)}_{\gamma\gamma;\,\mathrm{TPE}}$ is the above NLO TPE amplitude, Eq. (6.56). This yields the correction to the elastic differential cross section at NLO in HBχPT given by

$$\left[\frac{\mathrm{d}\sigma^{(\mathrm{NLO})}_{el}(Q^2)}{\mathrm{d}\Omega'_l}\right]_{\gamma\gamma}=\left[\frac{\mathrm{d}\sigma_{el}(Q^2)}{\mathrm{d}\Omega'_l}\right]_{\gamma}\delta^{(1)}_{\gamma\gamma}(Q^2)\,,\tag{6.58}$$

where the $\mathcal{O}(\alpha)$ fractional contribution from the virtual part is formally

$$\begin{aligned}\delta^{(1)}_{\gamma\gamma}(Q^2) &= \frac{2\sum_{spins}\mathcal{R}\mathrm{e}\left(\mathcal{M}^{(0)\dagger}_{\gamma}\mathcal{M}^{(1)}_{\gamma\gamma}+\mathcal{M}^{(0)\dagger}_{\gamma\gamma}\mathcal{M}^{(1)}_{\gamma}\right)}{\sum_{spins}|\mathcal{M}^{(0)}_{\gamma}|^2} - 2\mathscr{R}_Q \\ &= \mathbf{IR}^{(1)}_{\gamma\gamma} + \overline{\delta}^{(0)}_{\gamma\gamma}(Q^2)\mathscr{R}_Q + \overline{\delta}^{(\mathrm{box})}_{\gamma\gamma}(Q^2) + \delta^{(\mathrm{seagull})}_{\gamma\gamma}(Q^2)\,, \end{aligned} \tag{6.59}$$

where $\mathscr{R}_Q = Q^2/(2M^2)$ [cf. Eq. (6.9) in the first section], which gives the ratio of the NLO and LO Born contributions, is already of $\mathcal{O}(M^{-2})$, and $\overline{\delta}^{(0)}_{\gamma\gamma}$ is the finite part of the LO virtual correction, Eq. (6.37). The term

$$\mathbf{IR}^{(1)}_{\gamma\gamma} = \mathbf{IR}^{(0)}_{\gamma\gamma}\,\mathscr{R}_Q + \mathbf{IR}^{lp(1)}_{\gamma\gamma;\,\mathrm{TPE}}\,, \tag{6.60}$$

collects all the IR divergences arising from the one-loop lepton VC and TPE box and cross-box diagrams at NLO, with $\mathbf{IR}^{(0)}_{\gamma\gamma}$ already given earlier in Eq. (6.38), and

$$\begin{aligned}\mathbf{IR}^{lp(1)}_{\gamma\gamma;\,\mathrm{TPE}} &= \frac{\alpha Q^2}{\pi M}\left[\frac{1}{|\epsilon_{\mathrm{IR}}|}+\gamma_E-\ln\left(\frac{4\pi\mu^2}{-Q^2}\right)\right]\left[\frac{1}{2E\beta}\ln\sqrt{\frac{1+\beta}{1-\beta}}+\frac{1}{2E'\beta'}\ln\sqrt{\frac{1+\beta'}{1-\beta'}}\right] \\ &= \frac{\alpha Q^2}{\pi ME\beta}\left[\frac{1}{|\epsilon_{\mathrm{IR}}|}+\gamma_E-\ln\left(\frac{4\pi\mu^2}{-Q^2}\right)\right]\ln\sqrt{\frac{1+\beta}{1-\beta}}+\mathcal{O}\left(\frac{1}{M^2}\right). \end{aligned} \tag{6.61}$$

The remaining finite terms, namely [221],

$$\begin{aligned}\overline{\delta}^{(\mathrm{box})}_{\gamma\gamma}(Q^2) &= -\frac{\alpha Q^2}{\pi ME\beta}\left[\ln\left(\frac{-Q^2}{m_l^2}\right)\ln\sqrt{\frac{1+\beta}{1-\beta}}-\ln^2\sqrt{\frac{1+\beta}{1-\beta}}+\frac{\pi^2}{2}\right. \\ &\qquad \left.-\mathrm{Sp}\left(\frac{2\beta}{1+\beta}\right)\right]+\mathcal{O}\left(\frac{1}{M^2}\right), \\ \delta^{(\mathrm{seagull})}_{\gamma\gamma}(Q^2) &= \frac{2\mathcal{R}e\sum_{spin}\left(\mathcal{M}^{(0)\dagger}_{\gamma}\widetilde{\mathcal{M}}^{(i)}_{\mathrm{seagull}}\right)}{\sum_{spin}|\mathcal{M}_{\gamma}|^2} \\ &= -\frac{\alpha Q^2}{\pi ME\beta}\left[\frac{E^2\beta}{m_l^2}\left(\frac{4m_l^2}{Q^2+4E^2}\right)\left(\mathcal{I}_1+\mathcal{I}_2+\frac{Q^2}{m_l^2}\left(\mathcal{I}_3-\mathcal{I}_4\right)\right)\right]+\mathcal{O}\left(\frac{1}{M^2}\right) \end{aligned} \tag{6.62}$$

are finite arising from the NLO TPE integrals, as discussed in the previous chapter, where the Q^2 dependent integrals, $\mathcal{I}_{i=1,..,4} = \mathcal{I}_{i=1,...,4}(Q^2)$, are presented in Appendix C. Consequently, we see that all the one-loop virtual radiative and recoil contributions other than the TPE diagrams though formally appearing at NLO in the chiral power counting

scheme, are *de facto* kinematically suppressed by one more recoil order contributing at NNLO, i.e., at $\mathcal{O}(M^{-2})$. Such $1/M^2$ contributions are *per se* unnecessary in our present radiative analysis with $\mathcal{O}(M^{-2})$ working accuracy, nevertheless we prefer to retain only the IR-divergent parts for the time being in order to demonstrate their cancellations from the inelastic bremsstrahlung counterparts at NLO. Thus, at $\mathcal{O}(M^{-1})$ the finite part of the one-loop radiative and recoil corrections arises only due to the NLO TPE contributions and reads

$$\begin{aligned}\overline{\delta}^{(1)}_{\gamma\gamma}(Q^2) &= \overline{\delta}^{(\text{box})}_{\gamma\gamma}(Q^2) + \delta^{(\text{seagull})}_{\gamma\gamma}(Q^2) \\ &= -\frac{\alpha Q^2}{\pi M E \beta}\left[\ln\left(\frac{-Q^2}{m_l^2}\right)\ln\sqrt{\frac{1+\beta}{1-\beta}} - \ln^2\sqrt{\frac{1+\beta}{1-\beta}} + \frac{\pi^2}{2} - \text{Sp}\left(\frac{2\beta}{1+\beta}\right)\right. \\ &\quad \left. + \frac{4E^2\beta}{Q^2+4E^2}\left(\mathcal{I}_1 + \mathcal{I}_2 + \frac{Q^2}{m_l^2}\left(\mathcal{I}_3 - \mathcal{I}_4\right)\right)\right] + \mathcal{O}\left(\frac{1}{M^2}\right). \end{aligned} \tag{6.63}$$

6.3.2 Soft Bremsstrahlung Corrections at NLO

The soft bremsstrahlung corrections at NLO in HBχPT can arise from two kinds of diagrams: either leptons radiating with an NLO proton-photon vertex or proton radiating from the NLO vertices. In other words with proton bremsstrahlung contributions from proton-photon vertices explicitly vanishing at LO, the NLO bremsstrahlung diagrams constitute the leading non-vanishing radiative and recoil corrections along with the one-loop counterparts, namely, the NLO TPE diagrams. These lepton and proton bremsstrahlung diagrams at NLO are listed in Fig. [6.10], where γ^*_{soft} is used to denote the undetectable emitted soft photon. The lepton bremsstrahlung diagrams are denoted as $\text{Ri}^{l(1)}$ and $\text{Rf}^{l(1)}$, and the proton bremsstrahlung diagrams are denoted as $\text{Ri}^{p(1)}$, $\text{Rv}^{p(1)}$ and $\text{Rf}^{p(1)}$. As in the LO bremsstrahlung evaluations, it is legitimate to use SPA at NLO. In SPA, the structure of the NLO lepton bremsstrahlung amplitudes are analogous to the corresponding LO amplitudes in that they get factorized into the NLO Born amplitude $\mathcal{M}^{(1)}_{\gamma}$, namely,

$$\begin{aligned}\mathcal{M}^{l(1);\,\text{i}}_{\gamma\gamma^*} \overset{\gamma^*_{\text{soft}}}{\rightsquigarrow} \widetilde{\mathcal{M}^{l(1);\,\text{i}}_{\gamma\gamma^*}} &= e\mathcal{M}^{(1)}_{\gamma}\left(\frac{p\cdot\epsilon^*}{p\cdot k}\right), \\ \mathcal{M}^{l(1);\,\text{f}}_{\gamma\gamma^*} \overset{\gamma^*_{\text{soft}}}{\rightsquigarrow} \widetilde{\mathcal{M}^{l(1);\,\text{f}}_{\gamma\gamma^*}} &= -e\mathcal{M}^{(1)}_{\gamma}\left(\frac{p'\cdot\epsilon^*}{p'\cdot k}\right). \end{aligned} \tag{6.64}$$

In contrast the NLO proton bremsstrahlung amplitudes in the SPA gets factorized into the LO Born amplitudes, namely,

$$\mathcal{M}^{p(1);\,\mathrm{i}}_{\gamma\gamma^*} \overset{\gamma^*_{\rm soft}}{\rightsquigarrow} \widetilde{\mathcal{M}^{p(1);\,\mathrm{i}}_{\gamma\gamma^*}} = \frac{e}{M}\mathcal{M}^{(0)}_{\gamma}\left(\frac{p_p\cdot\epsilon^*}{v\cdot k}\right),$$
$$\mathcal{M}^{p(1);\,\mathrm{f}}_{\gamma\gamma^*} \overset{\gamma^*_{\rm soft}}{\rightsquigarrow} \widetilde{\mathcal{M}^{p(1);\,\mathrm{f}}_{\gamma\gamma^*}} = -\frac{e}{M}\mathcal{M}^{(0)}_{\gamma}\left(\frac{p'_p\cdot\epsilon^*}{v\cdot k}\right). \tag{6.65}$$

At $\mathcal{O}\left(\alpha^3, M^{-1}\right)$ only the interference between the LO and NLO bremsstrahlung amplitudes contributes to the cross section. The interference of the four NLO bremsstrahlung diagrams, $\mathrm{Ri}^{l(1)}$, $\mathrm{Rf}^{l(1)}$, $\mathrm{Ri}^{p(1)}$ and $\mathrm{Rf}^{p(1)}$, with the LO lepton bremsstrahlung diagrams, $\mathrm{Ri}^{l(0)}$ and $\mathrm{Rf}^{l(0)}$, lead to IR divergences. This is, however, not the case with the proton bremsstrahlung diagram, $\mathrm{Rv}^{p(1)}$, whose interference with the LO lepton bremsstrahlung diagrams yields a finite result. This diagram is in effect the counterpart of the finite TPE "seagull" diagram with a single proton-photon NLO vertex given by,

$$\mathcal{M}^{p(1);\,\mathrm{v}}_{\gamma\gamma^*} = -\frac{e^3}{MQ^2}\left[\bar{u}_l(p')(\epsilon^*\cdot\gamma)\,u_l(p)\right]\left[\chi^\dagger(p'_p)\chi(p_p)\right]. \tag{6.66}$$

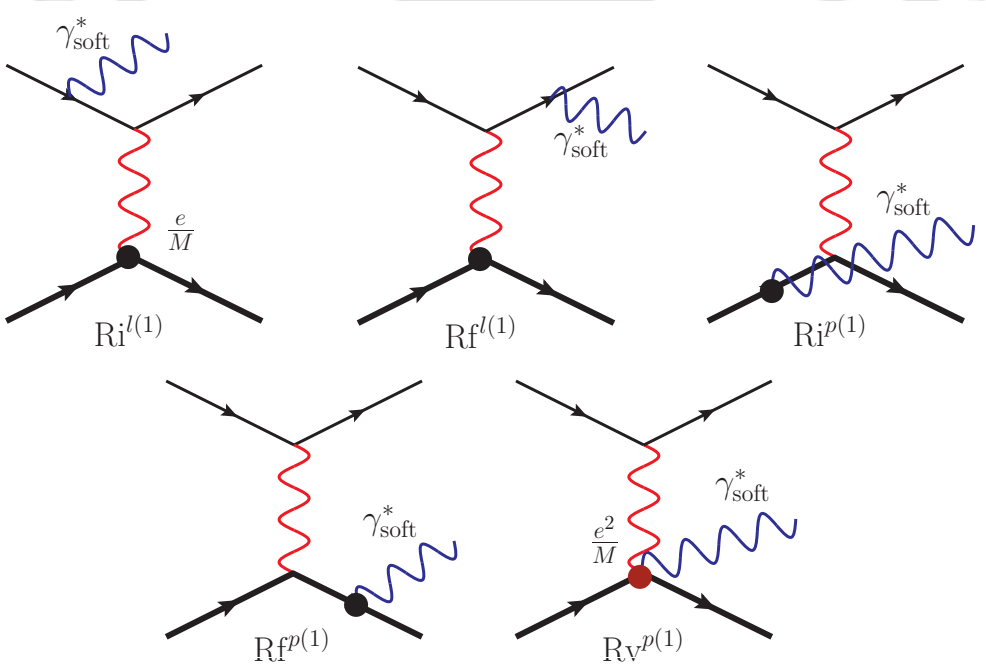

FIGURE 6.10: Soft photon ($\gamma^*_{\rm soft}$) bremsstrahlung diagrams contributing at NLO of HBχPT [i.e., $\mathcal{O}\left(e^3, \frac{1}{M}\right)$] contributing to the fractional radiative corrections to the ℓ-p scattering cross section, $\delta^{(1)}_{\gamma\gamma^*} \sim \mathcal{O}\left(\alpha, \frac{1}{M}\right)$. The dark blobs represent $\mathcal{O}(1/M)$ proton-photon vertices. In particular, the two-photon proton vertex (diagrams $\mathrm{Rv}^{p(1)}$) is of $\mathcal{O}(e^2/M)$.

Next, the square of the NLO bremsstrahlung amplitudes is given by,

$$\begin{aligned}\sum_{spins}|\mathcal{M}^{(1)}_{\gamma\gamma^*}|^2 \overset{\gamma^*_{\rm soft}}{\rightsquigarrow} 2\sum_{spins}\mathcal{R}\mathrm{e}\Bigg[&\left(\widetilde{\mathcal{M}^{l(0);\,\mathrm{i}}_{\gamma\gamma^*}}+\widetilde{\mathcal{M}^{l(0);\,\mathrm{f}}_{\gamma\gamma^*}}\right)^\dagger\left(\widetilde{\mathcal{M}^{l(1);\,\mathrm{i}}_{\gamma\gamma^*}}+\widetilde{\mathcal{M}^{l(1);\,\mathrm{f}}_{\gamma\gamma^*}}+\widetilde{\mathcal{M}^{p(1);\,\mathrm{i}}_{\gamma\gamma^*}}\right.\\&\left.+\widetilde{\mathcal{M}^{p(1);\,\mathrm{f}}_{\gamma\gamma^*}}\right)+\left(\mathcal{M}^{l(0);\,\mathrm{i}}_{\gamma\gamma^*}+\mathcal{M}^{l(0);\,\mathrm{f}}_{\gamma\gamma^*}\right)^\dagger\mathcal{M}^{p(1);\,\mathrm{v}}_{\gamma\gamma^*}\Bigg]\\
=\ -2e^2\sum_{spins}\mathcal{R}\mathrm{e}\Bigg[&(\mathcal{M}^{(0)\dagger}_{\gamma}\mathcal{M}^{(1)}_{\gamma})\left(\frac{m_l^2}{(p\cdot k)^2}+\frac{m_l^2}{(p'\cdot k)^2}-\frac{2p'\cdot p}{(p\cdot k)(p'\cdot k)}\right)\\&+\frac{Q^2}{2M}|\mathcal{M}^{(0)}_{\gamma}|^2\left(\frac{1}{(v\cdot k)(p\cdot k)}+\frac{1}{(v\cdot k)(p'\cdot k)}\right)\Bigg]\\
+2\sum_{spin}\mathcal{R}\mathrm{e}&\left[\left(\mathcal{M}^{l(0);\,\mathrm{i}}_{\gamma\gamma^*}+\mathcal{M}^{l(0);\,\mathrm{f}}_{\gamma\gamma^*}\right)^\dagger\mathcal{M}^{p(1);\,\mathrm{v}}_{\gamma\gamma^*}\right],\end{aligned}\tag{6.67}$$

where the last term being IR-finite is evaluated without SPA, which yields

$$\begin{aligned}2\sum_{spins}\mathcal{R}\mathrm{e}&\left[\left(\mathcal{M}^{l(0);\,\mathrm{i}}_{\gamma\gamma^*}+\mathcal{M}^{l(0);\,\mathrm{f}}_{\gamma\gamma^*}\right)^\dagger\mathcal{M}^{p(1);\,\mathrm{v}}_{\gamma\gamma^*}\right]=\frac{32e^6}{Q^2q^2}(E'_p+M)\\
&\times\Bigg[\frac{1}{p\cdot k}\Big\{-(Q^2/2+m_l^2)E_\gamma+m_l^2(E+E')-E'(\vec{p}\cdot\vec{k})+E(\vec{p}'\cdot\vec{k})\Big\}\\
&-\frac{1}{p'\cdot k}\Big\{(Q^2/2+m_l^2)E_\gamma+m_l^2(E+E')-E'(\vec{p}\cdot\vec{k})+E(\vec{p}'\cdot\vec{k})\Big\}\Bigg].\end{aligned}\tag{6.68}$$

Subsequently, the corresponding NLO correction to the bremsstrahlung differential cross section is obtained as

$$\begin{aligned}\left[\frac{\mathrm{d}\sigma^{(\mathrm{NLO})}_{br}(Q^2)}{\mathrm{d}\Omega'_l}\right]_{\gamma\gamma^*}\overset{\gamma^*_{\rm soft}}{\rightsquigarrow}\frac{\alpha}{2\pi^2}\left[\frac{\mathrm{d}\sigma_{el}(Q^2)}{\mathrm{d}\Omega'_l}\right]_\gamma\Bigg[&-\frac{Q^2}{M}(L_{\mathrm{i}}+L_{\mathrm{f}})\\&+(-L_{\mathrm{ii}}-L_{\mathrm{ff}}+L_{\mathrm{if}})\,\mathscr{R}_Q\Bigg]+\left[\frac{\mathrm{d}\sigma_{br}(Q^2)}{\mathrm{d}\Omega'_l}\right]^{lp(1);\,\mathrm{v}}_{\gamma\gamma^*},\end{aligned}\tag{6.69}$$

where $\mathscr{R}_Q = Q^2/(2M^2)$ [cf. Eq. (6.9) in the first section]. The integrals over the soft photon energy, namely, L_{ii}, L_{ff} and L_{if}, which arise here due to the interference of the LO and NLO lepton bremsstrahlung amplitudes, has already appeared in our LO results and evaluated using DR by boosting to the S-frame [cf. Eq. (6.44)]. In addition, the two new soft photon integrals, L_{i} and L_{f}, appearing at this order due to the interference of the NLO proton (external lines) bremsstrahlung amplitudes with the LO lepton bremsstrahlung

amplitudes, can similarly be evaluated in terms of S-frame quantities:

$$L_{\rm i}^{(S)} = \int \frac{{\rm d}^3\vec{k}_S}{2k_S}\frac{1}{(v\cdot k_S)(p_S\cdot k_S)} \overset{\rm DR}{\mapsto} \frac{1}{2}(2\pi\mu)^{2\epsilon_{\rm IR}}\int_0^{\eta\Delta_\gamma^*} k_S^{d-4}{\rm d}k_S \oiint {\rm d}^{d-2}\Omega_k^S \frac{1}{p_S\cdot k_S}$$
$$= \pi\left\{\frac{1}{\beta' E'}\left[\frac{1}{|\epsilon_{\rm IR}|}+\gamma_E-\ln\left(\frac{4\pi\mu^2}{-Q^2}\right)\right]\ln\sqrt{\frac{1+\beta'}{1-\beta'}}+2\widetilde{L}_{\rm i}^{(S)}\right\},$$

$$L_{\rm f}^{(S)} = \int \frac{{\rm d}^3\vec{k}_S}{2k_S}\frac{1}{(v\cdot k_S)(p'_S\cdot k_S)} \overset{\rm DR}{\mapsto} \frac{1}{2}(2\pi\mu)^{2\epsilon_{\rm IR}}\int_0^{\eta\Delta_\gamma^*} k_S^{d-4}{\rm d}k_S \oiint {\rm d}^{d-2}\Omega_k^S \frac{1}{p'_S\cdot k_S}$$
$$= \pi\left\{\frac{1}{\beta E}\left[\frac{1}{|\epsilon_{\rm IR}|}+\gamma_E-\ln\left(\frac{4\pi\mu^2}{-Q^2}\right)\right]\ln\sqrt{\frac{1+\beta}{1-\beta}}+2\widetilde{L}_{\rm f}^{(S)}\right\}, \tag{6.70}$$

where the IR-finite quantities $\widetilde{L}_{\rm i}^{(S)}$ and $\widetilde{L}_{\rm f}^{(S)}$ on transforming back to the *lab*-frame (with $E,\beta \rightleftharpoons E',\beta'$) are, respectively, given by

$$\widetilde{L}_{\rm i} = \frac{1}{2\beta E}\left[\ln\left(\frac{4\eta^2\Delta_\gamma^{*2}}{-Q^2}\right)\ln\sqrt{\frac{1+\beta}{1-\beta}}+\frac{1}{2}{\rm Sp}\left(\frac{2\beta}{\beta+1}\right)-\frac{1}{2}{\rm Sp}\left(\frac{2\beta}{\beta-1}\right)\right],$$
$$\widetilde{L}_{\rm f} = \frac{1}{2\beta' E'}\left[\ln\left(\frac{4\eta^2\Delta_\gamma^{*2}}{-Q^2}\right)\ln\sqrt{\frac{1+\beta'}{1-\beta'}}+\frac{1}{2}{\rm Sp}\left(\frac{2\beta'}{\beta'+1}\right)-\frac{1}{2}{\rm Sp}\left(\frac{2\beta'}{\beta'-1}\right)\right]. \tag{6.71}$$

The cross section $\left[\frac{{\rm d}\sigma_{br}}{{\rm d}\Omega'_l}\right]_{\gamma\gamma^*}^{lp(1);\,{\rm v}}$ given in Eq. (6.69) is completely finite and arises from Eq. (6.68). Moreover, this term, which arises due to the interference of the LO proton bremsstrahlung diagram ${\rm Rv}^{p(1)}$ (see Fig. [6.10]) and the NLO lepton bremsstrahlung diagrams ${\rm Ri}^{l(0)}$ and ${\rm Rf}^{l(0)}$ (see Fig. [6.6]), does not factorize into the LO Born cross section. In terms of the S-frame quantities this cross section is given by,

$$\left[\frac{{\rm d}\sigma_{br}(Q^2)}{{\rm d}\Omega'_l}\right]_{\gamma\gamma^*}^{lp(1);\,{\rm v}}\Bigg|_{S\text{-frame}} = \frac{\alpha^3}{\pi^2 Q^4 M}\left(\frac{\beta E}{E'}\right)\int_0^{\eta\Delta_\gamma^*} k_S\,{\rm d}k_S\Bigg[-\frac{Q^2}{M}+m_l^2(E+E')({\rm L}_{\rm iv}^{(S)}-{\rm L}_{\rm fv}^{(S)})$$
$$-k_S\left(\frac{Q^2}{2}+m_l^2\right)({\rm L}_{\rm iv}^{(S)}+{\rm L}_{\rm fv}^{(S)})+E'\mathbb{L}_{\rm iv}^{(S)}-E\mathbb{L}_{\rm fv}^{(S)}\Bigg]. \tag{6.72}$$

Notably, the assumption that the soft photon emission does not alter the elastic four-momentum transfer implies the approximation, $q^2 \to Q^2$. This simplification allows the photon phase-space integration to be performed in a closed analytical form, which otherwise must be only evaluated numerically. Now, ${\rm L}_{\rm iv}^{(S)}$, $\mathbb{L}_{\rm iv}^{(S)}$, ${\rm L}_{\rm fv}^{(S)}$ and $\mathbb{L}_{\rm fv}^{(S)}$ are finite

two-dimensional angular integrals which can be readily evaluated without continuing to d-dimensions, namely,

$$\begin{aligned}
\mathrm{L}_{\mathrm{iv}}^{(S)} &= \oiint \mathrm{d}\Omega_k^S \, \frac{1}{p_S\cdot k_S} = \frac{2\pi}{E'\beta' k_S}\ln\sqrt{\frac{1+\beta'}{1-\beta'}}\,,\\
\mathbb{L}_{\mathrm{iv}}^{(S)} &= \oiint \mathrm{d}\Omega_k^S \, \frac{p'_S\cdot k_S}{p_S\cdot k_S} = \frac{2\pi E}{E'\beta'}\left[\frac{1}{\beta'}\ln\sqrt{\frac{1+\beta'}{1-\beta'}}-2\right]\,,\\
\mathrm{L}_{\mathrm{fv}}^{(S)} &= \oiint \mathrm{d}\Omega_k^S \, \frac{1}{p'_S\cdot k_S} = \frac{2\pi}{E\beta k_S}\ln\sqrt{\frac{1+\beta}{1-\beta}}\,,\\
\mathbb{L}_{\mathrm{fv}}^{(S)} &= \oiint \mathrm{d}\Omega_k^S \, \frac{p_S\cdot k_S}{p'_S\cdot k_S} = \frac{2\pi E'}{E\beta}\left[\frac{1}{\beta}\ln\sqrt{\frac{1+\beta}{1-\beta}}-2\right]\,.
\end{aligned}\tag{6.73}$$

Plugging these expressions into Eq. (6.72), the photon energy/momenta in the S-frame is then integrated from $k_S = E_{\gamma^*}^S = 0$ to $\eta\Delta_\gamma^*$. The resulting expression when boosted back to the *lab*-frame yields the differential cross section of emitting a real soft photon of energy less than Δ_γ^* at NLO in HBχPT of the form

$$\left[\frac{\mathrm{d}\sigma_{br}^{(\mathrm{NLO})}(Q^2)}{\mathrm{d}\Omega_l'}\right]_{\gamma\gamma^*}^{(E_{\gamma^*}<\Delta_\gamma^*)} = \left[\frac{\mathrm{d}\sigma_{el}(Q^2)}{\mathrm{d}\Omega_l'}\right]_{\gamma}\delta_{\gamma\gamma^*}^{(1)}(Q^2)\,.\tag{6.74}$$

Expressing the $\mathcal{O}(\alpha)$ NLO inelastic contribution formally as $\delta_{\gamma\gamma^*}^{(1)} = \mathbf{IR}_{\gamma\gamma^*}^{(1)} + \overline{\delta}_{\gamma\gamma^*}^{(1)}$, its finite part is given as

$$\begin{aligned}
\overline{\delta}_{\gamma\gamma^*}^{(1)}(Q^2) &= \frac{\alpha}{\pi}\left[-\frac{Q^2}{M}(\widetilde{L}_{\mathrm{i}}+\widetilde{L}_{\mathrm{f}})+(-\widetilde{L}_{\mathrm{ii}}-\widetilde{L}_{\mathrm{ff}}+\widetilde{L}_{\mathrm{if}})\mathscr{R}_Q\right]+\delta_{\gamma\gamma^*}^{lp(1);\,\mathrm{v}}(Q^2)\\
&= -\frac{\alpha Q^2}{2\pi ME\beta}\left[\ln\left(\frac{4\eta^2\Delta_\gamma^{*2}}{-Q_l^2}\right)\ln\sqrt{\frac{1+\beta}{1-\beta}}+\frac{1}{2}\mathrm{Sp}\left(\frac{2\beta}{\beta+1}\right)-\frac{1}{2}\mathrm{Sp}\left(\frac{2\beta}{\beta-1}\right)\right]\\
&\quad -\frac{\alpha Q^2}{2\pi ME'\beta'}\left[\ln\left(\frac{4\eta^2\Delta_\gamma^{*2}}{-Q_l^2}\right)\ln\sqrt{\frac{1+\beta'}{1-\beta'}}+\frac{1}{2}\mathrm{Sp}\left(\frac{2\beta'}{\beta'+1}\right)-\frac{1}{2}\mathrm{Sp}\left(\frac{2\beta'}{\beta'-1}\right)\right]\\
&\quad +\overline{\delta}_{\gamma\gamma^*}^{(0)}(Q^2)\mathscr{R}_Q+\delta_{\gamma\gamma^*}^{lp(1);\,\mathrm{v}}(Q^2)\,,
\end{aligned}\tag{6.75}$$

whereas the term $\mathbf{IR}_{\gamma\gamma^*}^{(1)} = \mathbf{IR}_{\gamma\gamma^*}^{(0)}\mathscr{R}_Q + \mathbf{IR}_{\gamma\gamma^*}^{lp(1)}$, collects all the IR divergences arising from the inelastic soft bremsstrahlung contributions at NLO, with $\mathbf{IR}_{\gamma\gamma^*}^{(0)}$ given earlier in

Eq. (6.47), and

$$\mathbf{IR}^{lp(1)}_{\gamma\gamma^*} = -\frac{\alpha Q^2}{\pi M}\left[\frac{1}{|\epsilon_{\rm IR}|} + \gamma_E - \ln\left(\frac{4\pi\mu^2}{-Q^2}\right)\right]\left[\frac{1}{2E\beta}\ln\sqrt{\frac{1+\beta}{1-\beta}} + \frac{1}{2E'\beta'}\ln\sqrt{\frac{1+\beta'}{1-\beta'}}\right] \tag{6.76}$$

As expected, $\mathbf{IR}^{(1)}_{\gamma\gamma^*}$ is exactly equal and of opposite sign to $\mathbf{IR}^{(1)}_{\gamma\gamma}$ [cf. Eq. (6.60)], which arises due to the one-loop NLO virtual radiative and recoil corrections, and therefore, either terms drop out in the total sum of the real and virtual radiative corrections at NLO, namely, $\delta^{(1)}_{2\gamma} = \delta^{(1)}_{\gamma\gamma} + \delta^{(1)}_{\gamma\gamma^*}$ is completely IR-finite . Moreover, of the remaining finite terms in $\overline{\delta}^{(1)}_{\gamma\gamma^*}$, the terms proportional to $\mathscr{R}_Q = Q^2/(2M^2)$ may be excluded as they are *de facto* kinematically suppressed by one more recoil order, contributing at $\mathcal{O}(M^{-2})$. Next focusing on the last term $\delta^{lp(1);\,\rm v}_{\gamma\gamma^*}$, which as already mentioned represents the inelastic part of the contribution arising due to the interference of the NLO diagram $\mathrm{Rv}^{p(1)}$ with the LO diagrams $\mathrm{Ri}^{l(0)}$ and $\mathrm{Rf}^{l(0)}$, is given by the unfactorized form

$$\begin{aligned}
\delta^{lp(1);\,\rm v}_{\gamma\gamma^*}(Q^2) &= \left[\frac{{\rm d}\sigma_{br}(Q^2)}{{\rm d}\Omega'_l}\right]^{lp(1);\,\rm v}_{\gamma\gamma^*} \Bigg/ \left[\frac{{\rm d}\sigma_{el}(Q^2)}{{\rm d}\Omega'_l}\right]_{\gamma} \\
&= \frac{\alpha}{\pi M}\left(\frac{4m_l^2\eta}{Q^2+4EE'}\right) \\
&\quad\times\Bigg[-\frac{Q^2\eta^2\Delta^{*2}_\gamma}{2Mm_l^2} + \eta\Delta^*_\gamma(E+E')\left\{\frac{1}{E\beta}\ln\sqrt{\frac{1+\beta}{1-\beta}} - \frac{1}{E'\beta'}\ln\sqrt{\frac{1+\beta'}{1-\beta'}}\right\} \\
&\quad - \frac{\eta^2\Delta^{*2}_\gamma Q^2}{4m_l^2}\left(1+\frac{2m_l^2}{Q^2}\right)\left\{\frac{1}{E\beta}\ln\sqrt{\frac{1+\beta}{1-\beta}} + \frac{1}{E'\beta'}\ln\sqrt{\frac{1+\beta'}{1-\beta'}}\right\} \\
&\quad + \frac{\eta^2\Delta^{*2}_\gamma EE'}{m_l^2}\left\{\frac{1}{\beta^2 E}\ln\sqrt{\frac{1+\beta}{1-\beta}} - \frac{1}{\beta'^2E'}\ln\sqrt{\frac{1+\beta'}{1-\beta'}} - \frac{1}{\beta E} + \frac{1}{\beta' E'}\right\}\Bigg].
\end{aligned} \tag{6.77}$$

Now dropping the $1/M^2$ order terms, yields the finite part of the NLO Bremsstrahlung contribution, namely

$$\begin{aligned}
\overline{\delta}^{(1)}_{\gamma\gamma^*}(Q^2) = &-\frac{\alpha Q^2}{\pi M E\beta}\Bigg[\ln\left(\frac{4\eta^2\Delta^{*2}_\gamma}{-Q^2}\right)\ln\sqrt{\frac{1+\beta}{1-\beta}} + \frac{1}{2}{\rm Sp}\left(\frac{2\beta}{\beta+1}\right) - \frac{1}{2}{\rm Sp}\left(\frac{2\beta}{\beta-1}\right) \\
&+ \frac{2\eta^2\Delta^{*2}_\gamma}{Q^2+4E^2}\left(1+\frac{2m_l^2}{Q^2}\right)\ln\sqrt{\frac{1+\beta}{1-\beta}}\Bigg] + \mathcal{O}\left(\frac{1}{M^2}\right).
\end{aligned} \tag{6.78}$$

Finally, we display our IR-finite $\mathcal{O}(\alpha)$ (analytical) expression for the total fractional radiative and recoil corrections to the elastic lepton-proton differential scattering cross section accurate up to order $1/M$, i.e., NLO in HBχPT:

$$\begin{aligned}\delta_{2\gamma}^{(1)}(Q^2) &= \delta_{\gamma\gamma}^{(1)}(Q^2) + \delta_{\gamma\gamma^*}^{(1)}(Q^2) \equiv \overline{\delta}_{\gamma\gamma}^{(1)}(Q^2) + \overline{\delta}_{\gamma\gamma^*}^{(1)}(Q^2) \\ &= -\frac{\alpha Q^2}{\pi M E \beta}\left[\ln\left(\frac{4\eta^2\Delta_\gamma^{*2}}{-Q^2}\right)\ln\sqrt{\frac{1+\beta}{1-\beta}} + \frac{1}{2}\mathrm{Sp}\left(\frac{2\beta}{\beta+1}\right) - \frac{1}{2}\mathrm{Sp}\left(\frac{2\beta}{\beta-1}\right)\right. \\ &\quad + \frac{2\eta^2\Delta_\gamma^{*2}}{Q^2+4E^2}\left(1+\frac{2m_l^2}{Q^2}\right)\ln\sqrt{\frac{1+\beta}{1-\beta}} \\ &\quad + \ln\left(\frac{-Q^2}{m_l^2}\right)\ln\sqrt{\frac{1+\beta}{1-\beta}} - \ln^2\sqrt{\frac{1+\beta}{1-\beta}} + \frac{\pi^2}{2} - \mathrm{Sp}\left(\frac{2\beta}{1+\beta}\right) \\ &\quad \left. + \frac{4E^2\beta}{Q^2+4E^2}\left(\mathcal{I}_1 + \mathcal{I}_2 + \frac{Q^2}{m_l^2}\left(\mathcal{I}_3 - \mathcal{I}_4\right)\right)\right] + \mathcal{O}\left(\frac{1}{M^2}\right). \end{aligned} \tag{6.79}$$

Thus, using our previously derived expression for the total LO radiative correction $\delta_{2\gamma}^{(0)}$, Eq. (6.50), we can obtain the full $\mathcal{O}(\alpha)$ radiative and recoil corrections up-to-and-including NLO accuracy, formally expressed as the sum $\delta_{2\gamma} = \delta_{2\gamma}^{(0)} + \delta_{2\gamma}^{(1)}$. In the next section we present our improved numerical estimates by including the $1/M$ recoil corrections to our LO result presented in the previous section.

6.4 Numerical Results and Discussion

As already mentioned, all our radiative and recoil corrections depend on the value of the parameter Δ_γ^* which specific to the type of detector used and its threshold of soft photon detection. Theoretically, as we demonstrated in the previous section, this quantity also determines the upper limit of integration over the soft photon energy E. In all our numerical estimates we have chosen this threshold typically about 1 % of the incoming lepton energy which is also consistent with the technical design of the proposed MUSE experimental setup. Figure.[6.11] shows the IR-finite one-loop virtual (TPE) and soft photon bremsstrahlung fractional NLO contributions, $\overline{\delta}_{\gamma\gamma}^{(1)}$ and $\overline{\delta}_{\gamma\gamma^*}^{(1)}$, respectively, whose analytical expressions obtained were obtained in the previous section. Here we take the incoming lepton momentum as the MUSE specified beam momenta, namely, $p =$

115, 153, 210 MeV/c. The following observations describe the features of these NLO contributions:

- The TPE corrections exactly vanish as $Q^2 \to 0$, while the soft bremsstrahlung corrections become infinitesimally small and negative at $Q^2 = 0$ due to non-vanishing of the term $\delta_{\gamma\gamma^*}^{lp(1);\,\mathrm{v}}$. The net NLO correction at $Q^2 = 0$ is thus negative.
- The gross behavior of the both NLO corrections display roughly a linear rise with the square of the four-momentum transfer $|Q^2|$.
- As akin to the LO results, the NLO corrections are not very sensitive to the variation of the incident lepton beam momenta.
- Both the NLO contributions being comparable in magnitudes but of opposite signs exhibit large cancellations, resulting in about 5 % and 1 % radiative corrections, respectively, in case of electron and muon scatterings at the largest lepton beam momenta expected at MUSE. .

Next the total radiative and recoil corrections up-to-and-including NLO in HBχPT for electron and muon scattering associated with the MUSE kinematics are plotted in Fig. [6.12]. In the case of electron scattering, with the staggeringly large and negative bremsstrahlung contributions, the overall radiative corrections remain throughout negative monotonically increasing in magnitude with squared four-momentum transfer $|Q^2|$. The total corrections vary in the range of $20 - 25$ % in the MUSE kinematic domain. For muon scattering on the other hand, the radiative corrections in this low-energy domain are no larger than 2 %. However, unlike the electron case, they undergo a sign change; initially positive for very small momentum transfers, say, $|Q^2| \lesssim 0.035$ (GeV/c)^2, due to the dominant VP contributions in this region, which ultimately for larger $|Q^2|$ values turn negative as the VP corrections are superseded by the soft bremsstrahlung contributions. Notice, however, that for the lowest values of the MUSE lepton beam momenta, $p = |\vec{p}| \gtrsim 115$ MeV/c, the total corrections remains positive due to the VP dominance. The energy/-momentum dependence of the lepton beam on the individual LO and NLO components of the radiative corrections were hitherto not apparent in the MUSE kinematic domain ($115 < p < 210$ MeV/c). Nevertheless, the cumulative effect after adding up all the

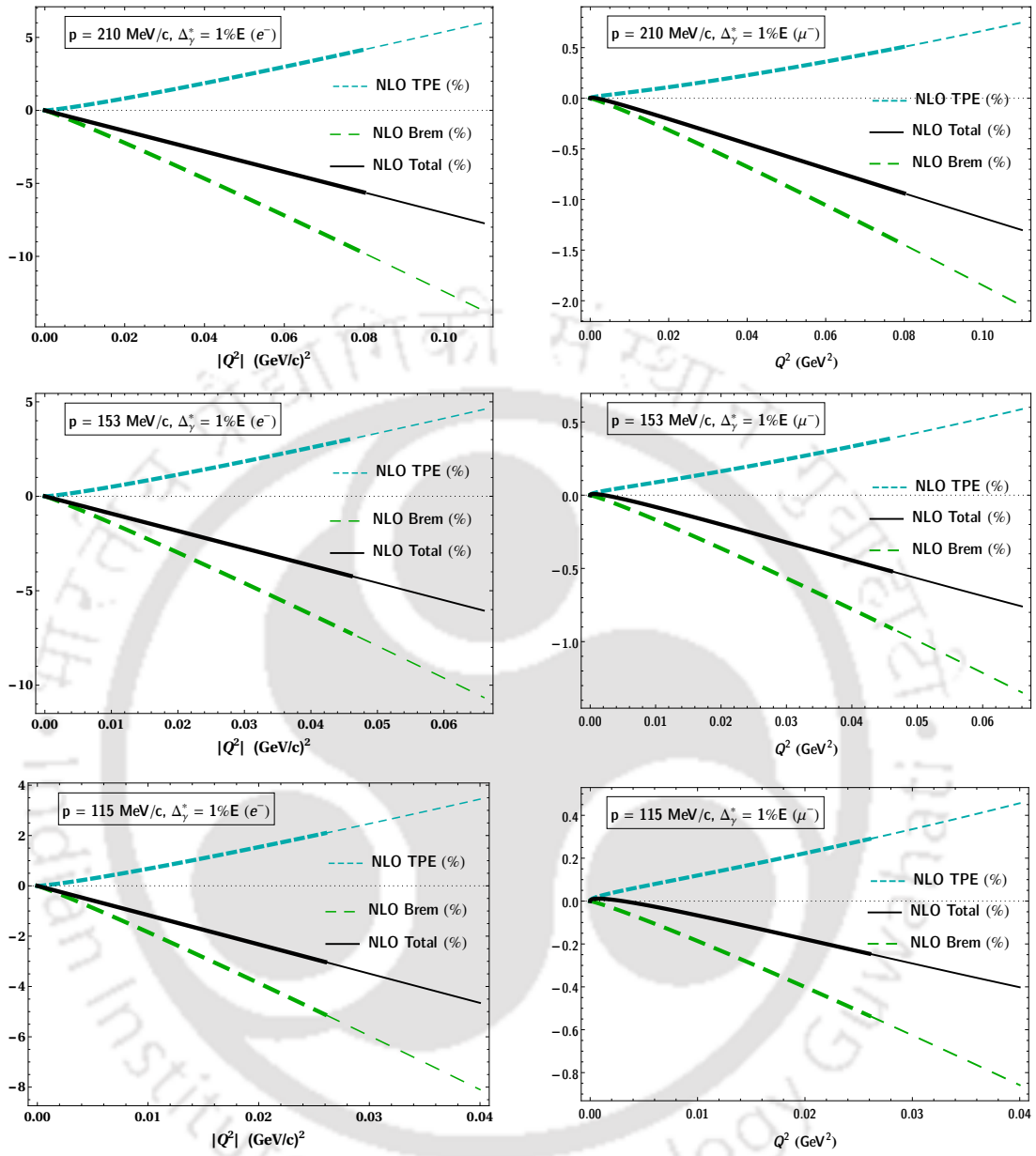

FIGURE 6.11: Fractional NLO radiative and recoil corrections (in percentage): one-loop virtual corrections due to the two-photon contributions $\overline{\delta}^{(1)}_{\gamma\gamma}$ (solid curves), and soft photon bremsstrahlung corrections $\overline{\delta}^{(1)}_{\gamma\gamma^*}$ (dashed curves), to the ep (left panel) and μp (right panel) elastic cross sections as a function of the squared four-momentum transfer $|Q^2|$ for the proposed MUSE beam momenta, namely, $p = 115$, 153, 210 MeV/c. The total NLO correction $\delta^{(1)}_{2\gamma}$ is also displayed. Each plot covers the full kinematically allowed scattering range, $0 < |Q^2| < |Q^2_{\rm max}|$, when $\theta \in [0, \pi]$ (cf. Table I of Chapter 5). The thickened portion of each curve corresponds to the MUSE kinematic cut, where $\theta \in [20^\circ, 100^\circ]$. The *lab*-frame detector resolution Δ^*_γ is taken to be 1 % of the incident lepton energy E.

contributions indeed generates a substantial energy dependence of about 5 % and 2 %, respectively, in case of the electronic and muonic results. Furthermore, this also amounts to more than an orders of magnitude difference between the two cases, especially for the lowest values of the beam momenta. Most importantly, a comparison of the relative magnitudes of the two orders of corrections, viz. NLO:LO in each case almost indicates a ratio as large as 1:1 for muon, in contrast to a mere 1:4 for electron. Evidently, a greater significance should be associated with the rapidly growing nature of the NLO contributions for muon scattering in regard to the MUSE kinematics. Finally, it may be worth mentioning that the NLO TPE corrections (i.e., the interference of the NLO TPE amplitudes with the LO elastic Born amplitude) as well as the NLO soft bremsstrahlung corrections (i.e., the interference of the LO lepton bremsstrahlung amplitudes with the NLO proton bremsstrahlung amplitudes) are lepton ($\ell^{\pm}$) *charge-dependent*. Hence, not only do the NLO corrections $\delta_{2\gamma}^{(1)}$ corresponding to the $\ell^{\pm}$p scattering processes change sign, the total corrections (LO+NLO), namely, $\delta_{2\gamma} = \delta_{2\gamma}^{(0)} + \delta_{2\gamma}^{(1)}$, are a bit smaller for ℓ^{+}p scatterings as compared to ℓ^{-}p scatterings. The numerical figures quoted in Table.[6.1] unambiguously reflect the above discussed features of our results.

Finally, we conclude this section by discussing our results pertaining to the estimate of the theoretical uncertainties. In this regard to the analysis presented in this chapter, two essential sources of uncertainties may be identified which we enumerate as follows:

1. Firstly, as already discussed in the last section, the only free parameter that our LO and NLO results for the radiative and recoil corrections to the ℓp elastic scattering process intrinsically rely on is the detector acceptance factor Δ_{γ}^{*} which requires external specifications depending on the experimental conditions. To this end, we give an assessment regarding the sensitivity of our result on this cut-off parameter. Fig. [6.13] shows the dependence of the our analytical result for the total fractional radiative correction, $\delta_{2\gamma} = \delta_{2\gamma}^{(0)} + \delta_{2\gamma}^{(1)}$ as Δ_{γ}^{*} is varied between 0.5 % and 5 % of the incident lepton beam energy E. It is reasonable to expect that the radiative corrections should naively decrease with larger values of the acceptance Δ_{γ}^{*}, as at least seen for the case of electron scattering. This is because, larger Δ_{γ}^{*} implies

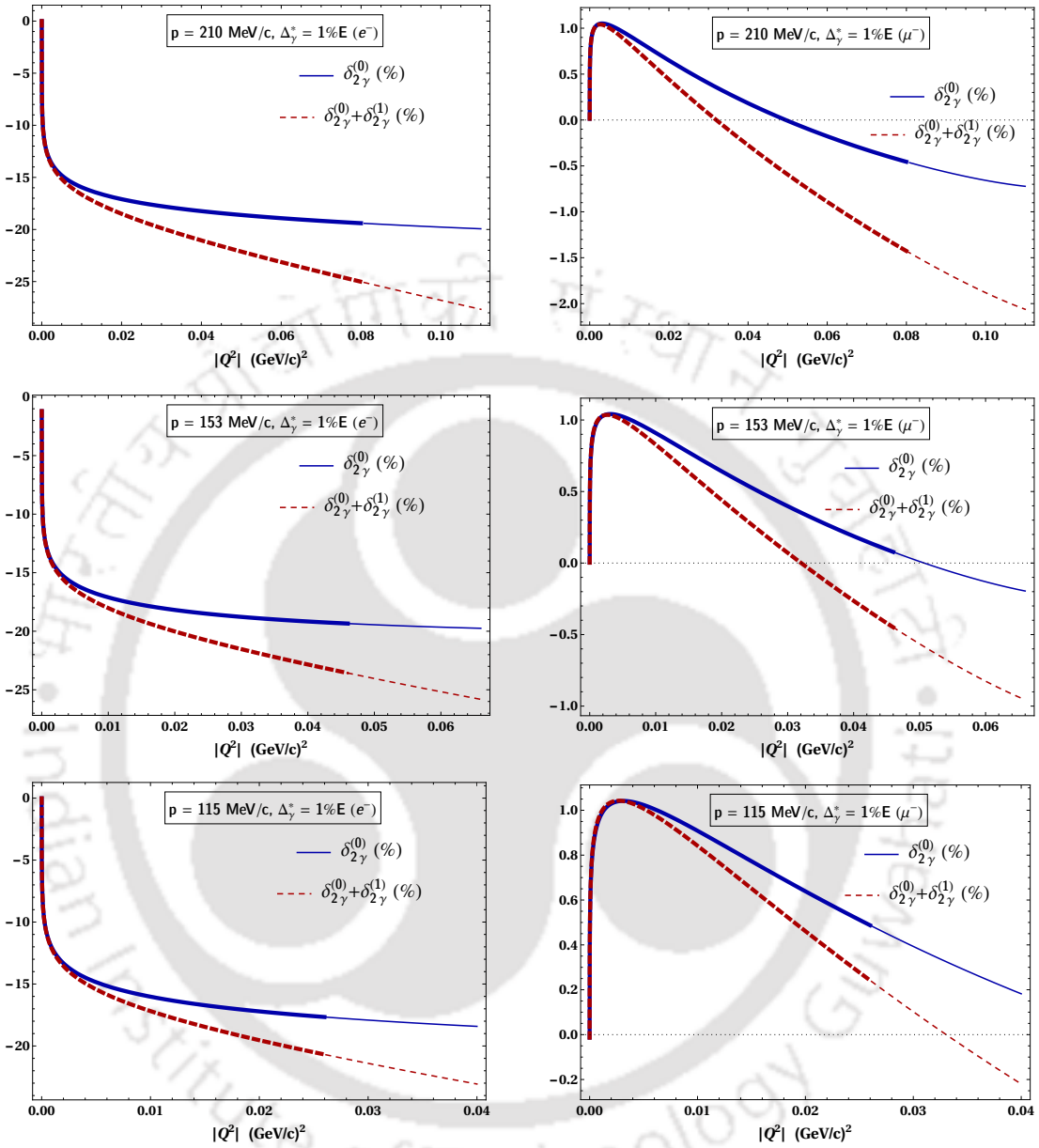

FIGURE 6.12: The total fractional radiative and recoil corrections (in percentage) up-to-and-including NLO in HBχPT to ep (left panel) and μp (right panel) elastic cross sections as a function of the squared four-momentum transfer $|Q^2|$ for the proposed MUSE beam momenta, namely, $p = 115, 153, 210$ MeV/c. The corresponding LO result are also displayed for comparison. Each plot covers the full kinematically allowed scattering range $0 < |Q^2| < |Q^2_{\rm max}|$ when $\theta \in [0, \pi]$ (cf. Table I of Chapter 5). The thickened portion of each curve corresponds to the MUSE kinematic cut, where $\theta \in [20^\circ, 100^\circ]$. The *lab*-frame detector resolution Δ_γ^* is taken to be 1 % of the incident lepton energy E.

p	$\lvert Q^2\rvert$	LO: $\delta_{2\gamma}^{(0)}$		NLO: $\delta_{2\gamma}^{(1)}$		LO+NLO: $\delta_{2\gamma}$		LO+NLO: $\delta_{2\gamma}$	
GeV/c	$(\text{GeV/c})^2$	$e^{\pm}p$	$\mu^{\pm}p$	$e^{\pm}p$	$\mu^{\pm}p$	$e^{-}p$	$\mu^{-}p$	$e^{+}p$	$\mu^{+}p$
0.115	0.01	-0.1592	0.0211	$\pm$0.0116	$\pm$0.0007	-0.1708	0.0204	-0.1476	0.0217
	0.02	-0.1700	0.0185	$\pm$0.0232	$\pm$0.0018	-0.1932	0.0167	-0.1467	0.0202
0.153	0.03	-0.1757	0.0160	$\pm$0.0275	$\pm$0.0032	-0.2032	0.0128	-0.1481	0.0192
	0.04	-0.1796	0.0139	$\pm$0.0367	$\pm$0.0044	-0.2163	0.0095	-0.1429	0.0183
0.210	0.05	-0.1828	0.0120	$\pm$0.0351	$\pm$0.0057	-0.2179	0.0062	-0.1476	0.0177
	0.07	-0.1868	0.0088	$\pm$0.0492	$\pm$0.0082	-0.2360	0.0006	-0.1377	0.0170

TABLE 6.1: Fractional radiative corrections at LO $\delta_{2\gamma}^{(0)}$, with recoil effect at NLO $\delta_{2\gamma}^{(1)}$, and the total radiative and recoil corrections LO+NLO $\delta_{2\gamma} = \delta_{2\gamma}^{(0)} + \delta_{2\gamma}^{(1)}$, evaluated in HB$\chi$PT, to $\ell^{\pm}$p elastic scattering cross sections for incoming lepton beam momentum, namely, $p = |\vec{p}| = 0.115\,, 0.153\,, 0.210$ GeV/c, and certain specific values of the squared four-momentum transfer chosen in the MUSE kinematic domain, namely, $|Q^2| = 0.01\,, 0.02\,, 0.03\,, 0.04\,, 0.05\,, 0.07$ $(\text{GeV/c})^2$. The results correspond to the *lab*-frame detector acceptance $\Delta_{\gamma}^{*} = 1\,\%$ of the incident lepton energy E.

smaller detector resolution in identifying emitted hard photons of larger energies with positive definite emission cross section, and thereby reducing the effective radiative correction. In this regard, the result for muon scattering in the expected MUSE kinematic domain is somewhat atypical due the changing sign of the overall radiative correction $\delta_{2\gamma}$. Furthermore, as the acceptance is varied between 0.5-5 MeV, the muon results are likely to be more sensitive, which in our case varies as much as 125 % with respect to our benchmark results obtained with $\Delta_{\gamma}^{*} = 1\,\%$ (red curves in Fig. [6.13]), in contrast to a mere 60 % for electron scattering. Of course such large error bands are gross over-estimations resulting from our exaggerated variation of the detector acceptance by an order of magnitude, although for sophisticated modern experiments like the MUSE, the acceptance window is small, typically between $1 - 2\,\%$.

2. Secondly, our HBχPT calculations indicate sizable NLO i.e., $\mathcal{O}(1/M)$ corrections for low-energy muon scattering in the MUSE kinematic domain, which become certainly as large as the LO corrections (cf. Fig. [6.12]). This might leave some

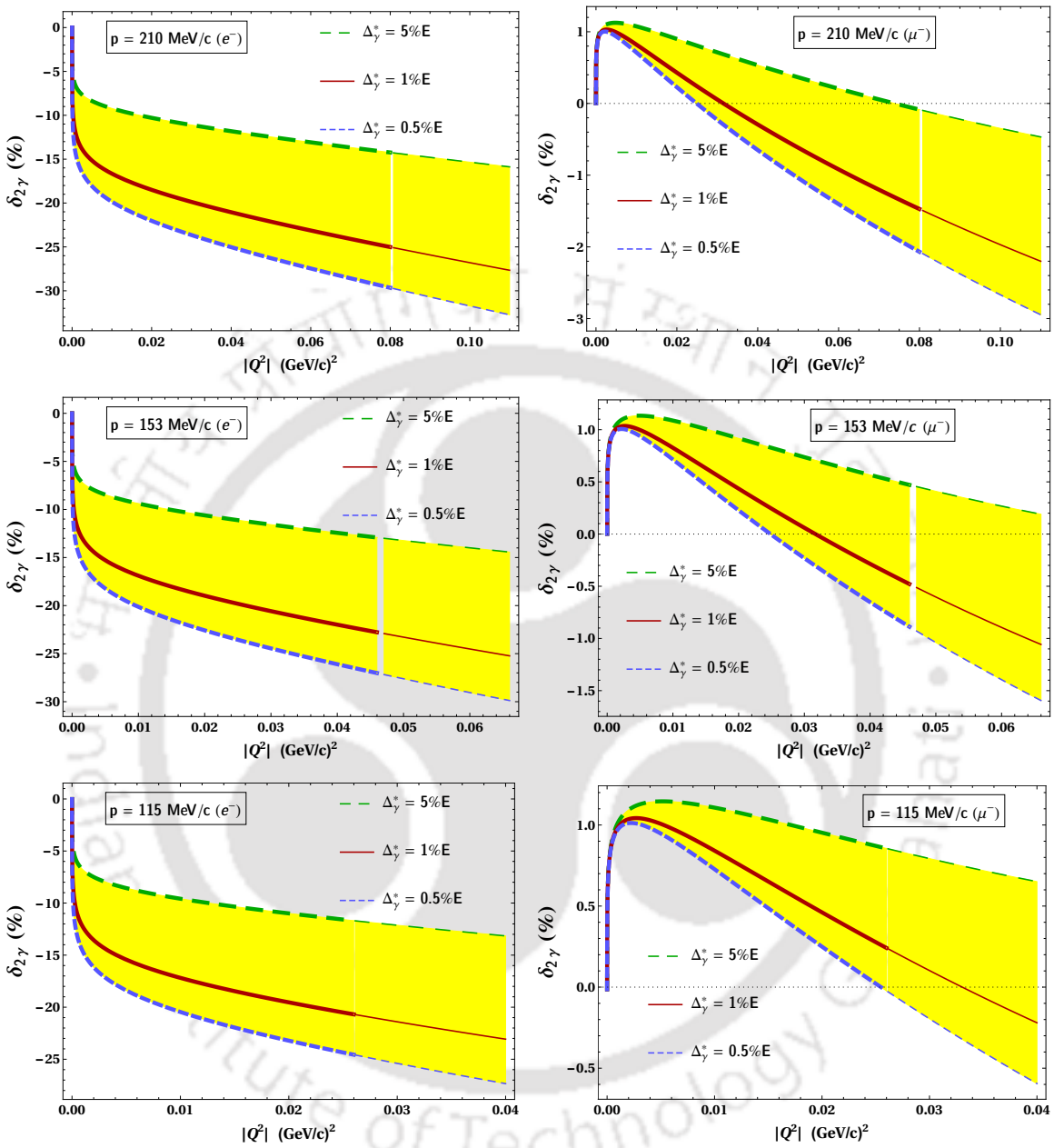

FIGURE 6.13: Variation of total fractional radiative and recoil correction up-to-and-including NLO in HBχPT to ep (left panel) and μp (right panel) elastic cross sections as a function of the squared four-momentum transfer $|Q^2|$ for the proposed MUSE beam momenta, namely, p = 115, 153, 210 MeV/c. Each plot covers the full kinematically allowed scattering range $0 < |Q^2| < |Q^2_{\rm max}|$ when $\theta \in [0, \pi]$ (cf. Table I of Chapter 5). The thickened portion of each curve corresponds to the MUSE kinematic cut, where $\theta \in [20^\circ, 100^\circ]$. The (yellow) band corresponds to the variation of the result with the *lab*-frame detector resolution $1\,\% < \Delta_\gamma^* < 5\,\%$ of the incident lepton energy E.

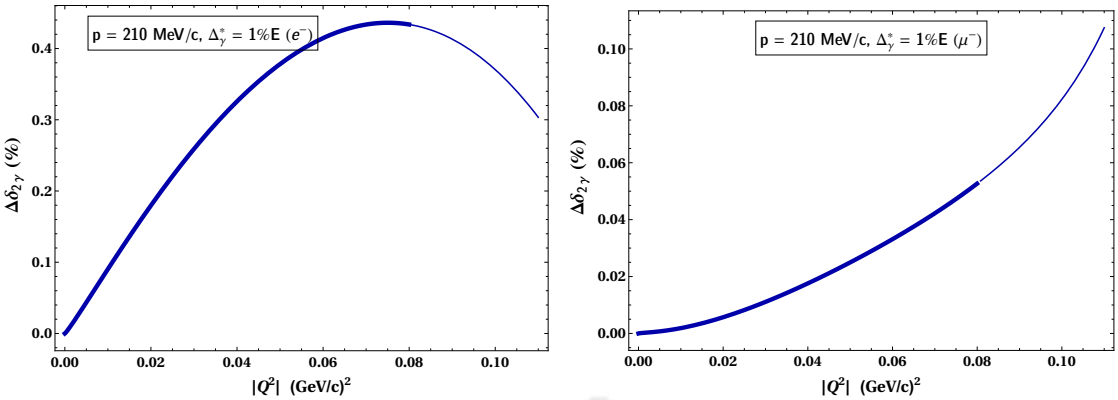

FIGURE 6.14: The neglected $\mathcal{O}(1/M^2)$ kinematical contributions arising from various analytical expressions for the NLO radiative and recoil corrections plotted as a function of the squared four-momentum transfer $|Q^2|$. The plot covers the full kinematically allowed scattering range, $0 < |Q^2| < |Q^2_{\rm max}|$, when $\theta \in [0, \pi]$ with incoming lepton momentum of $p = 210$ MeV/c. The thickened section of each curve corresponds to the MUSE kinematic cut, where $\theta \in [20°, 100°]$.

iota of doubt on the reliability of the EFT power counting in the present scenario where not only dynamical contributions from NNLO interaction were neglected, but also all $\mathcal{O}(1/M^2)$ terms of kinematical origin formally arising from various NLO expressions presented in this chapter, neglected as well.[7] Thus, a robust error estimate in this case would necessitate an NNLO assessment of the radiative and recoil corrections involving evaluation of complicated two-loop (photon and pion loops) contributions as well as inelastic proton polarizability contributions. While such an endeavor certainly lies beyond the scope of this work, a simplistic assessment of the aforementioned neglected $\mathcal{O}(1/M^2)$ kinematical terms (denoting them as $\Delta\delta_{2\gamma}$) could nevertheless serve as a naive indicator of the natural size of the NNLO contributions. This is demonstrated in Fig. [6.14] which ostensibly suggests that the NNLO corrections are about two orders of magnitude smaller than the NLO corrections, amounting no more than 0.4 % and 0.05 %, respectively for electron and muon scatterings.

[7]Here again we reiterate that there are no NNLO contributions to the fractional radiative corrections due to phase space integration since they drop out while taking the ratio with respect to the Born contribution.

6.5 Conclusion

In this chapter, we have presented a complete perturbative analysis of the radiative corrections to the lepton-proton elastic scattering process in the context of HBχPT. We included all the one-loop virtual and single soft (real) photon bremsstrahlung corrections, demonstrating that the respective IR divergences mutually cancel out separately at LO and NLO, leaving behind a finite physical radiative correction. In our analytical evaluations of the one-loop virtual diagrams, we invoke SPA in determining the TPE box amplitudes only. Otherwise, without SPA such loop integrals are rather intricate to be evaluated analytically, in which case one must resort to numerical evaluations using standard software packages. In the latter procedure, however, it may not be at all straightforward to explicitly project out the IR singular structures which are needed to be eliminated to ensure a finite cross section. On the other hand, in our estimations of the bremsstrahlung contributions due to the undetected soft photons below detector threshold Δ^*_γ, it is perfectly legitimate to use SPA as the well-known general methodology to extract the IR divergences [151]

As a part of our LO evaluations we have explicitly included the often neglected magnetic or Pauli form factor contributions to the lepton-photon vertex corrections. They potentially become quite relevant in the case of low-energy muon scattering. Going beyond the LO, our calculations revealed that the TPE and proton bremsstrahlung processes start contributing only at NLO, i.e, $\mathcal{O}(\alpha, M^{-1})$ in HBχPT, while for a non-zero proton vertex correction one needs to consider NNLO corrections, i.e., $\mathcal{O}(\alpha, M^{-2})$. All our analytical results presented in this chapter depend on one free parameter, namely, Δ^*_γ, which is fixed according to a given experimental design. Considering the projected level of accuracy of MUSE, we have demonstrated our numerical results using a reasonable benchmark value of the acceptance, namely, $\Delta^*_\gamma = 1\,\%$ of the incident beam lepton energy E. Subsequently, our numerical estimates suggest that the total radiative corrections up-to-and-including NLO for electron scattering can be as large as 25 %, while for muon scattering they are no more than 2 % in regard to the proposed MUSE kinematic domain. Despite of the apparent smallness of the total muonic corrections, the relevance of the near 100 % NLO:LO corrections is in effect much more significant in comparison to the electronic corrections,

especially in the context of MUSE kinematics. The largeness of the muon mass in the low-energy domain predominantly spoils the numerical convergence of the chiral series at the level of NLO accuracy. This naturally indicates the need for increasing the precision of our analysis by including NNLO corrections to ensure a more robust assessment of the muonic corrections. Needless to mention that such a rigorous NNLO analysis is undoubtedly a demanding task involving evaluations up to two-loop diagrams. Nevertheless, such a treatment of muon scattering is necessary to assess the insofar neglected proton's structure dependent effects, such as anomalous magnetic moment, and inelastic contributions, such as the effect of $\Delta(1232)$ resonance.

Chapter 7

Summary and Outlook

In this thesis we presented a detailed analysis of radiative correction to low-energy elastic lepton-proton scattering including the evaluation of the two-photon exchange process especially in view of the demand for high-precision data analysis that can be expected from of the ongoing efforts for the proposed MUSE experimental project at PSI. Moreover, current wisdom suggests that an unequivocal resolution to the proton radius puzzle is expected from a low-energy muon-proton scattering analysis. Naturally, the state-of-art data processing will need to incorporate proper model-independent consideration of hadronic effects to minimize the systematic uncertainties in the accurate extraction of observables. A low-energy effective field theoretical framework, such as Heavy Baryon Chiral Perturbation Theory (HBχPT), can play as indispensable role in providing a systematic analytical tool to assess the pertinent underlying non-perturbative *strong* dynamics. The work of this thesis pursued this approach for the various theoretical evaluations presented.

Firstly, it is known that the lepton-proton bremsstrahlung scattering process ($\ell + \mathrm{p} \to \ell + \mathrm{p} + \gamma^*$) constitutes a major background for the basic lepton-proton elastic process, which must be accounted accurately in the data processing before applying radiative corrections. Thus, at the very outset of the works presented in this thesis, we began with an EFT analysis of the bremsstrahlung process in view of investigating certain 'pathological' scenarios accounting for subtle differences between electron and muon scatterings hitherto neglected (in most high-energy processes), but becomes relevant, if not very significant, in the context of MUSE. While evaluating the bremsstrahlung process we observed that

radiation from proton does not contribute at leading order (LO) in HBχPT, but instead it starts contributing at next-to-leading order (NLO) as interference term with lepton bremsstrahlung. We found that the emitted photon spectra show strong peaking behavior along both the incoming and outgoing lepton directions, especially for electron bremsstrahlung. While the same can not be said in case muon bremsstrahlung which fails to exhibit the characteristic peaking behavior. We also demonstrated that NLO contributions for the electron scatterings are very small which turn out to be considerable for the muon scattering. An essential pathology was identified with the standard chiral power counting scheme associated with electron scattering, whereby the next-to-next-to-leading order (NNLO) contribution from the pion loop diagrams is kinematically enhanced amounting numerically as large as the NLO corrections. Consequently, a rigorous NNLO evaluation in HBχPT is demanded involving evaluation of all pion-loops diagrams and possible inclusion of intermediate excited nucleon states, such as the delta resonances. As an outlook of the work of the thesis, such efforts can be pursued in the future so as to confirm our present findings.

The next part of the work of this thesis focused on the very crucial components of the virtual radiative corrections to elastic lepton-proton scattering process, namely, the two-photon exchange (TPE) contribution. This issue has been extensively debated over the last two decades with the potentiality of ostensibly resolving several puzzling discrepancies that contradict the present day understanding of the proton structure. Notwithstanding the ambiguities of different approaches in estimating the inelastic TPE intermediate state contributions in the low-$|Q^2|$ domain, it has been unequivocally contended that a perturbative (diagrammatic) consideration of of the elastic intermediate proton contribution is substantive enough to largely improve systematics. Based on this inherent hypothesis, we presented a model-independent EFT estimate of the TPE amplitudes at NLO in the chiral power counting scheme using soft photon approximation (SPA) prescription. The resulting infrared free TPE fractional contribution to the elastic lepton-proton cross section is in good numerical agreement with existing model predictions based on phenomenological form factors. Again as a next step, it would be useful to extend our SPA analysis of considering the exact evaluation of the TPE loop-integrals (in particular, the four-point

function in the heavy baryon scheme) using standard packages and to examine the robustness of our present SPA results. An estimate of the NNLO corrections in HBχPT that include, e.g., contribution of pion-loops and the proton's magnetic moment, would also be helpful in improving the theoretical uncertainties involved in using the HBχPT approach. Additionally, the inelastic $\Delta(1232)$ resonance intermediate TPE contributions may be included to improve systematics.

The final part of the thesis was concerned with the model-independent low-energy EFT estimation of the total radiative correction to the elastic scattering process where hadronic structure and proton recoil corrections at NLO in HBχPT was incorporated. For this purpose, we combined our TPE evaluations with other virtual corrections, viz. vertex and vacuum polarization corrections, along with the soft photon bremsstrahlung correction which was also evaluated with the standard approximation, $q \approx Q$, akin to elastic kinematics in the $k \to 0$ limit. To contrast the proton bremsstrahlung and TPE, which start to contribute at NLO, the leading non-zero proton vertex correction only start contributing at NNLO, and hence excluded at the current level of accuracy. Notably, while evaluating the lepton-photon vertex corrections at LO we considered the often neglected magnetic or the pauli form factor, along with the dominant electric or Dirac form factor. It was observed that although the former contribution were negligibly small for electron scattering, a sizable contribution was obtained for muon scattering in the MUSE kinematic domain. We subsequently found that the total radiative correction up-to-and-including NLO for electron scattering is negative, growing up to as large as 25%, while for muon scattering it is a mere 2%, with the sign of the correction changing from positive to negative for $|Q^2| \simeq 0.04$ (GEV/c)^2 for increasing $|Q^2|$. We used a cut off parameter Δ^*_γ, namely, the detector acceptance, to divide to photon energy spectrum to soft and hard part for evaluating the soft bremsstrahlung contribution to radiative correction. Inevitably all our results were inherently dependent on the value of Δ^*_γ, which we choose $\sim 1\%$ of the incoming lepton energy for our numerical estimates. A relative comparison of the LO and NLO numerical results indicated a considerable degree of enhancement specially in our NLO results for muon scattering, potentially spoiling the convergence of the HBχPT power counting at our working accuracy. This is mainly due to the largeness of the muon mass relative to the low-energy MUSE kinematics. A more complete and

robust analysis up to NNLO is thus desirable, which other than pion-loop contributions to the proton vertex corrections, also brings in contribution from low-energy constant and inelastic proton polarizability (including various nucleon excitations and resonances).

Besides the issue of NNLO corrections to the lepton-proton elastic process, an accurate estimation of the inelastic *hard* bremsstrahlung background, viz. the elastic radiative tail, is also needed alongside for a complete "radiative unfolding" analysis applicable to future available "raw" scattering data from MUSE. In Chapter 4, a HBχPT estimation of the tail distribution was considered at NLO accuracy, but without proper consideration of the IR divergences associated with the elastic end-point (see also Ref. [212]). Notably, a detailed "recipe" of radiative tail analysis was already considered in Ref. [139] in the context of QED corrections to the *inelastic* virtual Compton scattering process (to contrast our *elastic* tail spectrum of interest). However, an apparent shortcoming of that analysis is the rather *ad hoc* treatment of the radiative corrections on the proton side, neglecting all hadronic structure effects. A HBχPT approach is thus needed to explore the prospects of systematical improvement of the elastic tail analysis in close analogy to the procedure given in Ref. [139], but with additional inclusion of hadronic effects in real internal radiation losses.

Another possible direction of extension of this thesis work is to investigate the isospin breaking contributions to the radiative corrections which were hitherto not been taken into account. It is interesting to note that even at $\mathcal{O}(\alpha)$ NLO accuracy we expect small amounts of "strong" isospin breaking (factorizable) contributions from the insertions of the finite LEC c_5 that is proportional to $m_d - m_u$, and will introduce additional IR-divergent TPE and bremsstrahlung diagrams. The complete NLO evaluation of the radiative corrections including the isospin violating diagrams will be pursued in future.

Appendix A

LO & NLO SU(2) HBχPT Lagrangians

This appendix is a continuation of Chapter 3 where we summarize display the relevant pieces of the *leading order* (LO) and *next-to-leading order* (NLO) HBχPT Lagrangian used in this thesis work along with the Feynman rules for the corresponding vertices. The Lagrangian ($\widehat{\mathcal{L}}^{(1)}_{\pi N}$) relevant for our study is [140, 215],

$$\widehat{\mathcal{L}}^{(1)}_{\pi N} = \bar{N}_v(iv\cdot\mathcal{D} + g_A S\cdot u)N_v \;;\; u_\mu \;=\; iu^\dagger\nabla_\mu U u^\dagger \,. \tag{A.1}$$

Here N_v denotes the heavy nucleon spinor field and $g_A \cong 1.26$ is the nucleon axial-vector coupling constant, which does not contribute to our amplitude at LO and NLO. It is convenient to choose the proton four-velocity to be $v^\mu = (1,\vec{0})$ which determines the covariant proton spin operator to be $S^\mu = (0, \frac{1}{2}\vec{\sigma})$. The covariant derivatives $\mathcal{D}_\mu$ and ∇_μ in Eq. (A.1) are defined as

$$\mathcal{D}_\mu \;=\; \partial_\mu + \Gamma_\mu - iv^{(s)}_\mu; \quad \Gamma_\mu = \frac{1}{2}[u^\dagger(\partial_\mu - ir_\mu)u + u(\partial_\mu - il_\mu)u^\dagger]\,, \tag{A.2}$$

$$\nabla_\mu U \;=\; \partial_\mu U - ir_\mu U + iUl_\mu \,. \tag{A.3}$$

The photon field $\mathcal{A}_\mu(x)$ is the only external vector source used in this work, and whose iso-scalar part enters as $v^{(s)}_\mu(x) = -e\frac{I}{2}\mathcal{A}_\mu(x)$, where I is the identity matrix. The *chiral*

connection Γ_μ and the *chiral vielbein* u_μ include the external iso-vector sources $r_\mu(x)$ and $l_\mu(x)$. In our work the left- and right- handed sources become $r_\mu(x) = l_\mu(x) = -e\frac{\tau_3}{2}\mathcal{A}_\mu(x)$. It may be noted that for lepton-proton scattering process, we everywhere set $U(x) = 1$ at the LO and NLO, where explicit pion fields are absent. The pion fields in $U(x)$ only enter the calculations at the NNLO through pion loop contributions. We also specify the NLO Lagrangian [140, 215], retaining, only the terms directly relevant to our analysis:

$$\widehat{\mathcal{L}}^{(2)}_{\pi N} = \bar{N}_v \frac{1}{2M}\Big\{(v\cdot\mathcal{D})^2 - \mathcal{D}\cdot\mathcal{D} - \frac{i}{2}\left[S^\mu, S^\nu\right]\Big[(1+\kappa_v)f^+_{\mu\nu} + 2(1+\kappa_s)v^{(s)}_{\mu\nu}\Big] + \cdots\Big\}N_v \quad \text{(A.4)}$$

Here, $f^+_{\mu\nu} = u^\dagger F^R_{\mu\nu} u + u F^L_{\mu\nu} u^\dagger = -e\left(\partial_\mu\mathcal{A}_\nu - \partial_\nu\mathcal{A}_\mu\right)\left(u^\dagger\mathcal{Q}u + u\mathcal{Q}u^\dagger\right)$, with $\mathcal{Q} = \mathrm{diag}(1,0)$ is the nucleon charge matrix, and

$$\begin{aligned} F^L_{\mu\nu} &= F^R_{\mu\nu} = \partial_\mu l_\nu - \partial_\nu l_\mu - i\left[l_\mu, l_\nu\right] = -e\frac{\tau_3}{2}\left(\partial_\mu\mathcal{A}_\nu - \partial_\nu\mathcal{A}_\mu\right), \\ v^{(s)}_{\mu\nu} &= \partial_\mu v^{(s)}_\nu - \partial_\nu v^{(s)}_\mu = -e\frac{I}{2}\left(\partial_\mu\mathcal{A}_\nu - \partial_\nu\mathcal{A}_\mu\right). \end{aligned} \quad \text{(A.5)}$$

Finally, we list the Feynman rules for the LO and NLO HBχPT propagators and vertices required in this work.

Vertices and propagator from $\widehat{\mathcal{L}}^{(1)}_{\pi N}$	Feynman Rule
Nucleon propagator (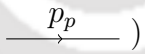)	$\frac{i}{v\cdot p_p + i0}$
One photon vertex ()	$\frac{ie}{2}(1+\tau^3)\epsilon^*\cdot v$

Vertices and propagator from $\widehat{\mathcal{L}}^{(2)}_{\pi N}$	Feynman Rule
Nucleon propagator (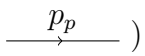)	$\frac{i}{2M}\left(1 - \frac{p_p^2}{(v\cdot p_p + i0)^2}\right)$
One photon vertex (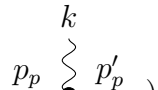)	$\frac{ie^2}{2M}(1+\tau^3)[\epsilon^*\cdot(p_p+p'_p) - (\epsilon^*\cdot v)\,v\cdot(p_p+p'_p)]$ $+\frac{ie}{2M}[S\cdot\epsilon,\, S\cdot k](1+\kappa_s+(1+\kappa_v)\tau^3)$
Two photon vertex (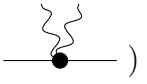)	$\frac{ie^2}{4M}(1+\tau^3)[\epsilon^*\cdot\epsilon - (\epsilon^*\cdot v)(\epsilon\cdot v)]$

Appendix B

Partial NLO amplitudes from Chapter:4

Here we display the ten partial amplitudes appearing in our NLO corrections to the lepton-proton bremsstrahlung differential cross section, Eq. (4.18):

$$
\begin{aligned}
W_{AE} \;=\; & -m_l^2 E_l(\vec{p}_p' \cdot \vec{p}') - m_l^2 E_l(\vec{p}_p \cdot \vec{p}') + m_l^2 E_l'(\vec{p}_p' \cdot \vec{k}) + m_l^2 E_l'(\vec{p}_p \cdot \vec{k}) - m_l^2 E_l'(\vec{p}_p' \cdot \vec{p}) \\
& - m_l^2 E_l'(\vec{p}_p \cdot \vec{p}) + m_l^2 E_\gamma^0(\vec{p}_p' \cdot \vec{p}') + m_l^2 E_\gamma^0(\vec{p}_p \cdot \vec{p}') + E_l (E_\gamma^0)^2 (\vec{p}_p \cdot \vec{p}') + E_l (E_\gamma^0)^2 (\vec{p}_p' \cdot \vec{p}') \\
& + E_l E_l' E_\gamma^0 (\vec{p}_p \cdot \vec{k}) + E_l E_l' E_\gamma^0 (\vec{p}_p' \cdot \vec{k}) - E_l' (\vec{p}_p' \cdot \vec{k})(\vec{p} \cdot \vec{k}) - E_l' (\vec{p}_p \cdot \vec{k})(\vec{p} \cdot \vec{k}) \\
& - E_\gamma^0 (\vec{p}_p' \cdot \vec{p}')(\vec{p} \cdot \vec{k}) - E_\gamma^0 (\vec{p}_p \cdot \vec{p}')(\vec{p} \cdot \vec{k}) \,,
\end{aligned}
$$

$$
\begin{aligned}
W_{AF} \;=\; & m_l^2 E_l(\vec{p}_p' \cdot \vec{k}) + m_l^2 E_l(\vec{p}_p \cdot \vec{k}) + m_l^2 E_l'(\vec{p}_p' \cdot \vec{k}) + m_l^2 E_l'(\vec{p}_p \cdot \vec{k}) + m_l^2 E_\gamma^0(\vec{p}_p' \cdot \vec{k}) + m_l^2 E_\gamma^0(\vec{p}_p \cdot \vec{p}) \\
& + m_l^2 E_\gamma^0(\vec{p}_p \cdot \vec{p}') + m_l^2 E_\gamma^0(\vec{p}_p \cdot \vec{k}) - m_l^2 E_\gamma^0(\vec{p}_p' \cdot \vec{p}') - m_l^2 E_\gamma^0(\vec{p}_p' \cdot \vec{p}) + E_l^2 E_l'(\vec{p}_p' \cdot \vec{p}') \\
& + E_l^2 E_l'(\vec{p}_p \cdot \vec{p}') + E_l^2 E_\gamma^0(\vec{p}_p' \cdot \vec{p}') + E_l^2 E_\gamma^0(\vec{p}_p \cdot \vec{p}') + E_l (E_l')^2 (\vec{p}_p' \cdot \vec{p}) + E_l (E_l')^2 (\vec{p}_p \cdot \vec{p}) \\
& - E_l (E_l')^2 (\vec{p}_p' \cdot \vec{k}) - E_l (E_l')^2 (\vec{p}_p \cdot \vec{k}) + E_l (\vec{p}_p' \cdot \vec{p})(\vec{p}' \cdot \vec{k}) + E_l (\vec{p}_p' \cdot \vec{p}')(\vec{p}' \cdot \vec{k}) + E_l (\vec{p}_p \cdot \vec{p})(\vec{p}' \cdot \vec{k}) \\
& + E_l (\vec{p}_p \cdot \vec{p}')(\vec{p}' \cdot \vec{k}) - E_l (\vec{p}_p' \cdot \vec{p}')(\vec{p} \cdot \vec{p}') - E_l (\vec{p}_p' \cdot \vec{p}')(\vec{p} \cdot \vec{k}) - E_l (\vec{p}_p \cdot \vec{p}')(\vec{p} \cdot \vec{p}') \\
& - E_l (\vec{p}_p \cdot \vec{p}')(\vec{p} \cdot \vec{k}) + E_l' (\vec{p}_p' \cdot \vec{k})(\vec{p} \cdot \vec{p}') + E_l' (\vec{p}_p \cdot \vec{k})(\vec{p} \cdot \vec{p}') - E_l' (\vec{p}_p \cdot \vec{p})(\vec{p} \cdot \vec{p}') \\
& - E_l' (\vec{p}_p \cdot \vec{p}')(\vec{p} \cdot \vec{k}) - E_l' (\vec{p}_p' \cdot \vec{p})(\vec{p} \cdot \vec{p}') - E_l' (\vec{p}_p' \cdot \vec{p}')(\vec{p} \cdot \vec{k}) - E_\gamma^0 (\vec{p}_p' \cdot \vec{p})(\vec{p} \cdot \vec{p}') \\
& + E_\gamma^0 (\vec{p}_p \cdot \vec{p})(\vec{p} \cdot \vec{p}') \,,
\end{aligned}
$$

$$
\begin{aligned}
W_{AG} \;=\; & m_l^2 E_l^2 E_\gamma^0 + E_l^3 E_l' E_\gamma^0 + 2m_l^2 E_l(\vec{p}_p\cdot\vec{p}) - m_l^2 E_l(\vec{p}_p\cdot\vec{k}) - m_l^2 E_l(\vec{p}\cdot\vec{k}) + 2E_l^2 E_l'(\vec{p}_p\cdot\vec{p}) \\
& - E_l^2 E_l'(\vec{p}_p\cdot\vec{k}) - E_l^2 E_l'(\vec{p}\cdot\vec{k}) - E_l' E_l E_\gamma^0(\vec{p}_p\cdot\vec{p}) + E_l^2 E_\gamma^0(\vec{p}\cdot\vec{p}') - E_l^2 E_\gamma^0(\vec{p}_p\cdot\vec{p}') \\
& + 2E_l(\vec{p}_p\cdot\vec{p})(\vec{p}\cdot\vec{p}') - E_l(\vec{p}_p\cdot\vec{p})(\vec{p}'\cdot\vec{k}) + E_l(\vec{p}_p\cdot\vec{p}')(\vec{p}\cdot\vec{k}) - E_l(\vec{p}_p\cdot\vec{k})(\vec{p}\cdot\vec{p}') \\
& - E_l(\vec{p}\cdot\vec{p}')(\vec{p}\cdot\vec{k})\,,
\end{aligned}
$$

$$
W_{AK} \;=\; EE_\gamma(EE'E_\gamma + E'm_l^2 - E'\,\vec{p}\cdot\vec{k} + Em_l^2 + E\,\vec{p}'\cdot\vec{k} - 2E_\gamma m_l^2 - E_\gamma\,\vec{p}\cdot\vec{p}')\,,
$$

$$
\begin{aligned}
W_{AH} \;=\; & m_l^2 E_l^2 E_\gamma^0 + E_l^3 E_l' E_\gamma^0 + m_l^2 E_l(\vec{p}_p'\cdot\vec{k}) - 2m_l^2 E_l(\vec{p}_p'\cdot\vec{p}) - m_l^2 E_l(\vec{p}\cdot\vec{k}) - 2E_l^2 E_l'(\vec{p}_p'\cdot\vec{p}) \\
& + E_l^2 E_l'(\vec{p}_p'\cdot\vec{k}) + E_l' E_l E_\gamma^0(\vec{p}_p'\cdot\vec{p}) - E_l^2 E_l'(\vec{p}\cdot\vec{k}) + E_l^2 E_\gamma^0(\vec{p}_p'\cdot\vec{p}') + E_l^2 E_\gamma^0(\vec{p}\cdot\vec{p}') \\
& + E_l(\vec{p}_p'\cdot\vec{p})(\vec{p}'\cdot\vec{k}) - 2E_l(\vec{p}_p'\cdot\vec{p})(\vec{p}'\cdot\vec{p}) + E_l(\vec{p}_p'\cdot\vec{k})(\vec{p}'\cdot\vec{p}) - E_l(\vec{p}_p'\cdot\vec{p}')(\vec{p}\cdot\vec{k}) \\
& - E_l(\vec{p}'\cdot\vec{p})(\vec{p}\cdot\vec{k})\,,
\end{aligned}
$$

$$
\begin{aligned}
W_{BE} \;=\; & - m_l^2 E_l(\vec{p}_p\cdot\vec{k}) - m_l^2 E_l(\vec{p}_p'\cdot\vec{k}) - m_l^2 E_l'(\vec{p}_p'\cdot\vec{k}) - m_l^2 E_l'(\vec{p}_p\cdot\vec{k}) + m_l^2 E_\gamma^0(\vec{p}_p\cdot\vec{p}') + m_l^2 E_\gamma^0(\vec{p}_p'\cdot\vec{p}') \\
& + m_l^2 E_\gamma^0(\vec{p}_p\cdot\vec{p}) - m_l^2 E_\gamma^0(\vec{p}_p'\cdot\vec{k}) - m_l^2 E_\gamma^0(\vec{p}_p'\cdot\vec{p}) - m_l^2 E_\gamma^0(\vec{p}_p\cdot\vec{k}) + E_l^2 E_l'(\vec{p}_p'\cdot\vec{p}') \\
& + E_l^2 E_l'(\vec{p}_p\cdot\vec{p}') + E_l^2 E_l'(\vec{p}_p\cdot\vec{k}) + E_l(E_l')^2(\vec{p}_p'\cdot\vec{p}) + E_l(E_l')^2(\vec{p}_p\cdot\vec{p}) - (E_l')^2 E_\gamma^0(\vec{p}_p'\cdot\vec{p}) \\
& - (E_l')^2 E_\gamma^0(\vec{p}_p\cdot\vec{p}) + E_l(\vec{p}_p'\cdot\vec{p})(\vec{p}'\cdot\vec{k}) + E_l(\vec{p}_p\cdot\vec{p})(\vec{p}'\cdot\vec{k}) - E_l(\vec{p}_p\cdot\vec{k})(\vec{p}\cdot\vec{p}') \\
& - E_l(\vec{p}_p'\cdot\vec{p}')(\vec{p}'\cdot\vec{p}) - E_l(\vec{p}_p'\cdot\vec{k})(\vec{p}'\cdot\vec{p}) + E_l'(\vec{p}_p\cdot\vec{p})(\vec{p}'\cdot\vec{k}) - E_l'(\vec{p}_p'\cdot\vec{p})(\vec{p}'\cdot\vec{p}) \\
& - E_l'(\vec{p}_p'\cdot\vec{p})(\vec{p}\cdot\vec{k}) - E_l'(\vec{p}_p'\cdot\vec{p}')(\vec{p}\cdot\vec{k}) - E_l'(\vec{p}_p\cdot\vec{p})(\vec{p}\cdot\vec{p}') - E_l'(\vec{p}_p\cdot\vec{p})(\vec{p}\cdot\vec{k}) \\
& - E_l'(\vec{p}_p\cdot\vec{p}')(\vec{p}\cdot\vec{k}) + E_\gamma^0(\vec{p}_p'\cdot\vec{p}')(\vec{p}\cdot\vec{p}') + E_\gamma^0(\vec{p}_p\cdot\vec{p}')(\vec{p}\cdot\vec{p}')\,,
\end{aligned}
$$

$$
\begin{aligned}
W_{BF} \;=\; & - m_l^2 E_l(\vec{p}_p'\cdot\vec{p}') - m_l^2 E_l(\vec{p}_p\cdot\vec{p}') - m_l^2 E_l(\vec{p}_p'\cdot\vec{k}) - m_l^2 E_l(\vec{p}_p\cdot\vec{k}) - m_l^2 E_l'(\vec{p}_p'\cdot\vec{p}) - m_l^2 E_l'(\vec{p}_p\cdot\vec{p}) \\
& - m_l^2 E_\gamma^0(\vec{p}_p'\cdot\vec{p}) - m_l^2 E_\gamma^0(\vec{p}_p\cdot\vec{p}) + E_l'(E_\gamma^0)^2(\vec{p}_p'\cdot\vec{p}) + E_l'(E_\gamma^0)^2(\vec{p}_p\cdot\vec{p}) + E_l E_l' E_\gamma^0(\vec{p}_p'\cdot\vec{k}) \\
& + E_l E_l' E_\gamma^0(\vec{p}_p\cdot\vec{k}) - E_l(\vec{p}_p'\cdot\vec{k})(\vec{p}'\cdot\vec{k}) - E_l(\vec{p}_p\cdot\vec{k})(\vec{p}'\cdot\vec{k}) - E_\gamma^0(\vec{p}_p'\cdot\vec{p})(\vec{p}'\cdot\vec{k}) \\
& - E_\gamma^0(\vec{p}_p\cdot\vec{p})(\vec{p}'\cdot\vec{k})\,,
\end{aligned}
$$

$$
\begin{aligned}
W_{BG} \;=\; & m_l^2(E_l')^2 E_\gamma^0 + E_l E_\gamma^0(E_l')^3 + 2m_l^2 E_l'(\vec{p}_p\cdot\vec{p}') + m_l^2 E_l'(\vec{p}_p\cdot\vec{k}) - m_l^2 E_l'(\vec{p}\,'\cdot\vec{k}) + 2E_l(E_l')^2(\vec{p}_p\cdot\vec{p}') \\
& + E_l(E_l')^2(\vec{p}_p\cdot\vec{k}) - E_l(E_l')^2(\vec{p}'\cdot\vec{k}) + E_l E_l' E_\gamma^0(\vec{p}_p\cdot\vec{p}') + (E_l')^2 E_\gamma^0(\vec{p}_p\cdot\vec{p}) + (E_l')^2 E_\gamma^0(\vec{p}'\cdot\vec{p}) \\
& + 2E_l'(\vec{p}_p\cdot\vec{p}')(\vec{p}'\cdot\vec{p}) + E_l'(\vec{p}_p\cdot\vec{k})(\vec{p}\cdot\vec{p}') + E_l'(\vec{p}_p\cdot\vec{p}')(\vec{p}\cdot\vec{k}) - E_l'(\vec{p}'\cdot\vec{k})(\vec{p}'\cdot\vec{p}) \\
& - E_l'(\vec{p}_p\cdot\vec{p})(\vec{p}'\cdot\vec{k})\,,
\end{aligned}
$$

$$
\begin{aligned}
W_{BH} \;=\; & -m_l^2(E_l')^2E_\gamma^0 - E_l(E_l')^3E_\gamma^0 + m_l^2E_l'(\vec{p}_p'\cdot\vec{k}) + m_l^2E_l'(\vec{p}'\cdot\vec{k}) + 2m_l^2E_l'(\vec{p}_p'\cdot\vec{p}') + 2E_l(E_l')^2(\vec{p}_p'\cdot\vec{p}') \\
& + E_l^2(E_l')^2(\vec{p}_p'\cdot\vec{k}) + E_l(E_l')^2(\vec{p}'\cdot\vec{k}) + E_lE_l'E_\gamma^0(\vec{p}_p'\cdot\vec{p}') + (E_l')^2E_\gamma^0(\vec{p}_p'\cdot\vec{p}) - (E_l')^2E_\gamma^0(\vec{p}'\cdot\vec{p}) \\
& + 2E_l'(\vec{p}_p'\cdot\vec{p}')(\vec{p}'\cdot\vec{p}) + E_l'(\vec{p}_p'\cdot\vec{p}')(\vec{p}\cdot\vec{k}) + E_l'(\vec{p}_p'\cdot\vec{k})(\vec{p}'\cdot\vec{p}) + E_l'(\vec{p}'\cdot\vec{k})(\vec{p}'\cdot\vec{p}) \\
& - E_l'(\vec{p}_p'\cdot\vec{p})(\vec{p}'\cdot\vec{k})\,,
\end{aligned}
$$

$$
W_{BK} \;=\; E'E_\gamma(EE'E_\gamma + E'm_l^2 - E'\,\vec{p}\cdot\vec{k} + Em_l^2 + E\,\vec{p}'\cdot\vec{k} + 2E_\gamma m_l^2 + E_\gamma\,\vec{p}\cdot\vec{p}')\,. \tag{B.1}
$$

In the laboratory frame or rest frame of the hadron target, the three-momentum of the proton, $|\vec{p}| = 0$. The expressions for the dot-products in our preferred frame of reference, Fig. [4.4], are:

$$
\begin{aligned}
\vec{p}\cdot\vec{p}' &= |\vec{p}'||\vec{p}|\cos\theta\,, \\
\vec{k}\cdot\vec{p}' &= E_\gamma|\vec{p}'|(\cos\gamma\,\cos\alpha + \sin\alpha\,\sin\gamma\,\cos\phi_\gamma)\,, \\
\vec{k}\cdot\vec{p} &= E_\gamma|\vec{p}|(\cos\zeta\,\cos\alpha + \sin\alpha\,\sin\zeta\,\cos\phi_\gamma)\,, \\
\vec{p}_p'\cdot\vec{p}' &= (\vec{Q}-\vec{k})\cdot\vec{p}' = |\vec{Q}||\vec{p}'|\cos\gamma - \vec{k}\cdot\vec{p}'\,, \\
\vec{p}_p'\cdot\vec{p} &= (\vec{Q}-\vec{k})\cdot\vec{p} = |\vec{Q}||\vec{p}|\cos\zeta - \vec{k}\cdot\vec{p}\,, \\
\vec{p}_p'\cdot\vec{k} &= (\vec{Q}-\vec{k})\cdot\vec{k} = |\vec{Q}|E_\gamma\cos\alpha - E_\gamma^2\,.
\end{aligned} \tag{B.2}
$$

Appendix C

Evaluation of TPE seagull diagram

Here we derive the TPE seagull amplitude $\mathcal{M}^{(i)}_{\rm seagull}$ (cf. diagram (i) in Fig. [5.1] of Chapter 5). The integral in Eq. (5.17) being both IR and UV finite does not require any regularization and is evaluated analytically in the 4-dimensional space-time. In section 5.3, it was shown *without* implementing SPA that due to cancellations among various NLO TPE amplitudes only the residual part of $\widetilde{\mathcal{M}}^{(i)}_{\rm seagull}$ proportional to $g^{\mu\nu}$ contributes to the cross section, namely,

$$\begin{aligned}\widetilde{\mathcal{M}}^{(i)}_{\rm seagull} &= -\frac{e^4}{M}\frac{1}{i}\int\frac{d^4k}{(2\pi)^4}\frac{\left[\bar{u}(p')\gamma^\mu(\not{p}-\not{k}+m_l)\gamma_\mu u(p)\right]\,\left[\chi^\dagger(p'_p)\chi(p_p)\right]}{k^2\,(Q-k)^2\,(k^2-2k\cdot p+i0)}\\ &= -\frac{e^4}{M}[\bar{u}(p')\gamma^\alpha\,\mathbb{I}_{\rm seagull}\,\gamma_\alpha u(p)]\,\left[\chi^\dagger(p'_p)\chi(p_p)\right],\end{aligned} \tag{C.1}$$

where the loop-integral appearing above is given by

$$\mathbb{I}_{\rm seagull} = \frac{1}{i}\int\frac{d^4k}{(2\pi)^4}\frac{\not{p}-\not{k}+m_l}{(k^2+i0)(Q-k)^2(k^2-2k\cdot p+i0)}$$

where k and $Q-k$ are the momenta of the two exchanged photons and $Q=p-p'$. Using Feynman parametrization and thereby shifting the integration variable, $k\to k+\beta$ where $\beta=(px+Qy)$ yields,

$$\mathbb{I}_{\rm seagull} = \frac{1}{i}\int_0^1\int_0^1\int_0^1 dx\,dy\,dz\,\delta(1-x-y-z)\int\frac{d^4k}{(2\pi)^4}\frac{2(\not{p}-\not{k}-\not{\beta}+m_l)}{[k^2-\Delta]^3}\,.$$

Integration over the loop momentum k, we obtain

$$\mathbb{I}_{\rm seagull} \;=\; -\frac{1}{16\pi^2}\int_0^1\int_0^1\int_0^1 dx\,dy\,dz\,\delta(1-x-y-z)\left[\frac{\not p-\not\beta+m_l}{\Delta}\right], \qquad \text{(C.2)}$$

where $\Delta=(px+Qy)^2-Q^2y$. Further, it is convenient to make a change of variables from (x,y,z) to (ω,ξ) using the transformation $x=\omega\xi$, $y=\omega(1-\xi)$ and $z=1-\omega$, which amounts to the following change of the integration measures, namely, $dx\,dy\,dz\,\delta(1-x-y-z)\mapsto\omega\,d\omega\,d\xi$. Thus, we obtain

$$\begin{aligned}
\mathbb{I}_{\rm seagull} &= -\frac{1}{16\pi^2}\int_0^1\int_0^1 d\omega d\xi\,\frac{m_l+\not p(1-\omega\xi)-\not Q\omega(1-\xi)}{[\omega(m_l^2\xi^2-Q^2\xi+Q^2)-Q^2(1-\xi)]}\\
&= -\frac{1}{16\pi^2}\int_0^1\int_0^1 d\omega d\xi\left[\frac{m_l+\not p}{\omega(m_l^2\xi^2-Q^2\xi+Q^2)+Q^2(\xi-1)}-\frac{\omega[\not Q+\xi(\not p-\not Q)]}{\omega(m_l^2\xi^2-Q^2\xi+Q^2)+Q^2(\xi-1)}\right]\\
&= -\frac{1}{16\pi^2m_l^2}\left[(m_l+\not p)\mathcal{I}_1-(\not p-\not Q)\left(\mathcal{I}_2+\frac{Q^2}{m_l^2}\mathcal{I}_3\right)-(2\not Q-\not p)\frac{Q^2}{m_l^2}\mathcal{I}_4+\not Q\left(\frac{Q^2}{m_l^2}\mathcal{I}_5-\mathcal{I}_6\right)\right], \qquad \text{(C.3)}
\end{aligned}$$

with

$$\begin{aligned}
\mathcal{I}_1(Q^2) &= \int_0^1 {\rm d}\xi\left[\frac{1}{\xi^2-\frac{Q^2}{m_l^2}\xi+\frac{Q^2}{m_l^2}}\right]\ln\left[\frac{m_l^2\xi^2}{Q^2(\xi-1)}\right],\\
\mathcal{I}_2(Q^2) &= \int_0^1 {\rm d}\xi\left[\frac{\xi}{\xi^2-\frac{Q^2}{m_l^2}\xi+\frac{Q^2}{m_l^2}}\right],\\
\mathcal{I}_3(Q^2) &= \int_0^1 {\rm d}\xi\left[\frac{\xi}{\xi^2-\frac{Q^2}{m_l^2}\xi+\frac{Q^2}{m_l^2}}\right]^2\ln\left[\frac{m_l^2\xi^2}{Q^2(\xi-1)}\right],\\
\mathcal{I}_4(Q^2) &= \int_0^1 {\rm d}\xi\left[\frac{\xi}{\left(\xi^2-\frac{Q^2}{m_l^2}\xi+\frac{Q^2}{m_l^2}\right)^2}\right]\ln\left[\frac{m_l^2\xi^2}{Q^2(\xi-1)}\right],\\
\mathcal{I}_5(Q^2) &= \int_0^1 {\rm d}\xi\left[\frac{1}{\xi^2-\frac{Q^2}{m_l^2}\xi+\frac{Q^2}{m_l^2}}\right]^2\ln\left[\frac{m_l^2\xi^2}{Q^2(\xi-1)}\right],\\
\mathcal{I}_6(Q^2) &= \int_0^1 {\rm d}\xi\left[\frac{1}{\xi^2-\frac{Q^2}{m_l^2}\xi+\frac{Q^2}{m_l^2}}\right]. \qquad \text{(C.4)}
\end{aligned}$$

Each of the above integrals are easily obtainable in closed forms using standard techniques or with *Mathematica*. Since some of these integral have rather elaborate expressions, we prefer to

omit their explicit expressions in this communication. Inserting the loop amplitude $\mathbb{I}_{\rm seagull}$ into Eq. (C.1) we obtain our final expression for the seagull amplitude,

$$\widetilde{\mathcal{M}}^{(i)}_{\rm seagull} = \frac{\alpha^2}{m_l^2 M}\left[\mathcal{N}_1\mathcal{I}_1 - \mathcal{N}_2\left(\mathcal{I}_2 + \frac{Q^2}{m_l^2}\mathcal{I}_3\right) - \mathcal{N}_3\left(\mathcal{I}_6 - \frac{Q^2}{m_l^2}\mathcal{I}_5\right) - \mathcal{N}_4\frac{Q^2}{m_l^2}\mathcal{I}_4\right], \quad \text{(C.5)}$$

where $\mathcal{N}_i \propto \mathcal{M}_\gamma$ $(i = 1, ..., 4)$ are defined as

$$\begin{aligned}
\mathcal{N}_1 &= [\bar{u}(p')\gamma^\mu(m_l + \not{p})\gamma_\mu u(p)][\chi_p^\dagger(p'_p)\chi_p(p_p)]\,,\\
\mathcal{N}_2 &= [\bar{u}(p')\gamma^\mu(\not{p} - \not{Q})\gamma_\mu u(p)][\chi_p^\dagger(p'_p)\chi_p(p_p)]\,,\\
\mathcal{N}_3 &= [\bar{u}(p')\gamma^\mu\not{Q}\gamma_\mu u(p)][\chi_p^\dagger(p'_p)\chi_p(p_p)]\,,\\
\mathcal{N}_4 &= [\bar{u}(p')\gamma^\mu(2Q - \not{p})\gamma_\mu u(p)][\chi_p^\dagger(p'_p)\chi_p(p_p)]\,. \qquad \text{(C.6)}
\end{aligned}$$

Thus, in essence we find that the seagull amplitude, unlike the TPE box amplitudes in SPA, *does not* naturally factorize into the LO amplitude $\mathcal{M}_\gamma$ times a Q^2 dependent function $f(Q^2)$. This result is consistent with the proposition made in Ref. [68] that the one-loop virtual radiative corrections, and in particular the TPE amplitudes, can be expressed as, $\mathcal{M}_{1-\rm Loop} = f(Q^2)\mathcal{M}_\gamma + \overline{\mathcal{M}}_{1-\rm Loop}$. The factorizable IR-divergent first term constitute the dominant, so-called *outer corrections*, independent of the hadron structure, while the non-factorizable IR-finite second term constitutes small corrections, the so-called *inner corrections*. In most works these latter corrections are hadron structure dependent and are often ignored in ultra-relativistic approximations. In HBχPT approach we find that the dominant TPE box diagrams in SPA can be identified with the former corrections, while the seagull term can be identified with the latter ones. At the order of our accuracy, the latter corrections are free of low-energy constants and, therefore, are hadron structure independent.

Finally, it is noteworthy that, while determining $\delta_{\gamma\gamma}^{(\rm seagull)}$, Eq. (5.32), the integrals $\mathcal{I}_5$ and $\mathcal{I}_6$ drop out of the calculation due to vanishing of spin trace of $\mathcal{N}_3$ with $\mathcal{M}_\gamma$, Eq. (5.5). We find

$$\sum_{spins}\mathcal{M}_\gamma^*\mathcal{N}_3 = 0\,, \qquad \text{(C.7)}$$

and

$$\begin{aligned}\sum_{spins}\mathcal{M}_{\gamma}^{*}\mathcal{N}_{1} &= -\sum_{spins}\mathcal{M}_{\gamma}^{*}\mathcal{N}_{2}=\sum_{spins}\mathcal{M}_{\gamma}^{*}\mathcal{N}_{4}\\ &= -\frac{16e^{2}m_{l}^{2}}{Q^{2}}(E+E')(E_{p}+M)(E'_{p}+M)\\ &= -\frac{128e^{2}m_{l}^{2}M^{2}E}{Q^{2}}\left[1+\mathcal{O}\left(\frac{1}{M}\right)\right]. \end{aligned} \tag{C.8}$$

Here we have used, $E' = E+\mathcal{O}(M^{-1})$ and $E'_p = M+\mathcal{O}(M^{-1})$, since the seagull diagram already is an NLO amplitude.

Appendix D

S-frame Detector Acceptance

In this Appendix, we discuss the transformation relations among kinematical quantities between the laboratory frame and the boosted S-frame [10, 47, 50, 139, 160]. The S-frame is defined as the center-of-mass system of the recoil proton and the soft bremsstrahlung photon, $\vec{p}\,'_p + \vec{k} = \vec{Q} = 0$. Here $\vec{p}\,'_p$ and $\vec{k}$ are the respective three-momenta of the recoil proton and the emitted soft photon, and $\vec{Q} = \vec{p} - \vec{p}\,' = \vec{p}\,'_p - \vec{p}_p$ is the three-momentum transferred in the ℓ-p elastic scattering process in the laboratory frame, i.e., the target proton three-momentum $\vec{p}_p = 0$. The maximum energy of the soft (undetected) photon fixes the upper limit of the bremsstrahlung energy integration and is conventionally taken as detector acceptance Δ^*_γ in the laboratory frame. This in essence corresponds to the maximal deviation of the outgoing lepton energy E' from its theoretical elastic limit E'^{el} while practically preserving elastic conditions, i.e., $E'^{el} - E' \leq \Delta^*_\gamma$. In the ensuing treatment using soft photon approximation we shall use, $E' \approx E'^{el}$. [1] In a boosted frame the maximum photon energy limit becomes a frame dependent quantity, which we denote as $\Delta_S \neq \Delta^*_\gamma$ in the S-frame. The phase-space integration for the laboratory frame differential cross section for the soft bremsstrahlung process, $\ell + \mathrm{p} \to \ell + \mathrm{p} + \gamma^*_{\mathrm{soft}}$, namely,

$$\left[\widetilde{\mathrm{d}\sigma}^{(\mathrm{LO,\,NLO})}_{br}\right]_{\gamma\gamma^*} = \frac{(2\pi)\delta^{lab}_k}{8ME'_pE}\,\frac{\mathrm{d}^3\vec{p}\,'}{(2\pi)^3 2E'}\,\frac{\mathrm{d}^3\vec{k}}{(2\pi)^3 2E_\gamma}\,\frac{1}{4}\sum_{spins}|\mathcal{M}^{(0,1)}_{\gamma\gamma^*}|^2\,, \tag{D.1}$$

with the LO/NLO squared amplitudes in the respective soft photon limits, Eqs. (6.42) and (6.67), are complicated by the dependence on the photon emission angles present in the energy

[1] In general, with real photon emissions, $E'^{el} \leq E'$. The equality only holds for the "strictly elastic" (non-radiative) kinematics which is evidently unrealistic in a given laboratory experiment. In this work, since we are concerned with the "physically elastic" process which naturally accompanies soft photon bremsstrahlung, $E' \approx E'^{el}$ is implicitly understood.

conserving δ-function, namely,

$$\delta_k^{lab} \equiv \delta\left(E + M - E' - \sqrt{(\vec{Q} - \vec{k})^2 + M^2} - E_{\gamma^*}\right),$$

appearing in the above expression. Consequently, the emitted photon radiation spectrum in the laboratory frame becomes anisotropic, being defined over a ellipsoidal integration volume which is difficult to evaluate analytically. However, by boosting to the S-frame the integration simplifies into a standard spherical one (see e.g., Ref. [47]), with the above δ-function becoming free of the photon angles in the soft photon limit. This effectively transforms the S-frame kinematics into one akin to a "reversed elastic" scenario in the soft photon limit, denoted by the constraint,

$$\delta^S \equiv \delta\Big(E'^S + E'^S_p - E^S - E^S_p\Big),$$

where the S-frame quantities are denoted by the superscript "S". In terms of the laboratory frame quantities, the following relationships can then be justified:

$$\begin{aligned}
&\text{(i)} \quad E'^S_p \approx M\,, && \text{(ii)}\ E^S \approx E' \approx E'^{\,el} = \frac{E}{\eta}\,,\\
&\text{(iii)} \quad E'^S \approx E\,, && \text{(iv)}\ E^S_p \approx E'_p\,,\\
&\text{(v)} \quad \cos\theta_S \approx \cos\theta\,, && \text{(vi)}\ \Delta_S \approx \eta\Delta^*_\gamma,
\end{aligned} \tag{D.2}$$

where $\eta = 1 + 2E\sin^2(\theta/2)/M$ is the laboratory frame proton recoil factor. In other words, the energy transformations between the two frames are easily effected by simply interchanging the energies between the initial and final states of the elastic process.

In view of pedagogical interests, we derive these relations between the two frames using soft photon approximation. We make use of the four-momentum conservation relation for the bremsstrahlung process, namely, $p + P - p' = P' + k$.

- First, we consider the invariant $(P' + k)^2$ in the S-frame:

$$(P'^S + k^S)^2 \;=\; M^2 + 2E'^S_p E^S_{\gamma^*} + 2(E^S_{\gamma^*})^2 \overset{\gamma_{\rm soft}}{\rightsquigarrow} M^2\,.$$

  Since $\vec{p}'^S_p + \vec{k}^S = 0$, we must have

$$(P'^S + k^S)^2 = (E'^S_p + E^S_\gamma)^2 \overset{\gamma_{\rm soft}}{\rightsquigarrow} (E'^S_p)^2\,,$$

which implies, $\boxed{E_p'^S \approx M}$.

- Second, we consider the invariant $p \cdot (P' + k)$. In the S-frame we have

$$p^S \cdot (P'^S + k^S) = E^S (E_p'^S + E_{\gamma^*}^S) \overset{\gamma_{\rm soft}}{\rightsquigarrow} M E^S \,,$$

while in the laboratory frame we have

$$p \cdot (P' + k) \;=\; p \cdot (P + Q) = ME + \frac{Q^2}{2} = ME'^{el} \,.$$

This implies, $\boxed{E^S \approx E'^{el}}$.

- Third, we consider the invariant $p' \cdot (P' + k)$.

$$\begin{aligned} p' \cdot (P' + k) &= p'^S \cdot (P'^S + k^S) \\ \hookrightarrow \quad p' \cdot (P + Q) &= E'^S (E_p'^S + E_{\gamma^*}^S) \\ \overset{\gamma_{\rm soft}}{\rightsquigarrow} \; ME'^{el} - \frac{Q^2}{2} &\approx ME'^S \,. \end{aligned}$$

Since, $E = E'^{el} - \frac{Q^2}{2M}$, the above relation implies, $\boxed{E'^S \approx E}$.

- Fourth, we consider the energy conservation in the S-frame:

$$\begin{aligned} E^S + E_p^S - E'^S &= E_p'^S + E_\gamma^S \,, \\ E_p^S &= E_p'^S + E_\gamma^S + E'^S - E^S \\ &\overset{\gamma_{\rm soft}}{\rightsquigarrow} M + E - E'^{el} \approx E_p' \,, \end{aligned}$$

where we have used the relations derived for E^S, E'^S and $E_p'^S$. Thus, $\boxed{E_p^S \approx E_p'}$.

- Fifth, we use the invariant expression for the squared four-momentum transfer, $Q^2 = Q_S^2$, in each frame:

$$\begin{aligned} Q^2 &= 2m_l^2 - 2EE'^{el}(1 - \beta\beta'^{el}\cos\theta) \,, \\ Q_S^2 &= 2m_l^2 - 2E^S E'^S (1 - \beta_S \beta_S' \cos\theta_S) \\ &\overset{\gamma_{\rm soft}}{\rightsquigarrow} 2m_l^2 - 2E'^{el} E (1 - \beta'^{el} \beta \cos\theta_S) \,. \end{aligned}$$

Using the relations derived for E^S, E'^S, it follows that $\boxed{\cos\theta_S \approx \cos\theta}$.

- Finally, squaring the aforementioned four-momentum conservation relation, then expressing the left and right hand sides in terms of the laboratory frame and S-frame quantities respectively, yields

$$2m_l^2 \quad - \quad 2p\cdot p' + 2M(E-E') = 2P'^S\cdot k^S = 2M\Delta_S\sqrt{1+\left(\frac{\Delta_S}{M}\right)^2} + 2\Delta_S^2\,,$$

where the maximal limit of the emitted soft photon energy in the S-frame is $E^S_{\gamma^*} = |\vec{k}^S| \lesssim \Delta_S \ll M$. Next to obtain an estimate for Δ_S in the soft photon approximation, we further neglect the lepton mass, $m_l \ll M$, such that the above relation becomes

$$M(E-E') \quad - \quad EE'(1-\cos\theta) = M\Delta_S\left[1+\mathcal{O}\left(\frac{\Delta_S}{M}\right)\right].$$

Furthermore, in the elastic limit, i.e, with $\Delta_S \to 0$ and $E' \to E'^{el}$, the above equation reduces to

$$M(E-E'^{el}) - EE'^{el}(1-\cos\theta) = 0\,.$$

Then, subtracting the latter relation from the former, yields our desired expression for Δ_S:

$$\Delta_S \quad = \quad (E'^{el}-E')\left[1+\frac{2E}{M}\sin^2\left(\frac{\theta}{2}\right)\right] + \mathcal{O}\left(\frac{\Delta_S}{M}\right) \approx \eta\Delta^*_\gamma\,.$$

Thus, the upper limit of the soft photon bremsstrahlung integrals (see Appendix B) in the S-frame is taken as $\boxed{\Delta_S \leq \eta\Delta^*_\gamma}$.

Bibliography

[1] E. Rutherford. LIV. Collision of α particles with light atoms. IV. An anomalous effect in nitrogen. *Philos. Mag.*, **37**:581, 1919.

[2] E. D. Bloom, D. H. Coward, H. DeStaebler, J. Drees, G. Miller, L. W. Mo, R. E. Taylor, M. Breidenbach, J. I. Friedman, G. C. Hartmann, and H. W. Kendall. High-energy inelastic $e-p$ scattering at 6° and 10°. *Phys. Rev. Lett.*, **23**:930–934, Oct 1969.

[3] M. Breidenbach, J. I. Friedman, H. W. Kendall, E. D. Bloom, D. H. Coward, H. DeStaebler, J. Drees, L. W. Mo, and R. E. Taylor. Observed Behavior of Highly Inelastic Electron-Proton Scattering. *Phys. Rev. Lett.*, 23:935–939, Oct 1969.

[4] Richard E. Taylor. Deep inelastic scattering: The early years. *Rev. of Mod. Phys.*, **63**(3): 573, 1991.

[5] M. R. Adams, S. Aid, P. L. Anthony, M. D. Baker, J. Bartlett, A. A. Bhatti, H. M. Braun, W. Busza, Janet M. Conrad, and G. Coutrakon. First measurements of jet production rates in deep-inelastic lepton-proton scattering. *Phys. Rev. Lett.*, **69**(7):1026, 1992.

[6] P. Z. Quintas, W. C. Leung, S. R. Mishra, F. Sciulli, C. Arroyo, K. T. Bachmann, R. E. Blair, C. Foudas, B. J. King, and W. C. Lefmann. Measurement of Λ QCD from ν μ-Fe nonsinglet structure functions at the Fermilab Tevatron. *Phys. Rev. Lett.*, **71**(9):1307, 1993.

[7] Re. Hofstadter, H. R. Fechter, and J. A. McIntyre. Scattering of high-energy electrons and the method of nuclear recoil. *Phys. Rev.*, **91**(2):422, 1953.

[8] R. Hofstadter and R. W. McAllister. Electron scattering from the proton. *Physical Review*, 98(1):217, 1955.

[9] E. E. Chambers and R. Hofstadter. Structure of the proton. *Phys. Rev.*, **103**(5):1454, 1956.

[10] L. W. Mo and Y. S. Tsai. Radiative Corrections to Elastic and Inelastic e p and mu p Scattering. *Rev. Mod. Phys.*, 41:205–235, 1969. doi: 10.1103/RevModPhys.41.205.

[11] Y. S. Tsai. Radiative corrections to electron scatterings. 1971.

[12] Zbigniew Was. Radiative corrections. Technical report, P00020602, 1994.

[13] J. Schwinger. Quantum electrodynamics. iii. the electromagnetic properties of the electronradiative corrections to scattering. *Phys. Rev.*, **76**(6):790, 1949.

[14] J. D. Walecka. Spectral functions in the static theory. *Il Nuovo Cimento (1955-1965)*, **11** (6):821–836, 1959.

[15] F. J. Ernst, R. G. Sachs, and K. C. Wali. Electromagnetic form factors of the nucleon. *Phys. Rev.*, **119**(3):1105, 1960.

[16] A. I. Akhiezer, Mikhail Rekalo, et al. Polarization phenomena in electron scattering by protons in the high energy region. In *Sov. Phys. Dokl.*, volume **13**, page 572, 1968.

[17] A. I. Akhiezer and Mikhail Rekalo. Polarization effects in the scattering of leptons by hadrons. *Fiz. Elem. Chast. Atom. Yadra*, **4**:662–688, 1974.

[18] V. Punjabi, Ch. F. Perdrisat, K. A. Aniol, F. T. Baker, J. Berthot, P. Y. Bertin, W. Bertozzi, A. Besson, L. Bimbot, and W. U. Boeglin. Proton elastic form factor ratios to q 2= 3.5 gev 2 by polarization transfer. *Phys. Rev. C*, **71**(5):055202, 2005.

[19] M. N. Rosenbluth. High energy elastic scattering of electrons on protons. *Phys. Rev.*, **79** (4):615, 1950.

[20] D. R. Yennie, M. M. Levy, and D. G. Ravenhall. Electromagnetic structure of nucleons. *Rev. of Mod. Phys.*, **29**(1):144, 1957.

[21] R. Pohl, A. Antognini, F. Nez, F. D. Amaro, F. Biraben, J. Cardoso, D. S. Covita, A. Dax, S. Dhawan, and L. M. P. Fernandes. The size of the proton. *Nature*, **466**(7303):213, 2010.

[22] J. Arrington, P. G. Blunden, and W. Melnitchouk. Review of two-photon exchange in electron scattering. *Prog. Part. Nucl. Phys.*, **66**:782–833, 2011. doi: 10.1016/j.ppnp.2011.07.003.

[23] R. Pohl, R. Gilman, G. A. Miller, and K. Pachucki. Muonic hydrogen and the proton radius puzzle. *Ann. Rev. of Nucl. and Part. Sci.*, **63**:175–204, 2013.

[24] J. C. Bernauer and R. Pohl. The proton radius problem. *Scientific American*, **310**(2): 32–39, 2014.

[25] C. E. Carlson. The proton radius puzzle. *Prog. in Part. and Nucl. Phys.*, **82**:59–77, 2015.

[26] J. J. Krauth, K. Schuhmann, M. Abdou Ahmed, F. D. Amaro, P. Amaro, F. Biraben, J. M. R. Cardoso, M. L. Carvalho, D. S. Covita, and A. Dax. The proton radius puzzle. *arXiv preprint arXiv:1706.00696*, 2017.

[27] D. Tucker-Smith and I. Yavin. Muonic hydrogen and MeV forces. *Phys. Rev. D*, **83**(10): 101702, 2011.

[28] V. Barger, C. W. Chiang, W. Y. Keung, and D. Marfatia. Proton size anomaly. *Phys. Rev. Lett.*, **106**(15):153001, 2011.

[29] V. Barger, C. W. Chiang, W. Y. Keung, and D. Marfatia. Constraint on parity-violating muonic forces. *Phys. Rev. Lett.*, **108**(8):081802, 2012.

[30] C. E. Carlson and B. C. Rislow. New physics and the proton radius problem. *Phys. Rev. D*, **86**(3):035013, 2012.

[31] N. Bezginov, T. Valdez, M. Horbatsch, A. Marsman, A. C. Vutha, and E. A. Hessels. A measurement of the atomic hydrogen Lamb shift and the proton charge radius. *Science*, **365**(6457):1007–1012, 2019.

[32] W. Xiong, A. Gasparian, H. Gao, D. Dutta, M. Khandaker, N. Liyanage, E. Pasyuk, C. Peng, X. Bai, and L. Ye. A small proton charge radius from an electron–proton scattering experiment. *Nature*, **575**(7781):147–150, 2019.

[33] M. Mihovilovič, H. Merkel, A. Weber, P. Achenbach, C. A. Gayoso, T. Beranek, J. Beričič, J. C. Bernauer, D. Bosnar, and R. Böhm. Initial state radiation experiment at MAMI. In *EPJ Web of Conf.*, volume **72**, page 00017. EDP Sciences, 2014.

[34] A. Gasparian, R. Pedroni, Z. Ahmed, M. Khandaker, V. Punjabi, C. Salgado, I. Akushevich, H. Gao, M. Huang, and S. Jawalkar. High precision measurement of the proton charge radius. *Proposal to Jefferson Lab, PAC-38 C12-11-106 https://www. jlab. org/-exp_prog/proposals/11/PR12-11-106. pdf*, 2011.

[35] J. C. Bernauer, P. Achenbach, C. Ayerbe Gayoso, R. Böhm, D. Bosnar, L. Debenjak, M. O. Distler, L. Doria, A. Esser, H. Fonvieille, J. M. Friedrich, J. Friedrich, M. Gómez Rodríguez de la Paz, M. Makek, H. Merkel, D. G. Middleton, U. Müller, L. Nungesser, J. Pochodzalla, M. Potokar, S. Sánchez Majos, B. S. Schlimme, S. Širca, Th. Walcher, and M. Weinriefer. High-precision determination of the electric and magnetic form factors of the proton. *Phys. Rev. Lett.*, **105**:242001, Dec 2010. doi: 10.1103/PhysRevLett.105.242001. URL https://link.aps.org/doi/10.1103/PhysRevLett.105.242001.

[36] J. C. Bernauer, M. O. Distler, J. Friedrich, Th. Walcher, P. Achenbach, C. Ayerbe Gayoso, R. Böhm, Damir Bosnar, L. Debenjak, and L. Doria. Electric and magnetic form factors of the proton. *Phys. Rev. C*, **90**(1):015206, 2014.

[37] M. O. Distler, J. C. Bernauer, and T. Walcher. The RMS charge radius of the proton and Zemach moments. *Phys. Lett. B*, **696**(4):343–347, 2011.

[38] M. Mihovilovič, A. B. Weber, P. Achenbach, T. Beranek, J. Beričič, J. C. Bernauer, R. Böhm, D. Bosnar, M. Cardinali, and L. Correa. First measurement of proton's charge form factor at very low Q^2 with initial state radiation. *Phys. Lett.B*, **771**:194–198, 2017.

[39] M. Mihovilovič and H. Merkel. ISR Experiment at A1-Collaboration. In *EPJ Web of Conf.*, volume **218**, page 04001. EDP Sciences, 2019.

[40] J. P. Karr and D. Marchand. Progress on the proton-radius puzzle, 2019.

[41] R. Gilman et al. Studying the Proton "Radius" Puzzle with μp Elastic Scattering. 2013.

[42] R. Gilman, E. J. Downie, G. Ron, S. Strauch, A. Afanasev, A. Akmal, J. Arrington, H. Atac, C. Ayerbe-Gayoso, and F. Benmokhtar. Technical Design Report for the Paul Scherrer Institute Experiment R-12-01.1: Studying the Proton Radius Puzzle with μ p Elastic Scattering. *arXiv preprint arXiv:1709.09753*, 2017.

[43] R. W. Ellsworth, A. C. Melissinos, J. H. Tinlot, H. von Briesen Jr., T. Yamanouchi, L. M. Lederman, M. J. Tannenbaum, R. L. Cool, and A. Maschke. Muon-proton elastic scattering at high momentum transfers. *Phys. Rev.*, **165**(5):1449, 1968.

[44] L. Camilleri, J. H. Christenson, M. Kramer, L. M. Lederman, Y. Nagashima, and T. Yamanouchi. High-Energy Muon-Proton Scattering: Muon-Electron Universality. *Phys. Rev. Lett.*, **23**(3):153, 1969.

[45] I. Kostoulas, A. Entenberg, H. Jöstlein, A. C. Melissinos, L. M. Lederman, P. Limon, M. May, P. Rapp, H. Gittleson, and T. Kirk. Muon-proton deep elastic scattering. *Phys. Rev. Lett.*, **32**(9):489, 1974.

[46] A. Entenberg, H. Jöstlein, I. Kostoulas, A. C. Melissions, L. M. Lederman, P. Limon, M. May, P. Rapp, H. Gittleson, and T. Kirk. Muon-proton deep inelastic scattering. *Phys. Rev. Lett.*, **32**(9):486, 1974.

[47] Y. S. Tsai. Radiative corrections to electron-proton scattering. *Phys. Rev.*, **122**(6):1898, 1961.

[48] L. C. Maximon. Comments on radiative corrections. *Rev. Mod. Phys.*, 41:193–204, 1969. doi: 10.1103/RevModPhys.41.193.

[49] Y. S. Tsai. Radiative corrections to electron scatterings. *Proceedings of Nucleon Structure Conference at Stanford*, 1963.

[50] L. C. Maximon and J. A. Tjon. Radiative corrections to electron proton scattering. *Phys. Rev. C*, **62**:054320, 2000. doi: 10.1103/PhysRevC.62.054320.

[51] L. N. Hand, D. Go Miller, and R. Wilson. Electric and magnetic form factors of the nucleon. *Rev. of Mod. Phys.*, **35**(2):335, 1963.

[52] J. Litt, G. Buschhorn, D. H. Coward, H. Destaebler, Luke W. Mo, Richard E. Taylor, Barry C. Barish, S. C. Loken, Jerome Pine, and Jerome I. Friedman. Measurement of the ratio of the proton form factors, G_E/G_M, at high momentum transfers and the question of scaling. *Phys. Lett. B*, **31**(1):40–44, 1970.

[53] R. C. Walker, B. W. Filippone, J. Jourdan, R. Milner, R. McKeown, D. Potterveld, L. Andivahis, R. Arnold, D. Benton, and P. Bosted. Measurements of the proton elastic form factors for $1Q23$ $(GeV/c)^2$ at SLAC. *Phys. Rev. D*, **49**(11):5671, 1994.

[54] P. E. Bosted. Empirical fit to the nucleon electromagnetic form factors. *Phys. Rev. C*, **51** (1):409, 1995.

[55] J. Arrington. How well do we know the electromagnetic form factors of the proton? *Phys. Rev. C*, **68**(3):034325, 2003.

[56] M. E. Christy, Abdellah Ahmidouch, C. S. Armstrong, John Arrington, Razmik Asaturyan, Steven Avery, O. K. Baker, Douglas H. Beck, H. P. Blok, and C. W. Bochna. Measurements of electron-proton elastic cross sections for $0.4 < Q^2 < 5.5$ $(GeV/c)^2$. *Phys. Rev. C*, **70**(1):015206, 2004.

[57] I. A. Qattan, J. Arrington, R. E. Segel, X. Zheng, K. Aniol, O. K. Baker, R. Beams, E. J. Brash, J. Calarco, and A. Camsonne. Precision Rosenbluth measurement of the proton elastic form factors. *Phys. Rev. Lett.*, **94**(14):142301, 2005.

[58] R. G. Arnold, C. E. Carlson, and F. Gross. Polarization transfer in elastic electron scattering from nucleons and deuterons. *Phys. Rev. C*, **23**(1):363, 1981.

[59] B. D. Milbrath, J. I. McIntyre, C. S. Armstrong, D. H. Barkhuff, William Bertozzi, J. P. Chen, Dan Dale, G. Dodson, K. A. Dow, and M. B. Epstein. Comparison of polarization observables in electron scattering from the proton and deuteron. *Phys. Rev. Lett.*, **80**(3): 452, 1998.

[60] D. H. Barkhuff, C. S. Armstrong, W. Bertozzi, J. P. Chen, D. Dale, G. Dodson, K. A. Dow, M. B. Epstein, M. Farkhondeh, and J. M. Finn. Measurement of recoil proton polarizations in the electrodisintegration of deuterium by polarized electrons. *Phys. Lett. B*, **470**(1-4):39–44, 1999.

[61] Mark K. Jones, K. A. Aniol, F. T. Baker, J. Berthot, P. Y. Bertin, W. Bertozzi, A. Besson, L. Bimbot, W. U. Boeglin, and E. J. Brash. G e p/g m p ratio by polarization transfer in e p e p. *Phys. Rev. Lett.*, **84**(7):1398, 2000.

[62] O. Gayou, K. Wijesooriya, A. Afanasev, M. Amarian, K. Aniol, S. Becher, K. Benslama, L. Bimbot, P. Bosted, and E. Brash. Measurements of the elastic electromagnetic form factor ratio μ p g ep/g mp via polarization transfer. *Phys. Rev. C*, **64**(3):038202, 2001.

[63] O. Gayou, K. A. Aniol, T. Averett, F. Benmokhtar, W. Bertozzi, L. Bimbot, E. J. Brash, J. R. Calarco, C. Cavata, and Z. Chai. Measurement of g e p/g m p in e p e p to q 2= 5.6 gev 2. *Phys. Rev. Lett.*, **88**(9):092301, 2002.

[64] A. J. R. Puckett, E. J. Brash, O. Gayou, M. K. Jones, L. Pentchev, C. F. Perdrisat, V. Punjabi, K. A. Aniol, T. Averett, and F. Benmokhtar. Final analysis of proton form factor ratio data at $Q^2 = 4.0, 4.8, and 5.6 GeV^2$. *Phys. Rev. C*, **85**(4):045203, 2012.

[65] A. J. R. Puckett, E. J. Brash, M. K. Jones, W. Luo, M. Meziane, L. Pentchev, C. F. Perdrisat, V. Punjabi, F. R. Wesselmann, and A. Ahmidouch. Recoil polarization measurements of the proton electromagnetic form factor ratio to q 2= 8.5 gev 2. *Phys. Rev. Lett.*, **104**(24):242301, 2010.

[66] J. Arrington. How well do we know the electromagnetic form-factors of the proton? *Phys. Rev. C*, **68**:034325, 2003. doi: 10.1103/PhysRevC.68.034325.

[67] P. A. M. Guichon and M. Vanderhaeghen. How to reconcile the rosenbluth and the polarization transfer methods in the measurement of the proton form factors. *Phys. Rev. Lett.*, **91**(14):142303, 2003.

[68] P. G. Blunden, W. Melnitchouk, and J. A. Tjon. Two-photon exchange and elastic electron-proton scattering. *Phys. Rev. Lett.*, **91**(14):142304, 2003.

[69] C. E. Carlson and M. Vanderhaeghen. Two-photon physics in hadronic processes. *Annu. Rev. Nucl. Part. Sci.*, **57**:171–204, 2007.

[70] C. F. Perdrisat, V. Punjabi, and M. Vanderhaeghen. Nucleon electromagnetic form factors. *Prog. in Part. and Nucl. Phys.*, **59**(2):694–764, 2007.

[71] A. Afanasev, P. G. Blunden, D. Hasell, and B. A. Raue. Two-photon exchange in elastic electron–proton scattering. *Prog. in Part. and Nucl. Phys.*, **95**:245–278, 2017.

[72] R. Hofstadter, H. R. Fechter, and J. A. McIntyre. High-energy electron scattering and nuclear structure determinations. *Phys. Rev.*, **92**(4):978, 1953.

[73] R. Hofstadter. Electron scattering and nuclear structure. *Rev. of Mod. Phys.*, **28**(3):214, 1956.

[74] R. Karplus, A. Klein, and J. Schwinger. Electrodynamic displacement of atomic energy levels. II. Lamb shift. *Phys. Rev.*, **86**(3):288, 1952.

[75] S. Thomas, H. Fleurbaey, S. Galtier, L. Julien, F. Biraben, and F. Nez. High-resolution hydrogen spectroscopy and the proton radius puzzle. *Annalen der Physik*, **531**(5):1800363, 2019.

[76] F. Biraben. Spectroscopy of atomic hydrogen. *The European Physical Journal Special Topics*, **172**(1):109–119, 2009.

[77] U. D. Jentschura. Proton radius, Darwin-Foldy term and radiative corrections. *The Euro. Phys. Jour. D*, **61**(1):7–14, 2011.

[78] P. J. Mohr and B. N. Taylor. CODATA recommended values of the fundamental physical constants: 2002. *Rev. of Mod. Phys.*, **77**(1):1, 2005.

[79] Peter J. Mohr, Barry N. Taylor, and David B. Newell. CODATA recommended values of the fundamental physical constants: 2006. *Jour. of Phys. and Chem. Ref. Data*, **80**(3): 633–1284, 2008.

[80] W. E. Lamb Jr. and R. C. Retherford. Fine structure of the hydrogen atom by a microwave method. *Phys. Rev.*, **72**(3):241, 1947.

[81] M. O. Scully and A. A. Svidzinsky. The Lamb shift yesterday, today, and tomorrow. *Science*, **328**(5983):1239–1241, 2010.

[82] M. Fischer, N. Kolachevsky, M. Zimmermann, R. Holzwarth, Th. Udem, T. W. Hänsch, M. Abgrall, J. Grünert, I. Maksimovic, and S. Bize. New limits on the drift of fundamental constants from laboratory measurements. *Phys. Rev. Lett.*, **92**(23):230802, 2004.

[83] B. De Beauvoir, F. Nez, L. Julien, B. Cagnac, F. Biraben, D. Touahri, L. Hilico, O. Acef, A. Clairon, and J. J. Zondy. Absolute frequency measurement of the 2 s- 8 s/d transitions in hydrogen and deuterium: New determination of the rydberg constant. *Phys. Rev. Lett.*, **78**(3):440, 1997.

[84] C. Schwob, L. Jozefowski, B. De Beauvoir, L. Hilico, F. Nez, L. Julien, F. Biraben, O. Acef, J. J. Zondy, and A. Clairon. Optical Frequency Measurement of the 2S-12D Transitions in Hydrogen and Deuterium: Rydberg Constant and Lamb Shift Determinations. *Phys. Rev. Lett.*, **82**(25):4960, 1999.

[85] D. Gotta. Precision spectroscopy of light exotic atoms. *Prog. in Part. and Nucl. Phys.*, **52**(1):133–195, 2004.

[86] Savely G. Karshenboim and Valery B. Smirnov. Recent Progress in the Precision Physics of Simple Atoms. In *Precision Physics of Simple Atomic Systems*, pages 1–12. Springer, 2003.

[87] M. Di Giacomo. A sensitive test of quantum electrodynamics: The 2S-2P energy difference of muonic hydrogen. *Nucl. Phys. B*, **11**(CERN-TH-1006-ERR):411–427, 1969.

[88] A. Placci, E. Polacco, E. Zavattini, K. Ziock, C. Carboni, U. Gastaldi, G. Gorini, and G. Torelli. Observation of muonic X-rays in hydrogen gas. *Phys. Lett. B*, **32**(5):413–415, 1970.

[89] H. Anderhub, H. Hofer, F. Kottmann, P. LeCoultre, D. Makowiecki, O. Pitzurra, B. Sapp, P. G. Seiler, M. Wälchli, and D. Taqqu. Search for the metastable 2S state in muonic hydrogen. *Phys. Lett. B*, **71**(2):443–445, 1977.

[90] P. O. Egan, S. Dhawan, V. W. Hughes, D. C. Lu, F. G. Mariam, Paul A. Souder, J. Vetter, G. Zu Putlitz, P. A. Thompson, and A. B. Denison. Search for long-lived 2 S muonic hydrogen in H_2 gas. *Phys. Rev. A*, **23**(3):1152, 1981.

[91] H. Anderhub, H. P. Von Arb, J. Böcklin, F. Dittus, R. Ferreira Marques, H. Hoper, F. Kottmann, D. Taqqu, and J. Unternährer. Measurement of the K-line intensity ratios in muonic hydrogen between 0.25 and 150 Torr gas pressures. *Phys. Lett. B*, **143**(1-3): 65–68, 1984.

[92] F. Kottmann, H. Daniel, F. J. Hartmann, P. Hauser, C. Maierl, V. E. Markushin, M. Mühlbauer, C. Petitjean, R. Pohl, and W. Schott. Kinetic energies of exotic H atoms at formation and cascade. *Hyperfine interactions*, **119**(1-4):3–10, 1999.

[93] R. Pohl, H. Daniel, F. J. Hartmann, P. Hauser, Y. W. Liu, F. Kottmann, C. Maierl, V. E. Markushin, M. Mühlbauer, and C. Petitjean. Observation of the Molecular Quenching of μp (2S) Atoms. *Hyperfine interactions*, **138**(1-4):35–40, 2001.

[94] R. Pohl, H. Daniel, F. J. Hartmann, P. Hauser, F. Kottmann, V. E. Markushin, M. Mühlbauer, C. Petitjean, W. Schott, and D. Taqqu. Observation of Long-Lived Muonic Hydrogen in the 2 S State. *Phys. Rev. Lett.*, **97**(19):193402, 2006.

[95] R. Pohl, F. Nez, L. M. Fernandes, F. D. Amaro, F. Biraben, J. M. R. Cardoso, D. S. Covita, A. Dax, S. Dhawan, and M. Diepold. Laser spectroscopy of muonic deuterium. *Science*, **353**(6300):669–673, 2016.

[96] D. Taqqu, F. Biraben, C. Conde, T. W. Hänsch, F. J. Hartmann, P. Hauser, P. Indelicato, P. Knowles, F. Kottmann, and F. Mulhauser. Laser spectroscopy of the Lamb shift in muonic hydrogen. *Hyperfine Interactions*, **119**(1-4):311–315, 1999.

[97] R. Pohl, F. Biraben, CAN Conde, C. Donche Gay, T. W. Hänsch, F. J. Hartmann, P. Hauser, V. W. Hughes, O. Huot, and P. Indelicato. Experiment to measure the Lamb shift in muonic hydrogen. *Hyperfine Interactions*, **127**(1-4):161–166, 2000.

[98] Th. Udem, A. Huber, B. Gross, J. Reichert, M. Prevedelli, M. Weitz, and Th. W. Hänsch. Phase-coherent measurement of the hydrogen 1 s- 2 s transition frequency with an optical frequency interval divider chain. *Phys. Rev. Lett.*, **79**(14):2646, 1997.

[99]

[100] I. Sick. On the rms-radius of the proton. *Phys. Lett. B*, **576**(1-2):62–67, 2003.

[101] Peter J. Mohr, Barry N. Taylor, and David B. Newell. Codata recommended values of the fundamental physical constants: 2010. *J. Phys. Chem. Ref. Data*, **41**(4):043109, 2012.

[102] J. Arrington. An Examination of Proton Charge Radius Extractions from e–p Scattering Data. *Journal of Physical and Chemical Reference Data*, **44**(3):031203, 2015.

[103] A. Antognini, F. Nez, K. Schuhmann, F. D Amaro, F. Biraben, J. M. Cardoso, D. S. Covita, A. Dax, S. Dhawan, and M. Diepold. Proton structure from the measurement of 2s-2p transition frequencies of muonic hydrogen. *Science*, **339**(6118):417–420, 2013.

[104] X. Zhan, K. Allada, D. S. Armstrong, J. Arrington, W. Bertozzi, W. Boeglin, J. P. Chen, K. Chirapatpimol, S. Choi, and E. Chudakov. High-precision measurement of the proton elastic form factor ratio μpge/gm at low q2. *Phys. Lett. B*, **705**(1-2):59–64, 2011.

[105] J. J. Krauth, M. Diepold, B. Franke, A. Antognini, F. Kottmann, and R. Pohl. Theory of the n= 2 levels in muonic deuterium. *Ann. of Phys.*, **366**:168–196, 2016.

[106] R. Pohl, F. Nez, T. Udem, A. Antognini, A. Beyer, H. Fleurbaey, A. Grinin, T. W. Hänsch, L. Julien, and F. Kottmann. Deuteron charge radius and rydberg constant from spectroscopy data in atomic deuterium. *Metrologia*, **54**(2):L1, 2017.

[107] Peter J. Mohr, David B. Newell, and Barry N. Taylor. CODATA Recommended Values of the Fundamental Physical Constants: 2014. *Rev. Mod. Phys.*, **88**(3):035009, 2016. doi: 10.1103/RevModPhys.88.035009.

[108] R. J. Hill and G. Paz. Model-independent extraction of the proton charge radius from electron scattering. *Phys. Rev. D*, **82**(11):113005, 2010.

[109] E. Kraus, K. E. Mesick, A. White, Ronald Gilman, and S. Strauch. Polynomial fits and the proton radius puzzle. *Phys. Rev. C*, **90**(4):045206, 2014.

[110] K. Griffioen, C. Carlson, and S. Maddox. Consistency of electron scattering data with a small proton radius. *Phys. Rev. C*, **93**(6):065207, 2016.

[111] Jan C. Bernauer and M. O. Distler. Avoiding common pitfalls and misconceptions in extractions of the proton radius. *arXiv preprint arXiv:1606.02159*, 2016.

[112] B. Adams, V. Anosov, N. Zhuravlev, G. V. Meshcheryakov, O. M. Kouznetsov, K. Kondo, R. R. Dusaev, S. Wallner, A. Kveton, and D. Keller. COMPASS++/AMBER: Proposal for Measurements at the M2 beam line of the CERN SPS Phase-1: 2022-2024. Technical report, 2019.

[113] O. Arnoult, F. Nez, L. Julien, and F. Biraben. Optical frequency measurement of the 1S–3S two-photon transition in hydrogen. *The Euro. Phys. Jour. D*, **60**(2):243–256, 2010.

[114] A. Beyer, J. Alnis, K. Khabarova, A. Matveev, C. G. Parthey, D. C. Yost, R. Pohl, T. Udem, T. W. Hänsch, and N. Kolachevsky. Precision spectroscopy of the 2S-4P transition in atomic hydrogen on a cryogenic beam of optically excited 2S atoms. *Annalen der Physik*, **525**(8-9):671–679, 2013.

[115] A. De Rujula. QED is not endangered by the proton's size. *Phys. Lett. B*, **693**(5):555–558, 2010.

[116] A. De Rujula. QED confronts the radius of the proton. *Phys. Lett. B*, **697**(1):26–31, 2011.

[117] B. Y. Wu and C. W. Kao. The third Zemach moment and the size of the proton. *arXiv preprint arXiv:1108.2968*, 2011.

[118] B. Batell, D. McKeen, and M. Pospelov. New parity-violating muonic forces and the proton charge radius. *Phys. Rev. Lett.*, **107**(1):011803, 2011.

[119] L. B. Wang and W. T. Ni. Proton radius puzzle and large extra dimensions. *Mod. Phys. Lett. A*, **28**(20):1350094, 2013.

[120] Roberto Onofrio. Proton radius puzzle and quantum gravity at the fermi scale. *EPL (Europhysics Letters)*, **104**(2):20002, 2013.

[121] Savely G. Karshenboim, David McKeen, and Maxim Pospelov. Constraints on muon-specific dark forces. *Phys. Rev. D*, **90**(7):073004, 2014.

[122] C. E. Carlson and M. Freid. Extending theories on muon-specific interactions. *Phys. Rev. D*, **92**(9):095024, 2015.

[123] Y. S. Liu, D. McKeen, and G. A. Miller. Electrophobic scalar boson and muonic puzzles. *Phys. Rev. Lett.*, **117**(10):101801, 2016.

[124] P. Mergell, Ulf-G. Meißner, and D. Drechsel. Dispersion-theoretical analysis of the nucleon electromagnetic form factors. *Nucl. Phys. A*, **596**(3-4):367–396, 1996.

[125] M. A. Belushkin, H. W. Hammer, and U. G. Meißner. Dispersion analysis of the nucleon form factors including meson continua. *Phys. Rev. C*, **75**(3):035202, 2007.

[126] I. T. Lorenz, Ulf-G. Meißner, H. W. Hammer, and Y-B. Dong. Theoretical constraints and systematic effects in the determination of the proton form factors. *Phys. Rev. D*, **91** (1):014023, 2015.

[127] H. W. Hammer and U. G. Meißner. The proton radius: From a puzzle to precision. *arXiv preprint arXiv:1912.03881*, 2019.

[128] Z. Ye, J. Arrington, R. J. Hill, and G. Lee. Proton and neutron electromagnetic form factors and uncertainties. *Phys. Lett. B*, **777**:8–15, 2018.

[129] J. M. Alarcon, D. W. Higinbotham, C. Weiss, and Z. Ye. Proton charge radius extraction from electron scattering data using dispersively improved chiral effective field theory. *Phys. Rev. C*, **99**(4):044303, 2019.

[130] T. Rostomyan. Status of the MUSE experiment. *Ukrainian Journal of Physics*, **64**(7): 624–624, 2019.

[131] A. Beyer, L. Maisenbacher, A. Matveev, R. Pohl, K. Khabarova, A. Grinin, T. Lamour, D. C. Yost, T. W. Hänsch, and N. Kolachevsky. The rydberg constant and proton size from atomic hydrogen. *Science*, **358**(6359):79–85, 2017.

[132] H. Fleurbaey, S. Galtier, S. Thomas, M. Bonnaud, L. Julien, F. Biraben, F. Nez, M. Abgrall, and J. Guéna. New measurement of the 1 s- 3 s transition frequency of hydrogen: contribution to the proton charge radius puzzle. *Phys. Rev. Lett.*, **120**(18):183001, 2018.

[133] S. Agostinelli, J. Allison, K. Amako, J. Apostolakis, H. Araujo, P. Arce, M. Asai, D. Axen, S. Banerjee, and G. Barrand. GEANT4a simulation toolkit. *Nuclear instruments and methods in physics research section A: Accelerators, Spectrometers, Detectors and Associated Equipment*, **506**(3):250–303, 2003.

[134] S. Strauch. The MUon Scattering Experiment (MUSE) at the Paul Scherrer Institute. *PoS*, page 136, 2018.

[135] A. Lahiri and P. B. Pal. *A first book of quantum field theory.* CRC Press, 2005.

[136] J. C. Ward. An identity in quantum electrodynamics. *Phys. Rev.*, **78**(2):182, 1950.

[137] Y. Takahashi. On the generalized Ward identity. *Il Nuovo Cimento (1955-1965)*, **6**(2): 371–375, 1957.

[138] M. E. Peskin. *An introduction to quantum field theory.* CRC press, 2018.

[139] M. Vanderhaeghen, J. M. Friedrich, D. Lhuillier, D. Marchand, L. Van Hoorebeke, and J. Van de Wiele. QED radiative corrections to virtual Compton scattering. *Phys. Rev. C*, **62**(2):025501, 2000.

[140] V. Bernard, N. Kaiser, and U. G. Meissner. Chiral dynamics in nucleons and nuclei. *Int. J. Mod. Phys.*, E4:193–346, 1995. doi: 10.1142/S0218301395000092.

[141] W. Greiner. Quantum electrodynamics of strong fields. In *Hadrons and Heavy Ions*, pages 95–226. Springer, 1985.

[142] Y. S. Tsai. High-energy electron-electron scattering. *Phys. Rev.*, **120**(1):269, 1960.

[143] R. P. Feynman. Space-time approach to quantum electrodynamics. *Phys. Rev.*, **76**(6): 769, 1949.

[144] J. L. Friar, J. Martorell, and D. W. L. Sprung. Hadronic vacuum polarization and the Lamb shift. *Phys. Rev. A*, **59**(5):4061, 1999.

[145] T. Kinoshita, B. Niić, and Y. Okamoto. Hadronic contributions to the anomalous magnetic moment of the muon. *Phys. Rev. D*, **31**(8):2108, 1985.

[146] T. Kinoshita, B. Nižić, and Y. Okamoto. Improved theory of the muon anomalous magnetic moment. *Phys. Rev. Lett.*, **52**(9):717, 1984.

[147] A. Afanasev, P. G. Blunden, D. Hasell, and B. A. Raue. Two-photon exchange in elastic electronproton scattering. *Prog. Part. Nucl. Phys.*, 95:245–278, 2017. doi: 10.1016/j.ppnp.2017.03.004.

[148] E. Haug and W. Nakel. *The elementary process of bremsstrahlung*, volume **73**. World Scientific, 2004.

[149] F. Bloch and A. Nordsieck. Note on the radiation field of the electron. *Phys. Rev.*, **52**(2): 54, 1937.

[150] J. M. Jauch and F. Rohrlich. The infrared divergence. *Helvetica Physica Acta*, **27**(7): 613–636, 1954.

[151] D. R. Yennie, S. C. Frautschi, and H. Suura. The infrared divergence phenomena and high-energy processes. *Ann. of Phys.*, **13**(3):379–452, 1961.

[152] L. D. Landau, L. D. Landau, L. D. J. Landau, L. LanDau, and L. Landau. On the energy loss of fast particles by ionization. 1944.

[153] R. Ent, B. W. Filippone, Naomi C. R. Makins, R. G. Milner, T. G. ONeill, and D. A. Wasson. Radiative corrections for (e, e p) reactions at GeV energies. *Phys. Rev. C*, **64** (5):054610, 2001.

[154] G. I. Gakh, M. I. Konchatnij, N. P. Merenkov, and Egle Tomasi-Gustafsson. Radiative corrections to elastic proton-electron scattering measured in coincidence. *Phys. Rev. C*, **95**(5):055207, 2017.

[155] A. Afanasev, I. Akushevich, and N. Merenkov. Model independent radiative corrections in processes of polarized electron-nucleon elastic scattering. *Phys. Rev. D*, **64**(11):113009, 2001.

[156] I. Akushevich, O. F. Filoti, A. Ilyichev, and N. Shumeiko. Monte Carlo generator ELRADGEN 2.0 for simulation of radiative events in elastic ep-scattering of polarized particles. *Comp. Phys. Comm.*, **183**(7):1448–1467, 2012.

[157] R. D. Bucoveanu and H. Spiesberger. QED radiative corrections for Polarized Lepton-Proton Scattering. *PoS*, SPIN2018:115, 2019. doi: 10.22323/1.346.0115.

[158] C. De Calan, H. Navelet, and J. Picard. Generalized radiative corrections for hadronic targets. *Nucl. Phys. B*, **348**(1):47–65, 1991.

[159] I. Akushevich, H. Gao, A. Ilyichev, and M. Meziane. Radiative corrections beyond the ultra relativistic limit in unpolarized ep elastic and Møller scatterings for the PRad Experiment at Jefferson Laboratory. *The Euro. Phys. Jour. A*, **51**(1):1, 2015.

[160] R. D. Bucoveanu and H. Spiesberger. Second-Order Leptonic Radiative Corrections for Lepton-Proton Scattering. 2018.

[161] R. P. Feynman. Relativistic cut-off for quantum electrodynamics. *Phys. Rev.*, **74**(10): 1430, 1948.

[162] A. I. Akhiezer and V. B. Berestetskii. Quantum Electrodynamics. (Engl. trans.), 1965.

[163] R. E. Gerasimov and V. S. Fadin. Analysis of approximations used in calculations of radiative corrections to electron-proton scattering cross section. *Phys. of Atom. Nucl.*, **78** (1):69–91, 2015.

[164] D. J. Gross and F. Wilczek. Ultraviolet behavior of non-abelian gauge theories. *Phys. Rev. Lett.*, **30**(26):1343, 1973.

[165] Y. Nambu and G. Jona-Lasinio. Dynamical model of elementary particles based on an analogy with superconductivity. ii. *Phys. Rev.*, **124**(1):246, 1961.

[166] Y. Nambu. Axial vector current conservation in weak interactions. *Phys. Rev. Lett.*, **4** (7):380, 1960.

[167] S. Weinberg. Phenomenological lagrangians. *Physica A: Statistical Mechanics and its Applications*, **96**(1-2):327–340, 1979.

[168] S. Weinberg. Effective field theory, past and future. In *Memorial Volume For Y. Nambu*, pages 1–24. World Scientific, 2016.

[169] Aneesh V. Manohar. Effective field theories. In *Perturbative and nonperturbative aspects of quantum field theory*, pages 311–362. Springer, 1977.

[170] M. Rho. The folk theorem on effective field theory: How does it fare in nuclear physics? *Journal of the Korean Physical Society*, **71**(7):374–395, 2017.

[171] T. Appelquist and J. Carazzone. Infrared singularities and massive fields. *Phys. Rev. D*, **11**(10):2856, 1975.

[172] Veronique Bernard, Norbert Kaiser, Joachim Kambor, and Ulf-G. Meißner. Chiral structure of the nucleon. *Nucl. Phys. B*, **388**(2):315–345, 1992.

[173] J. F. Donoghue, E. Golowich, and B. R. Holstein. *Dynamics of the standard model*, volume **35**. Cambridge university press, 2014.

[174] L. L. Foldy and S. A. Wouthuysen. On the dirac theory of spin 1/2 particles and its non-relativistic limit. *Phys. Rev.*, **78**(1):29, 1950.

[175] T. Mannel, W. Roberts, and Z. Ryzak. A Derivation of the heavy quark effective Lagrangian from QCD. *Nucl. Phys. B*, **368**(1):204–217, 1992.

[176] G. Ecker. Chiral symmetry. In *Broken Symmetries*, pages 83–129. Springer, 1999.

[177] S. L. Adler. Consistency conditions on the strong interactions implied by a partially conserved axial-vector current. ii. *Phys. Rev.*, **139**(6B):B1638, 1965.

[178] S. L. Adler and W. A. Bardeen. Absence of higher-order corrections in the anomalous axial-vector divergence equation. *Phys. Rev.*, **182**(5):1517, 1969.

[179] S. Vandoren and P. V. Nieuwenhuizen. Lectures on instantons. *arXiv preprint arXiv:0802.1862*, 2008.

[180] T. R. Hemmert, B. R. Holstein, and J. Kambor. Heavy baryon chiral perturbation theory with light deltas. *Jour. of Phys. G: Nucl. and Part. Phys.*, **24**(10):1831, 1998.

[181] Y. Kosmann-Schwarzbach. The Noether theorems. In *The Noether Theorems*, pages 55–64. Springer, 2011.

[182] E. P. Wigner. On the law of conservation of heavy particles. *Proceedings of the National Academy of Sciences of the United States of America*, **38**(5):449, 1952.

[183] H. Weyl. Elektron und gravitation. *Zeitschrift für Physik*, **56**(5-6):330–352, 1929.

[184] J. Goldstone. Field theories with Superconductor solutions. *Il Nuovo Cimento (1955-1965)*, **19**(1):154–164, 1961.

[185] J. Goldstone, A. Salam, and S. Weinberg. Broken symmetries. *Phys. Rev.*, **127**(3):965, 1962.

[186] C. Vafa and E. Witten. Restrictions on symmetry breaking in vector-like gauge theories. *Nucl. Phys. B*, **234**(1):173–188, 1984.

[187] M. L. Goldberger and S. B. Treiman. Form factors in β decay and μ capture. *Phys. Rev.*, **111**(1):354, 1958.

[188] A. A. Petrov and A. E. Blechman. *Effective Field Theories*. World Scientific, 2015.

[189] J. Gasser and H. Leutwyler. Chiral perturbation theory to one loop. *Annals of Physics*, **158**(1):142–210, 1984.

[190] Stefan Scherer. Introduction to chiral perturbation theory. In *Advances in Nuclear Physics, Volume 27*, pages 277–538. Springer, 2003.

[191] S. Coleman, J. Wess, and B. Zumino. Structure of phenomenological lagrangians. i. *Phys. Rev.*, **177**(5):2239, 1969.

[192] Curtis G. Callan Jr., S. Coleman, J. Wess, and B. Zumino. Structure of phenomenological Lagrangians. II. *Phys. Rev.*, **177**(5):2247, 1969.

[193] H. Leutwyler. On the foundations of chiral perturbation theory. *arXiv preprint hep-ph/9311274*, 1993.

[194] V. E. Herscovitz, F. Erasmo, and V. C. A. Zen. *Hadron Physics 94: Topics On The Structure And Interaction Of Hadronic Systems*. World Scientific, 1995.

[195] J. Gasser, M. E. Sainio, and A. Švarc. Nucleons with chiral loops. *Nucl. Phys. B*, **307**(4): 779–853, 1988.

[196] S. L. Adler. Calculation of the axial-vector coupling constant renormalization in β decay. *Phys. Rev. Lett.*, **14**(25):1051, 1965.

[197] W. I. Weisberger. Renormalization of the weak axial-vector coupling constant. *Phys. Rev. Lett.*, **14**(25):1047, 1965.

[198] V. F. Müller and J. Rothleitner. The Adler-Weisberger sum rule. *Zeitschrift für Physik*, **202**(1):349–363, 1967.

[199] S. Weinberg. WEINBERG 1967. *Phys. Rev. Lett*, **19**:1264, 1967.

[200] S. Weinberg. Pion scattering lengths. *Phys. Rev. Lett.*, **17**(11):616, 1966.

[201] Y. Tomozawa. Nuovo Cimento A 46, 707 (1966). *Phys. Rev. Lett*, **17**:616, 1966.

[202] N. M. Kroll and M. A. Ruderman. A theorem on photo-meson production near threshold and the suppression of pairs in pseudoscalar meson theory. *Phys. Rev.*, **93**(1):233, 1954.

[203] P. J. Ellis and H. B. Tang. Pion-nucleon scattering in a new approach to chiral perturbation theory. *Physical Review C*, **57**(6):3356, 1998.

[204] T. Becher and H. Leutwyler. Baryon chiral perturbation theory in manifestly Lorentz invariant form. *The Eur. Phys. Jour. C-Particles and Fields*, **9**(4):643–671, 1999.

[205] T. Becher. Lorentz invariant baryon ChPT. In *Chiral Dynamics*, pages 66–77. World Scientific, 2001.

[206] E. Jenkins and A. V. Manohar. Baryon chiral perturbation theory using a heavy fermion lagrangian. *Phys. Lett. B*, **255**(4):558–562, 1991.

[207] B. Grinstein. The static quark effective theory. *Nucl. Phys. B*, **339**(2):253–268, 1990.

[208] H. Georgi. An effective field theory for heavy quarks at low energies. *Phys. Lett. B*, **240** (3-4):447–450, 1990.

[209] J. Gasser. Hadron masses and the sigma commutator in light of chiral perturbation theory. *Annals of Phys.*, **136**(1):62–112, 1981.

[210] J. Gasser and H. Leutwyler. Quark masses. *Phys. Repo.*, **87**(3):77–169, 1982.

[211] A. Krause. Baryon matrix elements of the vector current in chiral perturbation theory. *Helvetica Physica Acta*, **63**(1/2):3–70, 1990.

[212] P. Talukdar, F. Myhrer, G. Meher, and U. Raha. Low-Energy Lepton-Proton Bremsstrahlung via Effective Field Theory. *Eur. Phys. J.*, A54(11):195, 2018. doi: 10.1140/epja/i2018-12629-8.

[213] F. Myhrer, P. Talukdar, and U. Raha. Lepton Bremsstrahlung at Low Energies. *Few-Body Syst.*, **59**(4):62, 2018.

[214] J. D. Bjorken and S. D. Drell. *Relativistic quantum mechanics*. McGraw-Hill, 1965.

[215] N. Fettes. Phd dissertation. *Univ. Bonn*, 2000.

[216] V. Bernard, H. W. Fearing, T. R. Hemmert, and U. G. Meißner. The form factors of the nucleon at small momentum transfer. *Nucl. Phys. A*, **635**(1-2):121–145, 1998.

[217] G. Ecker. Chiral invariant renormalization of the pion–nucleon interaction. *arXiv preprint hep-ph/9402337*, 1994.

[218] M. Luke and A. V. Manohar. Reparameterisation invariance constraints on heavy particle effective field theories. *Phys. Lett. B*, **286**(3-4):348–354, 1992.

[219] J. R. Dunning Jr., K. W. Chen, A. A. Cone, G. Hartwig, N. F. Ramsey, J. K. Walker, and R. Wilson. Quasi-elastic electron-deuteron scattering and neutron form factors. *Phys. Rev.*, **141**(4):1286, 1966.

[220] S. Ando, H. W. Fearing, V. Gudkov, K. Kubodera, F. Myhrer, S. Nakamura, and T. Sato. Neutron beta-decay in effective field theory. *Phys. Lett. B*, **595**(1-4):250–259, 2004.

[221] P. Talukdar, V. C. Shastry, U. Raha, and F. Myhrer. Lepton-proton two-photon exchange in chiral perturbation theory. *Phys. Rev. D*, **101**(1):013008, 2020.

[222] W. A. McKinley Jr. and H. Feshbach. The Coulomb scattering of relativistic electrons by nuclei. *Phys. Rev.*, **74**(12):1759, 1948.

[223] M. K. Jones et al. G_{E_p}/G_{M_p} ratio by polarization transfer in $\vec{e}\mathrm{p} \to \mathrm{e}\vec{p}$. *Phys. Rev. Lett.*, 84:1398–1402, 2000. doi: 10.1103/PhysRevLett.84.1398.

[224] Ed. J. Brash, A. Kozlov, Sh. Li, and Garth M. Huber. New empirical fits to the proton electromagnetic form factors. *Phys. Rev. C*, **65**(5):051001, 2002.

[225] O. Tomalak and M. Vanderhaeghen. Two-photon exchange corrections in elastic muon-proton scattering. *Phys. Rev. D*, **90**(1):013006, 2014.

[226] O. Tomalak and M. Vanderhaeghen. Subtracted dispersion relation formalism for the two-photon exchange correction to elastic electron-proton scattering: Comparison with data. *The Euro. Phys. Jour. A*, **51**(2):24, 2015.

[227] O. Tomalak and M. Vanderhaeghen. Two-photon exchange correction in elastic unpolarized electron-proton scattering at small momentum transfer. *Phys. Rev. D*, **93**(1):013023, 2016.

[228] O. Tomalak. Two-photon exchange correction to the hyperfine splitting in muonic hydrogen. *The Euro. Phys. Jour. C*, **77**(12):858, 2017.

[229] O. Tomalak and M. Vanderhaeghen. Two-photon exchange correction to muon–proton elastic scattering at low momentum transfer. *The Euro. Phys. Jour. C*, **76**(3):125, 2016.

[230] O. Koshchii and A. Afanasev. Charge asymmetry in elastic scattering of massive leptons on protons. *Phys. Rev.*, D96(1):016005, 2017. doi: 10.1103/PhysRevD.96.016005.

[231] I. Sick and D. Trautmann. On the rms radius of the deuteron. *Nucl. Phys. A*, **637**(5): 559–575, 1998.

[232] P. G. Blunden and I. Sick. Proton radii and two-photon exchange. *Phys. Rev. C*, **72**(5): 057601, 2005.

[233] G. t Hooft and M. Veltman. Scalar one-loop integrals. *Nucl. Phys. B*, **153**:365–401, 1979.

[234] G. Passarino and M. Veltman. One-loop corrections for $e^+ e^-$ annihilation into $\mu^+ \mu^-$ in the Weinberg model. *Nucl. Phys. B*, **160**(1):151–207, 1979.

[235] M. Beneke and V. A. Smirnov. Asymptotic expansion of Feynman integrals near threshold. *arXiv preprint hep-ph/9711391*, 1997.

[236] A. I. Davydychev and A. G. Grozin. HQET quark-gluon vertex at one loop. *The Euro. Phys. Jour. C-Particles and Fields*, **20**(2):333–342, 2001.

[237] J. Zupan. One loop scalar functions in the heavy-quark effective theory. *The Euro. Phys. Jour. C-Particles and Fields*, **25**(2):233–244, 2002.

[238] R. Gastmans and R. Meuldermans. Dimensional regularization of the infrared problem. *Nucl. Phys. B*, **63**:277–284, 1973.

[239] W. J. Marciano and A. Sirlin. Dimensional regularization of infrared divergences. *Nucl. Phys. B*, **88**(1):86–98, 1975.

[240] S. Scherer. Introduction to Chiral Perturbation Theory, 2002.

[241] Claude Itzykson and Jean-Bernard Zuber. *Quantum field theory*. Courier Corporation, 2012.

[242] F. E. Low. Bremsstrahlung of very low-energy quanta in elementary particle collisions. *Phys. Rev.*, **110**(4):974, 1958.